Hybrid Wireless Power Transfer System for Sensor Applications in Harsh Environments

Submitted in fulfilment of the requirements for the

Degree of Doctor of Philosophy

James Watt School of Engineering
College of Engineering
University of Glasgow
2025

"Tell me and I forget. Teach me and I remember. Involve me and I learn."

— Benjamin Franklin

"Give a man a fish and you feed him for a day; teach a man to fish and you feed him a lifetime."

— Laozi

Abstract

Wireless Power Transfer (WPT) is a promising solution to eliminate the dependence of low-power devices on batteries and cables. WPT technologies, including electric field coupling (EC-WPT), magnetic field coupling (MC-WPT), radio frequency (RF-WPT), laser (L-WPT), and ultrasound (U-WPT), each have inherent limitations. EC-WPT, MC-WPT, and U-WPT are restricted to short distances, L-WPT is limited by precise alignment, while metal, water and biological tissues are harsh transmission environment for RF-WPT. These constraints make powering devices in harsh environments, such as underwater, underground, within metal enclosures, distributed over long distances, or mobile, a significant challenge. Traditional battery-based, wired and independent WPT solutions are often impractical due to high maintenance costs, accessibility issues, and size limitations.

This study proposes a hybrid wireless power transmission system integrating RF-WPT and U-WPT to establish a dual-path energy transfer framework in air and metallic environments. The RF link enables long-range and omnidirectional energy transmission, while the ultrasonic link supports power safe penetration through metal, water, and biological tissues. However, integrating these two technologies is challenging due to their fundamentally different transmission mechanisms, necessitating distinct circuit architectures and components. This work develops a combined radio frequency and ultrasonic wireless power transfer (CRFU-WPT) architecture, analyses the link loss between RF and ultrasonic transmission, and establishes a power budgeting model for various application scenarios. An experimental validation demonstrates the system's capability to power a low-power Bluetooth sensor through a 10 mm metal plate with 0 dBm input, achieving a conversion circuit efficiency of 39.7%.

Contents

List of Tables

List of Figures

List of Associated Publications

- Jiang, Y., Zhong, M., Ma, Y., Khusna, E. M., Yi, Y., Ofiare, A., Al-Taai, Q., Al-Moathin, A. and Li, C. (2023) An X-band Lens Antenna Based on Metasurface. In: 16th UK-Europe-China Workshop on Millimetre Waves and Terahertz Technologies (UCMMT2023), Guangzhou, China, 31 Aug - 02 Sep 2023, ISBN 9798350339406 (doi: 10.1109/UCMMT58116.2023.10310524)

- Ma, Y., Jiang, Y. and Li, C. (2024) Combined RF-Ultrasonic Wireless Powering System for Sensor Applications in Harsh Environment. In: 2024 IEEE Radio and Wireless Week, San Antonio, TX, USA, 21-24 Jan 2024, pp. 87-90. ISBN 9798350340457 (doi: 10.1109/RWS56914.2024.10438557)

- Zhong, M., Jiang, Y., Ma, Y. and Li, C. (2024) An Ultra-wideband Off-axis Reflector Lens. 2024 IEEE Radio and Wireless Symposium (RWS), San Antonio, Texas, USA, 21-24 Jan 2024. ISBN 9798350340464 (doi: 10.1109/RWS56914.2024.10438633)

- Ma, Y., Jiang, Y. and Li, C. (2024) A universal model for ultrasonic energy transmission in various media. Sensors, 24(19), 6230. (doi: 10.3390/s24196230)

- Ma, Y. and Li, C. (2025) Experimental Demonstration of a Combined RF-Ultrasonic Wireless Powering System. In: IEEE Radio and Wireless Week, San Juan, Puerto Rico, 19-22 Jan 2025, (d**oi:** 10.1109/RWS62086.2025.10904837)

- Ma, Y., Jiang, Y and Li, C. (2025) Development of a Hybrid RF and Ultrasonic Wireless Power Transfer System. In: IEEE Transactions on Power Systems (In preparation)

Acknowledgement

I am indebted to many people whose contributions have been invaluable to this work. Their unwavering support and guidance have been instrumental in bringing this project to fruition.

I would like to extend my sincere appreciation to Professor **Chong Li** for his unique insights, guidance, and supervision throughout this research. His invaluable advice and direction have powerfully shaped this work. I also wish to acknowledge all past and present members of the **MATE Group** for their knowledge-sharing and the many enjoyable moments they have contributed. Special thanks to **Mingyan Zhong** and **Yunan Jiang** for assisting with this project and engaging in thought-provoking discussions.

I am particularly grateful to **Thomas O'Hara** and **Afesomeh Ofiare** for their training on laboratory equipment in Lab 109. My gratitude also goes to **Jing Wang**, **Huihua Cheng**, and **Efrilia Marifatul Khusna** for their continuous support and optimistic understanding.

I would like to thank the James Watt School of Engineering Technical Services Group for their dedication and hard work in fabricating the PCB evaluation boards used in this project.

A heartfelt thank you to my family and friends for their unwavering support throughout my academic journey. Their steadfast belief in me and their patience has been instrumental in keeping me grounded.

Lastly, I want to extend my heartfelt thanks to all the friends and colleagues who have made immeasurable contributions. Your humour, kindness, prayers, and wisdom have transformed this endeavour from a purely academic pursuit into a truly enriching life experience. I am deeply grateful.

Abbreviations

AC	Alternating current
BLE	Bluetooth Low Energy
CC	Constant current
CMOS	Complementary metal–oxide-semiconductor
CPT	Capacitive wireless power transfer
CRFU-WPT	Combined radio frequency and ultrasonic wireless power transmission
CW	Cockcroft Walton
DC	Directing current
EC-WPT	Electric coupling wireless power transfer
EIRP	Effective isotropic radiated power
EMI	Electromagnetic interference
ESR	Equivalent series resistance
ETSI	European Telecommunications Standards Institute
FCC	Federal Communications Commission
HEC	Hybrid energy converter
HEC	Hybrid energy converter
ICs	Integrated circuits
IoT	Internet of Things
ITU	International Telecommunication Union
LTS	Linear translation stage
L-WPT	Laser wireless power transfer
MC-WPT	Magnetic coupling wireless power transfer
MIMO	Multiple-input and multiple-output
MPMT	Multi-pole multi-throw
PA	Power amplifier
PV	Photovoltaic
PWM	Pulse width modulation
RFEH	Radio frequency Energy Harvesting
RF-WPT	Radio frequency wireless power transfer
SPDT	Single-pole double-throw
SPST	Single-pole single-throw
TTL	Transistor-transistor logic
UET	Ultrasonic energy transmission
U-WPT	Ultrasound wireless power transfer
WPT	Wireless power transfer

1 Introduction

Powering distributed sensors has long presented a significant challenge, especially in environments where traditional power supply methods are impractical or inefficient[1, 2, 3, 4]. Conventional approaches, such as laying cables or using batteries, are often unsuitable due to deployment constraints. Sensors used in fields like hydrology, biology, environmental monitoring, smart buildings, and implanted medical devices are frequently placed in harsh conditions, including underwater, underground, within concrete structures, in low-temperature environments, or inside sealed metal enclosures such as steel bridges, shipping containers, and pipelines[1, 5, 6, 7, 8, 9, 10, 11]. In these situations, conventional power solutions can be costly and are limited by the short lifespan of batteries, which makes maintenance and replacement challenging due to the sensors' physical inaccessibility[12, 13, 14].

Wireless power transmission (WPT) has emerged as a promising alternative to conventional methods[15, 16]. It eliminates the need for cables and batteries while providing continuous and stable power delivery over extended periods[17]. This technology addresses significant limitations related to battery lifespan and the high costs associated with replacing batteries or installing cables, especially in remote or hard-to-reach locations[18]. Several WPT methods have been developed, including electric field coupling (EC-WPT), magnetic field coupling (MC-WPT), radio frequency (RF-WPT), laser (L-WPT), and ultrasound (U-WPT). Each method has advantages; however, many encounter challenges when powering sensors in metal-enclosed environments[19]. EC-WPT, MC-WPT, RF-WPT, and L-WPT are particularly affected by the shielding effects of conductive materials, which obstruct energy transmission through metal barriers[20]. On the other hand, while U-WPT can penetrate metal, its relatively short transmission range makes it unsuitable for long-distance power supply applications[21, 22].

This project introduces a novel hybrid wireless power transfer system, termed Combined Radio Frequency and Ultrasonic Wireless Power Transfer (CRFU-WPT), aimed at addressing the inherent limitations of conventional WPT technologies in complex environments. The CRFU-WPT system leverages the complementary characteristics of radio frequency and ultrasonic energy transmission to enable robust, long-distance wireless power delivery across diverse propagation media.

This design uses RF-WPT for its long-range, omnidirectional transmission capability in open air, offering flexible deployment and reduced alignment constraints. Meanwhile, U-WPT is incorporated to facilitate efficient power transfer through challenging materials such as metals, water, biological tissues, and media, where electromagnetic waves are typically subject to significant attenuation. The integration of these two mechanisms allows for seamless energy delivery across air over long distances and dense media to penetrate, ensuring continuous and reliable power flow to sensor nodes deployed in electrically or physically isolated environments. Figure 1-1 illustrates the conceptual structure and application of the CRFU-WPT system.

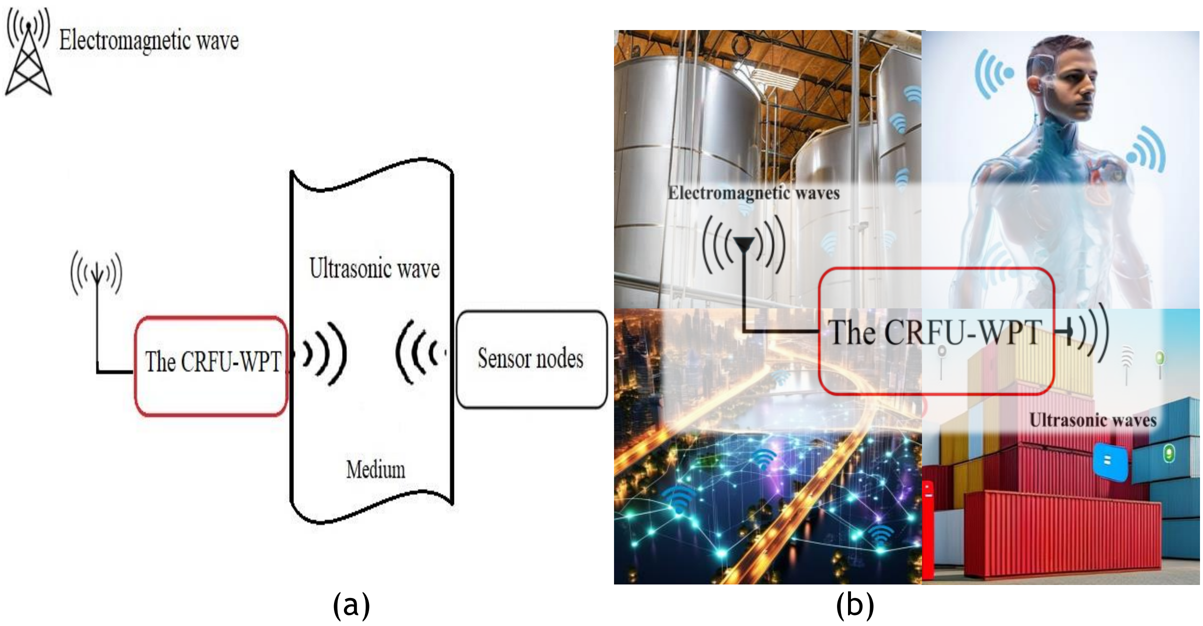

Figure 1-1. Illustration of the CRFU-WPT system, which harvests electromagnetic energy and emits it as ultrasonic waves (a) and its potential application scenarios in closed metal containers, steel bridges, shipping containers and oil pipelines (b).

The CRFU-WPT system addresses the limitations of conventional single-mode WPT technologies by integrating RF and ultrasonic transmission mechanisms into a unified architecture. Specifically, it overcomes the short-range constraints inherent to EC-WPT, MC-WPT, and U-WPT, as well as the barrier penetration issues commonly associated with RF-WPT and L-WPT. Through this hybrid design, CRFU-WPT significantly extends the effective operating range of wireless energy transmission and enhances the system’s adaptability across diverse and challenging environments.

This architecture is particularly advantageous in industrial facilities (e.g., enclosed metal tanks or pipelines), biomedical applications (e.g., implanted medical devices), and large-scale distributed IoT deployments in heterogeneous or dynamic terrains.

Furthermore, the CRFU-WPT system is compact and modular, facilitating seamless integration with various sensor nodes. Its multifunctional capabilities support both stationary and mobile sensing platforms. The system's ability to deliver stable and continuous power ensures long-term operational reliability, even under fluctuating environmental conditions.

Key Contributions and Achievements:

- Development of the CRFU-WPT system architecture.
- Establishment of power transmission models for RF and ultrasonic links.
- Design and testing critical components in the conversion circuit.
- Proposal for a time-division power management.
- Demonstration of an application case study.

This thesis is divided into five main chapters. Chapter 1 introduces the research background, motivation, and objectives of the project. It highlights the significance of hybrid wireless power transfer and discusses the challenges and application prospects of the proposed hybrid system. Chapter 2 provides a comprehensive review of existing wireless power transfer technologies, comparing their working principles, performance characteristics, application scenarios, and limitations. It also explores hybrid wireless power transfer approaches, outlining their benefits and summarising key insights relevant to system design. Chapter 3 presents the development of the CRFU-WPT system, covering the overall system architecture, modelling, circuit design, and hardware integration. This chapter establishes the theoretical and practical basis for system implementation. Chapter 4 reports and analyses the experimental results. It begins with individual modular tests of key subsystems, including the RF link, ultrasonic link, and conversion circuits, followed by a full system evaluation based on a real-world application case. Chapter 5 concludes the thesis by summarising the main research findings, assessing the overall system performance, and proposing potential directions for future development and optimisation.

2 Literature Review

With the widespread adoption of low-power devices, WPT has garnered significant attention in recent decades for its potential to revolutionise power delivery in distributed systems[23, 24, 25, 26]. Initially conceptualised by Nikola Tesla in the early 19th century, WPT has evolved into a multidisciplinary field with advancements in various methods[24]. These include EC-WPT, MC-WPT, U-WPT, L-WPT, and RF-WPT, each offering distinct advantages and facing specific limitations[27].

Hybrid systems that combine multiple technologies have been developed to address the shortcomings of individual WPT methods. These hybrid WPT systems aim to leverage the strengths of different approaches, achieving improved efficiency, adaptability, and scalability across diverse operating environments[28].

Despite considerable progress, challenges such as energy conversion efficiency, power density, and environmental adaptability remain critical research areas in WPT[20, 29]. Future developments are expected to enhance system efficiency, miniaturisation, and scalability to meet the increasing demand for wireless power applications in healthcare, smart cities, and industrial automation[18, 23, 30, 31].

The following sections will provide an in-depth overview of the primary WPT technologies, discussing their advantages, limitations, and application scenarios. Additionally, we will explore the current state of the art of hybrid WPT systems and their role in addressing existing challenges.

2.1 WPT Category

WPT technologies can be classified in various ways, including by transmission mechanism, transmission distance, and intended application. Among these, classification based on the transmission mechanism is one of the most fundamental and widely adopted approaches. In this discussion, WPT is categorised into five primary types according to their transmission mechanisms: EC-WPT, MC-WPT, U-WPT, L-WPT, and RF-WPT. The general physical mechanism of a typical WPT system is illustrated in Figure 2-1, which provides a conceptual overview of the energy transmission process from source to receiver.

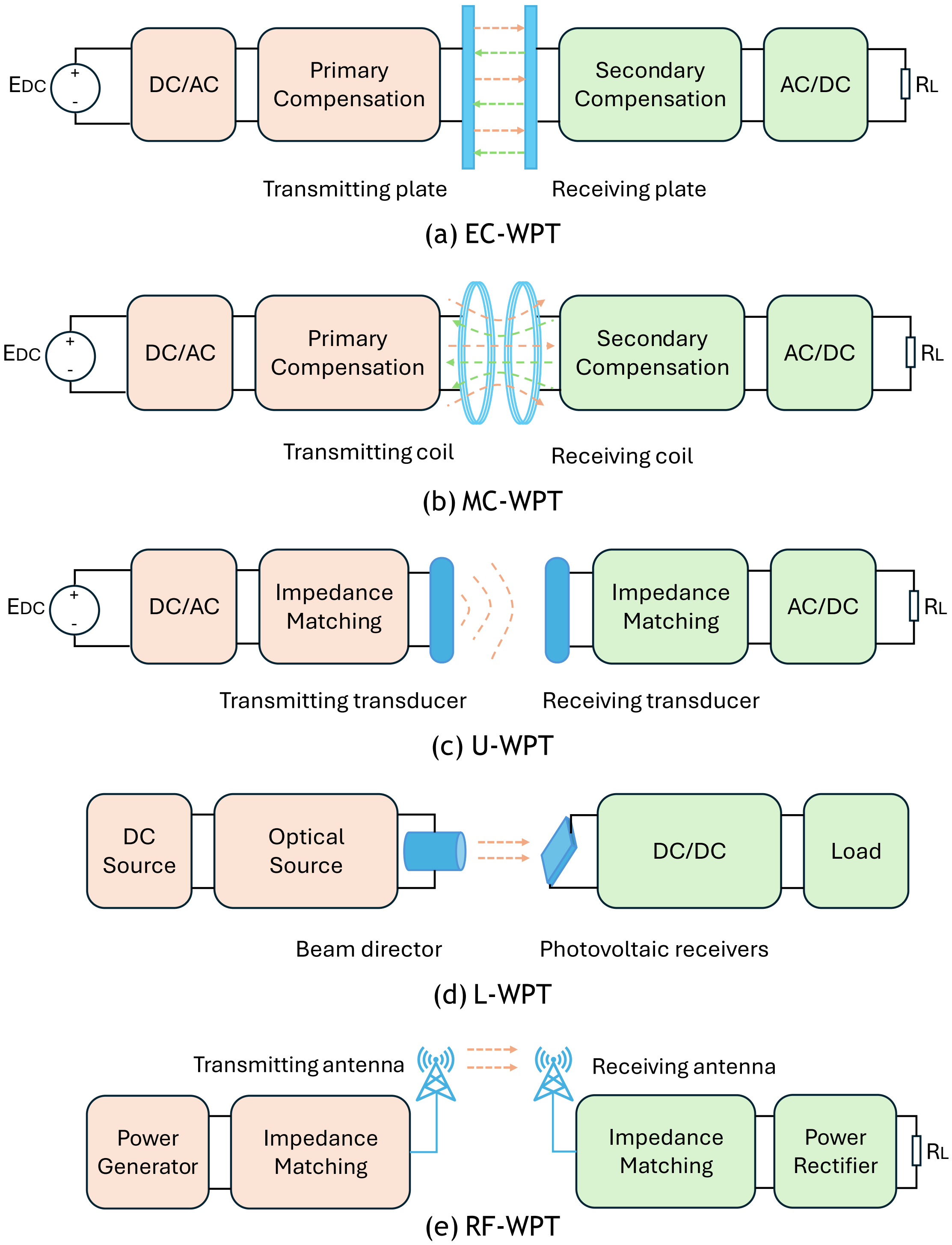

Figure 2-1. Mechanisms of typical WPT systems: EC-WPT (a), MC-WPT (b), U-WPT (c), L-WPT (d), and RF-WPT (e).

Each category of WPT exhibits different characteristics in terms of operating frequency, transmission distance, power level, and suitable applications. These differences determine their suitability for various practical applications, ranging from consumer electronics to industrial and biomedical systems. The following sections introduce the basic working principles and typical applications of each WPT type in detail.

2.1.1 Electric Field Coupling Wireless Power Transfer

EC-WPT, also known as capacitive wireless power transfer (CPT), enables power transfer without physical contact by utilising the electric field between conductive plates[32]. Characterised by its simple structure, lightweight design, and low cost, EC-WPT transfers energy across a gap through capacitive coupling between two electrodes, the transmitter and receiver, as shown in Figure 2-1 (a)[20].

EC-WPT operates by applying a high-frequency alternating current (AC) voltage to the transmitting electrode, generating an oscillating electric field. The receiving electrode, positioned opposite the transmitter, forms a capacitive coupling, enabling energy transfer through displacement current. The efficiency of this transfer is determined by the capacitance between the electrodes, which depends on factors such as electrode surface area, gap distance, and the dielectric properties of the medium. The AC signal is rectified and regulated at the receiving end to provide stable direct current (DC) power to the load.

The main advantages of EC-WPT are its compact and lightweight design, achieved by eliminating coils and magnetic components, and its simple structure, which reduces cost and complexity[20]. It is also resistant to magnetic interference, making it suitable for environments with strong magnetic fields[33]. However, EC-WPT has limitations, including reduced efficiency with increased plate distance, low power transmission capacity, sensitivity to environmental changes such as humidity, and the need for careful insulation due to high operating voltages[20].

EC-WPT is widely used in low-power and short-distance applications, such as wearable electronics, implantable medical devices, and charging stations for mobile devices and sensors[19, 32]. It is also employed in industrial settings to power sensors or components in rotating machinery, where direct access is impractical. M. Tamura et al. reported using EC-WPT to deliver 100 mW of power to implanted medical devices with an efficiency of approximately 35% [34]. This study highlights the suitability of EC-WPT for low-power biomedical applications, particularly where compact and lightweight designs are critical. In contrast, L. Yang et al. demonstrated the feasibility of a higher-power application, achieving a 100 W underwater power supply[35]. This finding underscores the adaptability of EC-WPT for environments where conventional wired connections are impractical, such as subsea sensors or robotic systems. B. Luo et al. extended the scope of EC-WPT to mobile vehicles, reporting a system capable of transmitting 653 W of power[36]. This study showcases the potential of EC-WPT in dynamic and high-power scenarios, such as electric vehicle charging and autonomous mobility solutions. Furthering the exploration of EC-WPT in aerial applications, C. Cai et al. proposed a scheme to deliver 212.1 W of power to drones with a DC-DC efficiency of 82.5%[37]. This research emphasises the role of EC-WPT in enabling extended operational durations for drones, particularly in industries like logistics, surveillance, and agriculture.

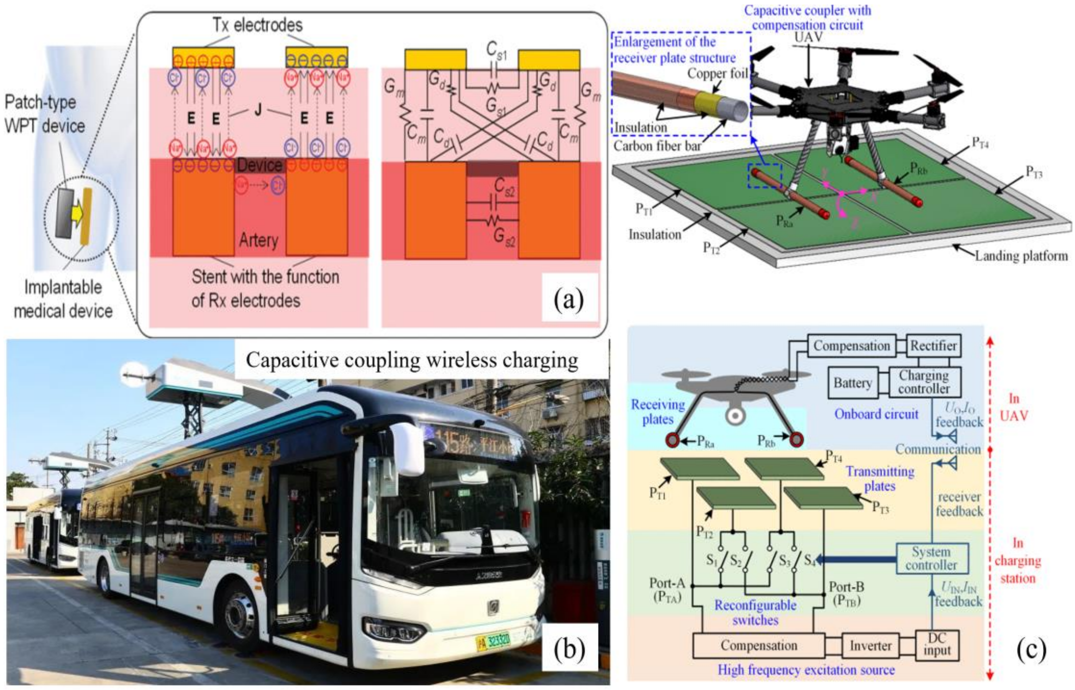

Figure 2-2. EC-WPT application solutions in implantable devices (a), electric vehicles (b), and UAV (c).

As shown in the Figure 2-2, existing studies collectively highlight the versatility and scalability of EC-WPT, demonstrating its potential in a wide range of applications—from low-power implantable medical devices to high-power systems such as electric buses and unmanned aerial vehicles. These examples reflect the adaptability of EC-WPT to both biomedical and transportation sectors. However, such applications are typically restricted to short-range power transfer, with the effective transmission distance generally limited to a few centimetres due to the nature of capacitive coupling.

2.1.2 Magnetic Field Coupling Wireless Power Transfer

MC-WPT is one of the most widely studied and implemented methods for wireless energy transmission[32, 38]. This technology primarily relies on electromagnetic induction, transferring energy between coils through a magnetic field, as shown in Figure 2-1 (b).

MC-WPT involves two main components: a transmitter coil and a receiver coil. The transmitter coil is energised with an AC, generating a time-varying magnetic field. This magnetic field induces an AC voltage in the receiver coil via mutual inductance. The induced voltage is converted into DC through rectification circuits to power electronic devices. Energy transfer efficiency depends on several factors, including the coupling coefficient, operational frequency, and alignment between the transmitter and receiver coils[39]. Strong coupling, typically achieved at close distances, enhances efficiency, making this method particularly effective for short-range applications[40].

MC-WPT offers several advantages, including high efficiency at short ranges, mature technological development, and safety due to the non-invasive nature of magnetic fields[41]. Additionally, resonant coupling enables an extended range without significant efficiency loss[42]. However, the technology faces challenges such as limited transmission distance, sensitivity to alignment between the transmitter and receiver, and potential electromagnetic interference (EMI) with nearby electronic devices[32, 41, 43, 44, 45]. Scaling up for high-power applications also introduces issues like heat generation and the need for advanced cooling mechanisms, making it more complex for such scenarios[46, 47].

MC-WPT is widely applied in consumer electronics for wireless charging of smartphones, smartwatches, and portable devices, in the automotive industry for electric vehicle charging, in the medical field for implantable and wearable devices, and in industrial automation for powering sensors and machinery[23, 48, 49, 50, 51]. Z. Ziqi proposed a solution for powering multiple devices in smart buildings, showcasing a system capable of powering a 50 W LED TV at 300 kHz and a 5 W mobile phone charger at 127 kHz as actual loads[52]. Similarly, X. Jin et al. demonstrated a 40 W WPT application for powering sensors in a smart greenhouse, highlighting its suitability for precision agriculture and environmental monitoring[53]. Y. Jia et al. reported an 800 W WPT system with constant current (CC) output designed to effectively handle air gaps and load variations, making it adaptable to fluctuating operational conditions[54]. In the automotive sector, X. Liu et al. developed a high-power WPT system capable of delivering 95.49 kW at an output voltage of 704 V, achieving a remarkable DC-DC efficiency of 96% to support electric vehicle charging[55].

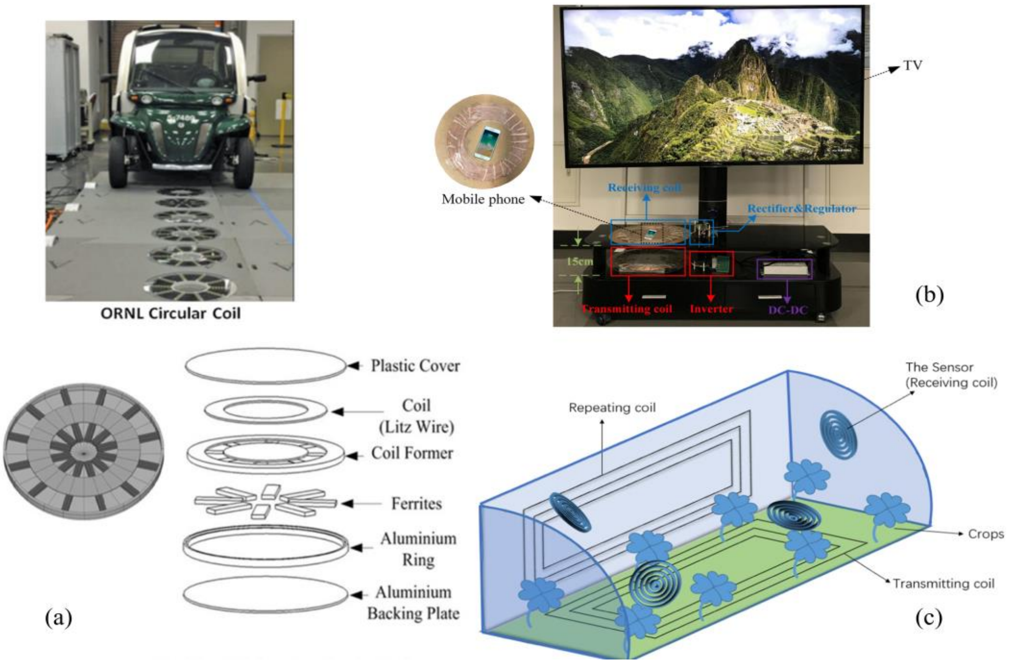

Figure 2-3. MC-WPT application solutions in electric vehicles (a), mobile phone and TV (b), and intelligent greenhouse (c).

As shown in the Figure 2-3, these studies collectively underscore MC-WPT's versatility and scalability, demonstrating its potential to meet the diverse power demands of modern applications, from low-power devices in smart environments to high-power systems for industrial and automotive use cases. However, its efficiency decreases rapidly with distance, and performance is highly sensitive to coil alignment. Challenges include energy losses due to nearby metals, heat generation in high-power applications, and susceptibility to EMI.

2.1.3 Ultrasound Wireless Power Transfer

U-WPT is an innovative and non-electromagnetic technology that utilises acoustic waves to transmit energy through air, water, or solid media[56]. Unlike conventional electromagnetic-based methods, U-WPT leverages the mechanical vibrations of ultrasonic waves to transfer energy, making it particularly suitable for environments where EMI or shielding is a concern[57]. U-WPT converts electrical energy into ultrasonic acoustic waves using a piezoelectric transducer. The transmitter generates high-frequency sound waves (typically above 20 kHz) propagating through the medium. At the receiver end, another piezoelectric transducer captures these waves and converts the mechanical vibrations into electrical energy, as shown in Figure 2-1 (c). The energy transfer efficiency depends on factors such as the medium's acoustic impedance, the transducers' alignment, and the operation frequency[58].

U-WPT offers several advantages, including its ability to avoid electromagnetic interference, making it suitable for sensitive environments like medical devices and industrial sensors[59]. It is also highly versatile and capable of transmitting energy through various media such as air, water, and solid materials while maintaining safety for biological tissues when operating at appropriate power levels[60]. Additionally, the directional nature of ultrasonic waves ensures localised energy transfer with minimal unintended losses[61]. However, U-WPT faces challenges such as medium-dependent efficiency, where performance decreases in less acoustically conducive environments like air, and limited power capacity, as high-intensity ultrasonic waves may cause heating or cavitation[62]. Precise alignment between the transmitter and receiver is critical for effective energy transfer, particularly over long distances, and high-intensity waves can generate acoustic noise or unwanted vibrations, potentially impacting user comfort and system usability [63].

Due to its unique advantages, U-WPT is gaining traction in several specialised fields. As shown in the Figure 2-4, in the medical sector, it is used to power implanted devices such as pacemakers and biosensors, where non-invasive power delivery is critical [64]. Underwater applications include powering submersible sensors and communication devices in aquatic environments [65]. In industrial settings, U-WPT is employed to wirelessly power sensors and actuators in harsh environments where traditional wiring is impractical [66].

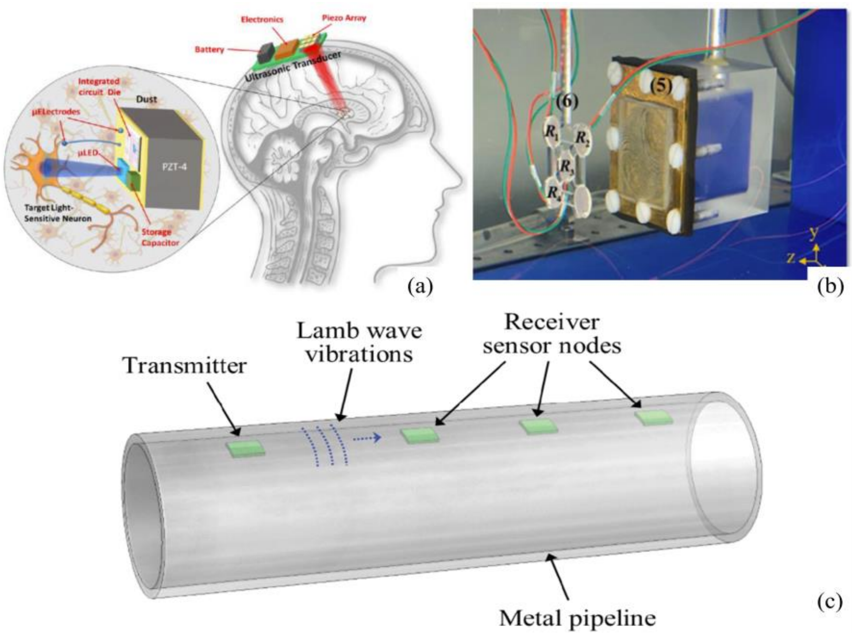

Figure 2-4. U-WPT application solutions in implantable devices (a), underwater (b), and metal pipeline (c).

Ultrasound wireless power transfer offers a promising alternative to conventional electromagnetic-based systems, particularly in specialised environments with critical EMI, biological safety, or medium compatibility. Despite its limitations, ongoing research and development are poised to expand its applicability and performance in the coming years.

2.1.4 Laser Wireless Power Transfer

L-WPT is an advanced technology that employs laser beams to transmit energy over long distances. L-WPT enables precise and efficient energy delivery to remote locations [67, 68]. L-WPT operates by generating a focused laser beam from a transmitter directed toward a photovoltaic (PV) cell or a similar optical receiver at the target location. The PV cell absorbs the laser energy and converts it into electrical power， as shown in Figure 2-1(d). The key factors influencing the efficiency of L-WPT include the wavelength of the laser, the design of the PV cell, the alignment between the transmitter and receiver, and environmental conditions such as atmospheric attenuation and beam scattering [25, 69].

L-WPT offers several advantages, including its capability for long-distance energy transmission with minimal losses, high power density suitable for demanding applications, and precision energy delivery due to the directional nature of laser beams [25, 70, 71, 72]. It is also immune to electromagnetic interference, making it ideal for sensitive environments [73]. However, the technology faces significant challenges, such as safety concerns from high-power laser beams, which can pose risks to human eyes and skin, and efficiency reductions caused by atmospheric interference like fog, dust, and rain [72, 73, 74, 75, 76]. Precise alignment between the transmitter and receiver is critical for effective energy transfer, particularly over long distances, and the current limitations in conversion efficiency at both the transmitter and receiver remain a hurdle for widespread adoption[67, 68, 77, 78, 79].

Figure 2-5 shows the application of L-WPT in UAV, space applications and underwater devices[80].

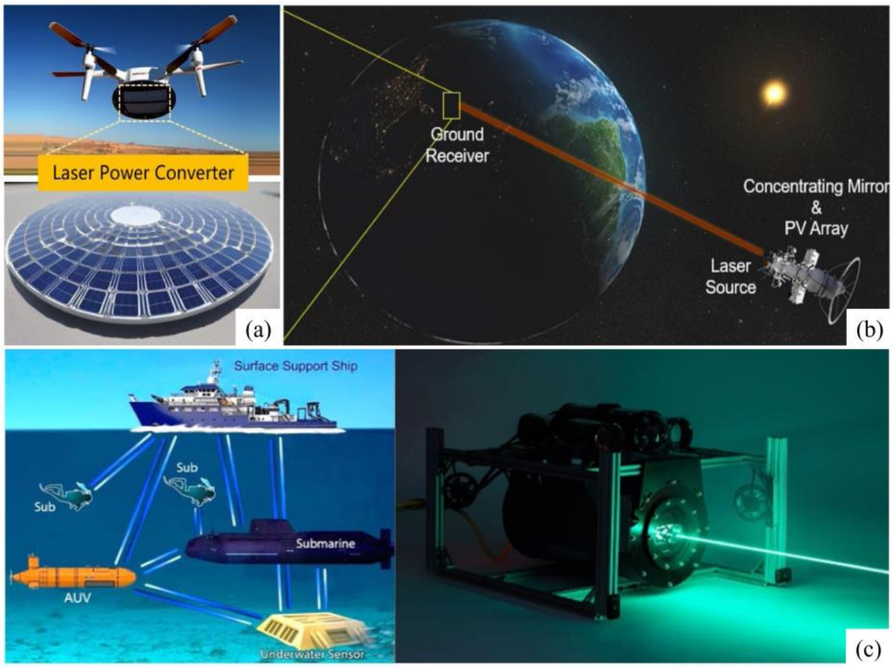

Figure 2-5. L-WPT application solutions in UAV (a), space applications (b), and underwater devices (c).

L-WPT shows great potential across diverse fields. In space, it powers satellites, stations, and lunar rovers, offering reliable, connection-free energy[81, 82]. On Earth, it extends UAV flight times by providing mid-flight energy and supports remote sensing and communication infrastructure, delivering power to otherwise inaccessible locations[83, 84, 85, 86].

2.1.5 Radio Frequency Wireless Power Transfer

RF-WPT is a versatile technology that offers broad applicability, flexibility, and adaptability[87]. It can accommodate varying power requirements over different distances[88]. This technology is commonly used to power IoT devices, satellites, and other low-power systems[89, 90, 91]. RF-WPT can also be customised or scaled to meet specific application needs, including supporting various power levels, charging multiple devices simultaneously, and enabling charging for devices in omnidirectional or irregular motion[23, 92, 93, 94].

RF-WPT can transmit energy over longer distances than EC-WPT, MC-WPT, and U-WPT. It converts electrical energy into radio frequency electromagnetic waves, which travel through free space to reach the receiver. The receiver typically consists of an antenna, an impedance-matching network, and a rectifier. These components work together to capture RF energy and convert it into usable electrical power, as shown in Figure 2-1 (e).

RF-WPT leverages electromagnetic waves, typically operating within the microwave or RF spectrum (ranging from MHz to GHz frequencies)[95]. The system consists of a transmitter that generates high-frequency signals emitted as electromagnetic waves via an antenna. These waves are transmitted through free space and received by a dedicated antenna at the receiver end. The system depends on several factors to maximise power transfer efficiency, including the design of high-gain directional antennas, precise frequency tuning, and minimal signal attenuation over the transmission path[96, 97, 98]. The captured RF energy is rectified and regulated to provide stable DC power to the load.

RF-WPT powers IoT sensors, wearables, satellites, remote monitors, and industrial systems, offering reliable, long-distance, and maintenance-free energy transfer[30, 90, 92, 99, 100, 101]. L. Schulthess et al. demonstrated an RF energy conversion system for micro IoT, achieving over 30% total power conversion efficiency at −10 dBm input power and a peak efficiency of 57% at 3 dBm, highlighting its suitability for IoT sensors[102]. C. Ivo et al. proposed a simultaneous wireless information and power transmission system for small mobile devices, transferring at least 6 dBm of power to a wearable device using a 2 GHz signal for tracking individuals at 0.5 meters[103]. J. Tepper et al. evaluated RF power transmission for low-power aircraft sensors, demonstrating a 28 mW system covering a 20-seat area[104]. In biomedical applications, S. A. A. Shah et al. developed an 82% maximum power conversion efficiency for implanted medical devices. At the same time, M. A. Tanha introduced an antenna-based RF system delivering 20 mW of power to a neonatal lung function sensor at 19 cm [105, 106]. In space applications, A. K. Shahjahan reviewed space-based wireless power transmission technologies, and M. Preyansh explored space solar power satellites that convert solar energy into microwaves for wireless transmission to Earth[107, 108]. These studies highlight the versatility and scalability of RF-WPT across a wide range of applications, from biomedical devices to aerospace technologies.

Figure 2-6 shows the application of RF-WPT in implantable devices, consumer electronics, short-range and long-range applications[28, 109, 110, 111].

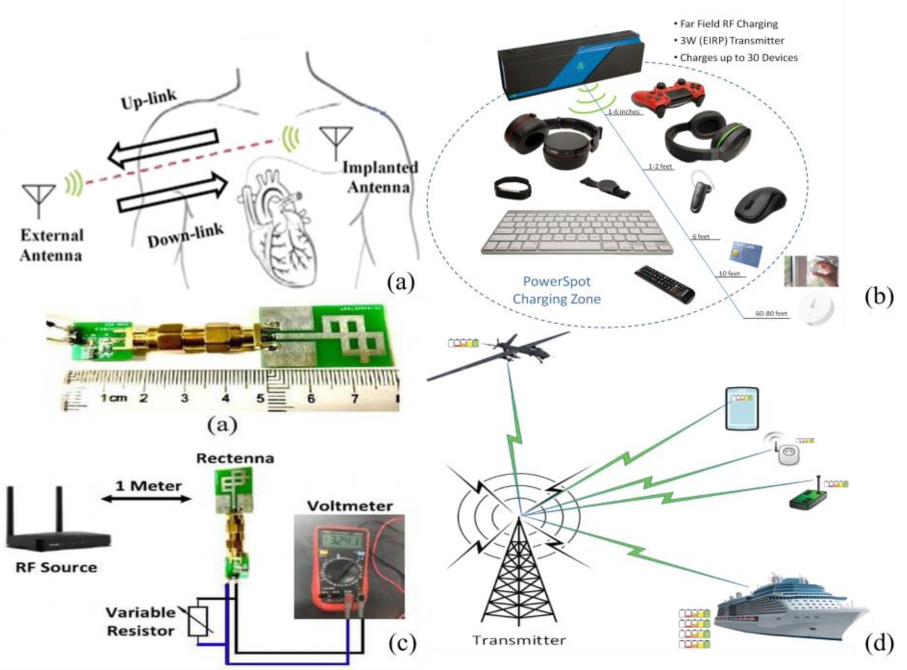

Figure 2-6. RF-WPT application solutions in implantable devices (a), consumer electronics (b), short-range (c) and long-range applications (d).

RF-WPT offers significant benefits, including long-range capability, flexibility, and the ability to power multiple devices simultaneously without requiring precise alignment [112, 113, 114, 115]. Additionally, its integration with wireless communication systems allows for concurrent energy and data transmission, making it highly adaptable to modern technological demands [24, 114, 116]. However, the technology faces efficiency limitations due to energy losses over long distances, strict spectrum regulations, and challenges in mitigating EMI [117, 118, 119]. Furthermore, health and safety concerns regarding prolonged exposure to high-power RF fields require strict adherence to international standards [120, 121, 122, 123].

2.2 Comparison of WPT

WPT technology has made significant advancements, with the latest research highlighting its potential to meet the diverse requirements of modern applications[124]. It is poised to address challenges across various fields, including consumer electronics, healthcare, industrial automation, and space exploration[125]. Each method—EC-WPT, MC-WPT, U-WPT, L-WPT, and RF-WPT—offers distinct advantages and limitations tailored to specific use cases. Table 2-1 presents a detailed comparison of these technologies, evaluating key metrics such as Power range, Transmission Range, Advantages, Limitations and application suitability. It provides a comprehensive understanding of their operational constraints and ideal applications.

Table 2-1. Comparison table of WPT technologies

	EC-WPT	MC-WPT	U-WPT	L-WPT	RF-WPT
Power range	mW to KW	mW to KW	mW to W	mW to KW	mW to KW
Transmission Range	mm to cm	mm to cm	mm to m	m to km	m to km
Advantages	High efficiency, Low cost, Light, flexibly	High efficiency, High power density	High biosafety, Metal penetration	Long distances, High directivity	Long distances, Omnidirectional
Limitation	Shot distance, Potential electric field hazards	Shot distance, Metal shielding, Sensitive to misalignment	Shot distance, High attenuation	Point to point, Sensitive to atmospheric	Metal shielding, Exposure risk
Application	Implantable medical, Electric Vehicle	Mobile phones, Wearables, Electric Vehicle	Underwater and implantable equipment	Spacecraft, satellite solar power station	Mobile device, Unmanned aerial vehicle

Among WPT technologies, EC-WPT, MC-WPT, and U-WPT are primarily suited for short-distance energy transmission. EC-WPT and MC-WPT can achieve power levels in the range of several kilowatts with high transmission efficiency; however, they pose potential risks associated with electric and magnetic field exposure. U-WPT, on the other hand, offers superior safety and the ability to penetrate conductive materials such as metal, water, and biological tissues. Still, its transmission efficiency is relatively low, limiting its applicability for high-power scenarios.

For long-distance transmission, L-WPT and RF-WPT are more suitable. L-WPT is characterised by its high directivity, which enables precise energy delivery to targeted locations, while RF-WPT can transmit energy omnidirectionally depending on antenna configurations. Nevertheless, both L-WPT and RF-WPT are constrained by metal shielding effects and carry potential risks associated with energy exposure.

Each WPT technology exhibits distinct advantages and limitations, necessitating careful consideration of the specific application requirements, environmental constraints, and safety standards to optimise their performance and applicability.

2.3 Hybrid WPT

Wireless power transfer technology overcomes the limitations of cables, providing an innovative solution for powering mobile devices and distributed sensors[126]. However, each WPT technology has advantages and disadvantages, leading to inherent application limitations[127]. A hybrid wireless power supply, which integrates two or more WPT technologies, seeks to combine the strengths of each while mitigating their shortcomings[29]. By merging different WPT methods, hybrid systems address challenges related to transmission distance, power levels, and environmental adaptability. For example, combining RF-WPT with magnetic field coupling enables medium-distance energy transmission while maintaining high efficiency for short-range applications[128]. Similarly, hybrid systems can adapt dynamically to specific application requirements and environmental conditions. In scenarios with obstacles, a combination of U-WPT and L-WPT can facilitate energy transmission through obstacle materials while supporting long-distance power delivery in open environments. This flexibility allows hybrid systems to achieve effective long-distance wireless power transmission, even with physical barriers[129].

Integrating EC-WPT and MC-WPT is a prominent research focus in the IoT because it can achieve efficient short-range charging and power coverage for various devices[130]. Due to their similar circuit structure, the two have been widely studied[36, 131, 132]. Another promising combination is U-WPT and RF-WPT, particularly in sensor networks and complex environments[133]. U-WPT provides energy transmission through obstacles in this configuration, while RF-WPT ensures long-range, wide-area energy coverage. Although direct studies on integrating U-WPT and RF-WPT remain limited, this combination holds significant potential for applications requiring both metal penetration and long-distance coverage.

While hybrid WPT technology presents a promising solution for addressing the diverse demands of modern applications by combining the strengths of multiple transmission methods, it also introduces several significant challenges. Effective coordination between different transmission techniques necessitates the development of advanced control algorithms to manage their operation seamlessly. Furthermore, hardware design must ensure compatibility and integration among components such as antennas, sensors, and receiving modules, which adds complexity to the system architecture.

Hybrid WPT systems also tend to involve higher production costs and may exhibit increased power consumption due to the concurrent use of multiple technologies. Additionally, the lack of mature industry standards for hybrid WPT complicates system interoperability and scalability. Further research is therefore required to enhance inter-technology coordination, improve overall system efficiency, and establish standardised protocols. Despite these challenges, hybrid WPT remains a critical direction for the future development of wireless power systems. It offers the potential for improved versatility, environmental adaptability, and application scope across industrial, biomedical, and IoT domains.

2.4 Summary

This chapter reviewed and compared key WPT technologies, including EC-WPT, MC-WPT, U-WPT, L-WPT, and RF-WPT. Each technique offers distinct advantages in specific domains but also faces inherent limitations that constrain broader applicability.EC-WPT and MC-WPT are well-suited for short-range, high-efficiency power delivery, making them ideal for wireless charging and near-field industrial applications. However, their dependence on near-field coupling limits range and requires precise alignment. U-WPT offers enhanced safety and effective penetration through conductive media such as metal or tissue, though it suffers from high attenuation in air and relatively low efficiency. In contrast, L-WPT and RF-WPT enable long-distance energy transfer, with L-WPT excelling in directional delivery and RF-WPT in omnidirectional flexibility. Nonetheless, both are limited by poor penetrability through metal and potential health or regulatory concerns related to electromagnetic exposure.

This analysis highlights that no single WPT method can fully meet the diverse needs of modern applications, particularly in environments involving structural barriers or heterogeneous materials. To overcome these limitations, hybrid WPT approaches have gained increasing attention. In particular, integrating RF and ultrasonic transmission leverages the long-range flexibility of RF and the penetrative capability of ultrasound, enabling robust energy delivery across varied media. Building on these findings, the next chapter introduces the Combined Radio Frequency and Ultrasonic Wireless Power Transfer (CRFU-WPT) system. This hybrid architecture is designed to enhance adaptability and performance in complex environments, supporting reliable power delivery for industrial, biomedical, and distributed sensor applications.

3 The CRFU-WPT System

3.1 Introduction

The Combined Radio Frequency and Ultrasonic Wireless Power Transmission (CRFU-WPT) system presents a promising solution by combining the strengths of RF-WPT and U-WPT. This hybrid approach addresses the limitations of single-technology systems, allowing for flexible, long-term, and stable power delivery to sensors. It eliminates the need for physical wiring and reduces the impact of environmental factors, such as weather conditions[133].

However, merging RF-WPT and U-WPT into a single hybrid system presents significant challenges due to their fundamentally different operating principles. RF-WPT transmits power using electromagnetic waves and operates at high frequencies with low power density, making it ideal for long-range, low-power applications[103]. In contrast, U-WPT utilises mechanical waves to transmit energy over short distances through high-density media, achieving higher power output at lower frequencies[59]. These differing operational mechanisms require careful system design to ensure compatibility between both technologies, efficient energy transfer, and seamless integration within the CRFU-WPT framework.

This chapter offers an in-depth analysis of the CRFU-WPT system's architecture， design and assembly. It examines the RF link model, the ultrasonic link model, and the conversion circuit, highlighting their unique characteristics and the essential technologies needed for integration. Additionally, it explores key design strategies to overcome the challenges posed by the differing operational requirements of RF-WPT and U-WPT.

To support this integration, the chapter also investigates the energy flow within the hybrid system, quantifying link losses to establish a clear relationship between energy input and output. This systematic analysis lays the groundwork for optimising the CRFU-WPT system's performance, ensuring reliable, efficient, and adaptable power delivery across various challenging operational environments.

3.2 System Architecture

The proposed CRFU-WPT system architecture comprises three primary components: the RF link, the ultrasonic link, and the hybrid energy converter (HEC). The RF link transmits energy from the RF transmitter to the converter via the antenna. The converter harvests RF energy and converts it into ultrasonic energy. The ultrasonic link is then transmitted to the load through the ultrasonic piezoelectric transducer.

Figure 3-1 Illustrates the system's energy flow, depicting the complete pathway of energy transmission from the RF transmitter to the load. This pathway comprises a series of interconnected components, including the RF transmitting antenna, the RF receiving antenna, the conversion circuit, the ultrasonic transmitting transducer, and the ultrasonic receiving transducer. Each element ensures seamless and efficient energy transmission throughout the system.

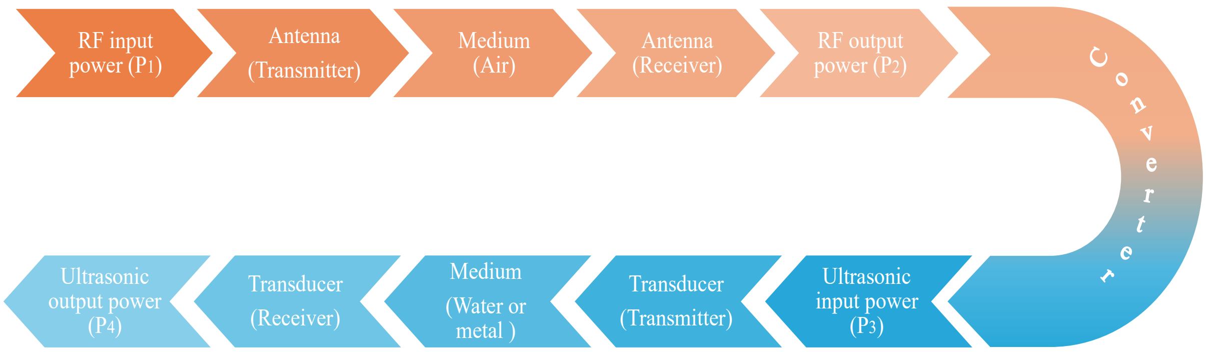

Figure 3-1. The system energy link consists of two parts: the input energy is transmitted through the antenna in the RF link, and then the energy is converted into ultrasonic energy by the conversion circuit and transmitted to the load through the transducer.

Figure 3-1 Illustrates the energy transmission process of the CRFU-WPT system. Initially, input energy is transmitted through the air as electromagnetic energy via the antenna. This energy is then converted into mechanical energy by the conversion circuit and transmitted through the metal or water as an ultrasonic wave delivered to the load by the piezoelectric transducer.

The system integrates both electromagnetic and mechanical energy in its operation. The conversion circuit plays a central role by transforming electromagnetic energy into mechanical energy. It consists of two primary components: the electromagnetic energy receiving end (RF energy collection) and the mechanical energy transmitting end (ultrasonic energy transmission). Furthermore, the conversion circuit manages energy, ensuring efficient system operation.

Therefore, the CRFU-WPT system comprises three main components: the RF link, the ultrasonic link, and the HEC. Figure 3-2 provides a detailed depiction of the system's architecture, showcasing the integration of the RF and ultrasonic links with the HEC. It highlights the role of each component within the energy flow and its contribution to the system's overall functionality.

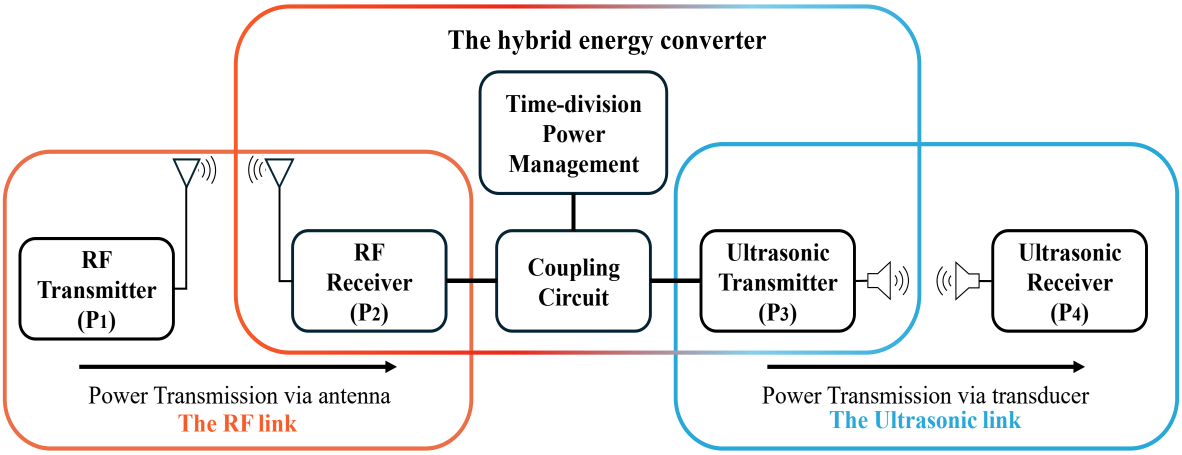

Figure 3-2. The CRFU-WPT system architecture. The orange block is the RF energy transfer link, and the blue block is the ultrasonic energy transfer link, where the P1 and P2 are the power from the transmitter and receiver of the antenna, and P3 and P4 are the power from the transmitter and receiver of the transducer. The middle block is the converting coupling framework.

It is noteworthy that when both the ultrasonic link and RF link operate with high efficiency, the power density of the ultrasonic link significantly exceeds that of the RF link. Specifically, the HWPT power received by the RF receiving antenna is lower than the driving power required for the piezoelectric transducer. Consequently, the design of the power management circuit must carefully consider these distinct characteristics, particularly the constraints imposed by power availability and system size. Given their mismatched power densities, the primary challenge in developing the proposed hybrid wireless power transmission system is the design of a practical coupling circuit for the RF and ultrasonic links. Furthermore, due to the limited power input of the RF link, incorporating a highly efficient power management system is essential.

A HEC is designed to efficiently couple the RF and ultrasonic links, as illustrated in Figure 3-3. The coupling circuit is tasked with harvesting RF energy within a range of 1 mW to 200 mW over an extended period and generating ultrasonic energy output between 500 mW and 1000 mW over shorter intervals. To enhance the versatility of this circuit across various applications, it is designed to adapt to different transmission distances and media. This is accomplished by accommodating antennas that operate at varying frequencies and transducers with differing frequency ranges. The coupling circuit is highly adaptable, optimising the RF antenna and ultrasonic energy transducer frequencies. These frequencies can be tuned within ranges of 1 MHz to 2.5 GHz for the RF link and 10 kHz to 1 MHz for the ultrasonic link, respectively. This adaptability ensures the circuit's relevance across various operational scenarios, making it suitable for diverse use cases.

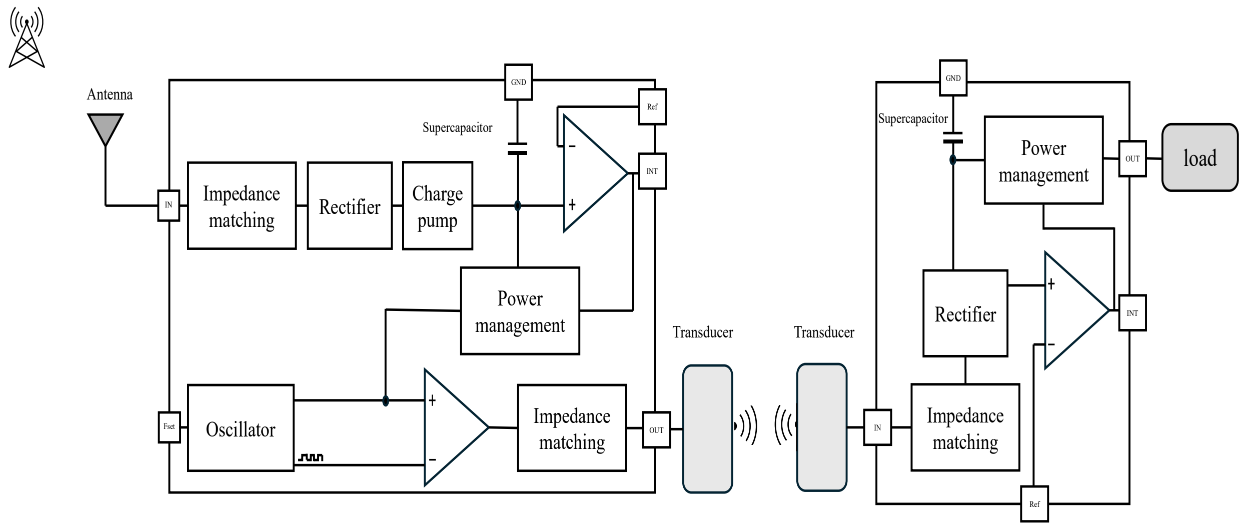

Figure 3-3. The CRFU-WPT system block diagram. The system including RF link, converter, ultrasonic link, and ultrasonic receiver. It mainly includes a matching network, rectifier, charge pump, oscillator, power amplifier, power management and ultrasonic receiver circuit.

The system comprises an RF link, an ultrasonic link, and a conversion circuit. The conversion circuit performs multiple functions: receiving electromagnetic energy, which includes input impedance matching, rectification, and voltage boosting; transmitting mechanical energy through components such as an oscillator and a power amplifier; and managing energy to coordinate the operation of the converter effectively. Additionally, the corresponding ultrasonic energy receiving circuit converts ultrasonic energy into stable electrical energy and supplies it to the load, ensuring reliable and consistent power delivery.

Given that RF energy transmission is subject to electromagnetic field exposure limitations, the permissible input power for the RF link is inherently constrained [134]. In contrast, ultrasonic energy transmission (UET) typically requires high instantaneous power at the transmitting transducer, resulting in a high-power density during operation. A time-division-based energy management strategy has been developed to reconcile this mismatch between low input power and high output demand.

The proposed energy management circuit serves two critical functions within the hybrid converter. First, it transforms low-amplitude, continuous RF input into high-power ultrasonic output by accumulating energy over time. Second, it provides an autonomous, power-free control mechanism that governs energy storage and release without requiring an external power supply. The circuit is designed to operate across a wide input voltage range, ensuring compatibility with harvested energy's fluctuating and intermittent nature. It can be flexibly configured to accommodate varying load conditions. Importantly, the management circuit is engineered for ultra-low power consumption to maximise system efficiency and energy utilisation.

In the time-division energy management scheme, RF energy is harvested and stored during an idle phase, followed by a brief high-power discharge phase in which ultrasonic energy is transmitted. Initially, the coupling interface to the ultrasonic transducer remains disconnected to prevent energy leakage. During this phase, harvested RF energy accumulates in a storage element, typically a supercapacitor. Once the stored energy exceeds a predefined threshold, the circuit activates the coupling stage, allowing the ultrasonic transducer to emit a high-power acoustic pulse for a short duration. The ratio of the charging (off) time to the discharging (on) time is determined by the available input power and the fixed output power required by the ultrasonic transmission stage. This process repeats cyclically, enabling continuous conversion from low-level RF input to be pulsed high-power ultrasonic output.

Similarly, due to the inherently low transmission efficiency of the UET link, the energy received at the ultrasonic receiving end is limited. A corresponding time-division mechanism is implemented on the receiver side to address this. By accumulating the incoming acoustic energy and regulating its release based on the instantaneous power demand of the load, the system ensures a stable and sufficient power supply despite the limited energy harvested during each cycle.

The energy accumulation process and the load switching on and off are shown in the timing diagram in Figure 3-4.

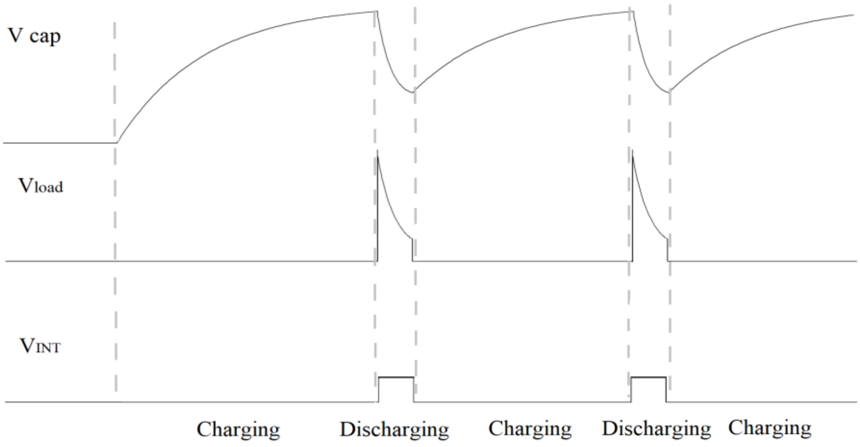

Figure 3-4. The timing diagram of the energy management circuit. When the energy collected in the capacitor accumulates to the set value, an interrupt signal is issued, and the load is turned on. When the energy does not meet the load power supply requirements, the interrupt signal disappears, and the load is turned off.

Time-division energy management allows the system to operate efficiently by dynamically regulating and distributing energy to subsequent stages, even under constrained input conditions. This approach optimises energy utilisation by alternating between energy accumulation and delivery phases, ensuring that each subsystem receives sufficient power without exceeding available input limits. By intelligently managing energy flow, the system can maintain stable performance, enhance reliability, and adapt to varying load requirements. This makes it particularly suitable for applications with intermittent or low-power energy sources.

3.2.1 The RF Link Model

RF-WPT utilises antennas to transmit energy over long distances through electromagnetic waves in the air. Due to the nature of electromagnetic waves, RF energy transmission enables extended transmission distances and flexible system design. It can also be configured for directional or omnidirectional transmission depending on specific application requirements. RF wireless energy transmission has been extensively studied in fields such as medical devices, drones and the Internet of Things (IoT) [103, 104, 106, 135, 136]This project leverages RF-WPT's advantages, including its long-range transmission and flexible configuration, to achieve efficient wireless energy transfer through the air.

3.2.1.1 RF Link Principle and Structure

RF-WPT is a method that uses electromagnetic waves to transmit energy from a transmitting antenna to a receiving antenna. It offers an efficient solution for wireless power delivery, especially in scenarios requiring mobility, design flexibility, and low power consumption. RF-WPT operation comprises four key stages: electromagnetic energy emission, wave propagation, energy reception, and power conditioning and storage. Each stage is described below.

Electromagnetic Energy Emission: In this stage, the transmitting antenna converts electrical energy from a signal source into electromagnetic waves. The emitted energy depends on frequency, directionality, polarisation, and output power. Antenna design is vital in determining radiation efficiency and coupling with the surrounding environment.

Electromagnetic Wave Propagation: The RF waves propagate through space at the speed of light from the transmitter to the receiver. Along the way, energy is attenuated due to distance, medium properties, and frequency-dependent losses.

Electromagnetic Energy Receive: The receiving antenna captures the transmitted RF energy and converts it back into electrical energy, typically in AC form.

Energy Management and Storage: Energy management involves converting the AC power received by the antenna into DC power through rectification, followed by collection and accumulation to ensure a stable and continuous power supply for subsequent circuits or loads.

Each stage of this process must be carefully designed to optimise efficiency, minimise losses, and address environmental and operational constraints.

The energy flow of the RF link is shown in the Figure 3-5.

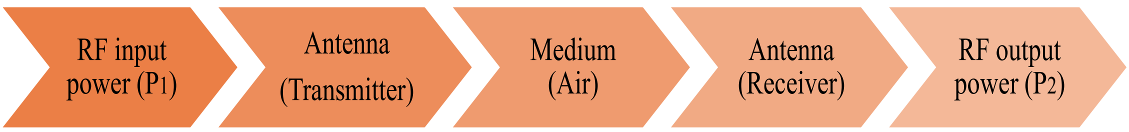

Figure 3-5. The RF link energy flow diagram.

A complete RF-WPT system typically consists of the RF transmitter, RF receiver, and power management that work together to achieve efficient energy transmission. Figure 3-6 shows the typical RF-WPT structure.

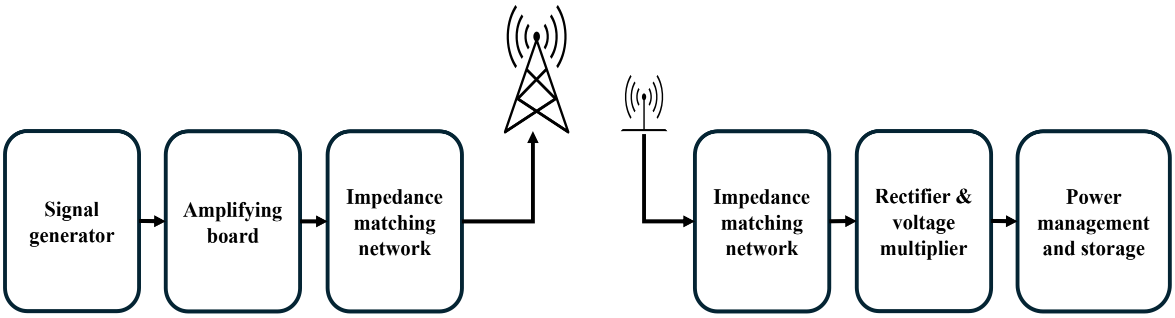

Figure 3-6. The RF-WPT link structure diagram.

At the transmitting end, the RF transmitter comprises a signal generator, a power amplifier, impedance matching equipment, and a transmitting antenna. The signal generator produces RF signals, typically operating between MHz and GHz, while the power amplifier amplifies the low-power RF signal to the necessary level for long-distance transmission. The antenna then converts the electrical energy into RF electromagnetic waves, with its design playing a crucial role in determining the signal's directionality and effective transmission range.

On the receiving end, the RF receiver captures the transmitted RF electromagnetic waves and converts them back into electrical energy. This is achieved through a receiving antenna, which collaborates with the transmitting antenna to capture the RF wave energy and deliver it to the receiving circuit. The captured RF signals are converted into DC power by a rectifier circuit, commonly employing diode bridge rectifiers or other RF rectifiers. Once converted, the electrical energy can be immediately utilised or stored in a battery for later use. Effective energy management is vital in distributing the received power to various loads, such as electronic devices and sensors. The energy management circuit ensures minimal energy loss during transmission and reception, thereby optimising the overall transmission efficiency of the system.

This project leverages the advantages of RF long-distance energy transmission, which is particularly well-suited for powering multiple small devices over large areas. This makes it an ideal solution for IoT and remote sensor applications.

3.2.1.2 RF Link loss

RF link focuses on the energy loss from the driving source to the load, which will be thoroughly discussed in relation to various application environments. These factors include antennas of different sizes, resonant frequencies, and varying transmission distances.

The primary losses in the RF link arise from electrical reflections, antenna losses, and transmission losses. As the resonant frequency increases, the electrical impedance matching in the system becomes increasingly complex. The losses observed in this study are shown in Figure 3-7. The various components of the loss will be discussed below based on the energy transfer path.

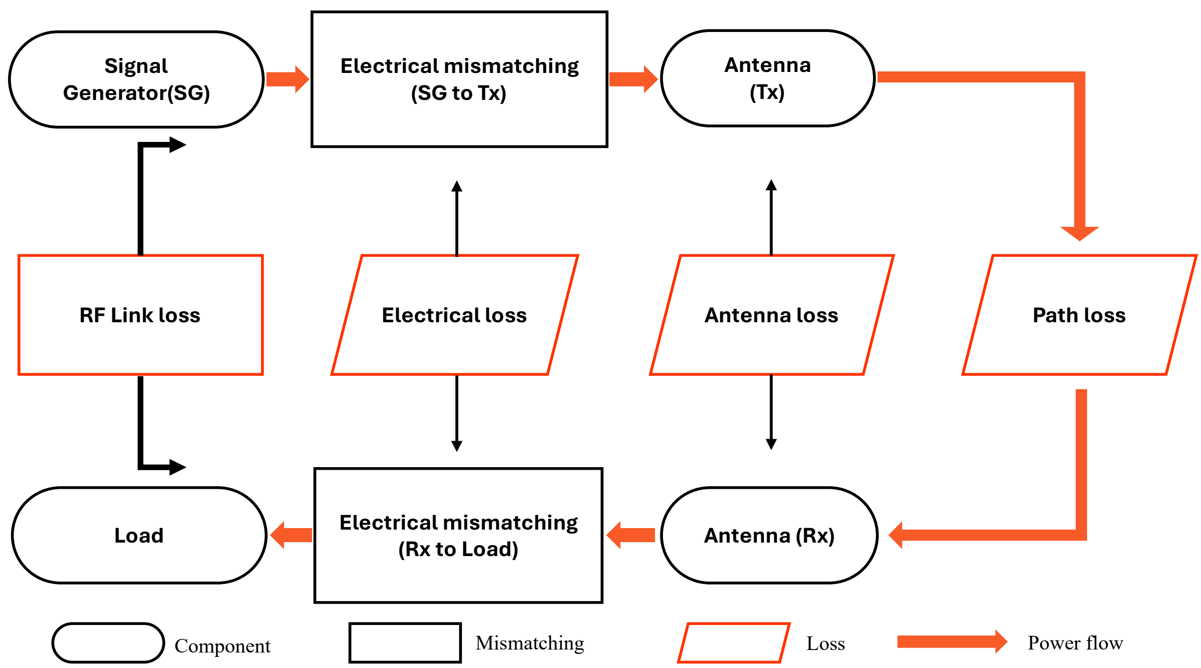

Figure 3-7. Flow diagram of RF link transmission loss. RF link loss mainly includes electrical loss, antenna loss, and medium loss.

A. RF Electrical Loss

Electrical loss refers to the return loss due to reflection when energy (in the form of an electrical signal) reaches the antenna, which usually occurs at impedance mismatches or discontinuities. Electrical loss is measured relatively and expressed by:

$$RF\ Electrical\ Loss\ (dB) = -10\,log(1 - |\Gamma_{RFE}|^2)\,, \tag{3-1}$$

where Γ_{RFE} is the RF reflection coefficient, and given by:

$$\Gamma_{RFE} = \frac{Z_{E1} - Z_{E2}}{Z_{E1} + Z_{E2}} \,, \tag{3-2}$$

where Z_{E1} is the electrical impedance of the driver, which can be the impedance of the signal generator or the receiver of the antenna. Z_{E2} is the electrical impedance of the load, which can be the impedance of the load or the transmitter of antenna. The impedance values of the antenna, signal generator, and load can determine electrical losses.

The impedance of an antenna is typically determined using the S-parameter (scattering parameter), which characterises how RF signals behave when they encounter a network or component, such as an antenna. The relationship between the S-parameter and the impedance of the antenna can be expressed as follows:

$$Z_a = Z_0 \frac{1 + S_{11}}{1 - S_{11}}, \tag{3-3}$$

Where Z_a is the impedance of the antenna, Z_0 is the characteristic impedance of the measurement system (usually 50 ohms or 75 ohms), S_{11} is the reflection coefficient, which represents the ratio of reflected power to incident power at the antenna input.

This relationship allows for calculating the antenna impedance from the measured S-parameter, enabling the analysis of the antenna's performance in matching and efficiency.

B. **Antenna Loss**

Antenna loss refers to the energy the antenna loses during transmission or reception. Due to material properties, design limitations, and environmental conditions, an antenna typically cannot convert all electrical energy into electromagnetic energy or vice versa, leading to less than 100% efficiency. This inefficiency results in a portion of the energy being dissipated as heat or lost to other forms, reducing the overall performance of the antenna.

Antenna loss primarily arises from conductor loss and dielectric loss. Conductor loss occurs due to the resistance of the antenna's conductive material, which generates heat as current flows through it, resulting in energy dissipation. This loss is particularly pronounced in high-frequency applications, where surface currents concentrate on the conductor's surface (known as the skin effect), further increasing loss. Dielectric loss results when the antenna is embedded in or coated with dielectric materials—such as plastic or rubber used for packaging. Certain dielectric materials absorb energy, leading to dissipation and reduced efficiency.

Antenna loss directly impacts the antenna's transmission and reception performance, especially in low-power or long-distance energy transmission applications. Increased antenna loss reduces energy transmission rates, limits transmission distances, and raises energy consumption. Therefore, in antenna design and selection, materials, structure, and environmental factors must be carefully considered to minimise loss and enhance efficiency.

The definition of antenna loss is expressed as:

$$antenna\ loss\ (dB) = -10\ log_{10}(\eta) = 10\ log_{10}\left(\frac{Radiated\ power}{Input\ power}\right), \tag{3-4}$$

The antenna loss intuitively reflecting the impact on the antenna's overall energy efficiency. This capability cannot be easily indicated by using common indicators such as gain and beamwidth. Determining the antenna loss presents a significant challenge due to the indirect nature of measuring radiated energy, which cannot be easily or directly quantified. In practical settings, antenna loss factors are typically derived from simulation models that incorporate details of the antenna's structural design and material properties. These simulations provide a theoretical estimation of loss based on expected performance in ideal conditions, offering a baseline against which empirical data can be compared. In practical applications, the antenna efficiency values provided in commercial antenna datasheets can serve as a reference for estimating antenna losses[137].

For RF-WPT applications, designing antennas with a minimal loss factor is a priority, as even slight inefficiencies in energy conversion or radiation can significantly affect overall system performance. The process of calculating antenna loss for RF-WPT systems involves conducting sampling tests to measure actual RF link loss across various scenarios and comparing these empirical values to the theoretical values obtained from simulations. This approach ensures that any deviation observed can be attributed to practical inefficiencies in the antenna, environmental effects, or unexpected material performance, rather than model inaccuracies alone.

Incorporating this empirical data, the antenna loss is then accounted for in the RF link model, allowing for a more accurate prediction of energy transfer efficiency across the link. This methodology enhances model precision and provides insights into the specific factors impacting antenna performance, such as environmental conditions or wear on materials. Consequently, this iterative process of simulation, testing, and model adjustment allows for optimized design and performance adjustments, which are essential for achieving reliable, high-efficiency RF-WPT in real-world applications.

Antenna gain is another critical parameter in RF-WPT, on the other hand, as it directly impacts the system's transmission efficiency. Taking into account the gain of the antenna, the loss of the antenna can be expressed as:

$$antenna\ loss\ (dB) = -10\ log_{10}(\eta) - G_T - G_R, \tag{3-5}$$

Where G_T and G_R are the gains of the transmitting antenna and the receiving antenna.

High-gain antennas are particularly valuable in RF-WPT applications because increasing gain is one of the most effective methods to improve energy transfer efficiency within the constraints of antenna size and transmission power. However, high-gain antennas come with a trade-off: they typically exhibit reduced directional range, concentrating energy within a narrower beamwidth. This characteristic can limit the coverage area, necessitating precise alignment between the transmitter and receiver for optimal energy transfer.

In RF-WPT systems, achieving high gain often involves optimising the antenna’s design, such as utilising phased arrays or parabolic reflectors, to increase directional focus. While this improves energy transfer to targeted areas, it also necessitates careful design considerations to ensure the system maintains the desired balance between high gain and sufficient directional range.

C. **RF Path Loss**

RF path loss represents the attenuation of RF energy as it travels from the transmitting antenna to the receiving antenna, which is affected by factors such as transmission distance, propagation environment, and obstacles along the path. This type of loss is a critical consideration in RF link design, as it significantly impacts transmission coverage, signal quality, and power budget requirements.

Path loss arises from several key factors, including medium loss and losses resulting from interactions with obstacles, such as reflection, diffraction, and penetration. Dielectric loss occurs as RF energy passes through materials with dielectric properties, which absorb a portion of the energy and convert it to heat, diminishing the signal strength. When RF waves encounter obstacles, the resulting reflection, diffraction, and penetration losses further reduce signal intensity. Reflection occurs when waves bounce off surfaces, potentially redirecting energy away from the receiving antenna; diffraction involves bending around objects, causing partial signal loss; and penetration involves energy passing through objects, which can significantly attenuate the signal depending on the material's properties.

RF path loss can be categorized into two primary types based on the application environment: indoor and outdoor path loss. Each has distinct characteristics due to differing propagation conditions, obstacles, and attenuation factors.

It is worth noting that path loss in RF-WPT occurs under far-field conditions, which correspond to distances beyond the Fraunhofer distance. The far-field, or Fraunhofer region, is where the electromagnetic waves are sufficiently far from the source that they appear as planar waves, enabling more predictable propagation characteristics. The Fraunhofer distance, D_f, can be defined as:

$$D_f = \frac{2D^2}{\lambda}, \tag{3-6}$$

where D is the largest dimension of the antenna (e.g., the diameter if circular), λ is the wavelength of the transmitted RF wave.

Beyond the Fraunhofer distance, RF waves experience predictable attenuation, allowing path loss to be modelled accurately. Next, indoor and outdoor path loss will be discussed.

Indoor Path Loss: Indoor environments introduce complex propagation dynamics due to walls, furniture, floors, and other structural obstacles that cause significant reflection, diffraction, and scattering. Indoor path loss is often modelled using general formulas from the ITU-R P.1238-12 model[138], which takes into account the type of building materials, floor attenuation, and distance. The indoor loss expression can be represented as:

$$PL_{indoor}\left(dB|_{d,f}\right) = 10\alpha\, log_{10}(d) + \beta + 10\gamma\, log_{10}(f)\,, \tag{3-7}$$

Where d is 3D direct distance between the transmitting and receiving stations (m), f is operating frequency (GHz), α is coefficient associated with the increase of the basic transmission loss with distance, β is coefficient associated with the offset value of the basic transmission loss, γ is coefficient associated with the increase of the basic transmission loss with frequency.

The recommended coefficient values for indoor propagation environments are provided in Table 3-1.

Table 3-1. Basic transmission loss coefficients

Environment	Frequency range (GHz)	Distance range (m)	α	β	γ
Office	0.3-83.5	2-27	1.46	34.62	2.03
Corridor	0.3-83.5	2-160	1.63	28.12	2.25
Industrial	0.625-70.28	2-102	2.34	24.62	2.06
Conference lecture room	0.625-82.0	2-21	1.61	28.82	2.37

Outdoor Path Loss: Outdoor environments generally experience less multipath reflection and diffraction compared to indoor environments, though factors such as terrain, buildings, and atmospheric conditions still contribute to signal attenuation. Outdoor path loss is often modelled using Site-general formulas from the ITU-R P.1411-

12 model when no significant obstructions are present[139]. The outdoor loss expression can be represented as:

$$PL_{outdoor}\left(dB|_{d,f}\right) = 10\alpha \, log_{10}(d) \; + \; \beta \; + \; 10\gamma \, log_{10}(f), \tag{3-8}$$

Where: d is 3D direct distance between the transmitting and receiving stations (m), f is operating frequency (GHz), α is the coefficient associated with the increase in the basic transmission loss with distance, β is the coefficient associated with the offset value of the basic transmission loss, γ is coefficient associated with the increase of the basic transmission loss with frequency.

The recommended values to be used for below-rooftop propagation in urban and suburban environments are provided in Table 3-2

Table 3-2. Basic transmission loss coefficients for below-rooftop propagation

Type of environment	Frequency range (GHz)	Line of sight Non-line-of-sight	Distance range (m)	α	β	γ
Urban high-rise, Urban low-rise/ Suburban	0.8-82	Line-of-sight	5-660	2.12	29.2	2.11
Urban high-rise	0.8-82	Non-line-of-sight	30-715	4.00	10.2	2.36
Urban low-rise/ Suburban	10-73	Non-line-of-sight	30-250	5.06	-4.68	2.02
Residential	0.8-73	Non-line-of-sight	30-170	3.01	18.8	2.07

In summary, the RF link loss is:

$$RF\ link\ loss\ (dB) = \ RF\ Electrical\ Loss + Antenna\ loss + RF\ path\ loss \tag{3-9}$$

The proposed RF link model quantitatively analyses the RF energy transfer process by systematically evaluating link losses, refining energy flow metrics, and predicting energy output based on given input parameters. By assessing each component of link loss, the model establishes a corresponding loss ratio, offering valuable insights into how energy diminishes throughout transmission. Fine-tuning key RF link model parameters—such as antenna characteristics, operational frequency, and the matching network configuration—enables the identification of optimal solutions aimed at minimizing losses. This process enhances overall transmission efficiency and system performance, making the model adaptable to diverse RF-WPT applications.

3.2.1.3 RF Link Energy Transmission Model

The energy transmission model outlines transferring energy from the input point P_1 to the output point P_2. Different transmission models are applied depending on the specific environment. This project primarily utilises two models: indoor transmission and outdoor transmission. For indoor applications, the ITU-R P.1238 model is employed, while the ITU-R P.1411 model is applied for outdoor scenario[138, 139].

The RF-WPT energy transmission model can be expressed as follows:

$$P_2\,(dBm) = P_1(dBm) - RF\ Link\ Loss\ (dB), \tag{3-10}$$

where P_1 is signal generator input power and P_2 is power management output power, while the RF link loss is the total loss of the RF link, which has been discussed in the previous section.

So, the RF-WPT energy transmission model can be expressed as follows:

$$\begin{aligned} P_2\,(dBm) &= P_1(dBm) - (\,RF\ Electrical\ Loss + Antenna\ loss + RF\ path\ loss) \\ &= P_1(dBm) - \left\{ \begin{matrix} [-10\,log(1-|\Gamma_{RFE}|^2)] + [-10\,log_{10}(\eta) - G_T - G_R] \\ +[10\alpha\,log_{10}(d) + \beta + 10\gamma\,log_{10}(f)] \end{matrix} \right\} \end{aligned} \tag{3-11}$$

It should be noted that antenna loss is often presented as antenna efficiency in some commercial antenna datasheets. In such cases, attention should be paid to unit consistency during calculations, particularly when converting between decibels (dB) and percentage values. Additionally, the parameters that estimate RF path loss should be appropriately selected based on the specific application environment. According to the application, the indoor application environment mainly includes corridors, halls, offices, and other environments with roof and wall reflections. The outdoor application environment mainly includes rural, over rooftops, street, or canyon environments.

3.2.1.4 RF Link Challenges and Technology Status

The RF link in wireless power transfer systems faces three primary challenges: transmission efficiency, safety, and environmental adaptability. These aspects are closely interrelated and significantly influence the system's feasibility in real-world applications.

The efficiency of RF energy transfer is mainly determined by the antenna's performance, the rectifier circuit, and environmental attenuation. Antenna design has seen substantial advancements, including developing high-efficiency meta-surface structures, broadband configurations, and high-gain directional antennas, collectively improving coupling and radiative efficiency. However, the rectification stage remains a bottleneck. Due to the typically low amplitude of received RF signals, the forward voltage of diodes cannot be ignored; when input power falls below the diode's threshold, rectification may not initiate. Additionally, the diode's cutoff frequency limits the usable RF bandwidth, restricting performance at higher frequencies. Moreover, electromagnetic wave propagation is inherently subject to free-space path loss, which increases with frequency and distance. Environmental factors—such as physical obstructions, atmospheric moisture, and cloud absorption—can further degrade signal strength. To address these issues, this study classifies RF propagation models into indoor and outdoor categories to better represent practical attenuation conditions in corridors, offices, open areas, and urban canyons.

The long-term biological impact of RF exposure remains a critical concern, particularly in densely populated areas where high-power transmission is required. While international guidelines impose strict exposure limits, research on RF-WPT deployment in industrial, unmanned, or enclosed environments remains limited. This work adopts a directional transmission approach to reduce unnecessary radiation, ensure compliance with safety standards, and minimise potential human exposure.

RF-WPT performance is susceptible to variations in deployment environments. Challenges such as frequency interference, multipath propagation, and user density can significantly impact system stability. The proposed system integrates multi-channel, wide-bandwidth acquisition circuits to address this, enhancing its ability to adapt to diverse and dynamic operating conditions. The design and implementation of these circuits will be elaborated in the following section.

3.2.2 The Ultrasonic Link Model

A crucial factor in U-WPT applications is understanding ultrasound propagation between the transmitter and receiver, as transmission efficiency profoundly impacts system design. Unlike RF links, ultrasonic links lack a reliable, broadly applicable model within existing research. While various U-WPT models have been proposed, they often fall short in precision or fail to apply universally across diverse environments and media. This project develops a generalised link loss-based model for ultrasonic links to address these limitations, incorporating factors such as medium properties, transmission distance, and boundary effects. The following section will review the latest developments in U-WPT modelling and provide a foundation for a link loss-based approach to enhance the model's universality and accuracy.

Wilt et al. [140] proposed a one-dimensional pressure transfer model to establish a piezoelectric-based ultrasonic acoustic power channel model. This model constructs a simple channel for energy transmission and verifies the excitation response. However, it only considers the electrical domain, with insufficient discussion of the mechanical domain, thus not fully demonstrating the energy transfer process. Du et al. [141] developed a two-dimensional energy transfer model based on piezoelectric transducers' radial and axial directions, improving the accuracy of the equivalent circuit of traditional piezoelectric transducers. Nonetheless, this model focuses on the performance of ring-shaped piezoelectric transducers, whereas most applications utilise circular plate transducers and do not demonstrate performance at various stages of energy transfer. Mendonca et al. [142] demonstrated a modelling method for Multiphysics networks in acoustic systems, including the transmission medium, distance, and frequency range. Their model incorporates physical components in both the acoustic and mechanical domains but only considers changes in resonant frequency without addressing the resulting changes caused by variations in other physical components across different applications. Jiao et al. [143] established a semi-analytical model of ultrasonic power transfer, discussing the accuracy of the model and the improvement in parameters. This model accounts for transducer and transmission distances but only verifies performance in a metallic medium. As the medium changes, the impedance of the transducer also changes, limiting the model's applicability across different media. Wu et al. [144] proposed and validated new equivalent circuit models of piezoelectric and non-piezoelectric components, considering UET channel losses in underwater power transfer systems. They used two-port T parameters to describe the UET channel, calculating input impedance, input power, and output power with the proposed model. However, the parameters for each link loss model are difficult to obtain or measure, and the model cannot show the losses in the system at each stage.

In response to the complexity and limitations of existing UET models, we propose a straightforward transmission model based on extensive experimentation, which provides an abstract representation of the ultrasonic energy transmission process, analysing and predicting the energy transmission relationships within the system. It primarily encompasses the system architecture, piezoelectric transducer model and transmission model.

3.2.2.1 Ultrasonic Link Principle and Structure

U-WPT utilises ultrasonic waves to achieve wireless energy transmission. Unlike traditional RF-based wireless power transfer, which employs electromagnetic waves, U-WPT relies on acoustic waves operating in the ultrasonic frequency range, typically above 20 kHz. This method is particularly effective in environments where RF signals experience significant attenuation, such as underwater or conductive materials. Similar to RF-WPT, the basic principle of U-WPT also includes four key processes: ultrasonic energy emission, transmission, reception and energy management and storage.

Ultrasonic Energy Emission: Ultrasonic energy emission begins with a piezoelectric transducer, which converts electrical energy from a signal generator into mechanical energy. This process leverages piezoelectric materials that deform in response to an oscillating electric field, generating high-frequency ultrasonic waves， which are transmitted into the medium。

Ultrasonic Energy Transmission: Ultrasonic energy propagates from the transmitting end of the transducer through a transmission medium to the receiving end. A notable advantage of ultrasonic energy transmission is its ability to safely and effectively penetrate various media, such as metal, water, body tissue, and concrete. This characteristic makes ultrasonic transmission particularly suitable for applications where traditional RF signals are ineffective due to high attenuation.

Ultrasonic Energy Reception: Ultrasonic energy is captured by the receiver of the piezoelectric transducer. The ultrasonic waves are converted back into electrical energy through the inverse piezoelectric effect, typically alternating current. This stage completes the acoustic-to-electrical energy conversion process.

Energy Management and Storage: Rectification subsequently converts the alternating current generated at the receiving end into direct current. Energy management systems ensure this energy's regulated and efficient storage in devices such as supercapacitors or batteries. These storage units accumulate the harvested energy and provide a stable and continuous power supply to the load, ensuring reliable operation even under intermittent energy transmission conditions.

combines efficient acoustic-electrical energy conversion, targeted propagation through suitable transmission media, and intelligent energy management to deliver reliable wireless power. This approach is advantageous in environments were conductive barriers, high attenuation, or regulatory constraints limit RF-based systems. By leveraging the mechanical nature of ultrasonic waves, U-WPT provides a viable solution for energy transmission through water, metals, or biological tissues—scenarios where traditional electromagnetic methods are ineffective.

The energy flow of the ultrasonic link is shown in the Figure 3-8.

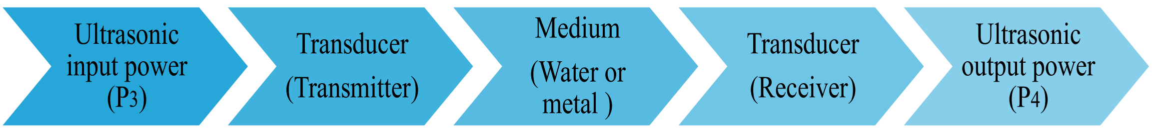

Figure 3-8. The ultrasonic link energy flow diagram.

The U-WPT model proposed in this study focuses on the application of piezoelectric transducers across various transmission media, with a primary emphasis on analysing the relationship between input and output energy as it varies across different media types and transmission distances [145]. Figure 3-9 illustrates the structure of the U-WPT system.

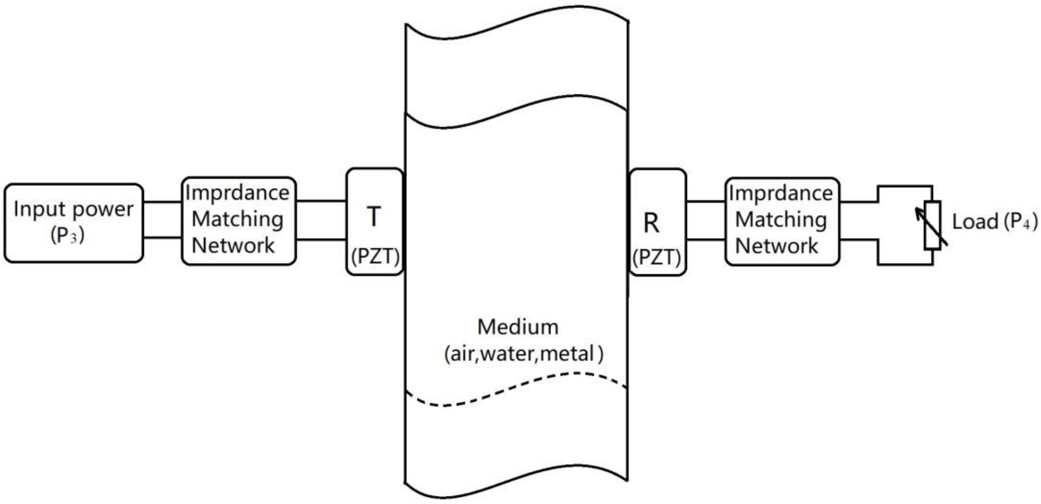

Figure 3-9. The U-WPT link structure for different transmission medium.

The UET model illustrates the conditions for maximum power transfer to the load. The transmitter is powered by a signal source (P_3) through an impedance matching network. In an ultrasonic form, the energy propagates through a medium before being sensed by the receiver. Another impedance matching network is often used between the receiver and the load (P_4).

3.2.2.2 Ultrasonic Link Loss

The ultrasonic link primarily investigates the energy losses from the driving source to the load. Ultrasonic link losses are evaluated in different application environments, considering electrical impedance mismatches, transducer size, resonant frequency, transmission medium, acoustic impedance mismatches across media boundaries, varying transmission distances, and wave interference (both constructive and destructive). Key losses within an ultrasonic link include electrical reflections, acoustic reflections, transducer inefficiencies, and dielectric transmission losses. As resonant frequencies increase, achieving effective impedance matching for electrical and acoustic components becomes increasingly challenging.

The losses observed in this study are illustrated in Figure 3-10. The individual components of loss regarding energy transfer pathways are discussed below.

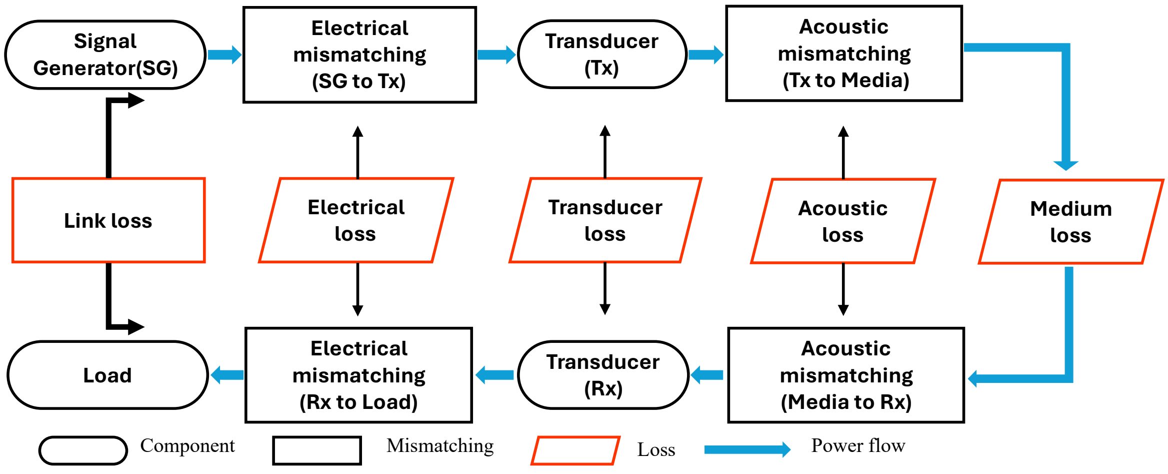

Figure 3-10. Flow diagram of ultrasonic link transmission loss. Ultrasonic link loss mainly includes electrical loss, transducer loss, acoustic loss and medium loss.

A. Electrical Loss

Electrical loss refers to the return loss due to reflection when energy (in the form of an electrical signal) reaches the transducer, which usually occurs at impedance mismatches or discontinuities. Electrical loss is measured relatively and expressed by:

$$Electrical\ Loss\ (dB) = -10\,log(1 - |\Gamma_{UE}|^2)\,, \tag{3-12}$$

where Γ_{UE} is the reflection coefficient, and given by:

$$\Gamma_E = \frac{Z_{E1} - Z_{E2}}{Z_{E1} + Z_{E2}}\,, \tag{3-13}$$

where $\mathrm{Z_{E1}}$ is the electrical impedance of the driver, which can be the impedance of the signal generator or the transducer receiver. $\mathrm{Z_{E2}}$ is the electrical impedance of the load, which can be the impedance of the load or the transducer transmitter. Electrical losses can be determined by the impedance values of the transducer, signal generator, and load.

B. Transducer Loss

Losses in piezoelectric transducers mainly include dielectric loss, elastic loss, and piezoelectric loss. These losses are characterized by the dielectric permittivity (β_{33}^S), elastic stiffness constant (C_{33}^D), and piezoelectric stiffness constant (h_{33}). Accurately measuring these coefficients in practical applications is challenging. Thus, a simpler method is used to express transducer loss.

In this study, energy is transferred through the medium as mechanical energy. Therefore, the electromechanical coupling coefficient $k^2$is a key metric for evaluating transducer losses. The k^2 is closely related to the efficiency of energy conversion between electrical and mechanical forms. Specifically, k^2 represents the ratio of stored mechanical energy to input electrical energy, indicating conversion efficiency. It also applies to the inverse scenario, representing the ratio of stored electrical energy to input mechanical energy[146].

$$k^2 = \frac{mechanical\ energy\ converted\ into\ electrical\ energy}{input\ mechanical\ energy}, \tag{3-14}$$

Or

$$k^2 = \frac{electrical\ energy\ converted\ into\ mechanical\ energy}{input\ electrical\ energy}, \tag{3-15}$$

where k^2 is related to the vibration mode and shape of the transducer. When the electric field is parallel to the direction of polarization, the induced strain is in the same direction as the electric field. For discs and rods shaped transducers, k^2 can be calculated as:

$$k_d^2 = \frac{\pi}{2}\frac{f_n}{f_m} tan\left[\frac{\pi}{2}\left(\frac{f_n - f_m}{f_m}\right)\right], \tag{3-16}$$

For transducers with other shapes, a general model is expressed as:

$$k_{eff}^2 = \frac{f_n^2 - f_m^2}{f_n^2}, \tag{3-17}$$

where f_m is minimum impedance frequency (resonance frequency), and f_n is maximum impedance frequency (anti-resonance frequency). However, k^2 does not account for dielectric losses or mechanical losses, nor recovery of unconverted energy. Therefore, the transducer loss is modified as:

$$Transducer\ loss\ (dB) = -10\ log(k^2). \tag{3-18}$$

C. **Acoustic Loss**

Acoustic loss primarily occurs at the boundaries where the transducer interfaces with the transmission medium. The acoustic impedance of the transducer typically differs from that of the transmission medium, resulting in boundary reflections.

Similar to electrical losses, the expression for acoustic boundary loss is governed by:

$$Acoustic\ Loss\ (dB) = -10\ log(1 - |\Gamma_A|^2), \tag{3-19}$$

Where Γ_A is the reflection coefficient, defined as:

$$\Gamma_A = \frac{Z_{A2} - Z_{A1}}{Z_{A2} + Z_{A1}}, \tag{3-20}$$

where Z_{A1} and Z_{A2} are the acoustic impedances of the transducer and the transmission medium.

D. **Ultrasonic Path Medium Loss**

Ultrasonic path medium loss refers to the energy dissipation as ultrasonic waves propagate from the transmitter to the receiver through a given medium. Since ultrasonic links typically span only a few to several tens of centimetres, the receiver may operate within both the near-field and far-field regions of the ultrasonic field. This dual-region operation substantially complicates the analysis of dielectric loss, as propagation characteristics and energy density differ markedly between these regions. Moreover, the lack of a standardised model for energy transmission between ultrasonic transducers further exacerbates the difficulty in accurately analysing and predicting energy transfer from transmitter to receiver.

This project proposes an innovative methodology that leverages the reciprocal network properties of ultrasonic transducers, employing acoustic pressure as an intermediate variable to characterise energy transmission within the ultrasonic link. By adopting this approach, the model effectively captures the bidirectional nature of energy transfer between transmitter and receiver. The subsequent sections delineate the model development process, progressing from the foundational transducer representation to a comprehensive ultrasonic link energy transmission model. This development involves modelling the intrinsic properties of transducers, analysing their reciprocal characteristics, and integrating pressure-based variables as mediators in the energy transmission pathway.

Firstly, transducers play a critical role in the ultrasonic energy transmission system. While some studies approximate the transducer emission as a point source, in practical scenarios, the transducer radius is often comparable to the ultrasonic wavelength and therefore cannot be neglected. Consequently, the transducer is modelled as an infinite planar piston to more accurately represent its physical behaviour. When the transducer features a rigid backing surface, it is further idealised as a boundless plane, as illustrated in Figure 3-11.

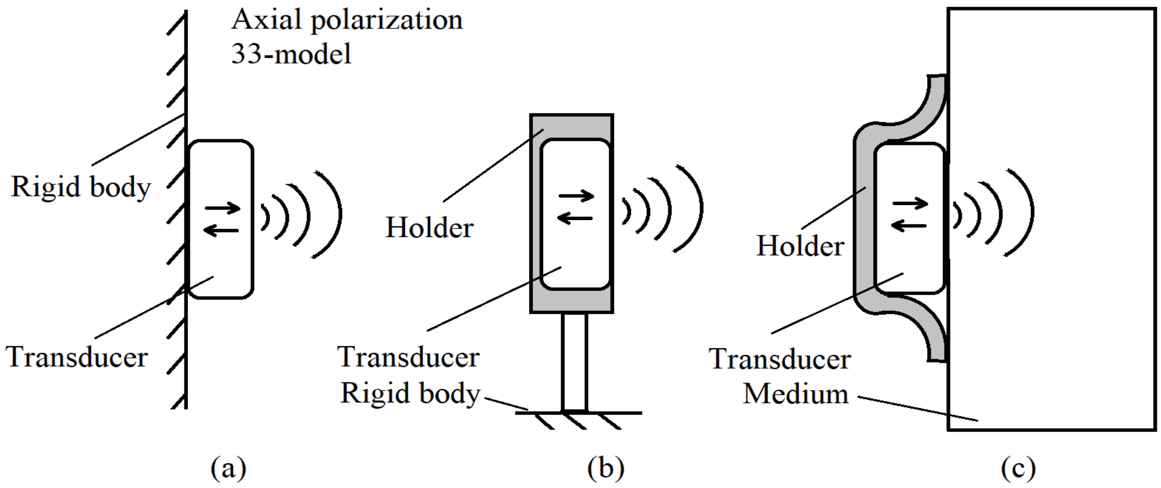

Figure 3-11. Schematic diagram of application of infinite planar piston model. This diagram exampled three different configurations for fixing the ultrasonic transducer. The transducer's vibrating surface moves along the axis, emitting ultrasonic waves in one direction: Transducer fixed on a rigid body (a), transducer fixed via holder on a rigid body (b), transducer directly attached to the medium via holder (c).

This study investigates the relationship between energy transfer efficiency and transmission distance in ultrasonic wireless power transfer systems across various media. An analytical model based on the infinite plane piston acoustic theory was developed to quantify medium-induced losses. This model characterises the energy transmission from the transmitting transducer to the receiving transducer, accounting for the acoustic properties of different propagation environments. Detailed derivations and model formulations are provided in the appendices under the Transducer Ultrasonic Infinite Plane Piston Acoustic Model. Although the classical circular piston acoustic model in an infinite rigid baffle has been extensively studied by researchers such as

Pierce[147], Bies and David[148], Kinesler et al[149], Meyer and Erwin[150], we propose an improved model for analysing and calculating ultrasonic energy transmission loss in different media. This model utilizes the reciprocal two-port network characteristics of the transducer, with pressure as an intermediate variable.

As illustrated in Figure 3-12, when the transmitter input power is Pin, the pressure is p_1 at observation point O located a distance r away. According to two-port reciprocity, if the pressure at observation point O is p_1, then the transducer's output power is Pin.

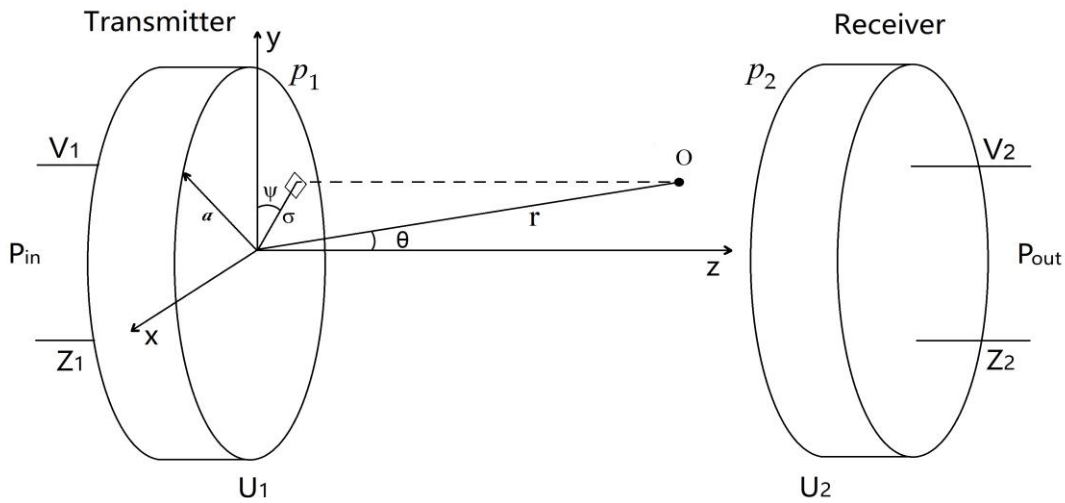

Figure 3-12. The transmitter with radius a and impedance Z1 emits ultrasonic waves outwards, driven by the input power Pin and voltage is V1. The emitted pressure is p1 and the amplitude of surface vibration velocity is U1. The receiver with same radius and impedance is Z2. The pressure at the receiver is p2, the amplitude of the surface vibration velocity is U2, the generated power is Pout and voltage is V2. The piston lies in the x-y plane and vibrates vertically parallel to the z-axis. The distance between the observation the point O and the centre of the piston is r, and the angle between the z-axis is θ.

As the transducer is driven by a simple harmonic wave, it can be modelled as a collection of small pulsating spheres. The equation governing the pulsating sphere model is:

$$U_0 = Ue^{j\omega t}, \tag{3-21}$$

where U_0 is the velocity at time t, and U is Initial amplitude. ω is angular frequency, which is $\omega = 2\pi f$, and f is the frequency.

According to acoustic theory, when the radius of the sphere is small enough compared to the length of the distance, the pressure at the observation point O at time t is [151]:

$$p(r,t) = j\rho c \frac{1}{\lambda} U \frac{1}{r} e^{j(\omega t - kr)}, \tag{3-22}$$

where p is the pressure, ρ is the density of the medium material, c is the wave speed in the medium, λ is the wavelength, r is the distance between pulsating sphere and observation point O, and k is the wave number, which is $k = \frac{2\pi f}{c}$,

Based on the transducer model shown as Figure 3-12, the total pressure p at observation point O is obtained by integrating over the surface of the piston as follows [149]:

$$p = \frac{j\rho ck}{2\pi r} U e^{j(\omega t - kr)} \int_0^a \sigma \, d\sigma \int_0^{2\pi} e^{jk\sigma \sin\theta \cos\psi} \, d\psi, \tag{3-23}$$

where a is the transducer radius.

The piston exhibits different behaviours in the near field and far field. In the far field, the piston shows significant directionality. In contrast, the near-field pressure field contains local maxima and minima, and the directionality is less pronounced. Therefore, the far-field and near-field conditions will be discussed separately.

the condition for a point of observation in the far field and near field is:

$$r \gg \frac{f a^2}{c}, \tag{3-24}$$

Since this study focuses on the relationship between energy transmission and transmission distance, the observation point is placed on the z-axis at a distance r. Consequently, the relationship between pressure and transmission distance is as follows:

For far field,

$$p = j\rho c \frac{Uka^2}{2r} e^{j\left[\omega t - \frac{k}{2}\left(\sqrt{r^2+a^2}+r\right)\right]}, \tag{3-25}$$

For near field,

$$p = j2\rho c U e^{j\omega t} \sin\left[\frac{k}{2}\left(\sqrt{r^2+a^2} - r\right)\right] e^{-j\frac{k}{2}\left(\sqrt{r^2+a^2}+r\right)}, \tag{3-26}$$

In an ideal free space without reflection or interference, energy decreases nonlinearly as transmission distance increases. This behaviour is influenced by the material properties and ultrasonic frequency. Figure 3-13 shows the pressure amplitude versus distance in an ideal, reflection-free space. The demonstration model utilizes aluminium medium, featuring a PZT-4 material transducer with a radius of 12.5 mm, driven at 10 dBm and 40 kHz.

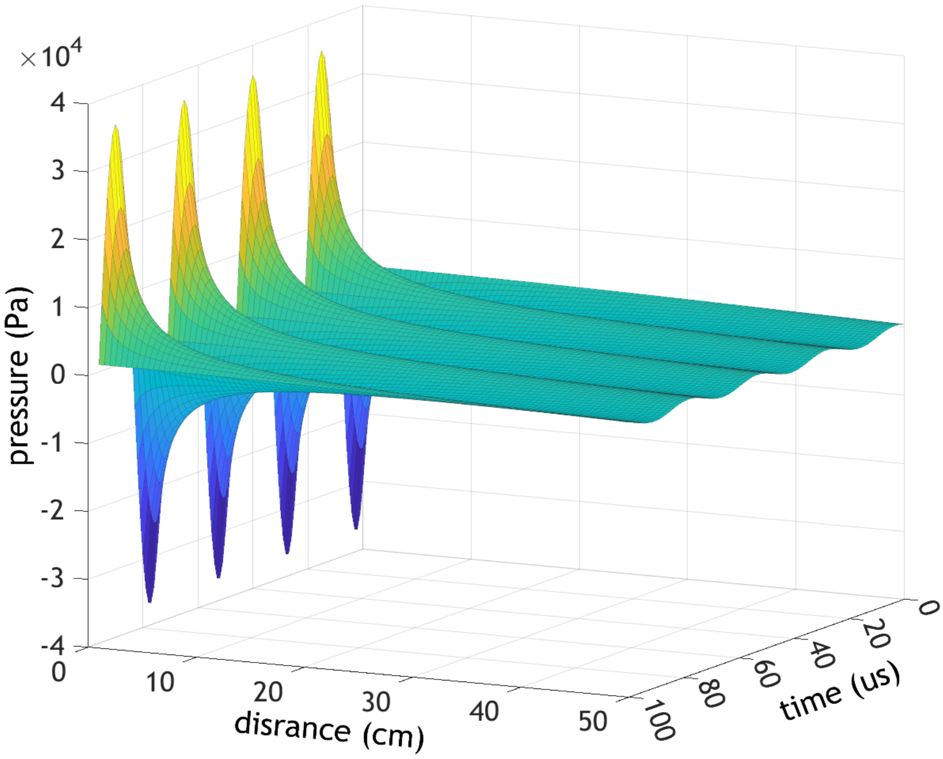

Figure 3-13. The relationship between pressure amplitude and distance and time in an ideal free space without reflection. The sound pressure amplitude decreases with distance due to medium losses. Additionally, since the driving source is a sine wave, the sound pressure oscillates over time as the frequency of source.

According to Figure 3-12, the expression of transducer power is:

$$P = \frac{V^2}{Z_E}, \tag{3-27}$$

Where P and V are the power and voltage, for the transmitter, P and V are the input power and input voltage, and for the receiver, P and V are the output power and output voltage. Z_E is the impedance real part of the transducer.

According to the working characteristics of the transducer, the piezoelectric coefficient (d33) of the transducer is introduced. The vibration speed of the medium is equated to that of the transducer, giving the expression for U:

$$U = \frac{dS}{dt} = \frac{d(d_{33} \times V)}{dt}, \tag{3-28}$$

where S is the displacement of the transducer's surface, and V is the voltage applied to the transducer.

In the UET system, the transducer's driving voltage is expressed as $Vsin(\omega t)$, and thus, the U is given by:

$$U = d_{33} \times V \times \omega, \tag{3-29}$$

Therefore, the transducer power is expressed as:

$$P = \frac{V^2}{Z_E} = \frac{1}{Z_E}\left(\frac{U}{d_{33} \times \omega}\right)^2. \tag{3-30}$$

The power relationship between the transmitter and the receiver is:

$$\frac{P_{in}}{P_{out}} = \frac{Z_{E2}}{Z_{E1}} \times \left(\frac{U_1}{U_2}\right)^2, \tag{3-31}$$

where $\mathrm{P_{in}}$ is input power to the transmitter, $\mathrm{P_{out}}$ is output power from receiver, $\mathrm{Z_{E1}}$ is the electrical impedance of the transducer transmitter. $\mathrm{Z_{E2}}$ is the electrical impedance of the transducer receiver. It is worth noting that the transducer in this part is considered ideal, assuming no losses occur during energy conversion. This simplification allows for a focus on the efficiency of other components within the system. While transducer-specific conversion losses have been explored under transducer loss analysis. This approach helps isolate areas for optimization and aligns theoretical model with practical considerations that influence real-world performance.

Due to transmitter-receiver reciprocity, the relationship between surface vibration velocities at distance r, based on the transmission model (3-25) and (3-26), is expressed as:

for far field,

$$\frac{U_1}{U_2} = \frac{4r}{ka^2} sin \frac{ka}{2} e^{j\frac{k}{2}(\sqrt{r^2+a^2}+r-a)}, \tag{3-32}$$

for near field,

$$\frac{U_1}{U_2} = sin \frac{ka}{2} csc \left[\frac{k}{2}\left(\sqrt{r^2+a^2}-r\right)\right] e^{j\frac{k}{2}(\sqrt{r^2+a^2}+r-a)}. \tag{3-33}$$

The energy at the receiver is influenced by both transmission losses and interference. Transmission interference arises from the superposition of ultrasound waves (mainly longitudinal waves) between the transmitter and receiver within the medium. Constructive and destructive interference occurs as the transmission distance varies. Therefore, the pressure at the receiver is minimum at nodes and maximum at antinodes.

In free space, the positions of nodes and antinodes based on transmission distance and wavelength are:

Nodes

$$r = 2n \times \frac{1}{4}\lambda, \tag{3-34}$$

Antinodes

$$r = (2n+1) \times \frac{1}{4}\lambda, \tag{3-35}$$

where n is the number of the nodes and antinode.

In enclosed spaces, transmission interference arises from the receiver surface and boundaries, leading to more complex results at the receiver. In UET systems, the receiver should be positioned at an antinode to maximize received energy.

The relationship between the input energy at the transmitter, the output energy at the receiver, and the transmission distance is established. This relationship is influenced by both the transmission medium and transducer characteristics. Based on the energy transmission model, once the transducer parameters are known, the energy transfer behaviours across different media and transmission distances can be predicted. This information is crucial for optimizing ultrasonic energy transmission systems and designing effective power budgets.

According to the ultrasonic link model, ultrasonic path medium loss is defined as:

For far field,

$$Ultrasonic\ Path\ Medium\ loss\ (dB) =$$

$$-10\log\left\{\frac{Z_{E2}}{Z_{E1}}\times\left[\frac{4r}{ka^2}sin\left(\frac{ka}{2}\right)e^{j\frac{k}{2}\left(\sqrt{r^2+a^2}+r-a\right)}\right]^2\right\}, \tag{3-36}$$

For near field,

$$Ultrasonic\ Path\ Medium\ loss\ (dB) =$$

$$-10\ log\left\{\frac{Z_{E2}}{Z_{E1}}\times\left[sin\left(\frac{ka}{2}\right)csc\left(\frac{k}{2}\left(\sqrt{r^2+a^2}-r\right)\right)e^{j\frac{k}{2}\left(\sqrt{r^2+a^2}+r-a\right)}\right]^2\right\}\ , \tag{3-37}$$

In summary, the ultrasonic path dielectric loss was determined through an in-depth analysis of the transducer model and its energy transfer characteristics, with pressure as the primary intermediate variable. This analysis is grounded in the piezoelectric ceramic transducer model, which utilizes the infinite plane piston approach to capture both near-field and far-field effects. This model effectively characterizes the transducer's pressure output across various transmission distances, with primary influencing factors including the medium's density, the speed of sound, the transducer's dimensions, and the surface vibration velocity.

Additionally, the transducer's functionality as a reciprocal network plays a crucial role: the transmitting transducer converts electrical energy into mechanical energy, while the receiving transducer converts this mechanical energy back into electrical energy. By studying the transducer's pressure behaviour, the model clarifies the energy transfer dynamics between these components. Consequently, this ultrasonic link model will more accurately forecast energy transfer across diverse media and transducer configurations, providing a valuable tool for optimizing ultrasonic energy transmission systems.

In summary, the main losses of the ultrasonic link include electrical loss, transducer loss, acoustic loss and path medium loss. They can be measured separately. By measuring, verifying and calibrating known parameters, a more accurate ultrasonic link model can be obtained. Therefore, ultrasonic link loss can be expressed as follows:

$$Ultrasonic\ Link\ Loss\ (dB) = Electrical\ loss + Transducer\ loss$$
$$+Acoustic\ loss + Medium\ loss \tag{3-38}$$

The proposed ultrasonic link model quantifies the ultrasonic energy transfer process by analysing link losses, refining the energy flow, and assisting in predicting the energy output based on the input. By examining the link losses, the corresponding loss ratio can be determined. Adjusting ultrasonic link model parameters, including transducer radius, frequency, and medium density, helps identify optimal solutions to minimise losses and optimise the system.

3.2.2.3 Ultrasonic Link Energy Transmission Model

The energy transfer model investigates the relationship between the energy input at the transmitter (P3) and the energy output at the receiver (P4). The U-WPT energy transmission model can be expressed as follows:

$$P_4\ (dBm)\ =\ P_3(dBm) - Ultrasonic\ Link\ Loss\ (dB), \tag{3-39}$$

where P3 is signal generator input power and P2 is power management output power, while the RF link loss is the total loss of RF link, which has been discussed in the previous section.

So, the U-WPT energy transmission model can be expressed as follows:

$$P_4\ (dBm)\ =\ P_3(dBm) - \begin{pmatrix} Electrical\ loss + Transducer\ loss \\ +Acoustic\ loss + Medium\ loss \end{pmatrix}$$

$$=\ P_3(dBm) + 10\ log(1 - |\Gamma_{UE}|^2) + 10\ log(k^2) + 10\ log(1 - |\Gamma_A|^2)$$

$$+\begin{cases} 10\log\left\{\dfrac{Z_{E2}}{Z_{E1}} \times \left[\dfrac{4r}{ka^2} sin\left(\dfrac{ka}{2}\right) e^{j\frac{k}{2}(\sqrt{r^2+a^2}+r-a)}\right]^2\right\}\ (far\ field) \\ 10\ log\left\{\dfrac{Z_{E2}}{Z_{E1}} \times \left[sin\left(\dfrac{ka}{2}\right) csc\left(\dfrac{k}{2}\left(\sqrt{r^2+a^2} - r\right)\right) e^{j\frac{k}{2}(\sqrt{r^2+a^2}+r-a)}\right]^2\right\}\ (near\ field) \end{cases} \tag{3-40}$$

The ultrasonic link energy transfer model effectively illustrates the process of ultrasonic power transmission, enabling adaptability across various application environments and energy requirements. By mapping out the specific parameters and losses involved, this model serves as a valuable tool for guiding the design of ultrasonic links, allowing for tailored adjustments that improve transmission efficiency and reliability. Consequently, it aids in the precise configuration of ultrasonic systems to meet the demands of specific operational contexts, thereby enhancing overall system performance.

3.2.2.4 Ultrasonic Link Challenges and Technology Status

Ultrasonic links transmit energy by propagating sound waves through air or solid materials, making them particularly effective for underwater, indoor, and low-power applications. Although U-WPT has shown high transmission efficiency and security in specific contexts, it still encounters significant challenges. These include issues related to transmission efficiency, distance, sensitivity to boundaries, directional limitations, transducer efficiency and physical size, and security concerns.

In terms of transmission efficiency, ultrasonic energy, like electromagnetic waves, undergoes significant attenuation as the transmission distance increases, especially in air. Higher frequencies also lead to increased energy loss. Consequently, this project employs electromagnetic waves for transmission in air and ultrasonic waves for metal or water media.

For transmission distance, the project is primarily designed to power sensor platforms. While the transmission range of U-WPT is inherently limited, the required distances within the sensor platform's application environment—such as across metal plates—are typically below 5 cm, making U-WPT suitable for this context.

Boundary sensitivity is another consideration, as changes in the ultrasonic link's medium can significantly affect transmission. Shifts in medium alter the acoustic impedance, and impedance discontinuities cause sound wave reflection, reducing transmission efficiency. The primary boundary effect in this project arises at the interface between the transducer and the transmission medium. To mitigate this, materials with similar acoustic impedance are used, and the contact surfaces are polished to minimize reflection.

In terms of directionality, proper alignment of the transducer's transmitter and receiver is crucial. Optimal U-WPT transmission efficiency is achieved when the transmitter is cantered on the receiver. To maintain alignment, this project employs a symmetrical magnetic shoulder around the transducer.

For transducer efficiency and size, limitations arise from transducer manufacturing capabilities. This project tested transducers of various materials and dimensions, selecting those most suitable for the specific requirements.

Lastly, regarding safety considerations, current limitations of ultrasound primarily involve concerns related to surface contact and auditory exposure. However, as this system is designed to power low-power devices, the operating power remains well below established safety thresholds—specifically, 3 W/cm^2 for surface intensity and 110 dB (6.32 Pa) for acoustic pressure levels [152, 153, 154, 155]. This ensures the system operates within safe bounds for both human interaction and long-term deployment.

3.2.3 Conversion Circuit

The conversion circuit is the central interface that integrates RF energy harvesting and ultrasonic transducer driving circuits through a well-designed energy management system. Its primary function is to convert electromagnetic energy, collected by the receiving antenna in the RF link, into usable electrical energy. This harvested energy is then regulated and directed by the energy management system to the ultrasonic transducer driver, which subsequently drives the transducer to emit ultrasonic energy in the ultrasonic link. Carefully coordinating energy flow between RF harvesting, management, and ultrasonic driving ensures efficient energy conversion and delivery. Figure 3-14 illustrates the energy flow within the converter, highlighting the conversion process between energies.

Figure 3-14. The converter energy flow diagram.

Given the limited received electromagnetic energy and the high-power demand of the ultrasonic transducer transmitter, the energy management circuit is tasked with efficiently collecting, accumulating, storing, and switching the constrained electromagnetic energy to the transducer driver. A time-sharing energy management strategy is employed, where in electromagnetic energy collection and ultrasonic energy transmission operate independently. In this approach, electromagnetic energy is accumulated and stored over an extended period, while the transducer driver operates intermittently for short durations to emit ultrasonic energy. This effectively resolves the power mismatch between energy collection and ultrasonic transmission.

The energy management circuit performs multiple critical functions, including collecting, rectifying, boosting, and storing electromagnetic energy within the RF link. Simultaneously, it manages the conduction and disconnection of the transducer driver to ensure seamless operation. Throughout this process, it is essential to maintain voltage compatibility, implement over-voltage and over-current protection mechanisms, and provide adjustable operation modes to adapt to diverse environmental conditions. Figure 3-15 illustrates the converter's structure, highlighting the function of the converter and the integration of its core components.

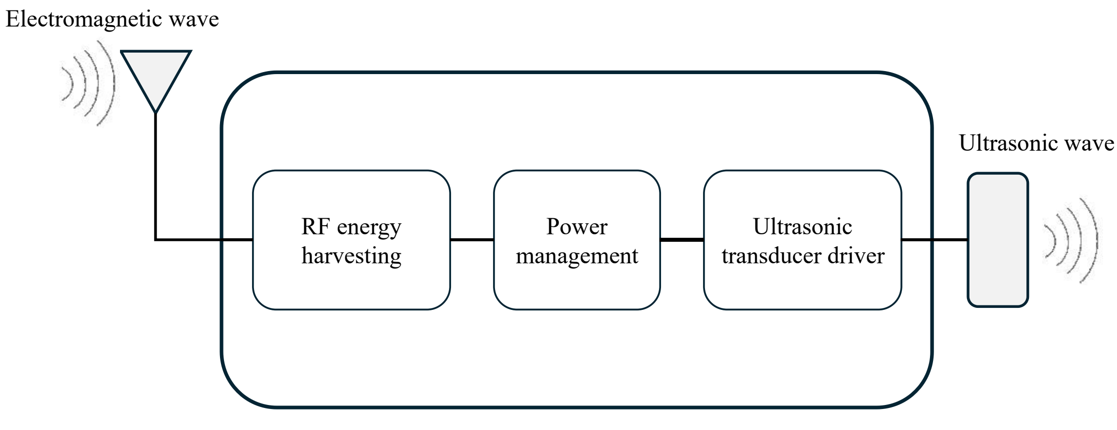

Figure 3-15. Schematic diagram of the converter structure. Its main function is to collect electromagnetic energy and emit ultrasonic energy.

The primary function of the converter is to facilitate the transition from electromagnetic energy collection to ultrasonic energy emission. It achieves this by integrating three key subsystems: the RF energy harvesting subsystem, the energy management subsystem, and the ultrasonic transducer driving subsystem. The interplay of these subsystems within the converter ensures an efficient transition from electromagnetic energy harvesting to ultrasonic energy transmission, optimising efficiency and reliability. Each subsystem plays a distinct role in the energy flow, which will be discussed below.

3.2.3.1 RF Energy Harvesting

RF energy harvesting converts electromagnetic energy into AC via an antenna, followed by a harvesting circuit that rectifies the AC into DC for subsequent use. This process involves two critical components: the input impedance matching network and the rectifier. The input impedance matching network is designed to minimise energy reflection and maximise power transfer, with its design heavily influenced by the operating frequency and bandwidth requirements. The rectifier, responsible for AC-to-DC conversion, offers various implementation options, including diode-based rectifiers, charge pumps, and active rectifiers employing MOSFETs. Each approach presents distinct advantages and trade-offs, which must be considered based on the specific application requirements.

A. **Input Impedance Matching Network**

Impedance matching is a fundamental aspect of RF wireless power transfer systems, as it directly affects power transfer efficiency and system performance. An input impedance matching network matches the impedance of the RF source to that of the load, such as an antenna or rectifier, to maximise power transfer and minimise signal reflections.

Even slight impedance mismatches in RF systems can lead to significant power losses due to reflected signals. Proper impedance matching ensures that the maximum amount of RF energy is delivered to the load, particularly at high frequencies. Moreover, effective matching can broaden the operational bandwidth, enhance the performance of broadband antennas and improve the frequency adaptability of the RF link.

Although signal-to-noise ratio and data integrity are not primary concerns in RF energy transmission, impedance mismatches still result in energy reflections that reduce overall transmission efficiency and may generate standing waves that degrade system stability.

Common types of impedance matching networks are L-type networks, π-type, T-type networks, and transformer-based matching[156].

L-type Network: Simple and frequently used for single-frequency matching, this network involves one inductor, and one capacitor arranged in various configurations to achieve impedance matching. Due to its simplicity, it is most effective in narrowband applications where minimal component use is advantageous.

π-type and T-type Networks: Composed of multiple reactive capacitors and inductors components, π-type and T-type networks are ideal for achieving impedance matching across a broader frequency range. These configurations offer greater design flexibility, enabling effective impedance matching for wideband applications and more complex impedance conditions.

Transformer-Based Matching: Utilizing RF transformers, these networks allow for impedance transformation and are particularly beneficial in low-frequency RF applications or when handling large impedance ratios. Transformer-based matching is advantageous when precise impedance scaling is needed, such as in high-impedance mismatch scenarios.

Figure 3-16 shows the common types of impedance matching networks, including low-pass and high-pass types. Although there are also band-pass and band-stop matching networks, they are combinations of the above networks. Each suited for specific frequency ranges and design needs. Various impedance matching networks are available for RF input impedance matching, allowing for flexible selection based on the specific impedance of the signal source and antenna. Choosing an appropriate matching network enables optimal power transfer and minimizes reflections, enhancing RF system efficiency and performance.

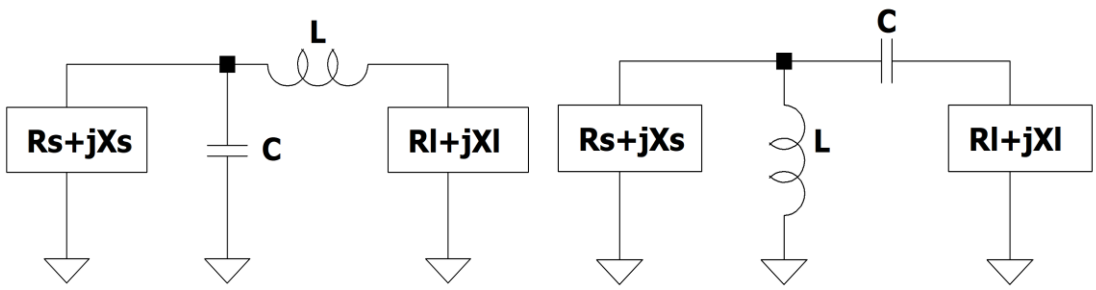

(a) L-type networks

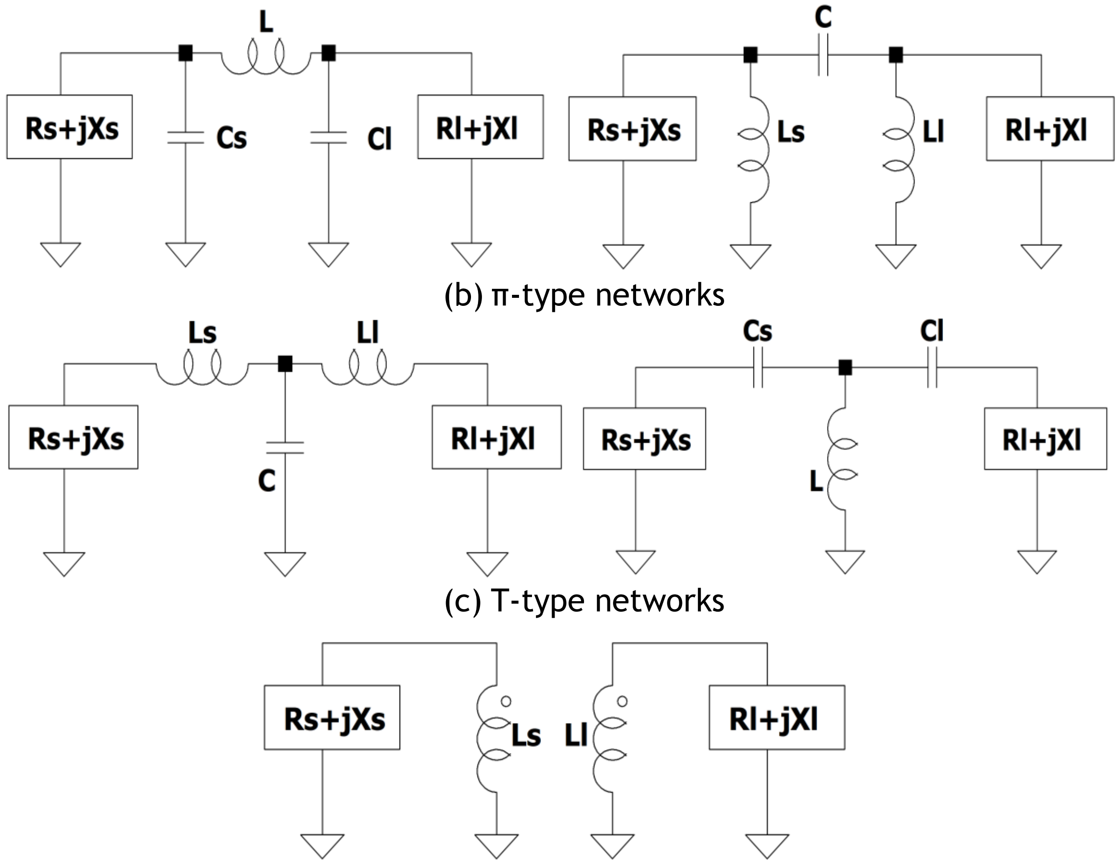

(b) π-type networks

(c) T-type networks

(d) transformer-type network

Figure 3-16. Common types of RF impedance matching networks: L-type networks (a), π-type (b), T-type networks (c), and transformer-type network (d) [156].

B. Rectifier

RF rectifier and charge pump are crucial components in RF Energy Harvesting (RFEH) systems, designed to convert the AC energy from an RF link into storable DC energy. Since AC energy cannot be directly stored, a highly efficient rectifier circuit is essential for effective energy harvesting, as it maximizes the usable power output. However, in RF links, the received energy is often very low, which poses a limitation, especially for diode-based rectifiers where the forward voltage is a significantly challenge.

In the context of this project, a detailed exploration of the RF rectifier’s operation, essential performance metrics, and existing design structures will be presented. The working principle will cover the AC-to-DC conversion mechanics, typically involving diodes or other nonlinear components to rectify the signal. Key performance indicators include rectification efficiency, sensitivity to low input power with the RF source.

Additionally, we will list established rectifier configurations, such as single-stage, multi-stage, and voltage-doubling architectures, which are each suited to different RFEH requirements depending on input power levels and application needs. This analysis will highlight the critical role of rectifier and charge pump design in ensuring effective RF energy harvesting, especially under low-energy conditions in the receiving circuit.

RF rectifiers utilize nonlinear components, primarily rectifier diodes, to convert the AC from the RF link into DC energy. The conversion process involves several key steps. Initially, the receiving antenna captures RF energy, which is then transmitted to the rectifier circuit through an impedance matching network, ensuring efficient energy transfer. The RF AC signal is subsequently rectified by a diode or other nonlinear component, converting it into pulsating DC energy. To achieve a stable DC voltage output, a filtering component, typically a capacitor or inductor, smooths out these pulsations.

If the input energy is high and the load power is low, and the output DC energy can meet the load requirements, the collected energy can be directly output to the low-power device through the current stabilizer. When the input energy is low and cannot meet the load requirements, it needs to be stored in a capacitor or battery after energy storage, accumulation and boosting, and then output to the load to meet the short-term energy requirements of the device.

When the input energy is sufficiently high and the power demand of the load is low, the output DC energy from the rectifier can be supplied directly to the low-power device via a current stabilizer, allowing for continuous operation without the need for additional storage. In this scenario, the energy transfer is straightforward, as the incoming power meets or exceeds the device's requirements.

Conversely, when the input energy is low and cannot directly fulfil the load's power needs, the harvested energy must be stored and managed more strategically. In such cases, the energy is accumulated in a capacitor or battery. This stored energy may then be boosted through a charge pump, ensuring that the necessary voltage level is met before outputting to the load. This method provides a reliable power supply for devices with intermittent or bursty power demands, allowing them to operate effectively even when the input energy fluctuates.

Various rectifier circuits have been developed for RF energy harvesting and wireless power transfer, each tailored to specific power requirements and frequency ranges. Selecting an appropriate circuit depends on factors such as input power level, operational frequency, and desired output characteristics. The following are some of the main types of rectifier circuits.

Half-wave Rectifier: The simplest configuration, using a single diode, suitable for low-power and compact applications. The schematic diagram is shown in the Figure 3-17.

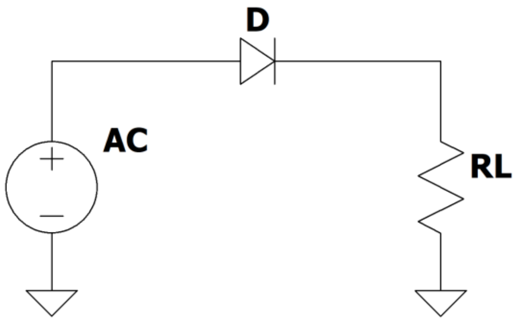

Figure 3-17. The schematic of half-wave rectifier circuit.

Often used in low-power RF energy harvesting for small devices like sensors and micro-powered electronics. In addition, some re-antennas usually use half-wave rectification. The half-wave rectifier circuit, which operates with a single diode, benefits from a small voltage drop across the diode. Its simplicity makes it suitable for integration within array rectifier antennas, where multiple rectifier outputs can be combined in parallel. However, as it only rectifies one half-cycle of the AC signal, the output is discontinuous, leading to efficiency levels below 50%. This lower efficiency, along with the interrupted DC output, limits its applicability in scenarios where a steady and high-efficiency DC supply is required.

Full-wave rectifier: There are two main configurations: one uses a centre-tapped transformer with two diodes, where each diode conducts during alternate cycles of the AC input. This setup provides effective rectification but requires a centre-tapped transformer, adding to size and cost. The other configuration, the bridge rectifier, consists of four diodes arranged in a bridge that converts the entire AC waveform to DC without needing a centre tap. This design is more compact and versatile, although it introduces a slightly higher voltage drop across the diodes. A full-wave rectifier converts both positive and negative cycles of an AC signal into DC output, resulting in greater efficiency and a smoother DC signal than half-wave rectification. The schematic diagram is shown in the Figure 3-18 [157].

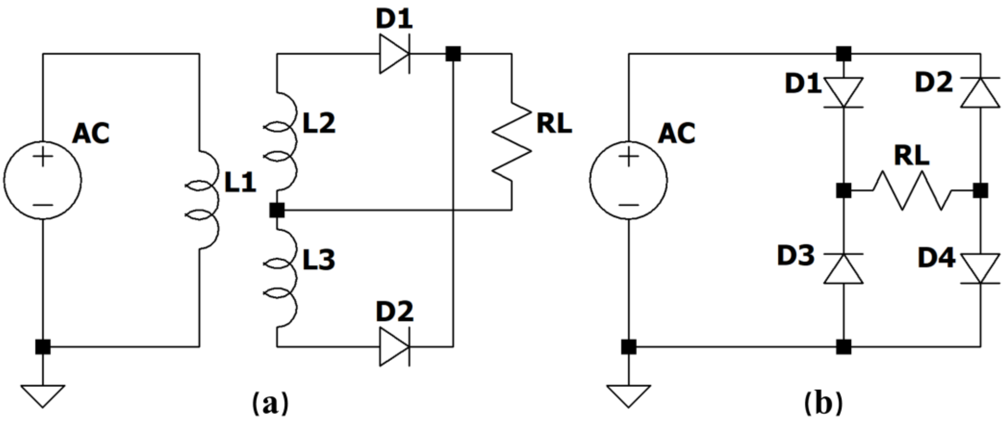

Figure 3-18. The schematic of full wave rectifier circuit. Transformer structure (a) and transformer-less structure (b).

Full-wave rectifier circuits are commonly used in high-power applications due to their ability to deliver stable output. The centre-tapped transformer design reduces the voltage drop to a single diode; however, the physical size of the transformer can restrict its use in space-constrained applications. In contrast, the full-bridge rectifier circuit is compact and easily integrated, but it has a double diode voltage drop, which is disadvantageous for RF links with low voltage input. This increased voltage drop significantly limits the sensitivity of the RF energy harvesting circuit, making it less effective in capturing low-power RF signals.

Frequency conversion rectifier: A frequency conversion rectifier works by converting a high-frequency RF signal into a lower-frequency AC signal before rectifying it into DC. This frequency reduction simplifies the rectification process, allowing for the use of standard diodes rather than specialized, high-speed ones. By operating at a lower frequency, the rectifier can leverage high-voltage diodes that are optimized for low-frequency applications, eliminating the need to compromise between frequency and output voltage. This approach is particularly beneficial for systems where stable high-voltage output is needed without the complexity of managing high-frequency rectification constraints. Figure 3-19 shows the circuit structure of variable frequency rectification.

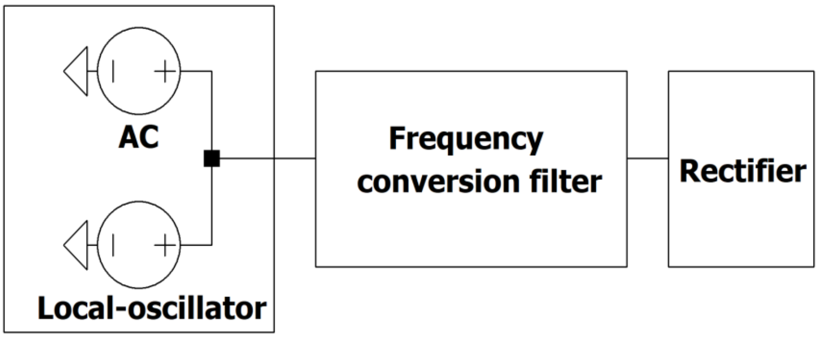

Figure 3-19. Schematic diagram of frequency conversion rectifier circuit structure

Frequency conversion rectification offers a way to overcome the frequency limitations of the RF link by down converting high-frequency signals to a lower frequency, making rectification easier. However, as illustrated in the schematic, this approach requires a local oscillator to generate a mixing signal and then filters to isolate the high-frequency energy for rectification. This setup introduces complexity by necessitating an external oscillation source, and it also results in significant energy loss due to the discarded high-frequency component. Consequently, while this technique can facilitate rectification at reduced frequencies, it comes at the cost of lower overall efficiency in the energy conversion process.

C. **Charge Pump**

A charge pump uses a series diode and capacitor network to gradually increase the input voltage in a "stage" manner. Each stage of the charge pump increases the output voltage, theoretically up to a multiple of the input voltage. The charge pump is fed by an RF signal. As the input voltage increases alternately, the capacitors are charged in stages, superimposing the voltage. The multiple of the output voltage depends specifically on the number of stages in the circuit. However, as more stages are added, the voltage drop and ripple increase. Figure 3-20 shows a Cockcroft–Walton (CW) charge pump and a Dickson charge pump [158, 159].

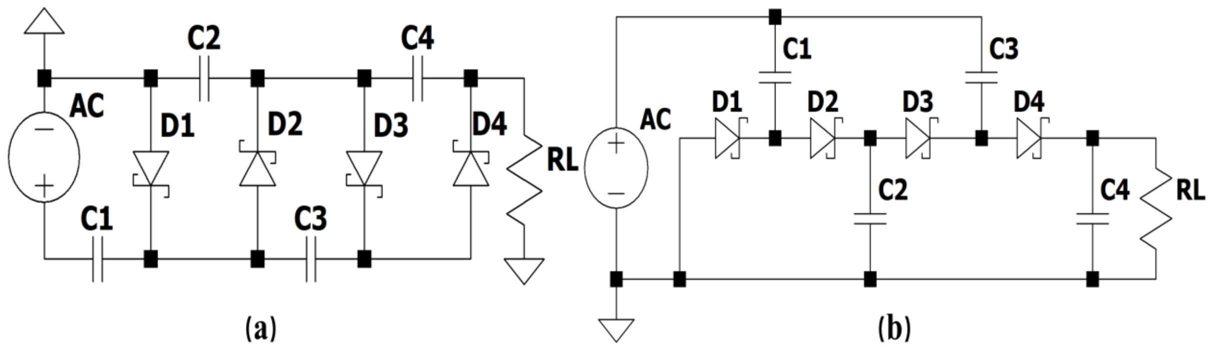

Figure 3-20. The schematic of charge pump circuit. Cockcroft–Walton structure (a) and Dickson structure (b).

Charge pumps are commonly applied in scenarios requiring very high output voltages, but in low-input RF links, they are also utilized to increase voltage levels to satisfy load requirements. However, the use of multiple diodes and capacitors in charge pumps introduces the size limitation. besides, series the diodes increased diode voltage drop, which reduce rectifier efficiency. Moreover, effective operation requires alternating diode forward-biased and reverse-biased, which relies on efficient diode recovery times. While Schottky diodes are typically chosen for their faster response, their performance drops notably when frequencies exceed 1 GHz, resulting in lower forward current and reverse voltage capabilities, which constrains high-voltage outputs. Consequently, designing an effective charge pump requires carefully balancing operating voltage and frequency to optimize performance.

D. Active Rectifier

Active rectifier replaces traditional diodes with active components, such as MOSFETs, achieving high rectification efficiency even at low input voltages. Active rectifiers offer significantly higher efficiency and sensitivity than diode-based rectifiers due to their lower forward voltage drop. This lower drop minimizes energy loss during rectification, making active rectifiers especially advantageous in applications where efficiency and sensitivity to low input power are critical. Schematic Figure 3-21 shows an active rectifier based on a charge pump[159].

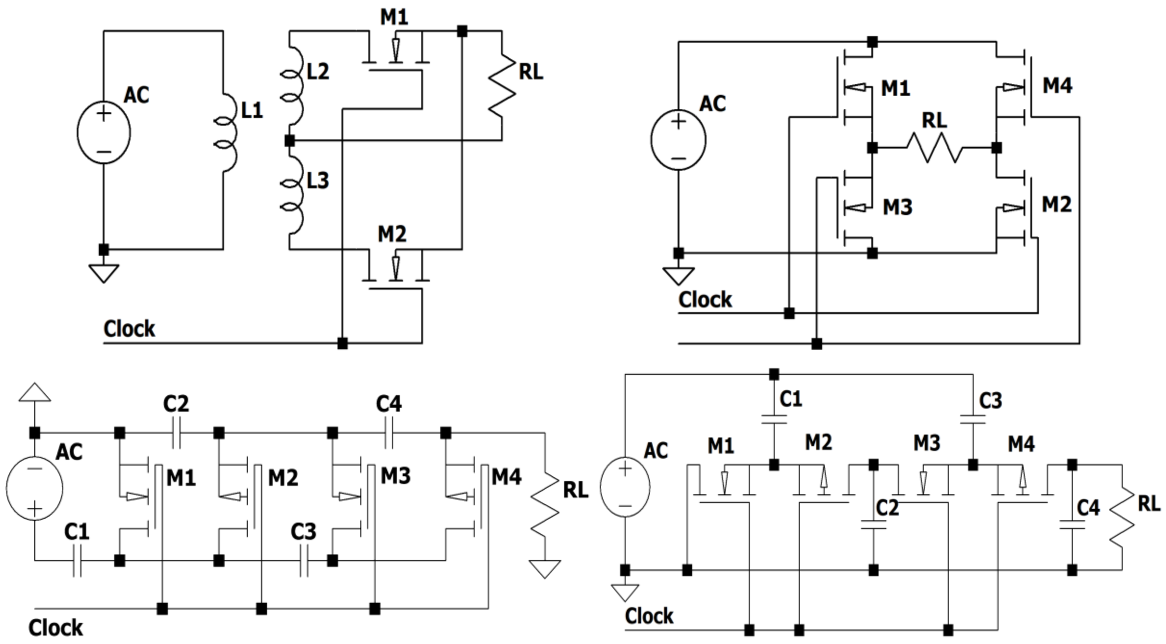

Figure 3-21. The schematic diagram of an active rectifier circuit utilizing a charge pump.

Active rectifiers, by employing components like MOSFETs, significantly improve energy conversion efficiency, making them well-suited for low-power RF energy harvesting and wireless power transfer systems. However, MOSFETs introduce some design challenges, as they require precise control signals to operate effectively. For instance, to function as a switch, the MOSFET's gate voltage must be driven by a clock signal that is typically above 5V. Achieving this voltage requires either additional control circuits or external power sources, which are often impractical and add complexity to RF energy harvesting systems, where minimal power and simplicity are essential.

This constraint limits the effectiveness of active rectifiers in RF energy harvesting, where available power is typically low, and complex control circuitry can reduce overall efficiency. Therefore, while active rectifiers offer advantages in conversion efficiency, balancing their operational requirements with system constraints remains a key challenge.

The RF rectifier plays a central role in RFEH systems, converting RF energy into usable DC power. Various rectifier designs are employed in RFEH, each with distinct limitations that necessitate customisation based on specific load demands and application conditions. The performance of diodes and other nonlinear components in RFEH remains limited, affecting efficiency and sensitivity. However, as energy harvesting technology advances, the efficiency and applicability of these rectifiers are likely to improve, broadening their potential for diverse applications.

In summary, the RFEH section typically consists of several key components: input impedance matching, the rectifier circuit, and the charge pump.

The input impedance matching network is critical for maximising the energy transferred from the RF source to the system. Various input impedance options have been discussed, allowing for selecting an appropriate matching network based on the specific input characteristics and design requirements. By optimising these components, the efficiency and performance of the RFEH system can be significantly improved.

In RF rectifiers, key performance indicators include conversion efficiency, input sensitivity, and output voltage. Conversion efficiency reflects how effectively RF energy is transformed into DC power and is heavily influenced by input power levels, frequency, and circuit design. With a fixed forward voltage, higher input power generally leads to higher conversion efficiency, as more of the input energy is harnessed as output. Input sensitivity, on the other hand, defines the minimum RF power required for the rectifier to function, with greater sensitivity enabling operation in environments with low RF power. This characteristic is essential for applications in energy-scarce environments, where weak RF signals need to be captured efficiently. A high-sensitivity rectifier design ensures the circuit remains responsive at lower input levels, thus widening its application scope.

Output voltage is also a fundamental aspect, representing the stable DC level provided by the rectifier under standard operating conditions. An efficient rectifier, potentially with a charge pump, can deliver adequate DC output even when input power is low. Since most loads have minimum voltage requirements, and as the load's power demand increases, so does the necessary minimum input voltage. These performance indicators collectively determine a rectifier's suitability, guiding both design and practical use in RF energy harvesting applications.

3.2.3.2 Power Management

The energy management circuit developed for this project plays a pivotal role in addressing the inherent challenges of RF energy harvesting and ultrasonic transmission.

Specifically, the system must reconcile the disparity between the limited energy input available from RFEH and the substantial power requirements of the ultrasonic transmitter. This discrepancy arises because RFEH is inherently constrained by the need to comply with electromagnetic exposure regulations and low power density at the receiver end. In contrast, the ultrasonic transmitter demands significant energy output to achieve the requisite power level for effective transmission and maintain a sufficient communication distance. This necessitates the design of an efficient and intelligently integrated energy management architecture.

The cornerstone of the energy management system is the boost converter, which addresses the low voltage output of the RFEH rectification circuit. The rectified voltage is typically insufficient to directly drive subsequent circuits or the ultrasonic transmitter. By increasing this low and variable voltage to a higher, stabilised level, the boost converter ensures that the energy is adequately conditioned for further processing. This step is essential for bridging the mismatch between input energy levels and the power requirements of the output stage.

Following the voltage conditioning, an energy storage module is integrated to accommodate the intermittent and limited nature of the harvested energy. The energy storage system, typically comprising capacitors or rechargeable batteries, accumulates the harvested energy over time. This mechanism ensures that sufficient energy is available to meet the periodic high-power demands of the ultrasonic transmitter. Without this energy accumulation, the transmitter would not be able to sustain its operation, compromising system reliability and efficiency.

A critical component of the energy management system is the voltage detection circuit, which monitors the state of the energy storage module. This circuit determines whether the stored energy has reached a sufficient threshold to enable the proper operation of the ultrasonic transmitter. By doing so, it prevents premature or inefficient energy release, ensuring that the transmitter operates within its designed power parameters. This detection mechanism is integral to optimising the utilisation of harvested energy and maintaining system efficiency.

To regulate the energy flow between the storage module and the ultrasonic transmitter, a switching commutation is incorporated. This mechanism operates in conjunction with the voltage detection circuit, connecting the energy storage to the transmitter only when the stored energy surpasses the required operational threshold. Conversely, when the stored energy falls below the threshold, the switch disconnects the transmitter, preventing inefficient operation and potential system instability. This dynamic control ensures that the transmitter receives energy only under optimal conditions, enhancing overall system performance.

The energy management system is thus composed of four key components—boost converter, energy storage, voltage detection circuit, and switching commutation —all functioning in a coordinated manner to achieve efficient energy conversion and utilisation. The architecture ensures that the ultrasonic transmitter is powered reliably despite the constraints of limited and fluctuating input energy.

The overall structure of the energy management circuit is illustrated in Figure 3-22, which elucidates the logical flow and interaction between its constituent components. This design not only optimises the use of scarce energy harvested from RFEH but also satisfies the high-power demands of ultrasonic transmission. The proposed system represents a robust and scalable solution for applications requiring energy efficiency, compactness, and reliable operation.

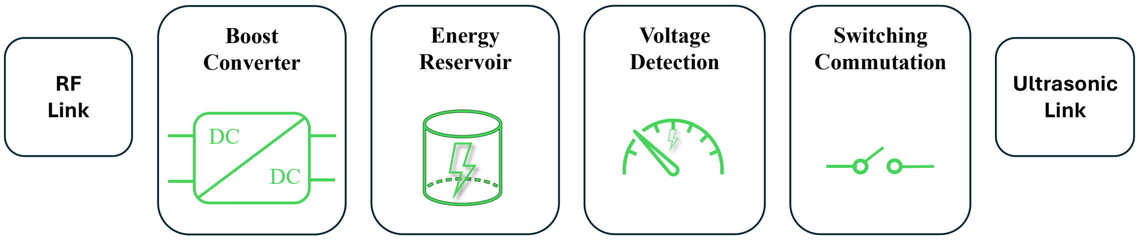

Figure 3-22. The structure of the energy management diagram

As shown in Figure 3-22, the energy management circuit must meet several key requirements. The boost converter should efficiently handle low input voltages while maximising conversion efficiency. The energy storage module must exhibit reliability across multiple charge-discharge cycles with low internal resistance. The voltage detection circuit should dynamically adjust to varying energy levels and consume minimal power. Finally, the switching mechanism must be reliable and energy-efficient to ensure effective delivery of stored energy to the load. Together, these components enable efficient energy transfer from the RFEH input to the ultrasonic transmitter output.

A. Boost circuit

The energy obtained through RF energy harvesting is typically limited, resulting in a low output voltage that is insufficient to power subsequent circuits directly. To address this, a boost circuit is employed to step up the output voltage and ensure a stable supply for downstream components, enabling them to operate efficiently under consistent conditions. The following Figure 3-23 example illustrates a boost circuit design tailored for RF energy harvesting applications, highlighting its functionality and effectiveness in voltage regulation[160].

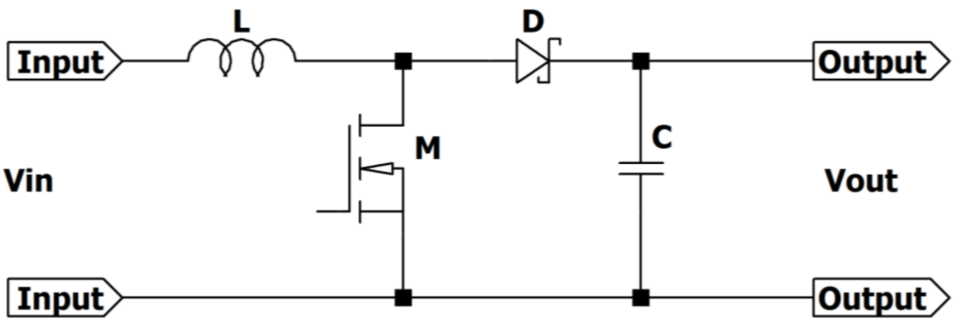

Figure 3-23. The basic schematic of a boost converter.

The boost converter is designed to step up the input voltage to a higher output voltage, using a combination of energy storage elements and controlled switching. The operation is based on two key stages:

Switch-on Stage: During this stage, the MOSFET (denoted as M) is turned on, creating a low-resistance path. Energy from the input voltage is stored in the inductor L, which builds up a magnetic field. Simultaneously, the capacitor C provides energy to the load. At this point, the diode D is reverse-biased, effectively isolating the load from the inductor.

Switch-off Stage: When the MOSFET M is turned off, the inductor L releases the stored energy as the magnetic field collapses. This creates an induced electromotive force that combines with the input voltage. The diode D becomes forward biased, allowing the combined voltage to charge the capacitor C and power the load.

Through this alternating operation, the converter steps up the input voltage. The relationship between the input voltage (Vin) and the output voltage (Vout) is determined by the duty cycle (D) of the MOSFET switching and is expressed as:

$$V_{out} = \frac{V_{in}}{1-D} \tag{3-41}$$

Where: D is the duty cycle of the MOSFET (ratio of on-time to total switching period).

As D approaches 1, the output voltage Vout increases significantly, but practical limitations such as switching losses and component tolerances must be considered, and the main losses including.

Conduction Losses: These occur due to the resistive components in the circuit, such as the inductor, MOSFET, and diode. The resistance and the current flowing through these components result in heat dissipation. Minimising conduction losses involves selecting components with lower resistance and optimising the circuit to reduce current flow, particularly during low-power operation.

Switching Losses: Switching losses arise during the transition of the MOSFET between on and off states. During these brief moments, both voltage and current overlap, leading to energy loss. Factors influencing switching losses include the MOSFET's on-resistance, drain-source voltage, and the frequency of operation.

Diode Reverse Recovery Losses: When the diode switches from conducting to blocking, it undergoes a reverse recovery phase where current flows in the reverse direction momentarily. This causes power losses. These can be minimised by using Schottky diodes or other diodes with short reverse recovery times, which are particularly suited for high-frequency applications.

Magnetic Core Losses: Inductors experience losses in their core material due to alternating magnetic fields, resulting in heat generation. These losses depend on the core material, operating frequency, and magnetic flux density. Selecting core materials with low loss characteristics and designing inductors to operate at lower flux densities can help reduce these losses.

Capacitor Losses: The equivalent series resistance (ESR) of the capacitor introduces losses as heat when current flows through it. This not only reduces the converter's efficiency but may also impact the capacitor's lifespan. Using capacitors with lower ESR ratings is an effective way to mitigate these losses, especially in high-current applications.

The boost converter for this project is designed specifically for RFEH applications, where maintaining efficiency and ensuring stable output voltage are critical. While energy management circuits will process the output, the output voltage ripple must remain within acceptable limits during design. Below is an introduction to the calculation of the key components involved in the design:

The inductor plays a vital role in storing energy during the MOSFET conduction phase and releasing it during the off phase. The inductance value L can be calculated using the following equation:

$$\mathrm{L} = \frac{V_{in} \times D}{f_{sw} \Delta I_L} \tag{3-42}$$

Where: V_{in} is the input voltage. ***D*** is the duty cycle. f_{sw} is the switching frequency. $\Delta I_L$is the desired peak-to-peak ripple current in the inductor, typically 20-40% of the average inductor current.

The output capacitor reduces the ripple voltage and provides energy to the load during the switching cycle. The capacitance C can be calculated using:

$$\mathrm{C} = \frac{I_{out} \times D}{f_{sw} \Delta V_{out}} \tag{3-43}$$

Where: I_{out} is the load current. ΔV_{out} is the acceptable ripple voltage on the output.

Low-ESR capacitors, such as ceramic or tantalum types, are preferred to minimise losses and ripple.

The diode must handle the peak current and reverse voltage of the converter. The peak current rating I_{peak} and reverse voltage rating $V_{reverse}$ are determined by:

Using a Schottky diode is recommended for lower forward voltage drop and reduced reverse recovery losses.

The MOSFET must support the peak current and voltage stresses in the circuit:

$$V_{DS} \geq V_{out}$$
$$I_{DS} \geq I_{peak} \tag{3-44}$$

Additionally, the MOSFET's on-resistance (R_{DS}) should be minimised to reduce conduction losses, and its gate charge should be low for efficient switching.

The output voltage ripple ΔV_{out} depends on the inductor current ripple and capacitor ESR:

$$\Delta V_{out} = \Delta I_L \times \left(ESR + \frac{1}{8f_{sw} \times C} \right) \tag{3-45}$$

Careful component selection ensures that the ripple remains within acceptable limits.

Once initial component values are calculated, the design may need iterative refinement based on simulation or testing to optimise performance under the expected load and input conditions. Special attention is paid to efficiency, ripple control, and thermal management for the constrained energy source in RFEH applications.

In addition to designing a custom boost converter, commercial integrated boost converter circuits were evaluated as alternatives for RFEH in this project. The Table 3-3 below summarises the performance characteristics of the selected integrated circuits (ICs).

Table 3-3. Commercial ICs boost converter performance for RFEH.

Part Number	Startup Voltage (mV)	Input voltage (V)	Output voltage (V)
LTC3108	20	0.02-0.5	2.3-5.1
LTC3106	850	0.3-5.1	2.1-4.3
TPS61200	500	0.3-7	1.8-5.5
SPV1050	550	0.55-18	2.2-5.3
BQ25570	600	0.1-5.1	2.2-5.5

It is worth noting that the LTC3180 uses a 1:100 transformer, which results in low startup voltage and input voltage.

When selecting ICs for energy harvesting, preference should be given to those with the lowest possible input voltage capability and an output voltage up to 5V, as this range satisfies the operating conditions of most electronic components. It is also essential to consider the startup voltage requirement of the ICs. While certain chips can function with very low input voltages during operation, their startup voltages might be significantly higher, which could limit their applicability in energy-constrained environments. Table 3-3 summarises the most advanced ICs currently available for energy harvesting applications. Commercial ICs provide efficient and compact alternatives to custom designs.

The primary function of a boost converter in RFEH is to elevate the collected RF energy's voltage to a level compatible with the output load, ensuring the load operates effectively. While many commercial integrated boost converters demonstrate the ability to function at exceptionally low input voltages, they typically necessitate a higher startup voltage to initiate operation. Additionally, it is important to note that while boost converters effectively increase the voltage, they do not augment the load capacity under the constraints of limited input energy. As a result, the system's efficiency and stability require the incorporation of energy management strategies. Energy management is critical for optimising system operation, balancing energy distribution, and maintaining consistent functionality despite variations in harvested energy.

B. **Energy reservoir**

Given that the input energy is lower than the required output energy, energy storage becomes an essential component of the system. The selection of energy storage devices must account for factors such as capacity, voltage range, maximum current handling, and internal resistance. Currently, the two primary options for energy storage in such applications are supercapacitors and batteries. The following sections will provide a detailed comparison of these two solutions, focusing on their respective advantages and limitations in the context of the project's requirements.

Supercapacitors and batteries offer distinct advantages in energy storage, making them suitable for different applications depending on the system requirements. Supercapacitors are renowned for their high-power density, which can reach up to 10,000 W/kg. This characteristic, combined with their ability to charge and discharge rapidly—within seconds to minutes—makes them ideal for applications requiring transient power, such as energy recovery systems and starting power for devices. Their longevity is another significant advantage; with a cycle life exceeding 500,000 cycles, they far surpass conventional batteries. Moreover, supercapacitors operate effectively across a wide temperature range (-40 ℃ to 70 ℃), making them highly suitable for extreme environmental conditions. However, their low energy density (typically 1–10 Wh/kg) limits their capacity to store energy for extended periods. Additionally, they exhibit a high self-discharge rate, which further restricts their use to short-term energy storage applications.

Batteries, on the other hand, excel in energy density, offering 100–300 Wh/kg, which is substantially higher than supercapacitors. This makes them suitable for long-term power supply applications, such as portable electronics and electric vehicles. Their relatively low self-discharge rate enhances their viability for such uses. However, batteries have several limitations, including slower charge and discharge rates, a narrower operating temperature range (-10 ℃ to 40 ℃), and a shorter cycle life of 500 to 3,000 cycles. Despite these drawbacks, batteries are a mature technology with well-established manufacturing processes, making them cost-effective and widely accessible.

In practical energy storage systems, the combination of supercapacitors and batteries often proves to be a more efficient solution. Supercapacitors can handle instantaneous high-power demands, such as load surges, while batteries ensure continuous power delivery over a prolonged duration. This hybrid approach leverages the strengths of both technologies, enabling systems to meet diverse energy requirements effectively. The Table 3-4 shows the performance of the two energy storage methods [161].

Table 3-4. Comparison of energy storage performance between supercapacitors and batteries

parameter	Supercapacitor	Battery
power density	1 to 10 Wh/kg	100 to 300 Wh/kg (lithium-ion batteries)
Charge/Discharge time	seconds to minutes	minutes to hours
cycle life	>500,000 times	500 to 3,000 times
temperature range	-40°C to +70°C	-10°C to +40 °C
Energy storage efficiency	>95%	70–90%
Self-discharge rate	20 to 40% per month	1 to 5% per month
Volume/Weight	Large size, light weight	Small size, high weight

For this project, where both transient and sustained energy needs are critical, the sensor applications of the operational demands and environmental constraints will guide the selection or combination of these storage solutions to optimise efficiency and reliability. The choice between batteries and supercapacitors largely depends on the specific energy supply requirements and the nature of the application. For instance, in scenarios where energy is supplied infrequently, such as in environmental monitoring systems where the energy supply occurs once a day, batteries are a more suitable option. The higher energy density of batteries allows them to store sufficient energy for long-term use, ensuring that the system remains operational over extended periods without frequent recharging. Additionally, their lower self-discharge rate and ability to provide steady power over time make them ideal for such applications, where sustained energy delivery is essential and intermittent charging is feasible.

Conversely, in applications where energy is supplied at shorter intervals, such as once a minute, supercapacitors would be a more appropriate choice. Supercapacitors excel in handling short bursts of high power, making them ideal for systems that require rapid charge and discharge cycles. With their high-power density and fast charging capabilities, supercapacitors are well-suited for situations where energy must be quickly stored and released within short periods. Their ability to efficiently handle transient loads ensures that the system can operate reliably in environments where frequent energy inputs and outputs occur.

In summary, the selection between batteries and supercapacitors depends on the operational characteristics of the energy supply and the specific demands of the application, such as the frequency of energy input, the duration of energy storage, operating environment temperature and the power requirements during operation. By matching the energy storage solution to the application's needs, it is possible to optimize performance and ensure long-term reliability.

C. **Voltage Detection**

Voltage detection is a critical component in the energy management of RFEH and ultrasonic drive circuits. In this system, a fundamental challenge arises from the mismatch between the input power of the RFEH and the power demand of the ultrasonic drive. The RFEH unit typically generates low and intermittent power, while the ultrasonic drive requires relatively high power over a short duration to operate effectively. To bridge this gap, an energy storage unit is introduced to accumulate energy during the harvesting phase and release it rapidly when the ultrasonic drive is active.

The operation of the energy storage unit necessitates precise monitoring to ensure system efficiency and reliability. Specifically, the energy storage unit must determine two key operational states: whether sufficient energy has been accumulated to meet the power requirements of the ultrasonic drive, and when to stop energy delivery to the ultrasonic drive.

Voltage is employed as the primary metric for energy management due to its capability to represent the energy state of the storage unit and its simplicity in implementation. For capacitors, voltage is directly proportional to the energy stored, while for batteries, voltage can indirectly indicate the state of charge within a given range. This makes voltage a versatile parameter that can serve as both an energy indicator and a control signal.

By monitoring the voltage of the energy storage unit, the system can assess whether sufficient energy has been accumulated to support the ultrasonic drive. Additionally, voltage thresholds can be used to control the switching circuit, ensuring efficient energy delivery to the load while avoiding over-discharge or under-utilisation of the energy storage unit.

Furthermore, voltage provides real-time feedback on the system's performance. It reflects the efficiency of the RFEH during the charging phase and the effectiveness of the energy delivery during the discharging phase. Consequently, voltage detection is not only essential for operational control but also for system diagnostics and optimisation.

The relationship between energy (E) and voltage (V) in the energy storage unit can be expressed as follows:
For supercapacitor,

$$E = \frac{1}{2} C(V_1^2 - V_2^2) \tag{3-46}$$

Where: E represents the stored energy (in joules, J), C is the capacitance (in farads, F) of the energy storage unit, and V1 and V2 represent the lower and upper voltage (in volts, V) thresholds of the energy storage unit, respectively, and additionally serve as control signals for deactivating and activating the switching circuit.
For battery,

$$\mathrm{E} = \mathrm{Q}(V_1 - V_2) \tag{3-47}$$

Where: Q is the charge capacity of the battery (in ampere-hour, Ah)

Since capacitors and batteries express capacity in fundamentally different ways, their analysis must be conducted separately. Capacitors typically specify capacity in terms of farads (F), which relate to their ability to store charge, while batteries measure capacity in ampere-hours (Ah), which reflect the amount of current they can supply over time. In addition, capacity, the voltage also represents the relationship between the RFEH input energy and the ultrasonic drive energy.

Assuming an idealised scenario where 100% of the input energy is transferred to the output, the relationship between energy and voltage can be expressed as follows:

$$\mathrm{P}_{RFEH} \times t_1 = \mathrm{P}_{Ultrasonic} \times t_2 \tag{3-48}$$

Where: P_{RFEH} is the input power from RFEH, $\mathrm{P}_{Ultrasonic}$ is the output power to drive transducer, t_1 and t_2 are the RFEH accumulation time and transducer operation time.

So, the voltage relationship between input and output is:
for supercapacitor,

$$\frac{1}{2}C(V_1^2 - V_2^2) = \frac{V_2^2 - V_1^2}{Z_E} t_2 \tag{3-49}$$

for battery,

$$\mathrm{Q}(V_1 - V_2) = \frac{V_2^2 - V_1^2}{Z_E} t_2 \tag{3-50}$$

Where Z_E is the impedance of the piezoelectric transducer loaded by the ultrasonic driving circuit.

It is important to highlight that although the theoretical relationship between the charging voltage and time for a capacitor and battery can be expressed as:

$$t = RC_{eq} \ln\left(\frac{V_C - V_1}{V_C - V_2}\right) \tag{3-51}$$

Where: R is equivalent internal resistance of the battery and supercapacitor (in ohm, Ω), C_{eq} is the equivalent capacity of batteries and supercapacitors and V_C is RFEH output voltage.

In this project, however, the limited input power from the RFEH means that the charging voltage cannot remain constant during the capacitor's charging process. The input energy varies with time due to fluctuations in harvested RF energy and the characteristics of the energy harvesting circuit. As a result, the charging process deviates from the standard exponential curve described above, becoming more complex and requiring dynamic analysis to account for variable input power and charging rates.

This non-ideal charging behaviour has implications for the energy storage design. It necessitates careful consideration of rated capacitance and the integration of energy management systems to ensure that sufficient energy is accumulated to meet the demands of the load, even under variable input conditions.

Voltage is used as a detection indicator of energy storage. Optimizing the voltage detection range and the capacity of energy storage elements can ensure the efficient operation of RFEH and ultrasonic drive. This optimisation strikes a balance between efficiency and reliability, catering to the project's energy constraints and load requirements.

Voltage detection circuits are tasked with monitoring the energy storage unit's voltage levels to ensure that energy accumulation and delivery align with the system's operational requirements. These circuits must be reliable, energy-efficient, and capable of providing precise voltage sampling under varying conditions. Two primary methods are employed for voltage detection: capacitor sampling and resistor sampling.

Each method has distinct advantages and limitations, making them suitable for different applications. Figure 3-24. Voltage detection of capacitor sampling and resistor sampling. illustrates these two sampling techniques, which are used to effectively monitor the voltage of capacitors and batteries. Proper selection of the sampling method ensures accurate voltage detection and easy integration into the energy management circuit.

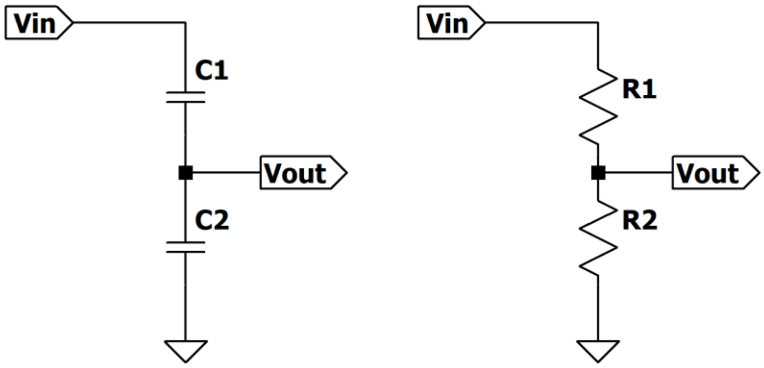

Figure 3-24. Voltage detection of capacitor sampling and resistor sampling.

The relationship between the output and input of capacitor sampling and resistor sampling is:

$$V_{out} = \frac{C_1}{C_1 + C_2} V_{in}$$

$$V_{out} = \frac{R_2}{R_1 + R_2} V_{in} \tag{3-52}$$

Capacitor sampling and resistor sampling methods each have distinct advantages and limitations, making them suitable for different applications in energy management.

Capacitor Sampling: This method is characterised by minimal output loss, particularly advantageous in RFEH systems where input energy is scarce. The loss in capacitor sampling arises from the ESR of the capacitor, which is typically very small, ensuring high efficiency. Moreover, when the energy storage element discharges, the energy stored in the sampling capacitor is also delivered to the load, further enhancing the overall energy utilisation. However, capacitor sampling has limited driving capability, as it primarily provides a voltage signal rather than significant current. Consequently, it is less suitable for driving components like thyristors but performs effectively when paired with MOSFETs, which require minimal gate drive current.

Resistor Sampling: In contrast, resistor sampling exhibits strong load-driving capabilities, making it better suited for applications requiring the operation of high-current components. Despite this advantage, resistor sampling incurs energy losses as heat due to the continuous flow of current through the resistor. Precision adjustable resistors, however, offer greater flexibility for fine-tuning the output, allowing for easy optimisation of the system's performance. This adjustability is less straightforward with capacitors, as variable capacitors are typically more limited in availability and range.

Capacitor sampling is particularly well-suited for applications where high efficiency and minimal energy losses are critical, such as in low-power systems like RFEH. In contrast, resistor sampling is advantageous in situations requiring strong driving capabilities and precise control of output adjustments. Balancing these trade-offs is essential to achieving optimal performance and efficiency in the overall circuit design, ensuring the energy management system aligns with the operational demands and constraints of the application.

Another noteworthy voltage detection scheme is the use of Zener diodes for threshold voltage detection, which is particularly suitable for energy management systems operating at a specific target voltage. The Zener diode leverages its unique breakdown characteristic to maintain a stable reference voltage when the input voltage exceeds its breakdown voltage. This property allows it to act as a precise threshold detector in the circuit.

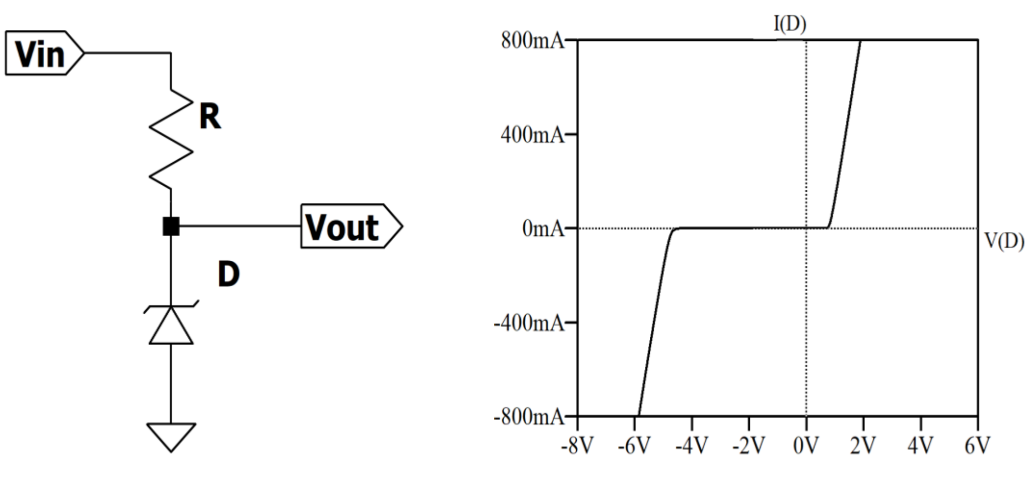

Figure 3-25. Typical Detection Circuit Using a Zener Diode and It's I-V Curve

As shown in Figure 3-25. Typical Detection Circuit Using a Zener Diode and It's I-V Curve, the typical circuit configuration includes a Zener diode connected in reverse bias across the energy storage unit. The diode remains non-conductive until the input voltage reaches its breakdown threshold, at which point it begins to conduct, providing a clear signal for the switching circuit. The corresponding I-V curve illustrates this behaviour, with negligible current flow below the breakdown voltage and a sharp increase once the threshold is reached. Currently the output voltage is about 5V.

This method offers simplicity and reliability, particularly for applications where a fixed voltage reference is required. However, its efficiency and adaptability may be limited compared to other voltage detection techniques, especially in scenarios involving varying input or output voltage conditions. Thus, while Zener diode detection is a robust option for systems with stable operational voltages, careful consideration is needed to determine its suitability in dynamic energy management environments.

The choice of voltage detection circuit depends on the system's priorities, such as efficiency, precision, or driving capability. By integrating the appropriate voltage detection circuit, the system can achieve effective energy management, balancing the demands of RF energy harvesting and ultrasonic drive.

In summary, voltage detection in this project must carefully balance the voltage range of the energy storage element based on the output power of the RFEH system and the power requirements of the ultrasonic drive. This ensures that the detection range aligns with both the energy harvesting capacity and the operational demands of the system. Furthermore, the choice between capacitor sampling and resistor sampling depends on the specific requirements of energy management. Capacitor sampling is ideal for applications where high efficiency and minimal energy loss are critical, particularly in low-power systems like RFEH. Conversely, resistor sampling is more suitable for applications that require robust load-driving capabilities and precise output regulation, making it the preferred option in scenarios demanding greater control and flexibility. Zener diode detection is suitable for fixing threshold voltage or providing reference voltage for energy management.

The next section will discuss the integration of voltage detection with switching circuits, highlighting how these components work together to maintain efficient and reliable system operation.

D. Switching Commutation circuit

The switching circuit serves as the execution mechanism within the energy management system, tasked with controlling the connection and disconnection of the ultrasonic drive circuit. This dynamic switching is crucial in balancing energy flow between the system's energy accumulation and energy utilisation phases, especially given the inherent energy disparity where the input energy from the RFEH circuit is significantly lower than the output energy required by the ultrasonic drive.

Voltage detection and switching circuits work in tandem to ensure efficient energy management in RFEH systems with ultrasonic drive circuits. The switching circuit is the executive mechanism responsible for regulating energy flow between the energy storage unit and the ultrasonic drive. At the same time, voltage detection provides the critical input signals determining the timing and conditions for switching operations.

During the energy accumulation phase, the switching circuit disconnects the ultrasonic drive to minimise losses and maximise energy storage efficiency within the RFEH circuit. By isolating the ultrasonic drive, this phase ensures that all harvested energy contributes to charging the storage unit without unnecessary dissipation.

Once the energy storage unit reaches a sufficient charge level, the switching circuit reconnects the ultrasonic drive, allowing the stored energy to power the transducer. However, as the stored energy depletes during operation, the efficiency of the ultrasonic drive diminishes. To maintain system efficiency and reliability, the switching circuit must promptly disconnect the ultrasonic drive and reinitiate the energy accumulation cycle.

This switching process requires precise voltage and energy monitoring to ensure seamless transitions between energy accumulation and utilisation phases, minimising system disruptions while optimising energy efficiency. The design of this circuit must balance fast response times, low power consumption, and reliability to meet the system's stringent performance requirements.

Therefore, careful consideration should be given to the appropriate design of the switching voltage range. The selection of this range should account for the operational requirements of the ultrasonic drive circuit. Specifically, the lower threshold must meet or exceed the minimum voltage required for proper functionality. In contrast, the upper threshold must remain within the safe maximum voltage to avoid potential damage or inefficiencies in the circuit.

In addition to ensuring the operational integrity of the ultrasonic drive, the switching voltage range must also avoid the low-efficiency range of the energy storage unit. During the charging phase, excessive voltage accumulation can reduce energy harvesting efficiency due to mismatches in the energy storage and harvesting systems. Similarly, operating within the low-efficiency range during discharging can lead to suboptimal energy utilisation for the ultrasonic drive.

Figure 3-26. Schematic diagram of the charging and discharging process of an energy storage. Illustrates the efficiency characteristics of the energy storage unit, identifying both the high-efficiency and low-efficiency regions during charging and discharging. By carefully selecting the switching voltage range, the system can ensure both efficient energy harvesting and effective operation of the ultrasonic drive.

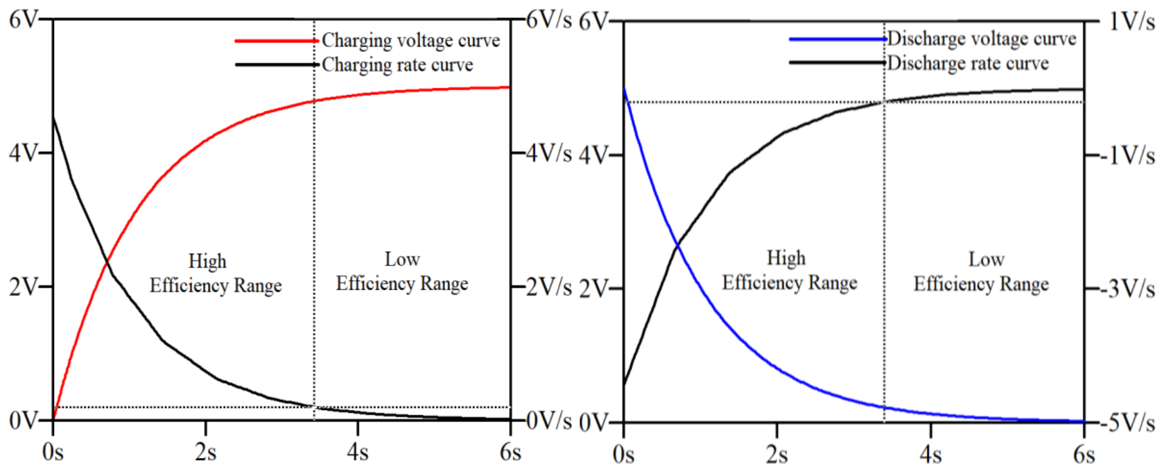

Figure 3-26. Schematic diagram of the charging and discharging process of an energy storage.

During the charging process, as the voltage of the energy storage element increases, the rate of voltage growth gradually decreases, leading to a reduction in the efficiency of the RFEH system in transferring energy to the storage element. To quantify this, we define the low-efficiency range of charging as the point where the voltage growth rate drops below 0.3 V/s. To avoid this inefficiency, the maximum switching voltage during the charging process must remain below the onset of this low-efficiency range.

Similarly, during the discharging process, as the voltage within the energy storage element decreases, the discharge rate slows, reducing the operational efficiency of the ultrasonic drive. To maintain efficiency, the minimum switching voltage during the discharge process must be set above the threshold of the low-efficiency discharge range.

By appropriately defining the voltage range for the switching circuit, the system ensures that RFEH operates at peak efficiency during energy harvesting and that the ultrasonic drive functions optimally during energy utilisation. Figure 3-27 Illustrates the high-efficiency operational voltage range of the energy storage element under the regulation of the switching circuit, ensuring a balance between efficiency and performance for both the RFEH system and the ultrasonic drive. The operational voltage range is shown after considering the minimum request for an ultrasonic driver.

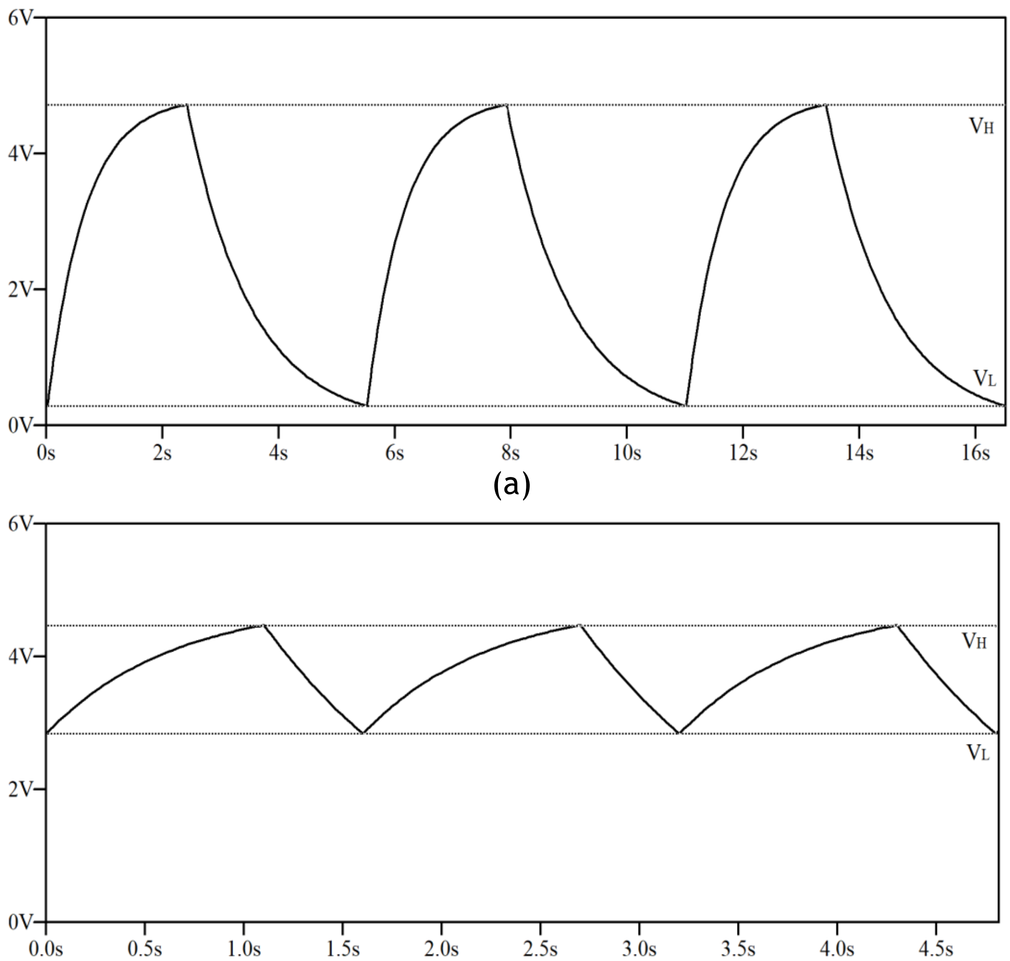

(a)

(b)

Figure 3-27. Schematic diagram of the voltage range for high efficiency operation of energy storage unit (a), and the voltage range after considering the minimum voltage requirement for ultrasonic drive (b).

Furthermore, the efficiency of the energy storage unit can be improved by increasing the charging voltage provided by the boost circuit in the RFEH system. This enhancement allows for a higher energy accumulation rate within the storage unit. Subsequently, precise voltage detection can be employed to regulate the output, ensuring that energy delivery aligns with the operational requirements of the ultrasonic drive circuit. Figure 3-28 Illustrates the voltage curve of the energy storage unit during the charging process. It also highlights the output voltage range after incorporating the constraints imposed by the ultrasonic drive voltage. The figure demonstrates how the charging voltage and subsequent voltage control contribute to maintaining efficient energy storage and release, thereby optimising the overall system performance.

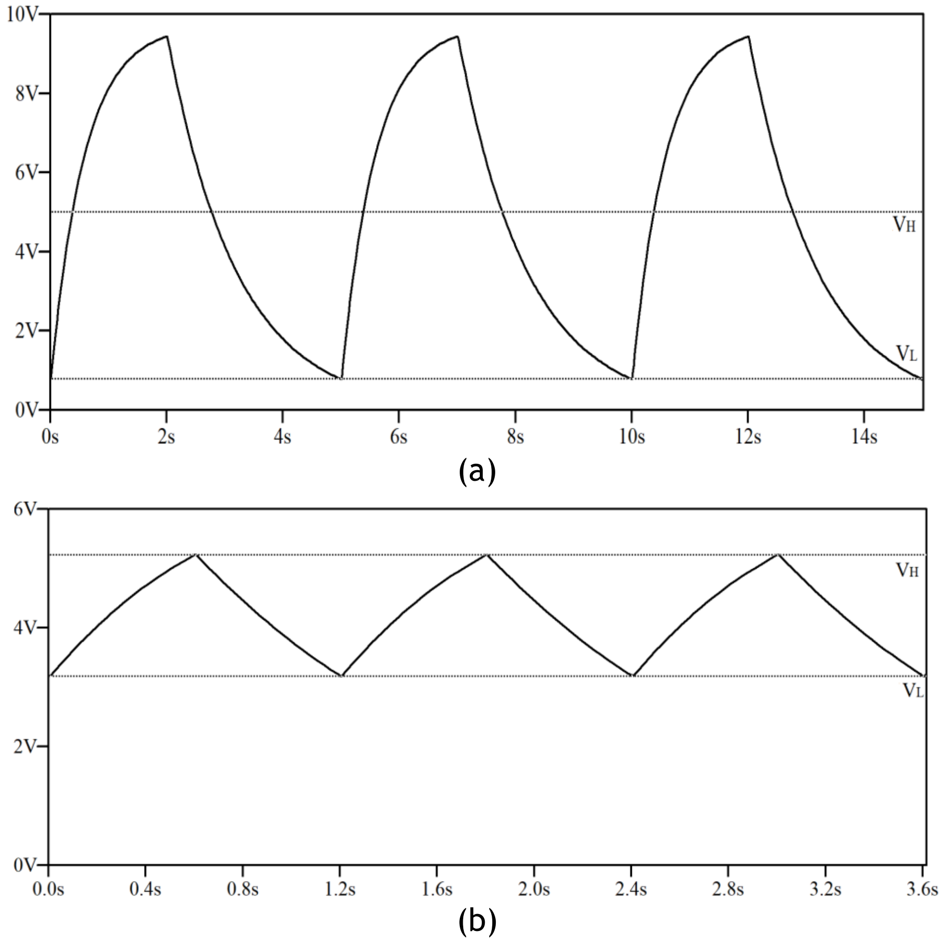

Figure 3-28. Schematic diagram of the voltage range for efficient operation after increasing the charging voltage of the energy storage unit (a), and the voltage range after considering the minimum voltage requirement for ultrasonic driving(b).

By comparing Figure 3-27(b) and Figure 3-27(b), it becomes evident that after increasing the charging voltage of the energy storage unit, the charging rate is faster when the voltage reaches the upper threshold of the voltage detection. This leads to improved charging efficiency. However, a higher charging voltage imposes greater demands on the boost converter in the RFEH system. This challenge becomes particularly pronounced when the input power of the RFEH is constrained, limiting the feasibility of excessively high charging voltages. A balance between the charging rate and the output voltage of the boost converter helps maintain the stable and efficient operation of both the boost converter and the energy storage unit. This balance ensures that the energy storage unit accumulates energy effectively without overburdening the boost converter, particularly under limited input power conditions. Proper voltage regulation improves the charging efficiency and supports the overall stability of system performance.

It is worth noting that Figure 3-27 and Figure 3-28 are intended solely to illustrate the voltage ranges for high-efficiency charging and discharging of the energy storage element, as well as the voltage range after considering the minimum operational requirements of the ultrasonic drive. This schematic does not account for the power dynamics of the RFEH and the ultrasonic drive. Consequently, the depicted charging and discharging durations are not representative of real-time performance. In practical operation, the charging process typically requires significantly more time than the discharging process due to the disparity in power levels between RFEH input and ultrasonic drive output.

In short, the selection of the control voltage for the switching circuit must integrate the high efficiency charging and discharging ranges of the energy storage element with the operational requirements of the ultrasonic drive. This ensures both optimal energy management and reliable system performance.

Once the voltage range of the switch circuit is established based on the design requirements, voltage detection operates alongside the switch circuit to maintain functionality within the specified voltage range. This coordination ensures reliable operation and supports the system’s overall efficiency.

Figure 3-29 Illustrates the operational mechanism of the switching circuit, showing how voltage detection governs the transition between the charging and discharging states to optimise energy utilisation and system stability.

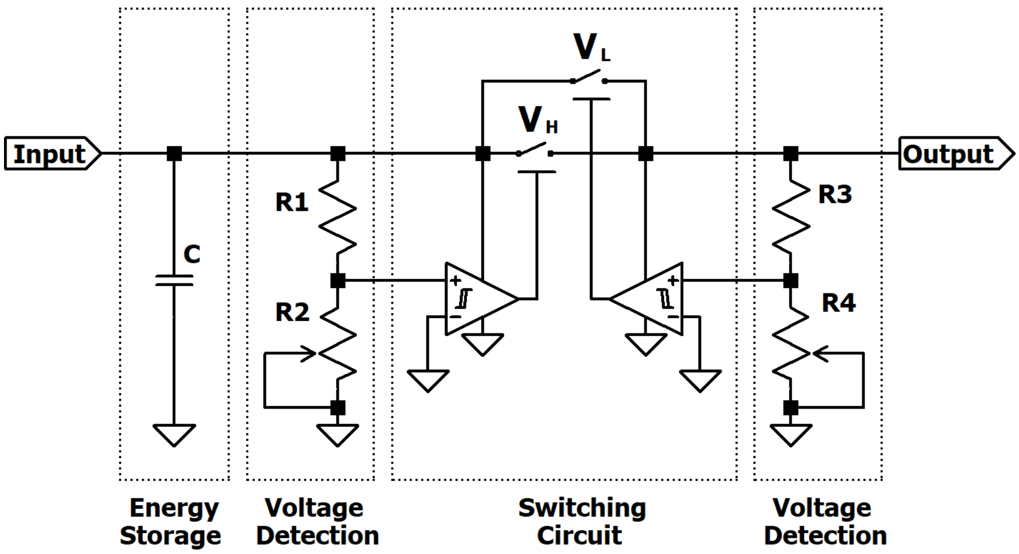

Figure 3-29. Schematic diagram of the switch circuit operation mechanism. V_H is the upper threshold of the voltage range, and V_L is the lower threshold of the voltage range. The switch is controlled by a combination of voltage detection and a trigger.

The operational mechanism of the switching circuit is designed to facilitate effective energy management and maintain stable output voltage control. When the voltage of the energy storage unit reaches the upper threshold V_H the V_H switch is activated, enabling energy transfer to the output. Concurrently, the V_L switch, which has a lower activation threshold than V_H, also turns on during this phase. As energy is discharged and the voltage declines, the V_H switch deactivates once the voltage falls below its upper threshold V_H. However, the V_L switch remains engaged until the voltage further decreases to its lower threshold V_L. When the voltage drops below V_L, the V_L switch disconnects, thereby isolating the output from the energy storage unit. Although VL's activation threshold is lower than VH's, its voltage detection is positioned downstream of V_H in the circuit. This configuration ensures that V_L is only activated in conjunction with V_H but disconnects by V_L trigger which maintains the output voltage within the predefined range between V_L and V_H. This coordinated mechanism is essential for ensuring system stability and optimising the efficiency of energy storage and discharge processes.

The operational mechanism of the switching circuit can be effectively illustrated using a logic circuit representation. In this model, the voltage thresholds of V_L and V_H are treated as inputs, and the state of the output (Out) is the resulting logic value. When the voltage exceeds the threshold of V_L or V_H, the corresponding input is assigned a value of 1; conversely, when the voltage falls below the threshold, the input is assigned a value of 0. Similarly, the output is designated as 1 when the circuit is active (turned on) and 0 when it is inactive (turned off).

The logical operation of the switching circuit is summarised in Table 3-5, which defines the relationships between the inputs (V_L and V_H) and the output (Out).

Table 3-5. Switching circuit operation truth table

V_L	V_H	Out
0	0	0
1	0	0
1	1	1
1	0	1
0	0	0

According to the results of the operation table, when the voltage reaches the upper threshold V_H, the Out is activated, while Out is deactivated when the voltage falls below the lower threshold V_L. Following this operational truth table, the corresponding logic circuit represents the logical relationships logical relationship is $Out = (V_L \cdot V_H) + (V_L \cdot \overline{V_H} \cdot Out)$. The circuit diagram is illustrated in Figure 3-30, demonstrating how the inputs V_L and V_H interact to control Out, ensuring the system operates within the desired voltage range.

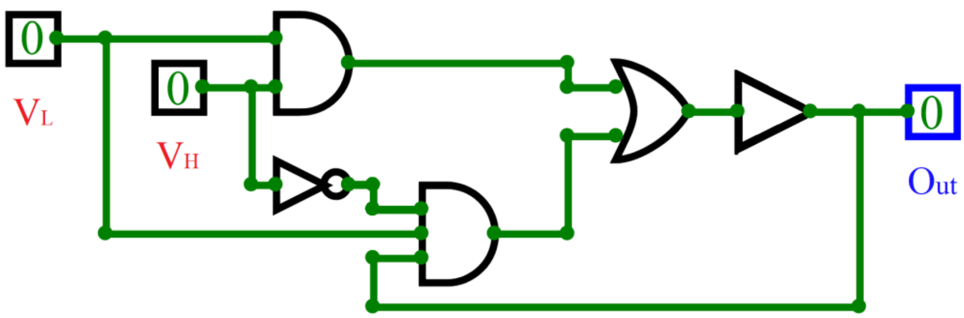

Figure 3-30. Digital logic circuit diagram of switching.

Based on the logical relationships described, a voltage-controlled switch circuit can be realised by selecting appropriate components and integrating them with voltage detection. Figure 3-31 shows one of the switching circuits.

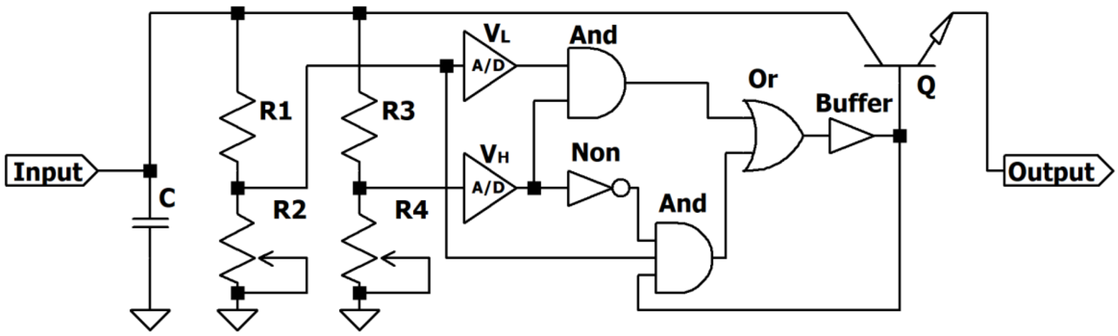

Figure 3-31. A voltage-controlled switching circuit based on the logical relationship.

Voltage-controlled switching circuits implemented with digital logic gates represent an option for switch circuit design due to their precision and programmability. Well-known SN7400 series and SN5400 series components can be selected. However, since the logic gate is the transistor-transistor logic (TTL) voltage, implementing logic functions at this voltage usually requires a stable power supply to operate effectively.

Given the limited power available in this project, alternative wide-voltage control solutions are necessary to address the challenges posed by fluctuating input power. These solutions must ensure reliable operation without relying on a dedicated stable power source. Considering the wide voltage range, high noise immunity, and low static power consumption characteristics of complementary metal–oxide-semiconductor (CMOS) circuits, the next section will introduce three types of CMOS-based voltage-controlled switch circuits: comparator-based switches, adjustable hysteresis triggers, and dedicated voltage-controlled switch ICs. These voltage-controlled switches can be configured to form a controller, as illustrated in Figure 3-29, facilitating reliable and efficient energy management within the system. Each approach will be detailed with respect to its design principles, operational characteristics, and advantages for energy-constrained applications, focusing on their suitability for energy-efficient and low-power systems.

Comparator-based switch: The voltage comparator is a device that compares two analogue input terminals and one output control terminal. In this project, the two input terminals are connected to the voltage detection circuit and a reference voltage. The reference voltage represents the switch voltage range's lower and upper threshold values. The output of the comparator is connected to a MOSFET, which controls the connection between the input and the output. This configuration enables precise switching based on the detected voltage levels, ensuring efficient energy management. The switching circuit of the voltage comparator is shown in the Figure 3-32.

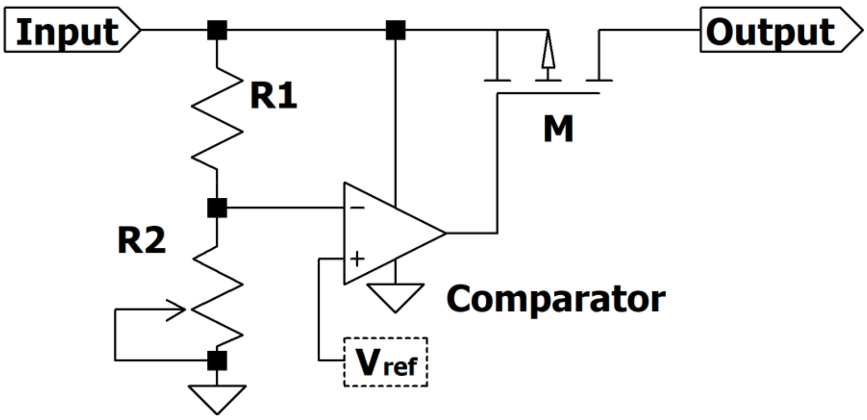

Figure 3-32. Voltage controlled switching circuit based on voltage comparator.

One input terminal of the voltage comparator is connected to the voltage detection point of the energy storage unit, while the other terminal is connected to the reference voltage. The threshold voltages (V_L and V_H) of the voltage-controlled switch are determined based on the following relationship:

$$V_{th} = \frac{R_1}{R_1+R_2} V_{ref} \tag{3-53}$$

The reference voltage V_{ref} is stable, which remains precision reference irrespective of variations in the input voltage.

For this project, selecting a lower output voltage and a sufficiently low operating current voltage reference device is essential, like MAX9060, REF35, and ADCMP380. A low-voltage reference ensures that the switch can function effectively under low-voltage conditions, enabling efficient operation even when the energy storage unit is minimally charged. Meanwhile, a low operating current reduces power consumption, further supporting energy conservation objectives.

Adjustable hysteresis Schmitt trigger switch: The hysteresis characteristics of a Schmitt trigger can serve as an effective control signal for the switch circuit, allowing operation within a defined voltage range. This is achieved by incorporating a suitable voltage detection circuit. However, traditional Schmitt triggers have fixed trigger voltages, which limit their ability to adapt to specific project requirements, such as setting customised threshold voltages for the energy storage unit. In contrast, the newly developed adjustable hysteresis Schmitt trigger provides the flexibility to modify the trigger voltage according to user-defined parameters[162]. Integrating the adjustable Schmitt trigger with a voltage detection circuit makes it possible to define a tailored threshold voltage range for the energy storage unit, thereby enhancing system adaptability and precision. Figure 3-33 illustrates the hysteresis characteristics of both the traditional fixed-voltage Schmitt trigger and the adjustable hysteresis Schmitt trigger, highlighting the advantages of the latter in dynamic voltage management applications.

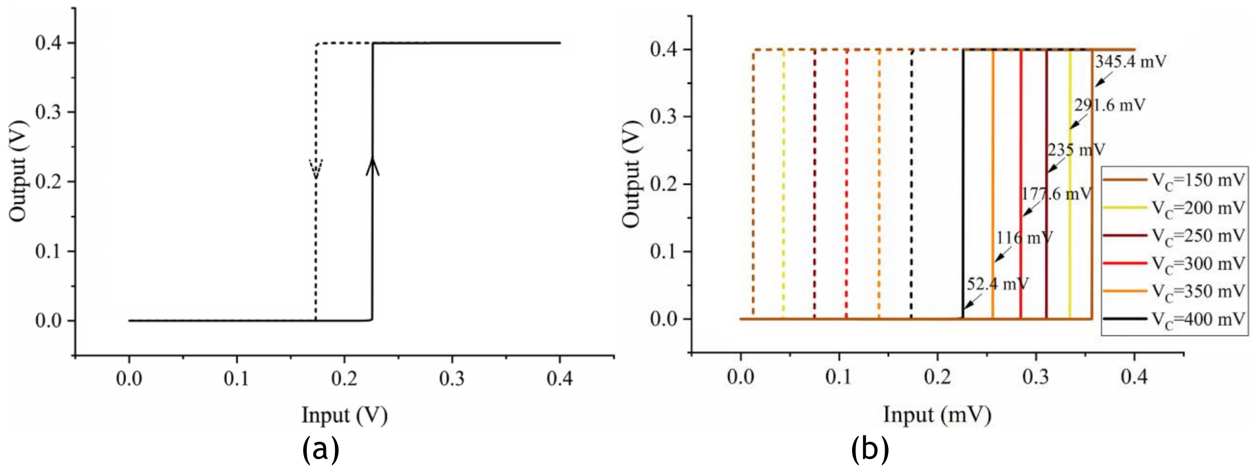

Figure 3-33. Schematic diagram of the voltage hysteresis characteristics of a traditional Schmitt trigger (a) and the adjustable voltage hysteresis characteristics (b). By adjusting the setting voltage V_C to adjust the trigger voltage.

The adjustable hysteresis of the Schmitt trigger is tuned using a control voltage (V_C), enabling linear adjustment of its threshold levels. This functionality facilitates the customisation of the lower (V_L) and upper (V_H) threshold voltages to align with the specific voltage adjustment range of the energy storage unit.

A voltage-controlled switch circuit can be realised by integrating an adjustable hysteresis Schmitt trigger with a voltage detection circuit. This configuration effectively ensures that the energy storage unit operates within its optimal voltage range, maintaining both efficiency and stability. The circuit design is illustrated in Figure 3-34.

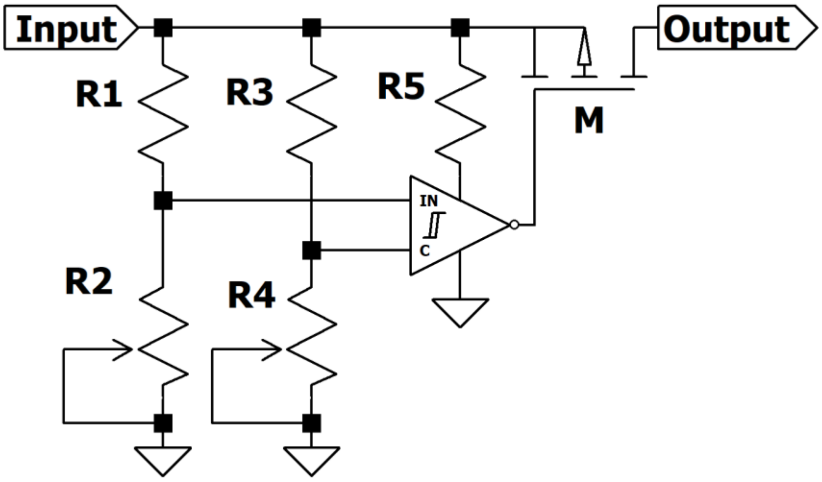

Figure 3-34. Voltage controlled switching circuit based on adjustable hysteresis Schmitt trigger.

Low-power adjustable hysteresis Schmitt triggers have been extensively studied and reported[162, 163, 164, 165]. When selecting a trigger for this project, it is crucial to prioritise designs with minimal power consumption to align with the energy efficiency requirements.

A voltage-controlled switch constructed using an adjustable hysteresis Schmitt trigger enables precise voltage regulation tailored to specific project requirements. Additionally, this approach simplifies the circuit design by requiring only a single switching element, thereby reducing complexity and enhancing reliability.

Voltage-controlled switch ICs: voltage-controlled switch ICs are widely utilised in analogue circuits due to their versatility and unique features. They are particularly effective in routing, switching, and selecting analogue signals. In the "on" state, their on-resistance (R_{ON}) is typically very low, often just a few ohms, significantly reducing energy losses during conduction. Conversely, they provide high input-output isolation in the "off" state to prevent energy leakage effectively.

These switches support a broad voltage range, accommodating a few to tens of volts or higher voltages. Additionally, they offer multi-channel configurations, including single-pole single-throw (SPST), single-pole double-throw (SPDT), and multi-pole multi-throw (MPMT), making them suitable for various applications. Furthermore, their simple control interface allows for straightforward operation, with switching controlled via basic high and low signal levels. When combined with a voltage detection circuit, voltage-controlled switches can provide efficient and reliable energy management, as illustrated in Figure 3-35.

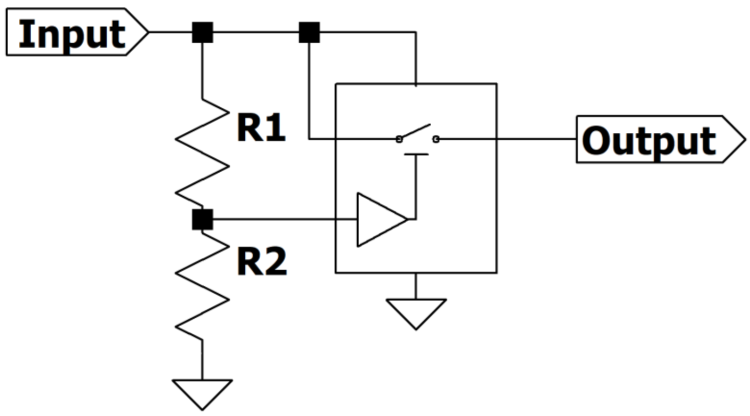

Figure 3-35. Voltage controlled switching circuit based on SPST.

The input terminal connects to the voltage-controlled switch via the voltage detection circuit, where switching actions are executed by comparing the input signal with the switch's internal reference voltage. It is important to note that while some voltage-controlled switch ICs include a built-in hysteresis function, this hysteresis voltage is typically fixed and not adjustable. Consequently, achieving flexible and stable voltage control requires designing a dual-control switch configuration, as depicted in Figure 3-29, to fulfil the energy management requirements effectively. To further support the implementation, Table 3-6 presents a selection of switch ICs suitable for this project's operational and efficiency criteria.

Table 3-6. Switch ICs for power management.

ICs Model	Supply Voltage Range (V)	Logic High Voltage (V)	Logic Low Voltage (V)	ON-State Resistance (Ω)	Off-State Leakage Current (nA)
TS5A3166	1.65-5.5	2.4	0.8	0.90	4.00
MAX4910	1.8-5.5	1.4	0.5	0.75	10.00
DG4157E	1.65-5.5	1.8	0.6	0.86	1.36
ADG821	1.8-5.5	2.0	0.8	0.50	0.01

Switching ICs offer a wide operating voltage range with consistent and stable on/off voltage thresholds. Their resistance is typically less than 1 ohm when in the on state, effectively minimising energy losses. In the off state, the leakage current is extremely low, which is advantageous for isolating the load and facilitating energy accumulation. Additionally, switching ICs are compact in size, making them suitable for space-constrained applications. However, the fixed parameters of these ICs may limit circuit design flexibility, necessitating careful consideration during system integration.

In summary, various options are available for designing the switching commutation circuit to concentrate energy and deliver it efficiently to the ultrasonic drive. The design process begins with calculating the high-efficiency voltage range based on the energy storage unit and the load characteristics of the ultrasonic drive. Next, the control thresholds of the switch circuit are determined in alignment with this voltage range. Finally, an appropriate voltage-controlled switch circuit is selected to ensure optimal performance and energy management, considering the operating voltage range and load current requirements.

3.2.3.3 Ultrasonic Transducer Driver

The driving of an ultrasonic transducer involves three key components: output impedance matching, an ultrasonic oscillator, and a power amplifier. Output impedance matching aligns the impedance of the transducer with that of the driving circuit, minimising energy reflection and ensuring efficient energy transfer. The ultrasonic oscillator generates a driving signal tuned to the transducer's resonant frequency. Due to the narrow bandwidth of the transducer’s resonant frequency and its susceptibility to drift caused by environmental changes, the oscillator’s frequency must be both adjustable and highly accurate to maintain optimal performance. In addition to precisely matching the transducer's operating frequency, the power amplifier must deliver high-efficiency performance while operating within the specified voltage range. This dual requirement ensures that the transducer is driven effectively without energy loss or excessive power consumption.

A. **Output Impedance Matching Network**

Similar to RF links, ultrasonic links also rely on impedance matching networks to optimize energy transmission and frequency adaptability. Although ultrasonic frequencies are lower than RF, the power levels are higher, making impedance mismatches a significant source of ultrasonic output power loss. In ultrasonic links, impedance matching primarily targets the interface between the ultrasonic oscillation source and the transducer. Common impedance matching networks, similar to those used in RF links, are illustrated in Figure 3-16.

B. **Ultrasonic Oscillator**

Ultrasonic oscillators are responsible for generating the drive signals for ultrasonic transducers, with typical frequencies ranging from 20 kHz to 100 MHz. For efficient energy transfer, the output frequency of the oscillator must align with the resonant frequency of the transducer. However, the resonant frequency bandwidth of the transducer is often very small, typically around 1 kHz, so the frequency of the ultrasonic oscillator needs to be accurately matched to the transducer. Moreover, the resonant frequency of the transducer can shift based on factors such as the application and the properties of the transmission medium. When the transducer operates in different environments, the interaction with the medium can cause the resonant frequency to offset. Therefore, to ensure compatibility and maintain optimal performance, the output frequency of the ultrasonic oscillator needs to be adjustable, allowing it to accommodate these frequency variations.

Various oscillators can be used to drive ultrasonic transducers, each with unique characteristics. These include RC (resistor-capacitor) oscillators, which rely on resistors and capacitors to generate stable frequencies; LC oscillators, which use inductors and capacitors and are well-suited for high-frequency applications; crystal oscillators, known for their precision and stability due to the resonance of a quartz crystal; transistor resonator, the switching function of the transistor is utilized to realize alternating switching output oscillating waveform through positive feedback; and integrated oscillators, which offer compact solutions with frequency stability and often include adjustable output options. Each type of oscillator may be selected based on the frequency stability, application requirements, and compatibility with the transducer. The following sections will introduce and analyse these classic oscillators in detail.

RC Oscillators: One of the simplest oscillators in both design and structure, primarily using an RC charging and discharging circuit to generate oscillations. This type of oscillator can operate in various configurations, but its simplicity makes it ideal for applications where high waveform quality and frequency accuracy are not critical. Two common implementations of RC oscillators are based on the Schmitt inverter and the operational amplifier. These configurations are widely used in low-precision applications due to their cost-effectiveness and straightforward design. The circuit structure is shown in Figure 3-36 [166, 167].

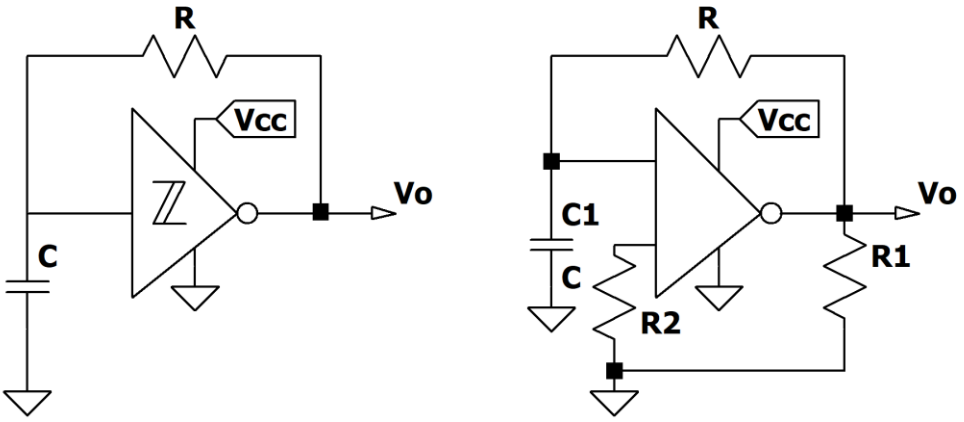

Figure 3-36. RC oscillator circuit based on Schmitt inverter and operational amplifier.

Schmitt inverters were initially developed as threshold-triggering components in digital logic circuits, where their hysteresis characteristics enable them to respond predictably to varying input signals. In RC oscillator applications, the charging and discharging behaviour of the capacitor in an RC network determines the voltage thresholds that trigger the Schmitt inverter, resulting in a stable square wave output.

Similarly, in RC oscillators based on operational amplifiers, the same charge–discharge voltages are used as reference levels for voltage comparison. Positive feedback is introduced to reinforce the output transitions, thereby sustaining stable oscillations. As illustrated in Figure 3-37, the capacitor voltage V(C) undergoes periodic charging and discharging cycles, which in turn generate the output waveform V(VO).

Both configurations use Schmitt inverters or operational amplifiers' inherent threshold and feedback characteristics to ensure reliable and continuous waveform generation, making them effective solutions for simple and low-power oscillator designs.

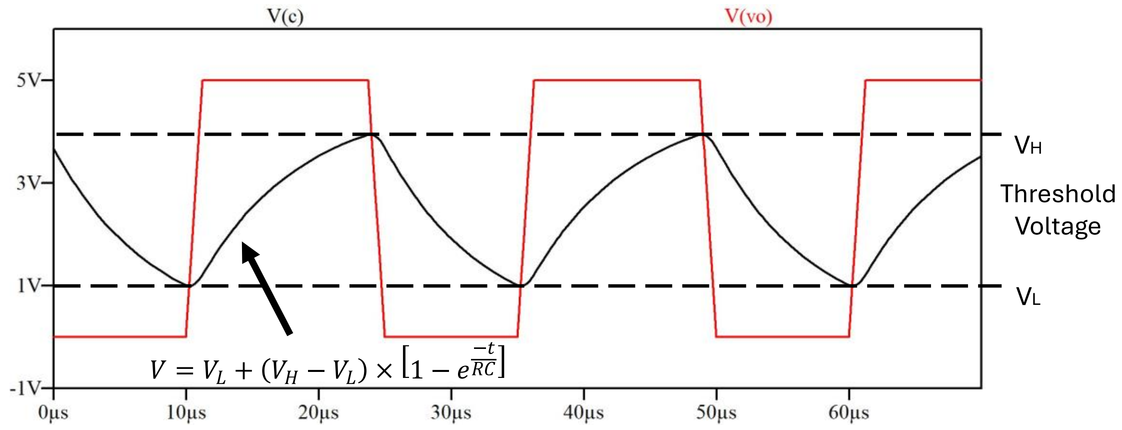

Figure 3-37. The charging and discharging process of capacitor C and the output waveform of the oscillator.

According to the charging and discharging process of Figure 3-36 and the circuit structure of Figure 3-37, the output frequencies of the two RC oscillators are shown below.

For the Schmitt inverter oscillator,

$$f = \frac{1}{0.693RC}, \tag{3-54}$$

For the operational amplifier oscillator,

$$f = \frac{1}{2RC \ln\left(1 + \frac{2R_1}{R_2}\right)}, \tag{3-55}$$

RC oscillators come in various configurations, and we present only the most basic design. In practical applications, additional considerations are necessary, such as power supply stability, output amplitude control, frequency drift, and protective circuitry. Overall, RC oscillators offer simplicity and compactness. However, they have limited interference resistance and produce lower output frequencies compared to other oscillators.

LC Oscillator: Traditional LC oscillators generate oscillatory waveforms through the resonance of inductors and capacitors, combined with feedback amplification. With advancements in transistor technology, LC oscillators now incorporate transistor-coupled resonances such as collector, emitter, and base resonances, in addition to traditional LC resonance. We focus on the typical Hartley and Colpitts oscillator circuits, illustrated in Figure 3-38 [168].

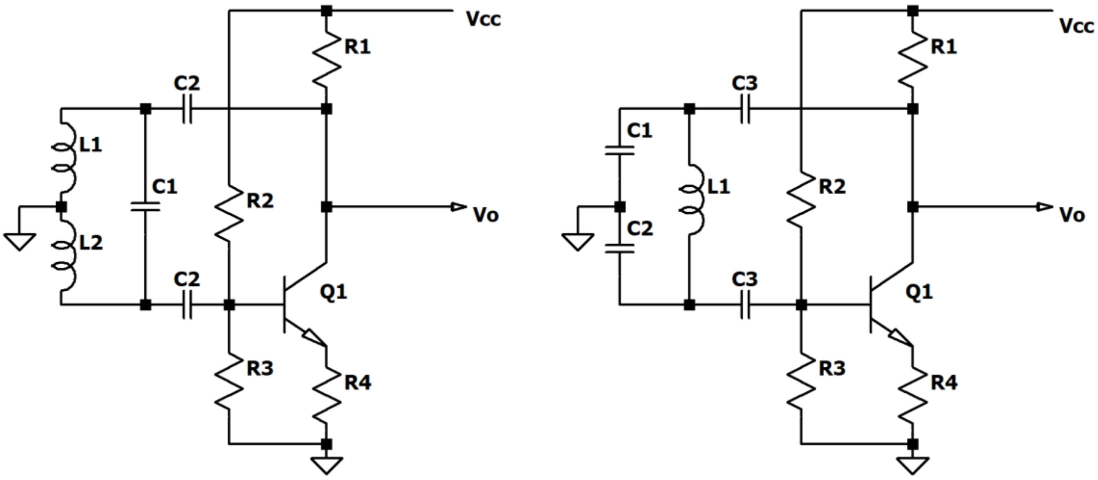

Figure 3-38. Typical Hartley and Colpitts oscillators

The widely used Hartley and Colpitts oscillators are RF signal generators and frequency synthesizers due to their straightforward designs. In the Hartley oscillator, inductors divide the voltage, and frequency adjustment is primarily achieved by varying capacitance. Conversely, the Colpitts oscillator divides voltage with capacitors, adjusting frequency mainly through changes in inductance. The resonant frequency for both circuits can be calculated as follows:

For the Hartley oscillator,

$$f = \frac{1}{2\pi\sqrt{L_{eq}C}} \tag{3-56}$$

where L_{eq} is the equivalent inductance of the series inductors.

For the Colpitts oscillator,

$$f = \frac{1}{2\pi\sqrt{C_{eq}L}} \tag{3-57}$$

where $C_{eq}$is the equivalent capacitance of the series capacitors.

These formulas provide the resonant frequency, facilitating precise adjustments in applications requiring stable drive signals.

Crystal Oscillator: A crystal oscillator uses the precise mechanical vibrations of a quartz crystal to produce a stable resonant signal, offering much greater frequency stability than RC and LC oscillators and a high temperature coefficient, making it ideal for applications requiring precise timing. While the frequency of a crystal oscillator can technically be fine-tuned by adding a series inductor or a parallel capacitor, it is typically designed as a fixed-frequency circuit due to its inherent accuracy and stability. This stability, which results from the crystal's consistent vibrational frequency, makes crystal oscillators indispensable in applications such as clocks, communication systems, and other devices needing reliable frequency standards. Figure 3-39 shows the symbol and equivalent circuit of a quartz crystal oscillator [169].

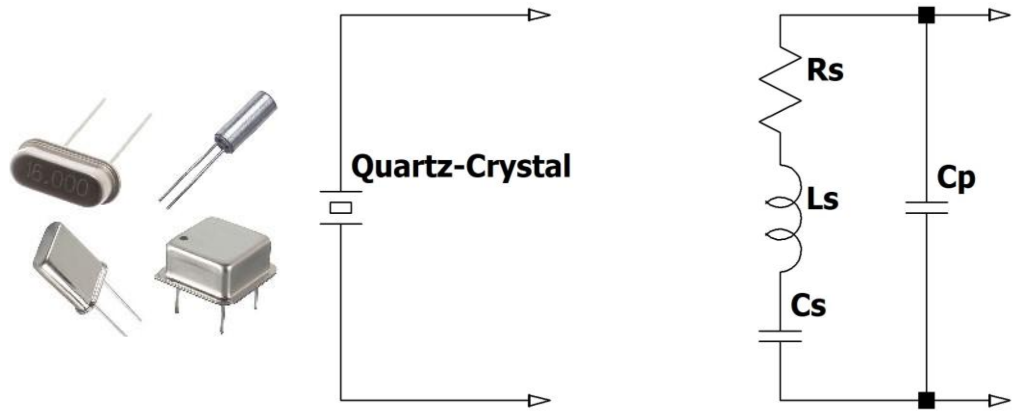

Figure 3-39. Quartz crystal electrical symbol and equivalent circuit.

Figure 3-39 illustrates the structure and equivalent circuit of a quartz crystal oscillator. The physical structure relies on the quartz crystal's mechanical vibrations to generate stable oscillations. The equivalent circuit includes components that simulate the crystal's electrical behaviour: an inductor (Ls), a capacitor (Cs), and a resistor (Rs), which represent the crystal's mass, compliance, and internal losses, respectively. These elements form a series-resonant RLC circuit that, along with a parallel capacitor (Cp), models the precise frequency control characteristic of the quartz crystal. When the very small equivalent resistance is ignored, the oscillation frequency can be calculated by the following formula.

Series resonant frequency,

$$f_s = \frac{1}{2\pi\sqrt{L_s C_s}} \tag{3-58}$$

Parallel resonant frequency,

$$f_p = \frac{1}{2\pi\sqrt{L_s\left(\frac{C_p C_s}{C_p + C_s}\right)}} \tag{3-59}$$

Oscillators based on crystal resonance come in a variety of structures, each catering to specific applications. Figure 3-40 shows examples of crystal oscillators based on Hartley and Colpitts configurations, as well as oscillators constructed with inverting Schmitt trigger circuits [169].

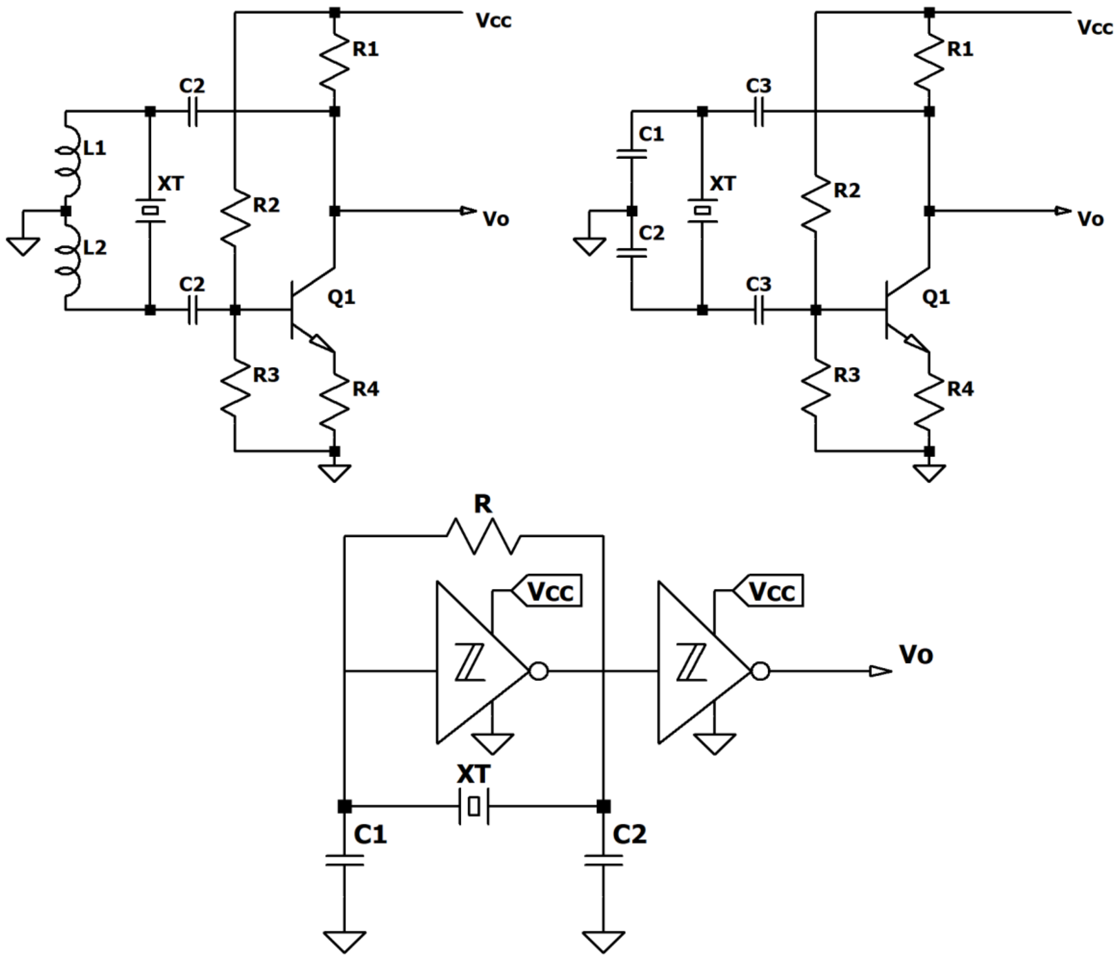

Figure 3-40. Based on crystal Hartley, Colpitts and Schmitt trigger oscillators.

Each oscillator design allows for the selection of a crystal suited to the desired output frequency, with Hartley and Colpitts configurations particularly well-suited to RF applications due to their stable output frequencies. These designs leverage the inherent stability of crystal resonance to ensure a reliable and consistent output frequency.

On the other hand, oscillators based on Schmitt inverting flip-flops use the threshold-switching characteristics of digital logic circuits to generate square waves, making them especially valuable in digital applications where precise waveform shape and timing consistency are crucial. Each type of oscillator offers unique benefits in terms of frequency stability, output waveform, and flexibility across diverse circuit applications.

Transistor Oscillator: Transistor oscillators represent another type of RC and LC oscillator, utilizing positive feedback to enable oscillation by switching the transistor on and off. Figure 3-41 shows two common configurations, showcasing the essential role of positive feedback in maintaining continuous oscillations in these circuits.

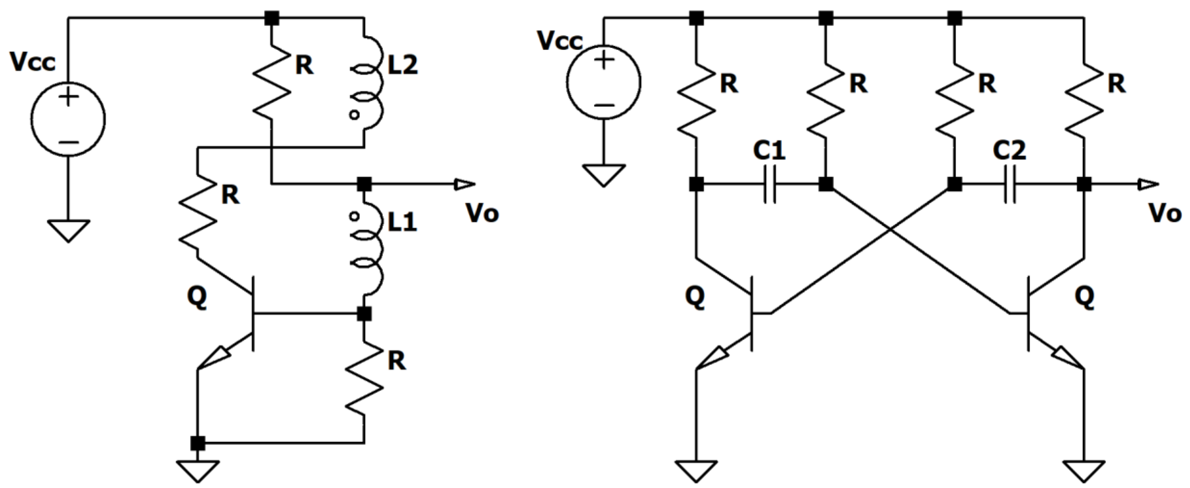

Figure 3-41. Mutual inductance oscillator and push-pull oscillator.

The output frequency of a transistor oscillator is determined by the input voltage and the feedback components, typically inductance (L) and capacitance (C). The charge and discharge cycle of the LC network controls the conduction and non-conduction states of the transistor. As a result, the rate of charge and discharge dictates the oscillation frequency. Mutual inductance oscillators are commonly used in switching power supplies, where their efficient feedback mechanism is beneficial for stable power conversion. On the other hand, push-pull oscillators are often employed in low-frequency, high-current applications such as lighting control, where their ability to drive high currents with alternating phases is crucial.

Integrated Oscillator: Integrated oscillators are designed using ICs, which take advantage of the inherent stability and simplicity of ICs to minimize the number of external components required. These IC-based designs benefit from the inclusion of protection circuits and feedback interfaces, which ensure the oscillator maintains a stable frequency output even under conditions of input voltage fluctuations. This makes integrated oscillators reliable for applications that require consistent performance despite variations in supply conditions. Figure 3-42 shows three typical integrated oscillator circuits and the corresponding calculations for adjusting their output frequencies. These configurations offer a compact and efficient solution for frequency generation in a variety of applications.

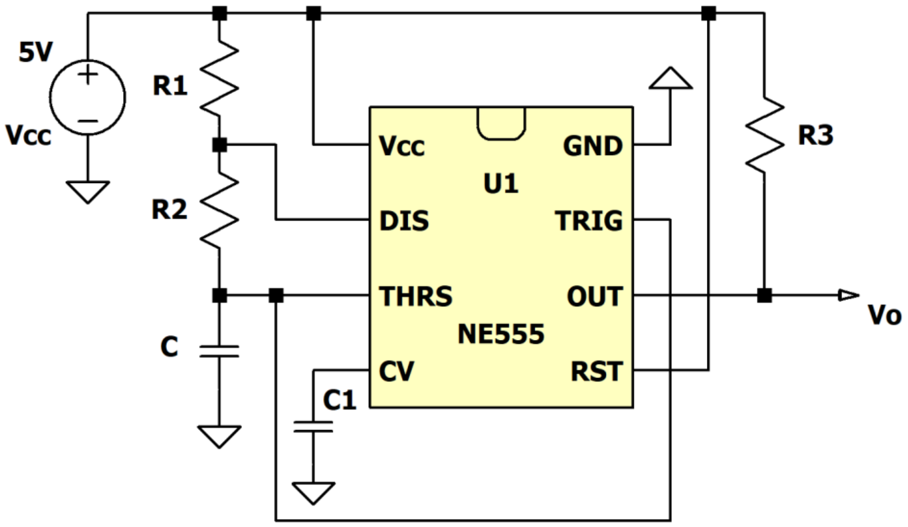

Figure 3-42 (a). Schematic diagram of oscillator circuit based on NE555.

NE555 outputs an oscillating waveform by comparing the voltages of R1, R2 and C. Its output frequency is as follows:

$$f = \frac{1.443}{C(R_1+2R_2)} \tag{3-60}$$

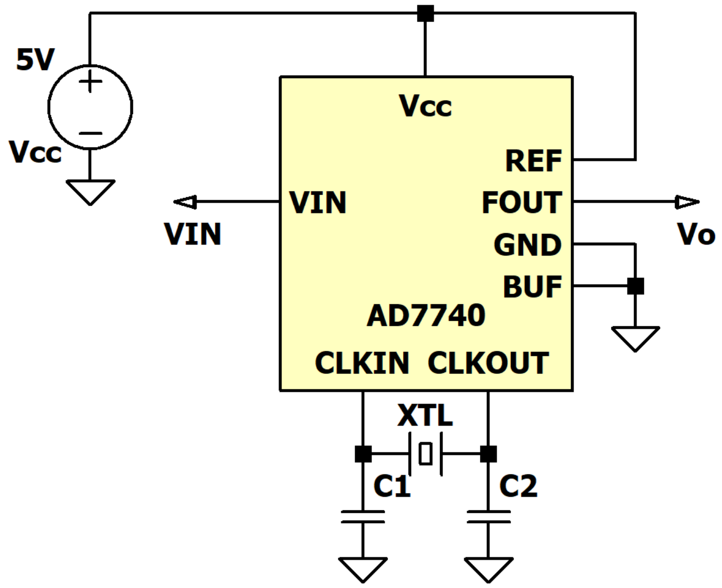

Figure 3-42 (b). Schematic diagram of oscillator circuit based on AD7740.

AD7740 is a voltage-controlled oscillator, which adjusts the output frequency by adjusting voltage of VIN. Its output frequency is as follows:

$$f = 0.1f_{\mathrm{CLKIN}} + 0.8\left(\frac{\mathrm{VIN}}{\mathrm{V_{REF}}} \times f_{\mathrm{CLKIN}}\right) \tag{3-61}$$

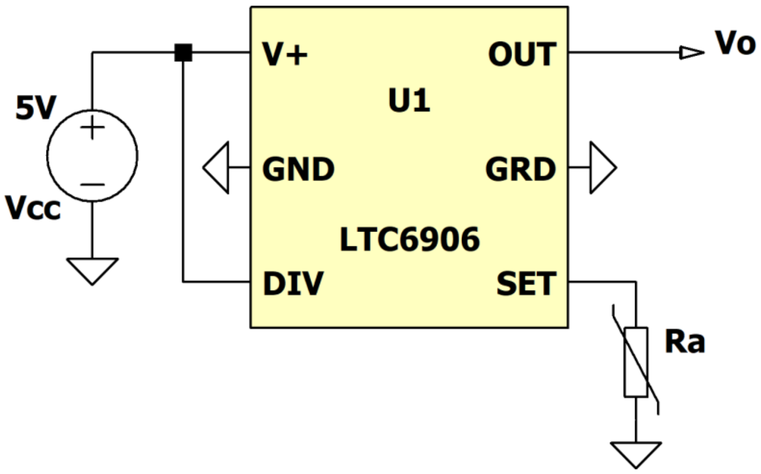

Figure 3-42 (c). Schematic diagram of oscillator circuit based on LTC6906.

LTC6906 adjusts the output frequency through the adjustable resistor Ra. By changing the DIV port, there are 3 frequency options. Its output frequency is as follows:

$$f = \frac{1\,MHz}{N} \times \left(\frac{100\,k}{R_a}\right), \mathrm{N} = \begin{cases} 10, DIV = Vcc \\ 3, DIV = OPEN \\ 1, DIV = GND \end{cases} \tag{3-62}$$

Integrated oscillators are highly suitable for applications requiring stable output waveforms. These oscillators are characterized by their simple structure and reliable output, making them easy to implement and ensuring consistent performance.

A significant advantage of integrated oscillators is that their output frequency and amplitude remain stable across a wide range of input voltages, guaranteeing dependable operation under various conditions. This stability is especially critical in applications such as clock generation, timing circuits, and signal processing, where predictable and stable performance is essential.

Furthermore, integrated oscillators typically feature frequency adjustment formulas, allowing users to easily modify the output frequency by adjusting external components like resistors and capacitors. This flexibility eliminates the need for complex tuning, making it simple to customize the oscillator to meet specific application requirements.

Integrated oscillators offer a compact, stable, and customizable solution for generating precise frequencies. They can maintain performance across a wide voltage range, and their simplicity and ease of adjustment make them easy for a broad range of electronic applications.

In summary, RC oscillators, LC oscillators, crystal oscillators, and integrated oscillators each offer distinct advantages and disadvantages for driving ultrasonic transducers. RC oscillators are simple and cost-effective but have output frequency instability, making them suitable for generating lower frequencies with reasonable stability. LC oscillators, using inductors and capacitors, are better suited for higher frequencies and offer improved stability, but the need for a stable input voltage also limits it. Crystal oscillators provide exceptional precision and frequency stability by utilising the resonant properties of quartz, making them ideal for applications that require accurate timing, but the frequency adjustment range of the crystal oscillator is limited. Integrated oscillators combine components in a compact package, often with adjustable frequency outputs, allowing for greater flexibility in adapting to varying transducer requirements, but the cost is higher. Each type of oscillator can thus be chosen based on the specific needs for stability, frequency range, and application compatibility.

C. **Power Amplifier**

The transmitting component for ultrasound is a piezoelectric ceramic transducer, which typically has a high impedance, often ranging from tens to thousands of ohms. To effectively transmit energy, the transducer's driving power must be substantial. While the ultrasonic oscillators discussed above meet the frequency requirements for driving the transducer, their output power is insufficient to drive the transducer to emit ultrasound with the required energy levels for effective energy transmission. Thus, a power amplifier (PA) is essential in the ultrasonic link to boost driving energy.

The driver selected for the ultrasonic transducer in this project must fulfil several critical requirements. High efficiency is essential as the input energy is limited, necessitating minimal energy losses to maximise power delivery to the transducer. This ensures that the available energy is used optimally for ultrasonic wave generation. A simple structure and compact size are also crucial because the driver needs to integrate with the sensor. These characteristics help meet the physical constraints of the system and facilitate ease of integration. Furthermore, strong applicability is required as the input voltage varies significantly. The driver must exhibit stable performance across a variable voltage range, ensuring consistent operation and reliable transducer driving under the given conditions. These considerations are integral to selecting a suitable driver topology for this project.

Power amplifiers come in various types; however, each has distinct characteristics regarding output power, operating mode, efficiency, and frequency. Amplifiers are categorized by "classes," which indicate differences in circuit configuration and operational mode. These include:

- **Linear amplifiers:** Class A, Class B, Class AB, and Class C.
- **Switching amplifiers:** Class D, Class E, Class F, and Class S.
- **Speciality classes:** Class G, Class H, Class J, Class T, linear variable gain, and dynamic voltage PA.

We will explore these amplifiers in detail to determine the most suitable type for driving the ultrasonic transducer effectively.

Class A amplifiers: Class A PAs are the most common type of amplifier topology because they use only one output switching transistor in the amplifier design. This single output transistor is biased in the amplification region in the middle of the load line, so it never enters the cutoff region or saturation region, allowing it to conduct current throughout 360 degrees of the input cycle. However, it is also because the output transistor of the Class A PA is never "turned off", making it relatively lossy, which is one of its main disadvantages.

Class A amplifiers have excellent linearity, high gain, and low signal distortion levels. However, Class A amplifiers are rarely used in high-power amplifier applications. It is often used for audio amplification and therefore used in high-fidelity audio designs. Figure 3-43 is a typical circuit of Class A amplifier [170].

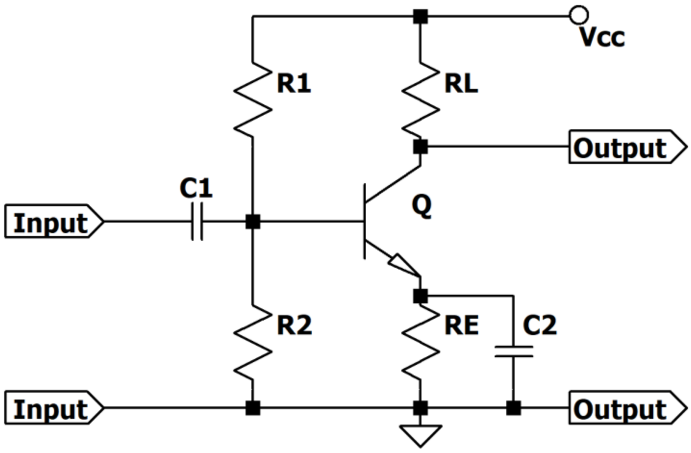

Figure 3-43. The basic schematic of a Class A amplifier.

Class A amplifiers maintain high linearity and gain because their output stage is always biased "on," meaning they constantly conduct current. This continuous base bias current leads to constant power dissipation, making Class A amplifiers inherently inefficient, with typical efficiency around 30%. This design results in significant heat generation, limiting their suitability for high-power amplification.

Moreover, the high no-load current of Class A amplifiers demands a robust power supply and signal source with adequate filtering to prevent hum and noise interference. Given their inefficiency and tendency to overheat, Class A amplifiers are unsuitable for ultrasonic energy transmission applications, especially in cases like this project, where input energy is limited.

Class B amplifiers: Class B PAs were developed to improve upon the efficiency and heat management limitations of Class A amplifiers. They use a pair of complementary transistors (either bipolar transistors or FETs) in a "push-pull" configuration, with each transistor amplifying only half of the input waveform. This approach eliminates quiescent current, as each transistor is off when not amplifying its respective half-cycle, resulting in minimal DC power draw and significantly improved efficiency compared to Class A amplifiers.

However, this efficiency boost comes at a cost: the need to switch transistors on and off introduces crossover distortion, reducing linearity. Despite this drawback, the enhanced efficiency of Class B amplifiers makes them suitable for higher power applications where energy conservation is more critical than pristine signal fidelity. Figure 3-44 is a typical circuit of Class B amplifier [170].

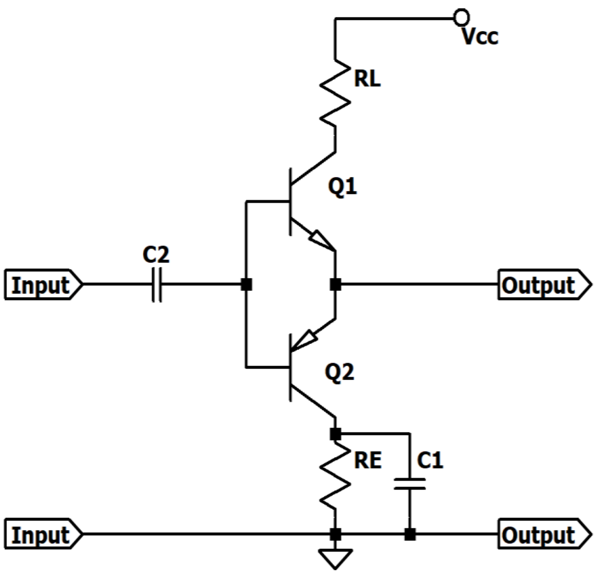

Figure 3-44. The basic schematic of a Class B amplifier.

In a Class B PA, as illustrated in Figure 3-44, operation relies on two complementary transistors in a push-pull arrangement. When the input signal is positive, the positively biased transistor Q1 is “on”, while the negatively biased transistor Q2 is “off”. Conversely, when the input signal becomes negative, Q1 turns “off” while Q2 turns "on". Each transistor thus conducts only during its respective half-cycle of the input signal. This alternation produces a full output waveform by combining the two halves.

However, due to a small voltage "dead zone" around the zero-crossing point (typically -0.7V to +0.7V due to the transistor's base-emitter threshold), parts of the waveform around zero voltage are not accurately amplified. This leads to zero-crossing distortion, or crossover distortion, as sections near the zero crossing are not fully reproduced. This makes Class B amplifiers less suitable for precision signal applications, as the distortion disrupts waveform integrity.

While Class B amplifiers achieve around 50% efficiency (higher than Class A), their crossover distortion can be problematic for systems with sensitive frequency responses. It is unfriendly for ultrasonic transducers with narrow resonance bandwidths. This distortion introduces noise and reduces energy transfer efficiency.

Class AB amplifiers: To overcome the zero-crossover distortion inherent in Class B amplifiers, the Class AB amplifier integrates the advantages of both Class A and Class B configurations. A small bias current is introduced in a Class AB design to ensure that both output transistors remain slightly conducting even when there is no input signal. This eliminates the "dead zone" near the input waveform's zero-crossing point, significantly reducing crossover distortion and enhancing output linearity.

The Class AB topology offers a balanced trade-off between the high linearity and low distortion of Class A operation and the higher efficiency of Class B amplifiers. As a result, Class AB amplifiers have become widely adopted in applications that demand both fidelity and efficiency, such as audio amplification and ultrasonic transducer driving.

The Class AB amplifier produces a smooth and continuous output waveform with minimal harmonic distortion by maintaining partial conduction across both transistors during the entire input cycle. Additionally, it generates less heat than a pure Class A amplifier, improving thermal performance and making it suitable for compact or thermally constrained designs. Given its ability to deliver clean signal amplification with reasonable power efficiency, the Class AB amplifier is a practical choice for ultrasonic driving applications. Figure 3-45 illustrates a typical Class AB amplifier circuit configuration [170].

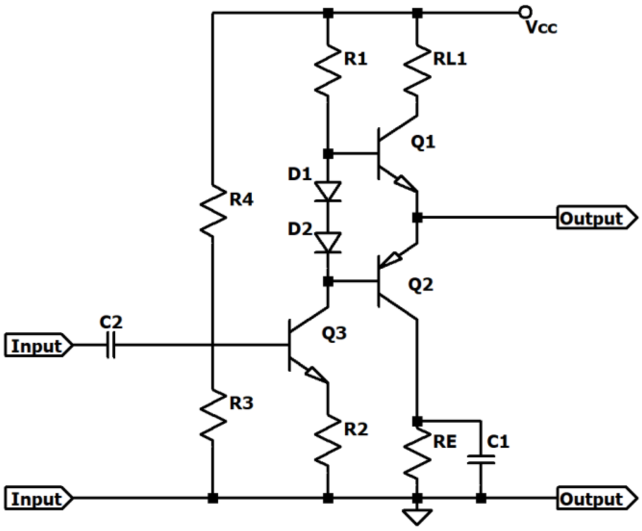

Figure 3-45. The basic schematic of a Class AB amplifier.

In the Class AB amplifier, as shown in Figure 3-45, the transistors Q1 and Q2 are positioned just at the edge of conduction using diodes D1， D2, and transistor Q3, which applies a small bias voltage. This setup keeps Q1 and Q2 "on" for slightly more than half of the input cycle, but still far from a full cycle, allowing each transistor to conduct for a bit longer than in Class B but without staying on continuously like in Class A.

This small bias voltage—often provided through diodes or resistors—eliminates the zero-crossover distortion present in Class B amplifiers while retaining higher efficiency than Class A. Thus, Class AB amplifiers achieve a balanced performance between efficiency and linearity, making them suitable for applications needing both.

While the Class AB amplifier's efficiency and linearity make it compatible with ultrasonic frequency and power requirements, it does require a stable Vcc to maintain the precise pre-bias needed to overcome crossover distortion. This need for a consistent power supply is a constraint in energy-limited systems, such as this project, where the available energy for maintaining a stable Vcc is restricted.

Class C amplifiers: Class C PAs offer the highest efficiency among linear amplifiers, typically achieving around 80%, but they are limited in terms of input frequency. These amplifiers operate by conducting for less than half of the input cycle, which reduces the time transistors spend "on," thus minimizing power loss and boosting efficiency. However, this design results in significant waveform distortion, meaning Class C amplifiers are typically only used in high-frequency RF applications or fixed-frequency amplification where signal purity is not a primary concern. Moreover, Class C amplifiers require a substantial bias voltage to operate, which demands a high-power oscillating signal to initiate and maintain conduction. While this configuration optimizes power efficiency, it is inherently unsuitable for low-frequency amplification due to its reliance on high-frequency operation and the inability to produce a clean waveform at lower frequencies. Figure 3-46 is a typical circuit of a Class C amplifier [170].

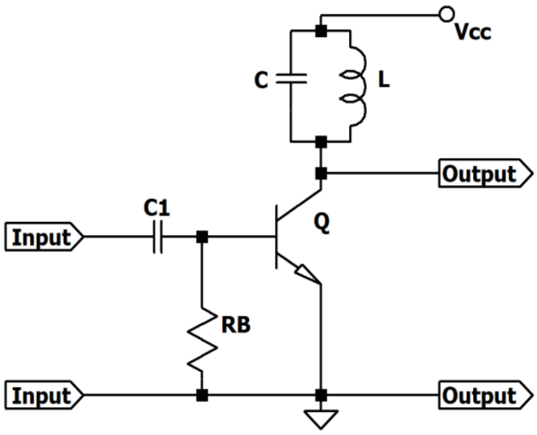

Figure 3-46. The basic schematic of a Class C amplifier.

In Class C amplifiers, as shown in Figure 3-46, the LC resonant circuit in the output stage generates a sine wave output by tuning to the input frequency. This setup ensures minimal distortion in the output waveform, provided that the input signal frequency precisely matches the resonant frequency of the LC circuit. However, in transducer drive applications, the resonant frequency of the transducer can shift depending on environmental factors, making it difficult to maintain alignment with the fixed frequency of the Class C amplifier.

This frequency mismatch poses a significant challenge, as even minor deviations between the input signal and the LC resonant frequency can result in increased distortion and reduced efficiency. Given the variability in the transducer's resonant frequency, achieving optimal performance with a Class C amplifier is challenging in practical applications requiring adaptive frequency response, such as ultrasonic energy transmission in dynamic environments.

Class D amplifiers: Class D amplifiers differ from traditional linear amplifiers by utilising switching technology to achieve exceptionally high efficiency, making them well-suited for applications requiring minimal energy loss and heat dissipation.

Commonly used to drive speakers in audio systems, RF equipment, and efficient power systems, Class D amplifiers operate by modulating the input signal into a series of pulses. This modulation, often achieved through pulse-width modulation (PWM) or similar techniques like pulse-density modulation, represents the amplitude of the input signal.

The transistors in Class D amplifiers, typically MOSFETs, act as electronic switches that alternate between fully "on" and fully "off" states. This switching behaviour minimises power dissipation because the transistors spend negligible time in transitional states where both current and voltage are high. With efficiencies exceeding 90%, these amplifiers generate much less heat compared to linear amplifiers, allowing for more compact designs and simplified thermal management systems.

In addition, Class D amplifiers can handle high currents, making them capable of delivering significant power to the load. Their operation at high switching frequencies, often in the range of hundreds of kHz to several MHz, ensures accurate signal reproduction and facilitates the use of smaller output filter components. Figure 3-47 is a typical circuit of a Class D amplifier [170].

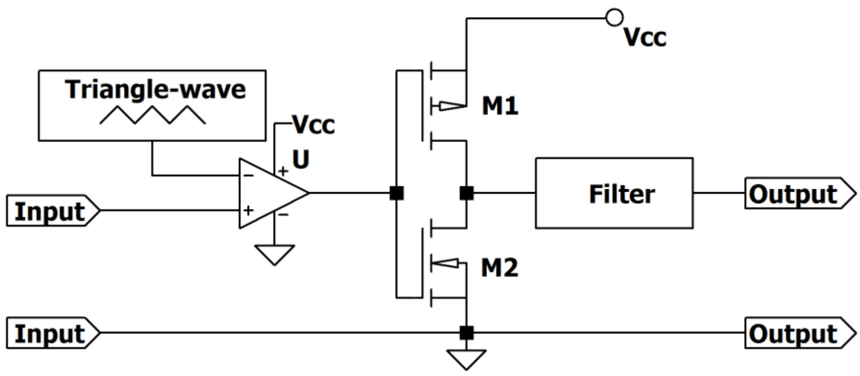

Figure 3-47. The basic schematic of a Class D amplifier.

Class D amplifiers combine the advantages of Class AB amplifiers, such as good linearity and minimal board space requirements, with the added benefit of superior power efficiency. These amplifiers are highly versatile and available in various configurations, making them suitable for diverse applications.

In low-power portable devices, such as mobile phones and laptops, Class D amplifiers are favoured for their ability to conserve battery life, meet compact board space requirements. In high-power applications, such as automotive audio systems and flat panel displays, their efficiency minimises heat dissipation and reduces the need for extensive thermal management.

Class D amplifiers are well-suited for driving ultrasonic transducers as they meet the required frequency and power ranges. However, their implementation necessitates additional components, such as trigger waveform generators and output filters, to minimise noise and ensure a clean signal. While these components enhance performance, they also increase the complexity of the transducer drive circuit design.

Class E amplifiers: Similar to Class D amplifiers, Class E amplifiers are also switching amplifiers that utilise transistors, typically MOSFETs, operating in fully "on" or fully "off" states to minimise conduction and switching losses. However, the load networks in Class E amplifiers are uniquely designed to optimise energy transfer by minimising switching losses and efficiently redirecting energy from the transistor's shunt capacitances to the load. This approach effectively eliminates the parasitic capacitance losses often observed in Class D amplifiers. Additionally, Class E amplifiers employ passive networks to remove the need for a trigger waveform generator, resulting in a simpler and more compact circuit structure. This design not only reduces complexity but also enhances efficiency, making Class E amplifiers particularly advantageous in applications where space and power optimisation are critical. Figure 3-48 is a typical circuit of Class E amplifier [170].

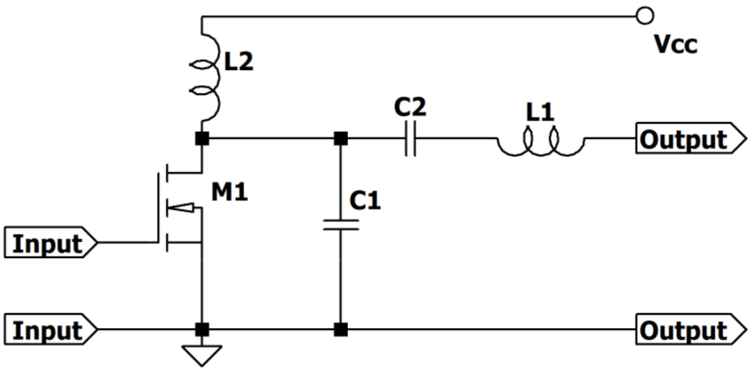

Figure 3-48. The basic schematic of a Class E amplifier.

As illustrated in Figure 3-48, the Class E amplifier connects the load to the power source through a series resonant circuit comprising L1 and C2. L2 functions as a choke, providing a path for the DC supply while blocking the AC input signal. C1, the shunt capacitor of transistor M1, offsets the voltage and current of the input source. This reduces switching losses and redirects the stored energy into the load, rather than dissipating it as heat.

In theory, the Class E amplifier can achieve 100% efficiency because the transistor ideally incurs no losses during operation. However, practical limitations arise because the transistor cannot switch instantaneously between "on" and "off" states, leading to some energy loss during transitions and thereby reducing overall efficiency. The Class E amplifier is highly versatile, with output power ranging from a few watts to tens of megawatts and operating frequencies spanning from a few kilohertz to several gigahertz. Additionally, the DC supply Vcc provides energy without affecting the bias voltage setting, simplifying the circuit design.

Given its capabilities, the Class E amplifier is well-suited for driving transducers, offering sufficient output power, frequency adaptability, and compatibility with a wide input voltage range. Its relatively simple circuit structure makes it a compelling option for transducer driving circuits.

Class F amplifiers: Class F amplifiers are also switching amplifiers, primarily used in high-power applications such as telecommunications, broadcasting, and satellite communications. Like Class E amplifiers, Class F designs aim to minimise switching losses by reducing the overlap between switching voltage and current. However, the distinguishing feature of Class F lies in using harmonic tuning to optimise performance.

Harmonic tuning in Class F amplifiers tailors the amplitude and phase of specific harmonic frequencies, enabling the output waveform to approximate a square wave. This optimisation reduces power dissipation and improves efficiency. Achieving effective harmonic tuning requires multiple tuning networks, which are crucial for controlling the desired harmonics and suppressing unwanted ones.

The design complexity of these networks increases significantly at higher input frequencies, as precise amplitude and phase adjustments are needed to achieve optimal harmonic tuning. Conversely, at lower frequencies, the tuning network's inductors must be larger to achieve the same effect, leading to increased circuit size and potential inefficiencies. Consequently, the operating frequency plays a critical role in the feasibility and design of Class F amplifiers. Figure 3-49 is a typical circuit of Class F amplifier [170].

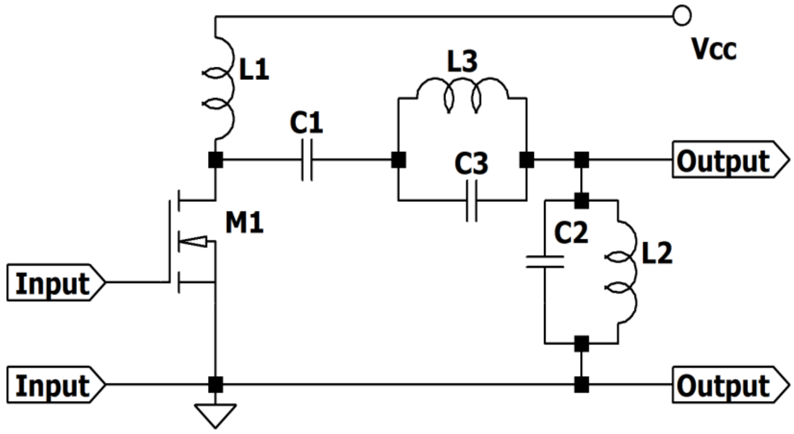

Figure 3-49. The basic schematic of a Class F amplifier.

As shown in Figure 3-49, the Class F amplifier employs L2, C2, and L3, C3 as part of the output tuning network, while L1 and C1 function as AC and DC blocking components. The output tuning network ensures harmonic control to improve efficiency and output power, and additional tuning stages may be incorporated based on specific design requirements. These networks are critical for shaping the output waveform and achieving the desired operating efficiency.

Theoretically, the efficiency of Class F amplifiers can reach 100% by optimally tuning harmonic amplitudes and phases to reduce power dissipation. However, practical implementations face inherent losses due to imperfect components and switching dynamics, resulting in actual efficiencies typically exceeding 85%. This level of performance makes Class F amplifiers highly suitable for applications demanding high power and efficiency, such as RF communications and broadcasting.

Despite their advantages, the design complexity of Class F amplifiers is a significant drawback. The need for multiple resonator networks and precise harmonic control makes their implementation challenging, particularly for low-frequency or high-frequency variable systems. These requirements increase the design overhead, size, and difficulty in achieving optimal performance. Consequently, while Class F amplifiers excel in high-power, fixed-frequency applications, they are less suitable for driving ultrasonic transducer circuits due to the complexity of harmonic network design and the variability of transducer resonance.

Class S amplifiers: The Class S amplifier operates by performing switching amplification after the input signal undergoes delta-sigma modulation. Its operation resembles that of a Class B amplifier in that it uses a push-pull configuration, but the key distinction lies in the use of delta-sigma modulation, which employs a very high sampling frequency and a negative feedback loop for precise input signal encoding. This modulation technique effectively filters out noise while enabling finer sampling of the input signal. The encoded signal is passed through a low-pass filter to extract the desired PWM signal. After amplification is demodulation. The demodulation process, typically involving sigma-delta techniques, reconstructs the amplified waveform, reducing distortion and enhancing fidelity. This encoding-amplification-decoding mechanism makes Class S amplifiers highly efficient and capable of delivering high-quality output, leading some researchers to classify them as linear amplifiers. Figure 3-50 is a typical circuit of Class S amplifier [170].

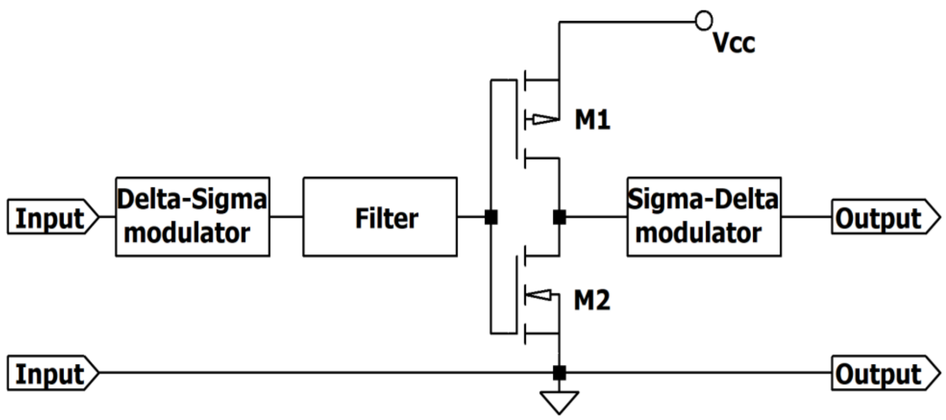

Figure 3-50. The basic schematic of a Class S amplifier.

As depicted in Figure 3-50, the circuit diagram of the Class S amplifier highlights its essential components: modulation, switching amplification, and demodulation stages. The switching amplification process ensures high efficiency and minimal power loss, while the precise modulation and demodulation mechanisms enable the Class S amplifier to achieve low distortion and superior fidelity.

These characteristics make the Class S amplifier particularly suitable for applications demanding high efficiency and low distortion, such as high-fidelity audio systems and specialised communication systems. Nevertheless, the inherent complexity of its modulation and demodulation circuits presents a significant challenge for ultrasonic drive. This complexity limits its adoption in applications where simplicity and low cost are primary considerations.

In addition to the power amplifiers discussed above, there are specialised amplifiers such as Class G, Class H, Class J, Class T, linear variable gain amplifiers, and dynamic voltage amplifiers. These amplifiers often serve niche applications or represent specific amplifier topologies. However, given the requirements of the ultrasonic transducer drive application and the constraints of this project, these specialised amplifiers are not considered suitable for the design. As such, they are not introduced in detail in this discussion.

In summary, power amplifiers come in various types, each offering distinct performance characteristics. Linear amplifiers, such as Class A, Class B, and Class AB, provide excellent signal fidelity but suffer from low efficiency. Class C amplifiers are the most efficient among linear designs but are best suited for fixed-frequency applications due to their limited frequency adaptability.

Switching amplifiers, known for their high efficiency, generally have lower signal fidelity compared to linear amplifiers. Class D and Class S amplifiers can achieve better signal restoration through high-frequency PWM techniques, but at the cost of increased design complexity and circuit size. On the other hand, Class E and Class F amplifiers feature simpler structures, rely on passive components, and accommodate wide input voltage variations, making them suitable for applications with unstable input sources, but they require accurate load feedback circuit design. Ultimately, the choice of amplifier should align with the specific requirements of the transducer and application environment, ensuring optimal performance and efficiency tailored to the given conditions.

3.2.3.4 Conversion Circuit Link Loss

The link loss of the conversion circuit refers to the energy loss from the RF energy input to the ultrasonic energy output. This loss primarily arises from the key functional modules of the circuit: the RF energy harvesting circuit (including input impedance matching and rectifier), the power management circuit (comprising the boost circuit, energy storage unit, voltage detection, and switching circuit), and the ultrasonic driving circuit (including the local oscillator circuit, power amplifier, and output impedance matching). Figure 3-51 illustrates the converter link loss.

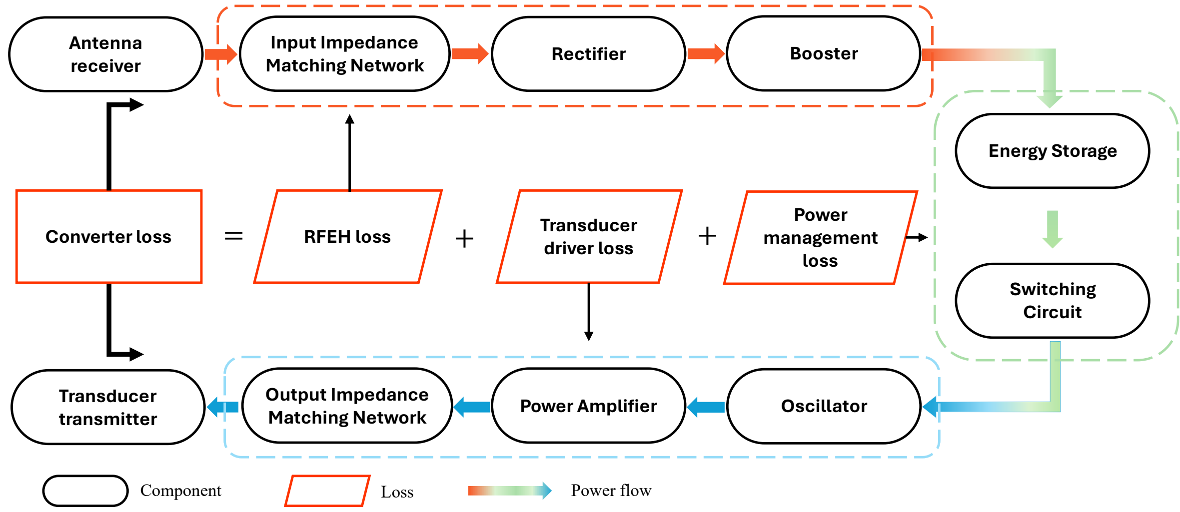

Figure 3-51. Flow diagram of converter link loss. It is including RFEH loss, transducer drive loss, and energy management loss.

Given the diversity in circuit design approaches tailored to specific application environments, the link loss in conversion circuits can vary significantly. Understanding and quantifying this link loss makes it possible to analyse inefficiency sources, identify underperforming modules, and establish a structured approach for optimising circuit performance. Consequently, it is necessary to systematically examine the primary sources of loss in each sub-circuit of the conversion circuit. This analysis aims to offer a comprehensive perspective on the factors influencing overall efficiency and to inform the development of effective design optimisation strategies.

In the RF energy harvesting circuit, the input impedance matching network typically consists of inductors and capacitors, where energy losses arise from parasitic resistance, dielectric dissipation, and resonance effects. Among these, mismatches in the resonant frequency represent the primary source of loss, given the limited input energy available. Consequently, the design of the impedance matching network should include a suitable bandwidth to mitigate losses associated with frequency variations.

Energy loss is attributed mainly to the diodes for the rectifier circuit and charge pump. These losses include the forward voltage drop, which dissipates energy as heat during conduction (approximately 0.7 V for silicon diodes and 0.2-0.4 V for Schottky diodes), and reverse recovery losses, which occur during the transition from conduction to blocking states. While Schottky diodes reduce reverse recovery losses compared to conventional diodes, their performance can still be constrained at higher frequencies.

For charge pumps using CMOS technology, despite the low on-resistance of MOSFETs, high-frequency operation increases switching losses, which scale with the operating frequency. To address these issues, the selection of an appropriate RF frequency band is essential for minimising energy losses and achieving efficient operation across the various components of the energy harvesting circuit.

In energy management circuits, the primary sources of loss are the boost circuits and switching circuits. These losses are similar to those in RF energy harvesting circuits and include MOSFET conduction losses, diode forward voltage drops, and switching losses. Consequently, the selection and design of components follow principles similar to those used in RFEH circuits.

Where feasible, integrated circuit solutions are preferred due to their higher integration and compact design, which often results in reduced energy losses. However, when using IC-based solutions, it is important to carefully evaluate the supported voltage range and any application-specific constraints to ensure compatibility with the overall system design and operating requirements.

In ultrasonic drive circuits, losses in the impedance matching network are comparable to those in RF energy harvesting circuits, involving parasitic resistances, dielectric losses, and mismatched resonance losses. Like energy management circuits, IC-based solutions are often preferred for the oscillator component due to their compact design and efficiency.

However, the power amplifier within the ultrasonic drive circuit requires a higher degree of frequency and impedance matched to ensure optimal performance. This match is necessary because the amplifier must align with the specific characteristics of the piezoelectric transducer, including its impedance and frequency response. The appropriate power amplifier design selection should consider both the application requirements and the performance parameters of the piezoelectric transducer to achieve efficient energy transfer and minimal loss.

In summary, the losses within the conversion circuit vary significantly due to the diversity of design approaches and the specific requirements of different applications. To systematically address these variations, the link loss of the conversion circuit is expressed as:

$$\text{Conversion loss (dBm)} = \text{RFEH Loss} + \text{Power Management Loss}$$
$$+\text{Ultrasonic Drive Loss,} \qquad (3\text{-}63)$$

which provides a comprehensive framework for analysing energy transfer efficiency across the circuit.

Given the complexity of circuit design and the diverse characteristics of component parameters, the analysis of link loss within each subcircuit of the conversion circuit is conducted by tracing the energy flow. This approach ensures that loss mechanisms at each stage are accurately identified. The generalised loss expression for the subcircuits is as follows:

$$X_{\text{Loss}} = 10\log_{10}\frac{\mathrm{P}_{In}}{\mathrm{P}_{Out}} \qquad (3\text{-}64)$$

Where: X_{Loss} represents the loss in a particular sub-circuit, such as rectifier loss, amplifier loss, oscillator loss, etc. P_{In} is the input power to the sub-circuit, which is sourced from the output of the previous stage. P_{Out} is the output power from the sub-circuit, which is transferred to the next stage or to the load.

This expression highlights the direct relationship between the input and output power of each sub-circuit and provides a clear framework and comparison parameter for quantifying the loss in each individual stage of the conversion process. By minimizing X_{Loss} it is possible to improve the overall efficiency of the conversion circuit.

3.2.4 Overall Energy Flow Framework

The energy transmission process in the CRFU-WPT system consists of three sequential stages. First, input power is transmitted via electromagnetic waves from the RF transmitting antenna to the RF receiving antenna. The received RF energy is then accumulated, regulated, and managed by the conversion circuit. In the next stage, energy is transferred acoustically from the ultrasonic transmitting transducer to the receiving transducer through the propagation medium. Finally, the acoustic energy is converted back into electrical form and delivered to the load by the receiving-side circuitry.

Given that the system involves multiple forms of energy—electromagnetic, mechanical, and electrical—the development of a unified and scalable energy transmission model is inherently complex. To address this, the link loss method is adopted to formulate a generalised energy transmission framework. This approach abstracts each stage in the transmission path as a distinct link characterised by its associated loss, allowing the overall model to remain modular. Modifications to system components (e.g. replacing a transducer or altering circuit parameters) require only an update to the corresponding link loss term, without affecting the structure of the model as a whole. This modularity offers high flexibility and adaptability across different application scenarios.

As illustrated in Figure 3-1, which depicts the energy flow of the system, the main power transfer path is from the input power (P_1) to the output power (P_4). The overall power transfer relationship is therefore expressed as:

$$P_4\,(dBm) = P_1(dBm) - RF\ Link\ Loss\ (dB) - Conversion\ Loss(dB) \\ - Ultrasonic\ link\ Loss(dB), \tag{3-65}$$

Each of the individual loss components—RF link loss, conversion loss, and ultrasonic link loss—has been analysed in detail in the previous sections of this chapter. This framework not only enables the performance evaluation of the current system but also facilitates future scalability and design optimisation by isolating individual loss contributors. Moreover, the link-based model provides a practical basis for power budgeting, allowing for predictive analysis of power availability across different stages of the transmission chain.

3.3 System Design

The design of an RFU-WPT system is an extensive and intricate task that involves constructing a complete circuit structure based on the overall system framework. It also necessitates the seamless coordination of all subsystems to ensure efficient operation. This study considers diverse application scenarios and load requirements and discussed the design and optimisation of key components within the subsystem.

The system design process follows a structured methodology. Initially, a detailed power budget is calculated for specific loads and application modes. Based on the energy flow within the system, appropriate key components are selected. The compatibility of voltage and current levels is then evaluated to facilitate the integration and assembly of these components. Finally, an iterative approach is adopted to optimise the system design.

Accordingly, this chapter is organised into three main sections, including power budget, system components system assembly.

3.3.1 Power Budget

This project employs wireless energy transmission via RF and ultrasound to power wireless sensors. At the outset of the design process, it is essential to establish a power budget that reflects the sensor's application environment and energy requirements. The power budget is primarily determined by the relationship between the output power and the performance of the RF link, ultrasonic link, and conversion circuit.

- **RF Link**: The characteristics of the RF link are calculated using Figure 3-7 and Equation 3-11.
- **Ultrasonic Link**: The parameters of the ultrasonic link are determined using Figure 3-10 and Equation 3-40.
- **Conversion Circuit**: The conversion circuit can be designed in various configurations based on application-specific requirements, and its losses are quantified using Equation 3-64.

The overall input-output relationship of the system can be expressed as:

$$\mathrm{P}_{Out} = \mathrm{P}_{In} - RF_{Loss} - Ultrasonic_{Loss} - Conversion_{Loss} \tag{3-66}$$

Here, P_{Out} represents the power to load, while P_{In} is the power to transmitting antenna, and losses accounts for the RF link, ultrasonic link, and conversion circuit.

Once the conversion circuit is finalised, the input power requirements will be influenced by the transmission distances of the RF and ultrasonic links. Figure 3-52 shows a case to illustrate the relationship between these characteristics and the required input power. Assuming a conversion circuit efficiency is 90% and a target output of 1 mW, the antenna's gain is 30 dBi and works at 2.4 GHz. The UET link transmission medium is aluminium, and the transducer is PZT-8, which works at 40 kHz.

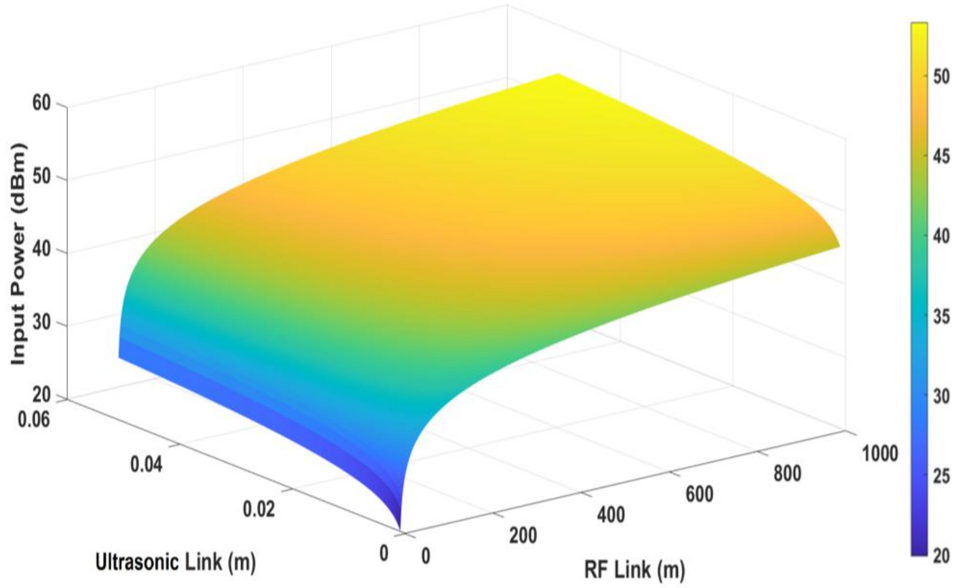

Figure 3-52. Power budget diagram of input power versus transmission distance.

The power budget of the system is established according to application needs and energy transfer models. This analysis aids in evaluating the antenna's output power and the transmission ranges for both RF and ultrasound links. It is important to highlight that the exposure risks associated with RF power and ultrasonic power must be carefully evaluated. These risks should be addressed in accordance with the safety exposure guidelines discussed in Chapter 3. This ensures that the wireless energy transmission system operates within safe limits for human exposure while maintaining effective power delivery to the wireless sensors.

3.3.2 System Components

The system design is also discussed in terms of three key components: the RF link, the ultrasonic link, and the conversion circuit. The RF link primarily focuses on the selection and optimisation of the antenna to ensure efficient energy harvesting and transmission. The ultrasonic link centres on the piezoelectric transducer and the design of the ultrasonic receiving circuit. The conversion circuit is configured following the schematic in Figure 3-3, ensuring effective integration of energy management and converter functionalities.

3.3.2.1 Antenna

The selection and design of antennas for RF energy transmission require careful consideration of multiple factors, including frequency, bandwidth, directivity, polarization, size, and efficiency[171]. These parameters must be optimised to ensure compliance with regulations and achieve efficient energy transfer while accommodating the specific requirements of the project.

The frequency of operation is a critical parameter in antenna design and must first align with regulatory restrictions. These restrictions are established by international and national regulatory bodies, such as the International Telecommunication Union (ITU), the Federal Communications Commission (FCC), and the European Telecommunications Standards Institute (ETSI). Their primary objective is to prevent interference with reserved frequency bands and to control power limits in license-free bands. For instance, common license-free bands, including 433 MHz, 868 MHz, 915 MHz, and 2.4 GHz, typically impose stringent transmission power limits, such as a maximum transmitter effective isotropic radiated power (EIRP) from FCC is 36 dBm. While these bands are easily accessible, such power restrictions often constrain their suitability for high-efficiency energy transmission. In addition, frequency selection influences transmission distance and antenna size. Lower frequencies experience reduced attenuation, making them more suitable for long-distance energy transfer; however, they also require larger antenna designs, necessitating a trade-off between operational range and physical dimensions. Although multi-band antennas have been widely reported for RF energy harvesting applications, they are less appropriate for RF energy transmission involving specific emission sources due to the challenges posed by impedance matching and design complexity[172, 173, 174]. For this reason, single-band antennas tailored to the chosen operational frequency are favoured in this project.

In terms of bandwidth, RF energy transmission primarily requires a tolerance to frequency drift and adequate impedance matching. Excessively broad bandwidths are unnecessary and may introduce inefficiencies, as the design focus is on maintaining stable operation within a predefined frequency range.

Directivity and polarization play pivotal roles in determining the flexibility and efficiency of the antenna system[175]. High-gain antennas are particularly advantageous for energy transmission, as they concentrate energy within a specific direction, thereby enhancing efficiency. This makes them ideal for use as transmitting antennas. On the other hand, low-gain antennas are better suited for receiving applications due to their inherent flexibility, which is important when the precise alignment of the receiving antenna cannot be guaranteed. Furthermore, in systems employing a single transmitting antenna and multiple receiving antennas, multi-beam transmitting antennas can significantly improve energy distribution [176]. To mitigate power losses arising from polarization mismatches, circularly polarized antennas are recommended, as they ensure compatibility across diverse deployment scenarios.

Antenna efficiency, a multifaceted performance metric, depends on design choices and operational parameters. High-gain antennas, such as parabolic and horn antennas, are often more efficient for applications requiring focused energy transmission. Additionally, innovative designs, including resonant loop array antennas and Meta-surface antennas, demonstrate excellent efficiency and are promising alternatives for advanced applications[177]. Furthermore, the integration of RF lenses represents a cutting-edge approach to improving transmission efficiency. RF lenses optimise the phase and direction of RF waves, focusing energy directly onto the receiving antenna. This reduces dispersion and enhances power density, as illustrated in Figure 3-53, making them particularly beneficial in scenarios requiring precise energy delivery.

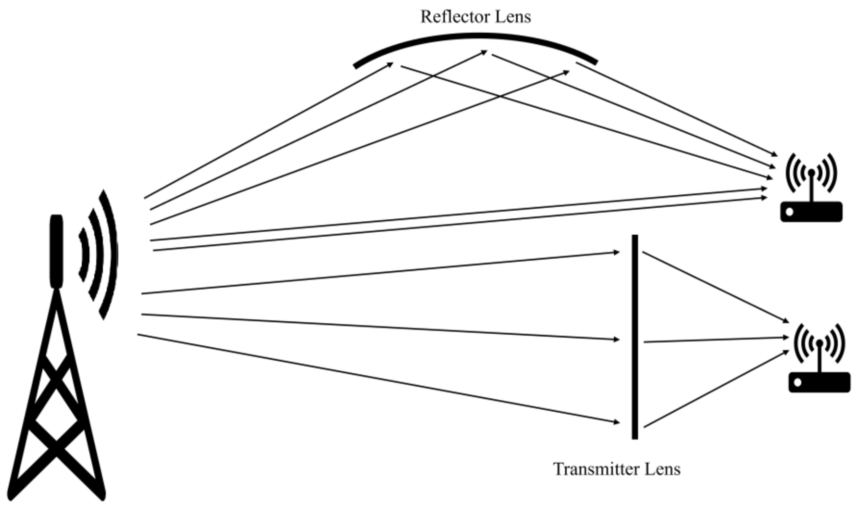

Figure 3-53. Schematic diagram of improving RF energy transmission efficiency through lenses.

Numerous studies have demonstrated that RF transmission efficiency can be significantly enhanced through the use of lenses [178, 179, 180, 181]. These lenses effectively focus and direct RF energy, reducing dispersion and improving energy density at the receiving end. With the advancement of Meta-surface technology, the design and fabrication of such lenses have become increasingly accessible. For instance, M. Zhong, et al. reported the development of a lens capable of dynamically adjusting its focal length and direction to meet specific application requirements [182]. This lens features a straightforward design and structure, relying on a single-layer substrate. Despite its simplicity, it has been shown to markedly improve RF transmission efficiency. The adaptability of this lens to varying operational conditions highlights its potential for integration into energy transmission systems.

Optimised antenna design and selection can be achieved by systematically evaluating key factors such as frequency, bandwidth, directivity, polarization, and physical size. This approach ensures compliance with regulatory standards while enhancing energy transmission efficiency. Furthermore, emerging technologies, including Meta-surfaces and RF lenses, offer promising avenues for significantly improving energy transmission performance and deserve further exploration.

3.3.2.2 Transducer

The design and selection of piezoelectric transducers for ultrasonic energy transmission require a comprehensive consideration of working modes, material properties, operating frequency, and the specific requirements of the application environment. This process ensures not only efficient energy transmission but also the fulfilment of application-specific constraints. A systematic approach to transducer design involves careful evaluation of the operating environment, resonant frequency selection, and material characteristics to optimise performance.

The operational environment significantly influences the design requirements of the transducer. Different mediums impose unique constraints on transducer functionality and material compatibility. When ultrasonic energy is transmitted through water, the transducer must be waterproof to prevent damage or loss of functionality. Furthermore, the electrodes should not be exposed on the surface, as this could lead to corrosion or energy dissipation due to water-induced electrical effects. The use of hermetically sealed designs or protective coatings is essential to maintain durability and performance.

For biomedical applications, where body tissue serves as the transmission medium, the transducer must be fabricated using biocompatible materials to avoid adverse biological reactions. Heavy metals and toxic substances must be avoided in the transducer's composition. Additionally, the design must adhere to medical standards and ensure minimal heat generation to avoid tissue damage. When the transmission medium is metal, the acoustic impedance mismatch between the transducer and the medium becomes a critical consideration. The use of transducers made from materials similar to the metal medium can significantly improve acoustic impedance matching, thereby reduce energy losses and enhance efficiency.

The selection of a suitable resonant frequency is a key design parameter in ultrasonic transducers, as it directly affects transmission efficiency and distance. The frequency must align with the characteristics of the medium: Lower frequencies are typically used for long-distance energy transmission due to reduced attenuation in the medium. Higher frequencies are preferable for applications requiring precise energy focusing but are more susceptible to attenuation, limiting their effective range. Selecting the optimal resonant frequency requires balancing these trade-offs while considering the acoustic properties of the medium and the desired application outcomes.

The performance of piezoelectric transducers is intrinsically linked to the properties of the materials used. High-performance transducers typically exhibit: Materials with low internal energy losses are essential to maximise the conversion of electrical energy into mechanical energy. A high electromechanical coupling coefficient ensures efficient energy transfer between the electrical and mechanical domains, which is particularly important for maintaining performance in demanding applications. Materials with high piezoelectric coefficients generate larger mechanical displacements for a given electric field, increasing the transducer's effectiveness in energy transmission.

The selection and design of piezoelectric transducers are pivotal in achieving efficient ultrasonic energy transmission. By carefully addressing environmental constraints, optimising resonant frequency, and selecting high-performance materials, transducers can be tailored to meet the specific demands of diverse applications. Such a rigorous and systematic approach not only enhances transmission efficiency but also ensures reliability and compatibility with the intended operational environment.

3.3.2.3 Converter

The conversion circuit forms the core of this project, encompassing RF energy harvesting, ultrasonic drive, and power management. Its design should be tailored to the application environments of the RF and ultrasonic links, ensuring efficient energy transfer while meeting the constraints imposed by various operating conditions. A systematic design process considers the power budget, input power levels, and iterative calculations to refine performance. Each subsystem within the conversion circuit requires careful optimisation to achieve overall system efficiency and reliability.

A. **RF Energy Harvesting**

For harvesting and converting RF energy into usable electrical energy. Its primary components include input impedance matching, rectifiers, and charge pumps.

The input impedance matching network: it plays a pivotal role in optimising energy transfer by matching the antenna's impedance to the subsequent stages of the circuit, such as the rectifier or charge pump[183, 184]. This network is designed primarily based on the operating frequency and impedance characteristics of the antenna. For single-band antennas, the design process is relatively straightforward, as it involves matching the impedance at a specific frequency. The task becomes significantly more complex for multi-band antennas, where the impedance should be calculated and matched across multiple frequency bands. This requires sophisticated design methodologies, often involving iterative simulations and the use of tuneable or broadband matching techniques to achieve acceptable performance across all targeted frequency ranges. In addition to frequency considerations, the matching network must account for bandwidth and voltage tolerance. Although RF energy transmission typically operates at a fixed frequency, slight frequency drifts can occur due to environmental variations or system imperfections. To address these drifts, the matching network must exhibit a degree of tolerance to ensure stable and efficient energy transfer without requiring constant recalibration.

To minimise energy losses, it is critical to use components with low equivalent series resistance (ESR) in the matching network. However, such components often come with lower voltage tolerance, posing a risk of breakdown under higher operating voltages. To mitigate this, voltage redundancy must be incorporated into the design, ensuring the components can operate safely within their specified limits. Careful selection of components, guided by thorough evaluation of their data sheet specifications, is essential to achieve an optimal balance between performance, durability, and system stability. By addressing these design considerations comprehensively, the input impedance matching network can effectively enhance the efficiency and reliability of the RF energy transmission system.

Rectifiers and Charge Pumps: Diodes play a pivotal role in the design of rectifiers and charge pumps, with their characteristics significantly influencing the efficiency and stability of the circuit. Diodes with low forward voltage are preferred for reducing the startup voltage, enabling operation under low input energy conditions. Although there is a significant amount of literature on low forward voltage diodes, commercially available options with low voltage are still relatively scarce[185, 186, 187, 188]. Moreover, diodes with high reverse voltage are suitable for circuits requiring higher operating voltage levels, ensuring reliable performance under demanding conditions. A shorter recovery time allows diodes to function efficiently at higher operating frequencies, a crucial consideration for high-frequency RFEH. While charge pumps can amplify input signals and generate DC outputs, they inherently introduce instability into the circuit. High gain in charge pumps tends to amplify even minor input fluctuations, resulting in larger output variations. This instability not only increases the tolerance requirements for circuit components but also heightens the risk of damage to sensitive elements. Consequently, the design of charge pumps must carefully balance gain and stability to ensure reliable operation. For applications where input energy levels are sufficiently high to generate the required clock signal, active rectifiers present a compelling alternative. These rectifiers provide superior rectification efficiency compared to passive counterparts, owing to their ability to synchronise with the input signal and minimise energy losses. However, their implementation requires additional considerations, such as clock signal generation and control, which may influence the overall circuit complexity.

B. Power Management

The energy management subsystem ensures the optimal utilisation of harvested energy. Its key components include boost circuits, energy storage units, voltage detection, and switch circuits[189].

The boost circuit: it is responsible for elevating low input voltages to levels suitable for powering the load or charging energy storage devices. Its design and selection are guided by the output voltage and current requirements, as well as the characteristics of the input energy source.

Modern boost circuits often rely on ICs, which offer mature, reliable, and compact solutions for voltage conversion. These ICs typically integrate key functionalities, such as switching transistors, feedback control loops, and protection mechanisms, thereby simplifying the circuit design process. The choice of boost IC depends on the specific application requirements, including the desired output voltage, load current, efficiency, and input voltage range.

One of the primary considerations in the design of a boost circuit is the input voltage level, particularly in scenarios where the input energy is limited or variable. For such applications, low-startup-voltage ICs are highly desirable. These ICs are designed to operate effectively even when the input voltage is minimal, enabling the system to harvest and utilise energy from weak or intermittent sources. For instance, in wireless energy transfer systems or energy-harvesting applications, the input voltage might fluctuate significantly, and the boost circuit must be capable of maintaining stable operation across these variations. The efficiency of the boost circuit is another critical factor, particularly in energy-constrained environments. High-efficiency designs minimise energy losses during the voltage conversion process, thereby maximising the amount of power delivered to the load. This can be achieved through careful selection of components, such as low-resistance inductors and high-efficiency diodes or synchronous rectifiers, as well as optimising the operating frequency and control algorithms of the boost IC.

The design and implementation of a boost circuit must balance multiple factors, including startup voltage, efficiency, output stability, and thermal performance. By selecting appropriate ICs and optimising the circuit parameters, it is possible to achieve reliable and efficient voltage boosting for a wide range of applications, ensuring the effective utilisation of available energy resources.

Energy storage: it provides a buffer for intermittent or variable power inputs, to ensure consistent energy availability. The choice between energy storage technologies, such as supercapacitors and batteries, depends on the specific requirements of the application, including charge-discharge frequency, load characteristics, and operational lifetime.

Supercapacitors are well-suited for applications requiring frequent charge and discharge cycles, as they exhibit high cycle durability compared to traditional batteries. Their ability to deliver high power density makes them ideal for applications with rapid energy demands or high load frequencies. Moreover, supercapacitors can operate effectively across a wide voltage range, offering flexibility in energy management systems. However, their relatively low energy density compared to batteries limits their utility in scenarios requiring extended energy supply durations. Supercapacitors are often employed in conjunction with batteries to balance power delivery and energy capacity, leveraging the strengths of both technologies. Batteries, on the other hand, are better suited for applications with lower charge-discharge frequencies and where energy density is a priority. They provide a stable and reliable energy source over longer periods, making them ideal for applications where energy demand is steady or predictable. However, batteries typically have a limited number of charge-discharge cycles compared to supercapacitors, and their performance can degrade over time, especially under high-load or high-temperature conditions.

The integration of energy storage systems into the overall design requires careful consideration of parameters such as charging voltage, current, and efficiency. For instance, the charging circuit must be designed to match the characteristics of the selected energy storage device, ensuring optimal performance without overcharging or excessive energy losses. Additionally, thermal management is critical for both supercapacitors and batteries to prevent overheating and ensure longevity. The choice between supercapacitors and batteries depends on the application's specific requirements. While supercapacitors excel in high-frequency-charging and discharging, high-power-demand scenarios, batteries are more suitable for sustained energy delivery over time. A hybrid approach, combining both technologies, can often provide an optimal balance of power and energy capacity, enhancing the performance and reliability of the energy storage subsystem.

Voltage detection: it is providing control signal for switching circuit in management systems, ensuring the proper monitoring and regulation of voltage levels to maintain system stability and protect components from damage. The choice of voltage detection method depends on the trade-offs between efficiency, drive capability, and design complexity, which vary depending on the application requirements.

Capacitive sampling is a highly efficient method that utilises the charge-discharge properties of capacitors to measure voltage. This approach introduces minimal energy loss, making it well-suited for low-power systems where efficiency is a priority. However, capacitive sampling has limited drive strength, which can restrict its use in applications requiring significant current to drive subsequent stages of the circuit. This limitation may necessitate additional amplification stages to achieve the desired signal strength, slightly increasing system complexity. Resistive sampling, on the other hand, provides robust drive capability by directly dividing the input voltage using resistive elements. This method is straightforward to implement and capable of handling higher power demands, making it a reliable choice for systems requiring strong signal driving. However, resistive sampling is inherently less efficient than capacitive sampling, as it introduces continuous power losses proportional to the current passing through the resistive network. These losses can be mitigated by carefully selecting high-resistance values, but this approach may reduce the dynamic response speed of the system. Zener diodes offer a simple and reliable method for voltage detection, operating within a fixed voltage range determined by their breakdown voltage. Zener diodes are highly stable and capable of providing precise voltage thresholds. However, their fixed detection range limits flexibility, making them less suitable for applications with varying voltage requirements. Additionally, the current passing through the Zener diode during operation contributes to energy losses, which must be accounted for in power-sensitive systems.

In practical applications, the selection of a voltage detection method depends on the system's specific needs. For instance, low-power applications may favour capacitive sampling for its efficiency, while high-current or dynamic systems may opt for resistive sampling despite its higher losses. Zener diodes are often used in fixed-voltage applications where simplicity and precision are key priorities. To achieve optimal performance, voltage detection is often integrated into a broader energy management strategy, combining the strengths of multiple methods. For example, capacitive sampling might be used for continuous monitoring, with Zener diodes providing protection against voltage spikes. Such an integrated approach ensures accurate and efficient voltage regulation while meeting the diverse demands of modern energy systems.

Switching Circuit: Its primary function is to regulate the connection and disconnection between energy storage unit and ultrasonic transducer drive, ensuring that energy accumulation is optimised while minimising subsequent circuit losses. This control is essential for achieving high overall efficiency in the system.

Efficient operation requires precise control over the charging and discharging processes of the energy storage unit to keep it within a high-efficiency range. Various control methods can be employed to achieve this, depending on the design requirements and application constraints. Voltage comparators and adjustable hysteresis Schmitt triggers provide flexible design options, allowing for customised control thresholds and adaptive performance. These components can be tailored to respond to specific voltage conditions, enabling efficient energy management.

On the other hand, switching ICs offer stable and straightforward operation within a fixed voltage range. They are particularly suitable for applications where simplicity and reliability are prioritised over customisation. By leveraging these switching control methods, the circuit ensures efficient energy transfer and utilisation.

C. **Ultrasonic Transducer Drive**

The ultrasonic transducer drive subsystem comprises three key components: an oscillator, a power amplifier, and an output impedance matching network.

The output impedance matching network: it is responsible for optimally matching the output of the power amplifier to the piezoelectric transducer, facilitating efficient energy transfer while minimising reflection and power losses. However, its design is inherently more complex compared to the input impedance matching networks used in RF systems. This complexity arises from the inherent variability of the transducer's resonant frequency and impedance, which are influenced by environmental factors. For instance, variations in the depth of the transducer submerged in water can significantly alter its impedance and resonant frequency, necessitating adjustments to the matching network. To address these challenges, site-specific impedance data must be collected under actual operating conditions to inform the design of the output impedance matching network. This data allows for the creation of a tailored network capable of adapting to environmental changes while maintaining efficient energy transfer. The design process often involves iterative calculations and simulations to ensure compatibility with the transducer's dynamic impedance characteristics and resonant frequency shifts. By accounting for these factors, the output impedance matching network can ensure reliable and efficient operation across a range of environmental conditions.

The oscillator: providing the drive signal required to excite the piezoelectric transducer at its resonant frequency. This resonance ensures efficient energy conversion and transmission, as it aligns the electrical and mechanical oscillations of the system.

Several types of oscillators are commonly used in this context, each with unique characteristics and advantages. RC (resistor-capacitor) and LC (inductor-capacitor) oscillators are highly versatile, offering the ability to fine-tune the output frequency by adjusting variable capacitors and inductors. This flexibility makes them particularly suitable for applications requiring adaptable or precise frequency settings. However, their stability can be sensitive to environmental changes, and they may require periodic recalibration to maintain performance. Crystal oscillators, on the other hand, are renowned for their exceptional frequency stability. They generate signals based on the natural resonance of a quartz crystal, which is minimally affected by temperature and aging. This stability makes them ideal for applications where a consistent frequency is paramount. However, their frequency is fixed to the natural resonance of the crystal, allowing only limited fine-tuning. IC-based oscillators combine compactness and ease of design, offering integrated solutions that are particularly useful for applications with stringent space or complexity constraints. Despite their simplicity, IC-based oscillators typically operate within a limited frequency range, necessitating careful selection to ensure compatibility with the transducer's resonant frequency.

Choosing the appropriate oscillator involves balancing these considerations against the specific requirements of the application. For example, systems requiring flexibility might benefit from RC or LC oscillators, while those prioritizing stability could favour crystal oscillators. In space-constrained designs, IC-based oscillators may be the most practical choice. Ultimately, the oscillator must be precisely matched to the resonant frequency of the piezoelectric transducer to maximise efficiency and maintain system performance.

Power amplifiers: amplifying the oscillator's signal to a level sufficient to drive the piezoelectric transducer effectively. The choice of power amplifier is critical, as it directly affects the efficiency, signal quality, and overall performance of the system.

Linear amplifiers are a traditional choice for driving piezoelectric transducers due to their ability to produce high-quality, distortion-free signals across a wide frequency range. These amplifiers are well-suited for applications where maintaining the fidelity of the drive signal is paramount, such as in sensitive ultrasonic systems. However, their efficiency tends to be low, especially at higher power levels, as a significant portion of the input power is dissipated as heat. This characteristic makes linear amplifiers more appropriate for systems where input power is abundant or where thermal management can be effectively implemented. In contrast, switching amplifiers, particularly Class E and Class F designs, are highly efficient and are increasingly favoured for ultrasonic energy transmission applications. These amplifiers achieve high efficiency by operating in a switching mode, where transistors act as on/off switches, minimising energy loss during operation. Class E and Class F amplifiers are notable for their ability to amplify high-frequency signals using passive components without requiring external pulse-width modulation (PWM) signals, simplifying their operation. Despite their advantages, the design of switching amplifiers presents unique challenges. Accurate modelling and precise calculations are necessary to ensure that the amplifier's output frequency matches the resonant frequency of the transducer. The use of high-quality, tightly specified components is also essential to minimise losses and maintain frequency accuracy. For example, variations in the characteristics of inductors and capacitors can introduce deviations in the output frequency, potentially reducing the amplifier's efficiency and effectiveness.

Selecting the appropriate power amplifier for an ultrasonic system involves a careful trade-off between efficiency and signal quality, guided by the specific requirements of the application. For low-power, high-precision systems, linear amplifiers may still be preferred. However, for energy-focused applications where efficiency is paramount, switching amplifiers such as Class E and Class F provide a compelling solution, provided their design challenges can be addressed.

In summary, the design of the conversion circuit is a multifaceted process that necessitates a thorough evaluation of power levels, application-specific needs, and environmental conditions. Each subsystem (RF energy acquisition, ultrasonic drive, and energy management) demands tailored designs to optimise efficiency and minimise losses. Through iterative optimisation and the careful selection of components, the conversion circuit can deliver robust performance and high reliability, effectively adapting to diverse application scenarios and operational challenges.

3.3.2.4 Ultrasonic Energy Receiving and Load

The ultrasonic energy receiving circuit is part of the ultrasonic link. This circuit exhibits similarities to its RF energy receiving, incorporating fundamental components such as input impedance matching and rectification. However, a distinguishing factor is the significantly lower operating frequency of ultrasonic link compared to RF link. This difference necessitates adjustments in circuit design while maintaining the shared objective of minimising losses and maximising efficiency. The principles guiding the design of RF energy receiving circuits can provide valuable insights for ultrasonic circuits, with appropriate modifications to account for the frequency characteristics and specific application requirements of ultrasonic energy transfer.

One of the key challenges in ultrasonic energy receiving arises from the discontinuous of ultrasonic energy transmission. This discontinuity directly affects the energy supply at the receiving end, necessitating the design of platform capable of accommodating interruptions. To address this, sensors integrated with ultrasonic energy receivers should either possess power-off storage capabilities or operate intermittently, aligning their activity with the availability of energy. For instance, sensors might perform low-frequency operations such as temperature measurements at hourly intervals or longer, depending on the energy availability.

To further mitigate the effects of discontinuous energy supply, energy management strategies, similar to conversion circuits, can be implemented at the receiving end. By integrating energy storage unit, such as capacitors or batteries, the intermittent energy harvested from ultrasonic transmission can be cached. This stored energy can then be utilised to power the load in a regulated, low-power mode, enabling sustained operation even under interrupted supply conditions. However, this approach imposes stringent constraints on the power consumption of the load, which should be sufficiently low to ensure the practicality of the system. Table 3-7 provides examples of low-power sensors.

Table 3-7. Examples of Low Power Sensors

Model	Type	Voltage range	Sampling rate	Average power consumption	Typical Applications
X7F202	Radar sensor	1.8-3.3 V	2100/s	100 uW	Presence detection
MS1089	Temperature sensor	1.8-3.6 V	1/min	50 nW	Environmental monitoring
MS8891A	Capacitive sensor	1.8-4.5 V	2/s	1.3 uW	Human body detection
BMA400	Accelerometer	1.2-3.6 V	25/s	26 uW	Alarm system
BMP280	Pressure sensor	1.2-3.6 V	1/s	4.5 uW	Weather forecast

It is worth noting that although the average power consumption of the sensors shown is very low, auxiliary circuits including data reading and storage circuits and data transmission circuits are required to ensure sensor operation, which requires additional energy.

3.4 System Assembly

System assembly comprehensively integrates all hybrid wireless energy transmission system components into a compact and coherent structure. This process is not merely a physical arrangement of parts, but a critical phase that ensures functional compatibility, electrical integrity, and system-level performance. Effective assembly enables smooth energy transfer across different subsystems, laying the foundation for system stability and efficiency.

A key consideration in the assembly process is aligning electrical characteristics, particularly the input and output voltage and current ranges of interconnected components. For example, the rectifier's output voltage must fall within the acceptable input range of the subsequent power management or energy storage module. Mismatches in these parameters can lead to electrical stress, component failure, or inefficient operation. Therefore, precise electrical matching is essential to safeguard system reliability and maintain optimal power transfer efficiency.

Given that each subsystem offers multiple configuration options, the assembly stage provides the flexibility to tailor component selection and matching based on specific application requirements and operating modes. This modularity allows the system to be adapted for various use cases while maintaining high efficiency and performance.

Due to the inherently limited power in wireless energy transmission systems, the assembly process must prioritise low power consumption and high conversion efficiency. These considerations are essential to supporting long-distance transmission, ensuring stable energy delivery, and providing sufficient power for the target application.

Figure 3-54 presents an overview of the system's primary components, illustrating the key parameters, energy flow directions, and optional configurations involved in the assembly. This schematic serves as a framework for understanding the functional relationships between subsystems and guiding the design of a robust and efficient wireless energy transmission platform.

In addition to the core components, the system must integrate auxiliary protection circuits, such as overvoltage and overcurrent safeguards. These protective features are critical for preventing damage caused by transient electrical events or configuration mismatches during operation.

The intended application environment and energy transmission characteristics should inform component selection. For example, in the ultrasonic energy transfer (UET) link, the energy management unit at the receiving end may be omitted if the load operates synchronously with the inherently discontinuous energy supply， which eliminates the need for intermediate energy storage or voltage regulation, simplifying the system design and reducing losses.

Overall, this flexible and modular approach to system assembly ensures that the final configuration can be optimised for performance, reliability, and cost-effectiveness across various application scenarios. By addressing core operational needs and necessary protective measures, the assembly process forms a solid foundation for deploying practical and scalable wireless energy transmission systems.

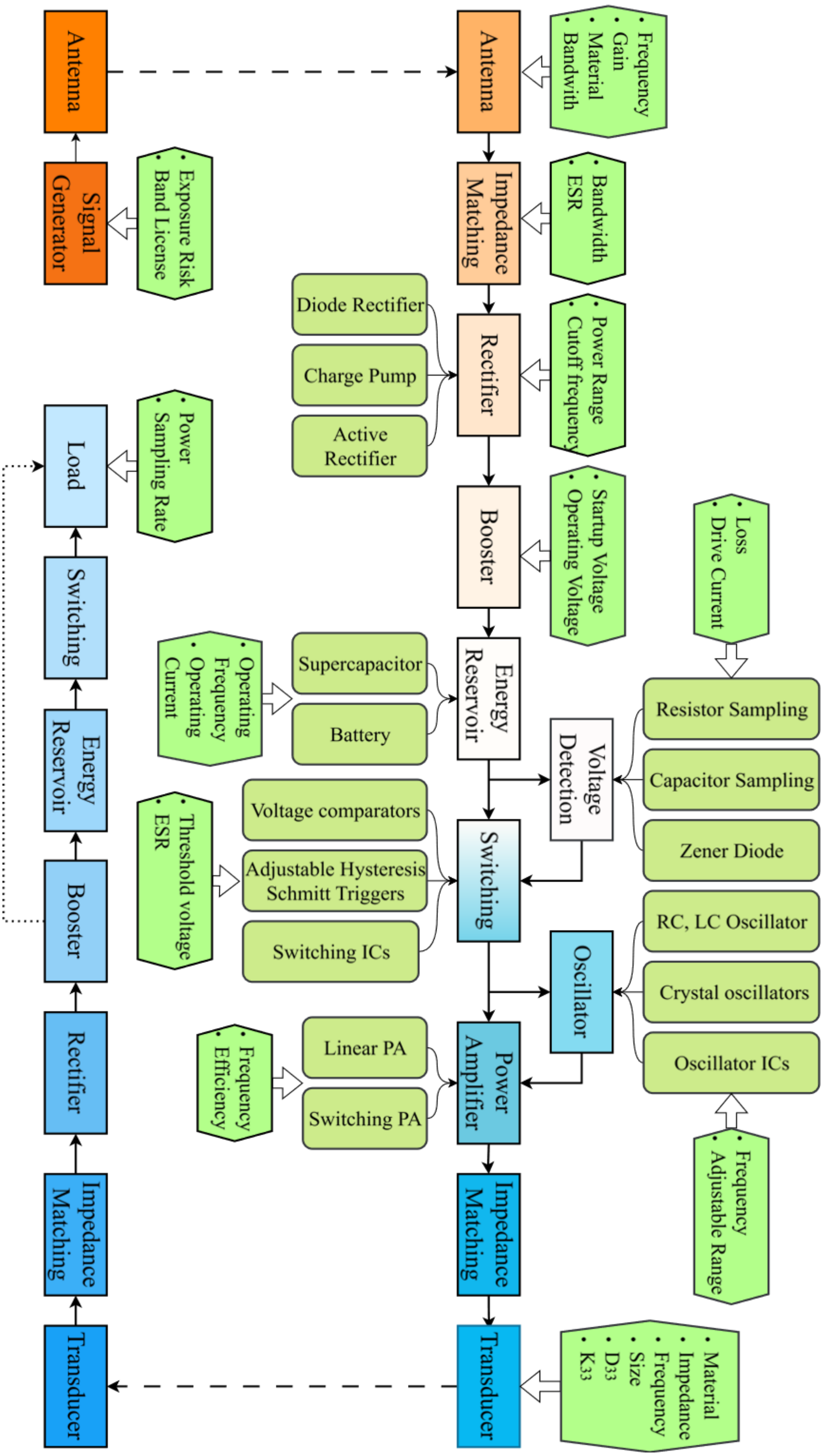

Figure 3-54. System assembly flow chart of the main components, including component options and key parameters.

3.5 Summary

This chapter presents the design and implementation of the CRFU-WPT system. The proposed system aims to address the limitations of single-mode WPT by integrating the complementary strengths of RF and ultrasonic energy transmission pathways within a unified and adaptive architecture.

The system architecture was developed around three core modules: the RF link, the conversion circuit, and the ultrasonic link. Each module was modelled and analysed individually using a link loss approach, enabling the quantification of energy dissipation across the transmission chain. This modular modelling strategy supports a precise system performance evaluation and facilitates scalability, optimisation, and predictive power budgeting.

The system design process followed reverse energy flow logic, beginning with the load requirements and tracing backwards to determine the specifications of the ultrasonic and RF transmission stages. This method ensures that all components—from ultrasonic drivers to RF transmitters—are aligned with the power demand of the end application. Particular attention was given to sub-circuit design, energy management integration, and parameter compatibility across transmission domains.

During the assembly phase, practical integration considerations such as overvoltage and overcurrent protection, frequency band regulations, and RF exposure limits were addressed to ensure operational safety and reliability. The compact, modular structure of the system enhances its adaptability for diverse applications, including industrial monitoring in metal enclosures, biomedical implants, and distributed sensor networks operating in structurally or electromagnetically challenging environments.

Overall, the CRFU-WPT system demonstrates a robust and scalable solution for wireless energy transfer in heterogeneous and constrained settings. The systematic design framework established in this chapter lays the groundwork for further development, enabling both near-term prototyping and future enhancements in control algorithms, miniaturisation, and energy efficiency.

4 System Test Result and Discussion

4.1 Introduction

The CRFU-WPT system is a hybrid wireless power transfer architecture integrating RF-WPT and U-WPT technologies. This chapter comprehensively evaluates the system's performance through a series of targeted experiments and analyses. The testing process focuses on validating the theoretical models and assessing the functional efficiency of the core subsystems.

First, the RF link tests are conducted to verify the electromagnetic energy transmission model. These experiments analyse the link performance under varying environmental conditions, quantify loss mechanisms, and identify dominant factors affecting transmission efficiency. Based on the findings, strategies for minimising RF link losses are proposed.

Next, the ultrasonic link tests evaluate the accuracy of the acoustic energy transmission model. The experiments investigate transmission losses across different propagation media and transducer configurations, highlighting critical factors such as acoustic impedance mismatches, attenuation, and transducer performance. Corresponding mitigation techniques are suggested to improve link reliability and power transfer efficiency.

Subsequently, the conversion circuit tests examine the performance of key functional modules, including the rectifier, boost converter, conversion controller, oscillator, and power amplifier. These modules are assessed according to the system architecture to ensure that they collectively support stable and efficient energy conversion throughout the transmission pathway.

Finally, a practical case study is presented, in which the CRFU-WPT system is deployed to wirelessly power a Bluetooth Low Energy (BLE) device. This application scenario demonstrates the system’s real-world feasibility, stability, and adaptability for low-power wireless sensor networks.

4.2 RF Link Test

RF link testing primarily involves validating the energy transfer model of the RF link and analysing the effects of different frequencies and gain levels.

Due to the inability to replicate long-distance outdoor transmission conditions in the laboratory, the RF link test is conducted in two environments: an anechoic chamber and a corridor. To accommodate the size and portability requirements of the test antenna, a wideband antenna with a frequency range of 8-12 GHz is used to evaluate the performance of the RF link across various frequencies and gain levels. The test setup is illustrated in Figure 4-1.

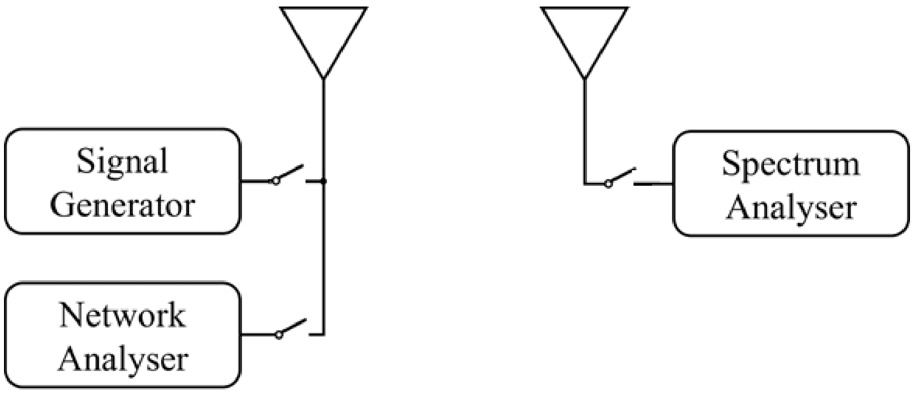

Figure 4-1. Schematic diagram of RF link test including transmitting antenna and receiving antenna, signal generator, network analyser and spectrum analyser. The test environment is an anechoic chamber and corridor.

When testing in a darkroom, plug in a network analyser. When testing in a hallway, plug in a signal generator and a spectrum analyser.

4.2.1 The RF Link Experimental Setup

Experimental tests were conducted in two distinct environments to validate the RF link transmission model: an anechoic chamber and a typical indoor corridor. These tests assessed the model's accuracy under controlled and reflective conditions. The experimental setup used for both scenarios is illustrated in Figure 4-2.

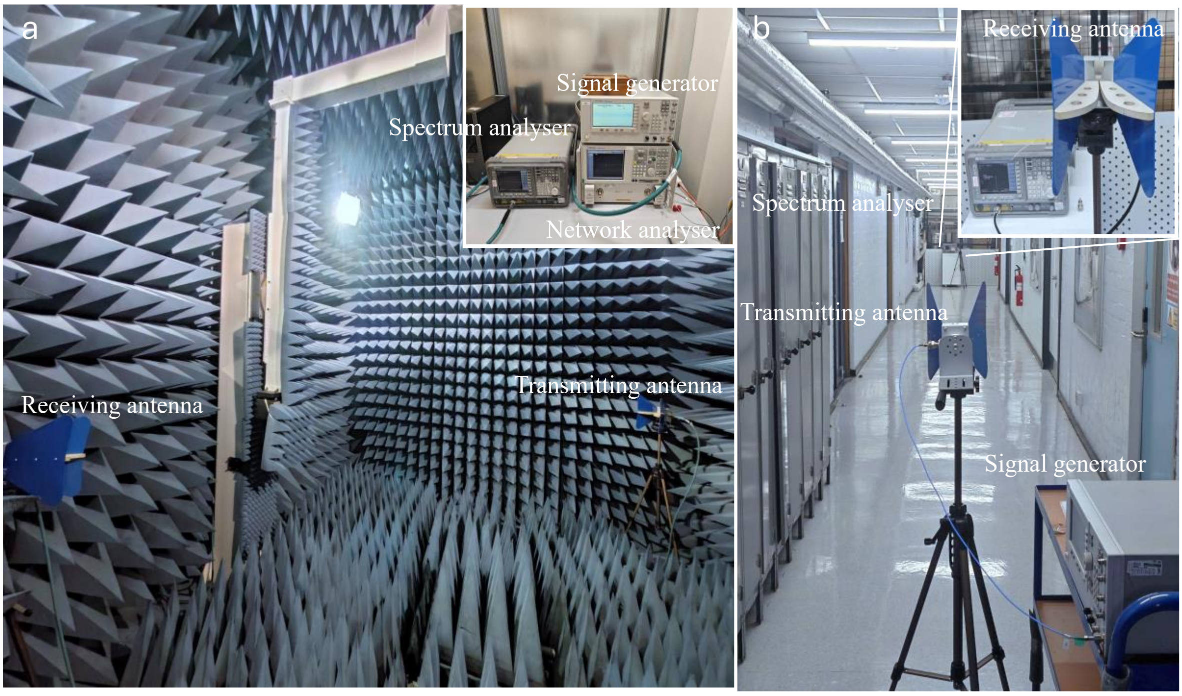

Figure 4-2. The RF link test setup diagram is in an anechoic chamber experiment (a) and in a corridor experiment (b).

Figure 4-2 illustrates the RF link test setup, showcasing two distinct experimental environments: the anechoic chamber and a corridor. The anechoic chamber experiment provides a controlled environment with minimal electromagnetic interference and reflections, enabling accurate assessment of RF signal propagation, power transmission efficiency, and antenna performance. In contrast, the corridor experiment simulates a real-world scenario with reflective surfaces and environmental interferences, providing insights into the system's performance under practical conditions. This dual-environment approach ensures a comprehensive evaluation of the RF link, balancing ideal conditions with realistic application scenarios.

For the convenience of testing, the antenna uses a wide bandwidth dual-ridged horn antenna (PowerLOG® 70180). The transmitting antenna is powered by the signal generator (Agilent Technologies Model E8257D), while the receiving antenna's output is connected to a spectrum analyser (Agilent Technologies Model HP/E4404B). A network analyser (Agilent Technologies Model E8362B) is used to detect the centre frequency and reflection coefficient. Since the antenna, signal generator, network analyser and spectrum analyser with the50-ohm impedance ports, no impedance matching network is required. Table 4-1 is the antenna frequency test points and the corresponding gains.

Table 4-1. Antenna test point frequency and gain.

Test point	Frequency (GHz)	Gain (dBi)
1	2.0	7.8
2	2.5	8.4
3	3.0	9.8
4	3.5	9.6
5	4.0	10.2

In the anechoic chamber, antennas were positioned at both ends to gather data on the impact of different frequencies and gain levels on the RF link. In the corridor, antennas were placed at varying distances to evaluate the effect of distance on the RF link performance.

4.2.2 The RF Link Result

The RF link was evaluated through experimental measurements conducted in an anechoic chamber and a corridor environment, using a wide-bandwidth antenna to validate the RF transmission model and investigate the relationship between input and output power. In the anechoic chamber, the power relationship was analysed across a range of frequencies to eliminate the influence of environmental reflections and isolate intrinsic link characteristics. In the corridor setup, measurements focused on assessing the effect of transmission distance on power performance, accounting for multipath propagation and environmental attenuation. These tests provided comprehensive insight into RF link behaviour under controlled and realistic conditions.

First, based on the experimental setup, the S-parameters of the test antenna are characterised to evaluate its performance. These parameters, particularly the reflection coefficient (S_{11}), provide crucial insights into the antenna's impedance matching and transmission characteristics. Analysing the S-parameters to assess the efficiency and compatibility of the antenna within the RF link model, ensuring accurate correlation between experimental results and theoretical predictions. Figure 4-3 shows the reflection coefficient results of the antenna.

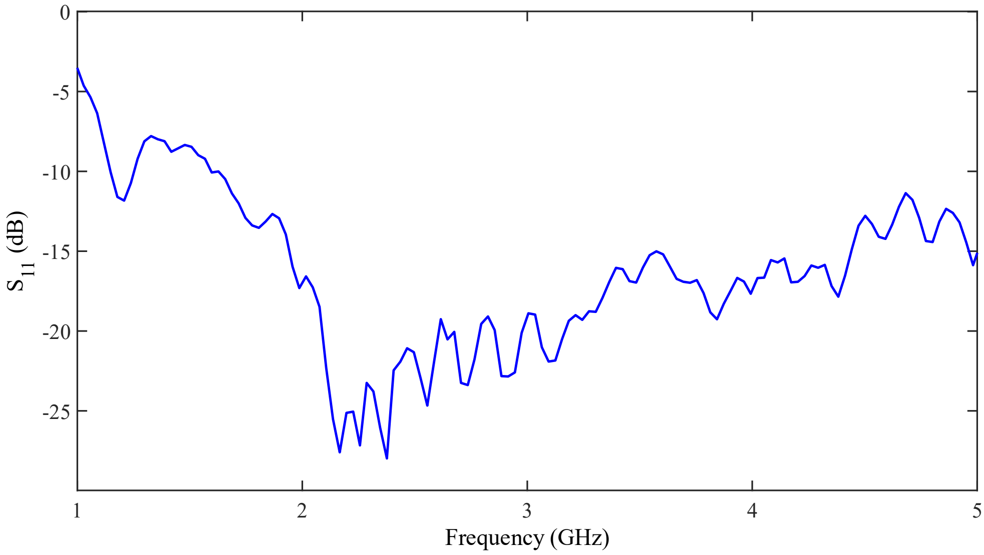

Figure 4-3. The S-parameter results of the antenna, particularly within the 2 to 4 GHz frequency range selected for the experimental setup.

Since the test antenna is a wideband design, the 2-4 GHz frequency band was selected for the anechoic chamber experiment. The S11 results indicate that the antenna achieves a reflection coefficient of less than -15 dB across this range, signifying excellent impedance matching. This level of performance ensures minimal power reflection, which is essential for accurate testing and reliable energy transfer in the RF link model.

The energy transmission performance of the antenna across different frequencies was evaluated in an anechoic chamber, with the results presented in Table 4-2. These measurements demonstrate the relationship between frequency and transmitted power, providing the effect of different frequencies on energy transmission.

Table 4-2. RF link loss test results in an anechoic chamber

Test point	Frequency (GHz)	Model value (dB)	Test value (dB)	Error (dB)
1	2.0	34.96	36.77	1.81
2	2.5	35.64	37.48	1.84
3	3.0	34.51	36.37	1.86
4	3.5	36.26	38.11	1.85
5	4.0	36.37	38.17	1.80

Where: the model value is calculated using the RF link outdoor suburban model.

Due to limitations in laboratory conditions, an anechoic chamber was used to emulate an open-field environment for testing the RF link loss across a range of frequencies. The measured RF link loss values were consistently higher than those predicted by the theoretical model; however, the deviations remained small and exhibited a stable trend. This indicates that the measured data reliably follow the theoretical prediction regarding trend and variation.

The primary source of the discrepancy is attributed to a systematic error arising from the difference between the nominal antenna gain specified in the datasheet and the actual gain observed in the experimental setup. Additionally, as antenna gain varies with frequency, removing the gain factor from the analysis reveals a clear trend: RF link loss increases with frequency. This observation is in agreement with the theoretical expectations described by Equations (3-7) and (3-8), further validating the model's predictive capability.

The antenna was positioned in a corridor to simulate an indoor application environment, and the RF link loss at 2.5 GHz was evaluated over varying transmission distances up to 10 metres. This setup aimed to assess the performance of the RF link under conditions representative of indoor environments. The measured link loss as a function of transmission distance is presented in Figure 4-4.

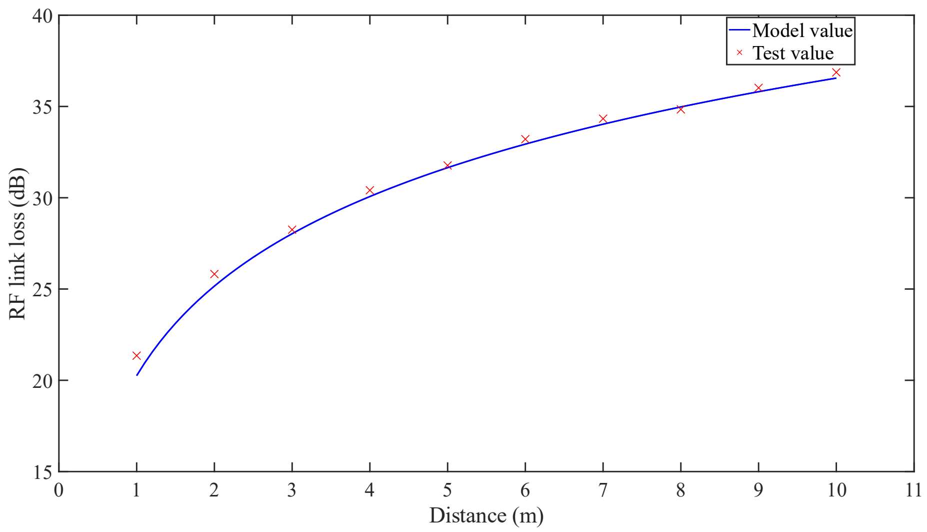

Figure 4-4. Comparison between modelled and measured RF link loss values over distance in an indoor corridor environment. The blue curve represents the theoretical model values, while red crosses indicate the corresponding measured values.

As shown in the figure, the RF link loss increases with distance, but the rate of increase gradually decreases as the distance grows. The measured data points closely follow the theoretical predictions of the indoor corridor model, with only minor deviations. These discrepancies can be primarily attributed to environmental factors such as wall reflectivity variations and objects along the corridor, which introduce additional multipath effects.

Despite these minor differences, the overall alignment between the experimental results and the model validates the applicability of the corridor-based RF link model for predicting path loss in similar indoor settings. Consequently, the model offers a reliable foundation for system-level design and performance estimation in constrained indoor environments.

4.2.3 Optimal Energy Transfer and Reduction of Loss

Optimal RF energy transfer and loss mitigation are essential for maximising energy efficiency in wireless power transfer (WPT) systems. Several key factors influence RF energy transfer performance, including impedance matching, antenna gain, operating frequency, and spatial configuration.

Impedance matching ensures maximum power transfer between the transmitter and receiver. According to the RF link model (Equation 3-1), proper impedance matching minimises the reflection coefficient, thereby reducing electrical losses. In the presented setup, the tested antenna and the signal source are designed with an impedance of 50 ohms, ensuring effective impedance matching and thus reducing reflection-related inefficiencies. Antenna gain also plays a vital role in efficient RF energy transmission. High-gain antennas, particularly those capable of beamforming, can concentrate the radiated energy in a specific direction, reducing link loss as described in Equation 3-5. This directional focus improves energy delivery efficiency and mitigates unnecessary radiation in undesired directions. Operating frequency must be selected carefully, as it directly affects propagation characteristics and link loss. While higher frequencies can support smaller antennas and wider bandwidths, they also result in increased path loss, as indicated by Equations 3-7 and 3-8. Thus, frequency selection involves a trade-off between system miniaturisation and transmission efficiency. In addition to these parameters, reducing the physical distance between the transmitting and receiving antennas and employing directional antennas can further enhance energy concentration and minimise propagation losses.

In summary, achieving efficient RF energy transfer and minimising associated losses requires a holistic approach combining precise impedance matching, strategic antenna selection, frequency optimisation, and spatial alignment. These measures improve system performance and reliable power delivery in RF-based WPT applications.

4.3 Ultrasonic Link Test

Ultrasonic link testing primarily involves validating the energy transmission model of the ultrasonic link and assessing the effects of different transducers and transmission media on its performance.

The ultrasonic energy transmission model was benchmarked by investigating the effects of transducers with different frequencies and sizes on energy transmission. The transmission media tested include three materials with significant density differences: air, water, and 6082 aluminium alloy. The test setup is illustrated in Figure 4-5.

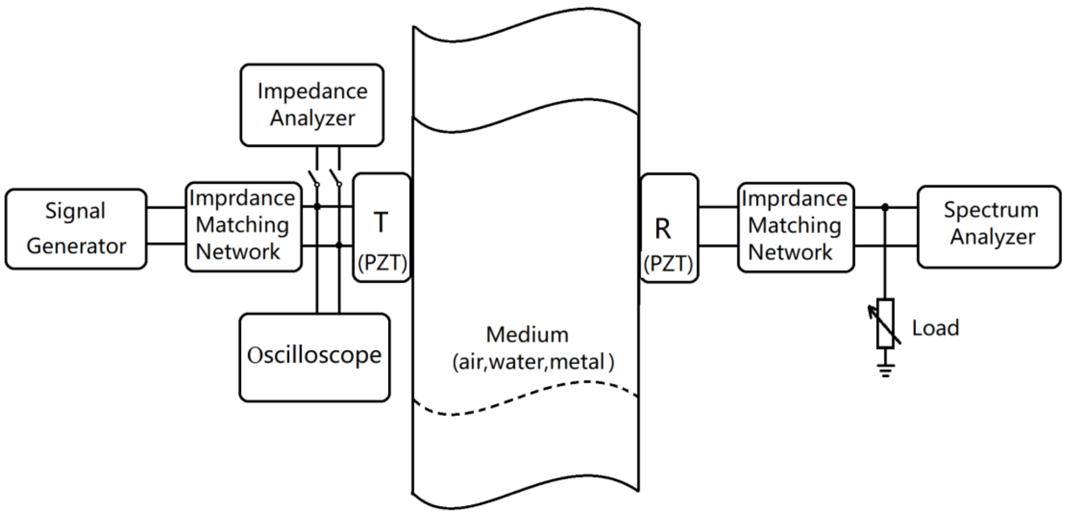

Figure 4-5. Experimental setup for U-WPT performance evaluation across different transmission media (air, water, and metal).

U-WPT system test including signal generator, impedance matching networks, transmit transducer (T), transmission medium (air, water or metal), receive transducer (R), and spectrum analyser (from left to right). An impedance analyser and a spectrum analyser are used to measure the input and output impedance of the T and R transducers, respectively. An oscilloscope is used to monitor the input voltage.

4.3.1 The Ultrasonic Link Experimental Setup

Experimental tests were carried out to validate the UET model and the corresponding transmission framework developed in this study. The experimental system and setup are illustrated in Figure 4-6, showing the key components and configurations used to assess model accuracy under practical operating conditions. These tests aimed to confirm theoretical predictions and evaluate the system's performance across different media and transmission distances.

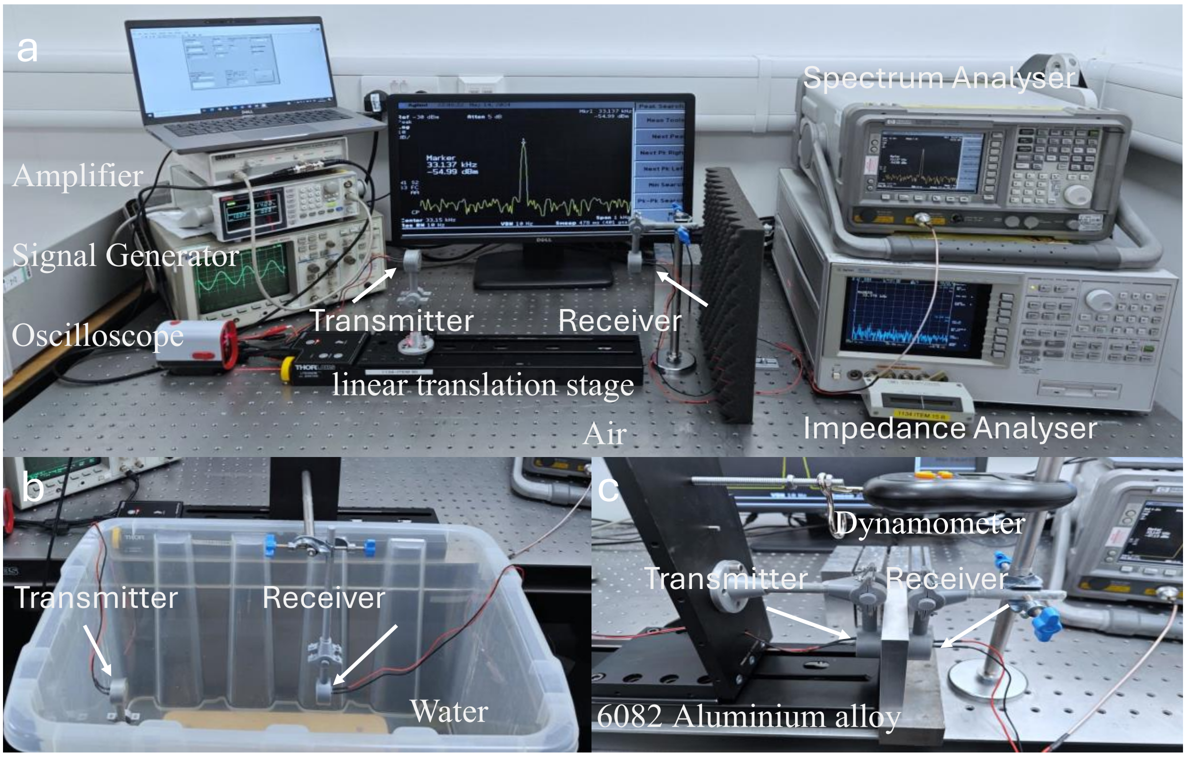

Figure 4-6. Experimental setups for verifying the transmission model for three different scenarios air (a), under water (b), and metal (c).

An AFG-21005 function generator and a WA301 power amplifier were used to drive the transducer transmitter. The amplifier had a maximum output peak-to-peak voltage of 30 V and an output impedance of 50 Ω. The output voltage of the transducer in different media was monitored using an HP-54600B oscilloscope. The resonant frequency and impedance of the transducer in various media were measured using an Agilent 4294A impedance analyser. Additionally, an HP-E4404B spectrum analyser, with a 50 Ω input impedance, was employed to measure the output power from the receiving transducer.

Table 4-3 shows the parameters required for the test system [190].

Table 4-3. The parameters used in the UET test.

Material	Parameters	Unit	Value
Air	density	kg/m^3	1.29
	sound velocity	m/s	343
	acoustic impedance	$10^6 \times kg/m^2\,s$	0.0034
Water	density	kg/m^3	997
	sound velocity	m/s	1497
	acoustic impedance	$10^6 \times kg/m^2\,s$	1.49
Aluminium	density	kg/m3	2700
	sound velocity	m/s	6420
	acoustic impedance	$10^6 \times kg/m^2\,s$	17.33
Transducer A	frequency	kHz	40
	diameter	mm	18
	acoustic impedance	$10^6 \times kg/m^2\,s$	30.8
Transducer B	frequency	kHz	33
	diameter	mm	25
	acoustic impedance	$10^6 \times kg/m^2\,s$	30.8

Two types of ultrasonic transducers were used for testing: transducer A is MCUSD18A40S09RS-30C from Multicomp, and transducer B is 328ET/R250 from Pro-Wave Electronic Co., Ltd.

Transducer A was used both as a transmitter and receiver (T/R), while transducer B operated as an independent transmitter (T) and receiver (R). The transducer is rigidly mounted to the test platform via a 3D-printed bracket to ensure compliance with the infinite plane piston model for the transducer. A linear translation stage (LTS) rail from Thorlabs, Inc. was used to vary the distance between the transmitting and receiving transducers.

The transmission media examined in this study included air, water, and 6082 aluminium alloy. For air, the testing distance ranged from 0 mm to 290 mm with a step size of 0.1 mm. Since the wavelength of a 40 kHz ultrasonic wave in air is about 8.58mm, considering the reflection of 1/4 wavelength, the test step is set to 0.1mm to accurately capture sound waves' reflection and interference results. It controls the movement of the transducer, and its minimum repeatable incremental movement is 4 μm.

The same distance range was tested in water, but with a step size of 1 mm. For aluminium, due to the challenges associated with modifying the metal's thickness and the actual requirements of metal penetration applications, the tests were conducted at fixed distances of 5 mm, 10 mm, 15 mm, 20 mm, 25 mm, and 30 mm.

4.3.2 The UET Link Loss Measurement

4.3.2.1 For Electrical Loss

Electrical losses arise from impedance mismatches between the driving source and the ultrasonic transducer, based on the electrical reflection model. The test procedure includes measuring the transducer's impedance in various application environments and the driver circuit. The driving source, consisting of a signal generator and power amplifier, is set with a standard impedance of 50 ohms. Notably, the impedance of the transducer varies with changes in the application environment. Therefore, the first step is to measure the transducer's impedance under different environmental conditions. The impedance responses of two ultrasonic transducers were tested in three transmission media. Impedance is mainly influenced by the pressure exerted on the transducer's surface by the transmission medium: in air and water, this pressure varies with height, while in the metallic medium, it is affected by the force exerted on both ends of the transducer.

Given that changes in atmospheric pressure are minimal and difficult to measure in the laboratory, the experiment focused on the impedance variation in water and aluminium mediums. The pressure on the transducer's surface was altered by adjusting the depth of the transducer in water and by adjusting the force applied in the aluminium medium.

4.3.2.2 For Transducer Loss

Using the transducer impedance test results, the resonant frequency (f_m) and anti-resonant frequency (f_n), were identified, and the electromechanical coupling coefficient (k_d^2). was calculated using the equation (3-18). To measure transducer losses, the transmitting and receiving ends were directly connected to create a medium-free energy transmission channel. The correction factors for transducer losses were determined by comparing the transmitted and received energy, while accounting for electrical losses.

4.3.2.3 For Acoustic Loss

Acoustic loss, primarily boundary loss. It can be calculated using equation (3-19) according to the material parameters, including density, acoustic velocity, and acoustic impedance. Since the transducer's packaging is made of aluminium, its acoustic parameters match those of aluminium.

4.3.2.4 For Medium Loss

Medium loss was measured by varying the transmission distance, following the transmission models in equations (3-36, 3-37), or by analysing the relationship between transmitted and received power. As medium loss is influenced by constructive and destructive interference, this test was combined with transmission distance analysis. The test distances and step sizes were set according to the wavelength of ultrasonic waves in different media.

4.3.3 The Ultrasonic Link Result

This section presents the UET results comparing model predictions with experimental observations. The UET models were validated in different media and with two piezoelectric transducers (A and B).

4.3.4 Impedance Variations Across Medium

While the transducer's impedance remains stable in air, its characteristics change significantly when used in different environments. Figure 4-7 and Figure 4-8 illustrate the impedance characteristics of transducer A(T/R) and transducer B(T) and B(R) in various media.

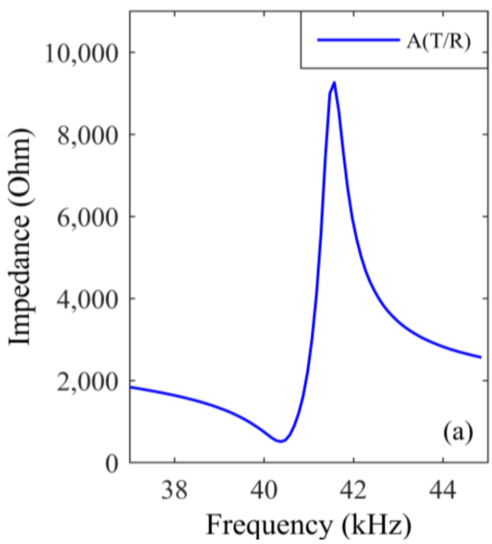

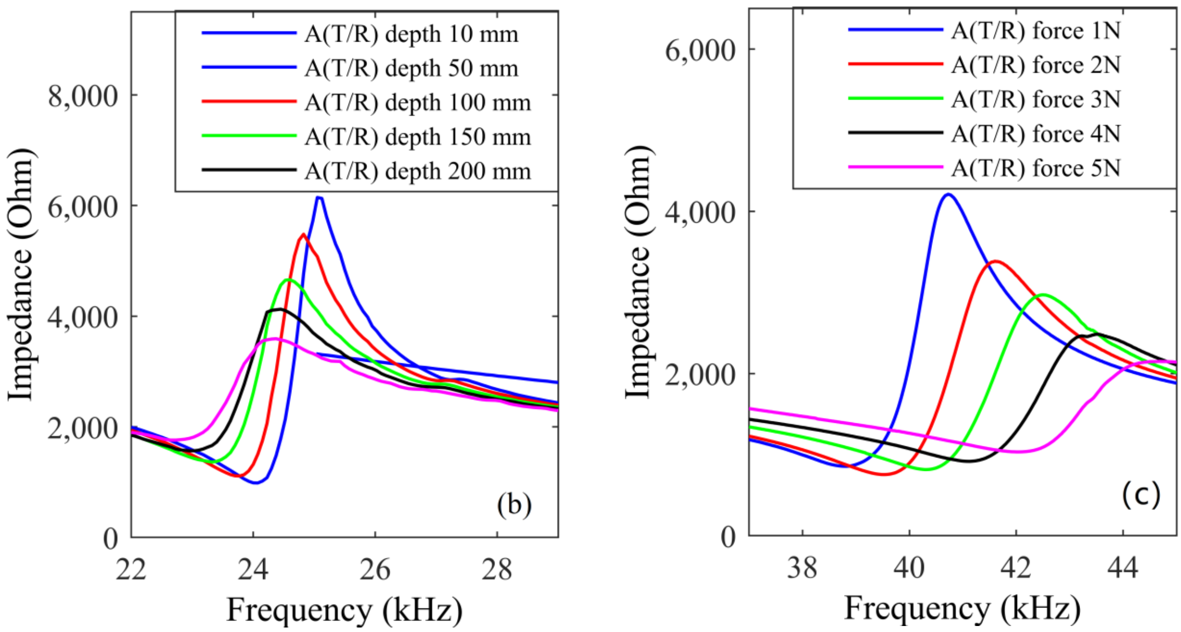

Figure 4-7. The impedance characteristics of transducers A for air (a), water (b), and aluminium(c). The air test condition was set at the laboratory ambient atmospheric pressure and 25 °C. For water, the transducer was submerged at depths of 10 mm, 50 mm, 100 mm, 150 mm, and 200 mm, respectively. For aluminium, the pressure applied at both ends of the transducer, with values of 1 N, 2 N, 3 N, 4 N, and 5 N, respectively.

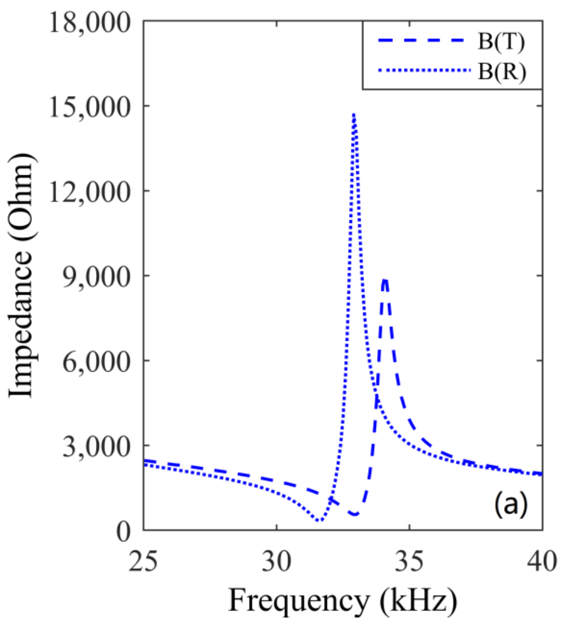

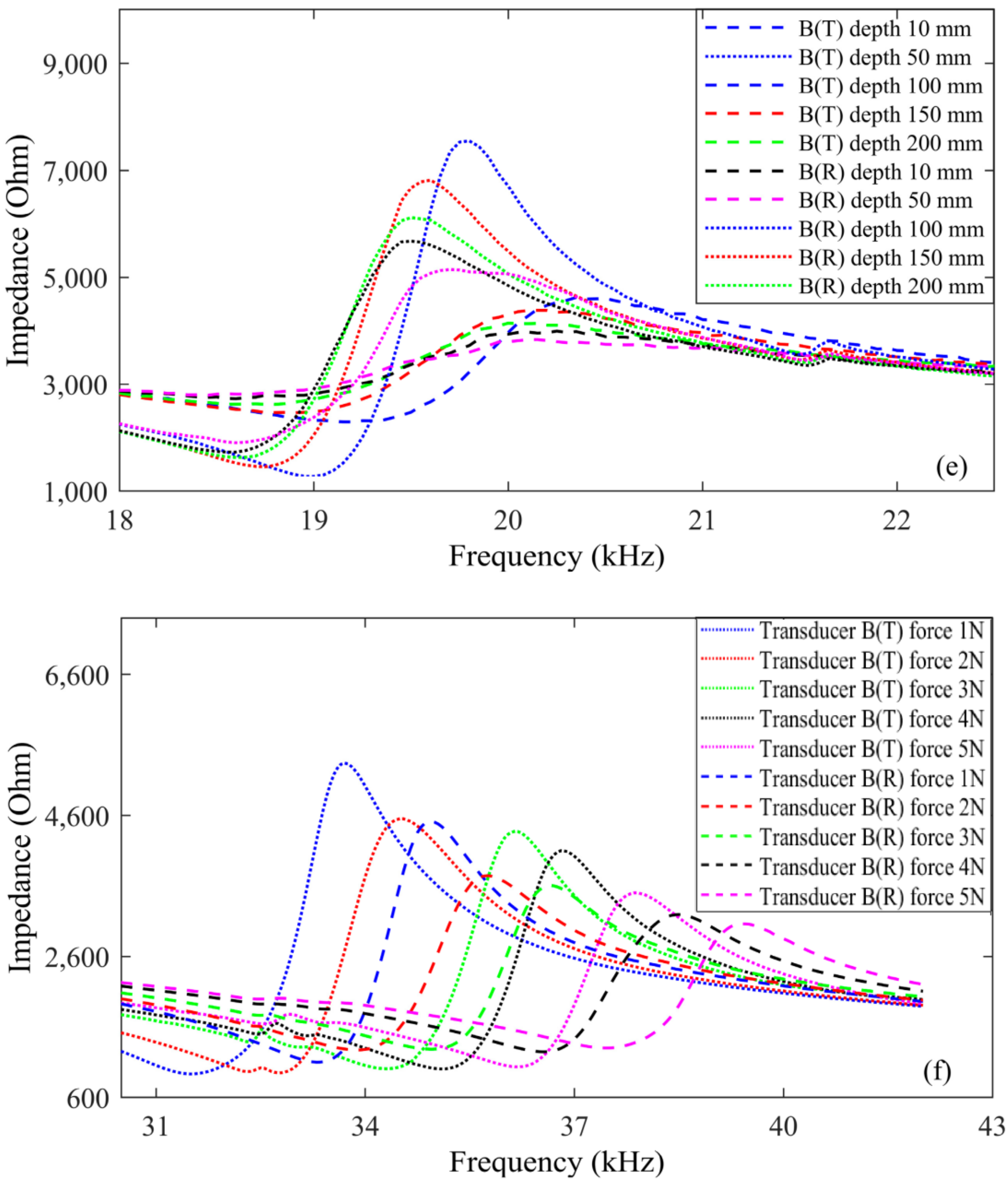

Figure 4-8. The impedance characteristics of transducers B for air (a), water (b), and aluminium (c). The air test condition was set at the laboratory ambient atmospheric pressure and 25 °C. For water, the transducer was submerged at depths of 10 mm, 50 mm, 100 mm, 150 mm, and 200 mm, respectively. For aluminium, the pressure applied at both ends of the transducer, with values of 1 N, 2 N, 3 N, 4 N, and 5 N, respectively.

The resonant frequency and impedance of the transducer change based on the environment, influenced by the pressure on the transducer surface. For air, this pressure is governed by atmospheric conditions, while for water, it depends on immersion depth, and for metal, it is influenced by the applied force. The result for the impedance of transducer significant variations was observed in water and aluminium.

For air Figure 4-7 (a), Figure 4-8 (a) show the performance of the transducer under laboratory conditions. In practical applications, the condition that affects atmospheric pressure is altitude. Since altitude cannot be significantly changed in the laboratory, only the test results under laboratory conditions are shown.

For water, Figure 4-7 (b) and Figure 4-8 (b)show the performance of the transducer underwater. Increasing depth decreases the transducer's resonant frequency, increases its minimum impedance, and decreases its maximum impedance. Environmental changes can cause frequency and impedance mismatches, which in turn impact both electrical and transducer losses in the link.

For aluminium, Figure 4-7 (c) and Figure 4-8 (c) show the performance of the transducer attached to aluminium. Increasing the force on the transducer significantly raises its resonant frequency, slightly increases the minimum impedance, and markedly reduces the maximum impedance. Similarly, changes in the application environment alter the transducer's resonant frequency and impedance, leading to variations in both electrical and transducer losses in the link.

Overall, for transducers operating under different environmental conditions, calculating the losses individually based on the model improves its accuracy compared to models that do not account for link loss. In addition, the results also show that in order to ensure the matching of the frequency and impedance of the system, it is necessary to adjust the frequency and impedance matching network of the driving source according to the resonant frequency and impedance of the actual application, rather than relying on a driving source with a fixed frequency and fixed impedance matching network.

4.3.5 The UET Link Loss

Table 4-4 presents the calculated electrical, transducer, and acoustic losses for the transmitting and receiving transducers under specific conditions, including a 150 mm water depth and a 5 N preload on the aluminium interface. These values are based on the system model and verified by impedance measurements. Electrical loss results from circuit dissipation and impedance mismatch. Transducer loss is due to inefficiencies in electromechanical conversion, while acoustic loss represents the attenuation of ultrasonic waves during transmission through the medium.

Table 4-4. Link losses of different media.

Loss(dB)	Transducer	Air	Water (Depth = 150 mm)	Aluminium (Force = 5 N)
Electrical Loss	B (T)	5.19	11.49	5.65
	B (R)	15.54	10.27	18.86
	A (T/R)	4.88	9.21	4.37
Transducer Loss	B (T)	10.33	6.20	11.37
	B (R)	9.79	7.89	10.13
	A (T/R)	11.25	8.10	10.22
Acoustic loss	B (T)	33.55	5.35	0.35
	B (R)	33.55	5.35	0.35
	A (T/R)	33.55	5.35	0.35

Note: The driving source and load impedance were set to 50 Ω. Water tests were conducted at a depth of 150 mm, while a force of 5 N was applied in the aluminium tests.

In a fixed application environment, the system's three losses remain constant. Electrical loss is primarily determined by the impedance of both the signal source and the transducer. When the application environment changes, variations in electrical loss occur due to changes in the transducer's impedance. For example, the transducer's impedance experiences greater fluctuations underwater than when applied to aluminium. As a result, the electrical loss underwater is more pronounced than that observed with aluminium, especially when compared to the loss in air. While the inherent transducer loss of the transducer is governed by its performance characteristics, environmental factors still influence the magnitude of these losses. For instance, the transducer's loss differs between air and water, though the variation is relatively small.

Conversely, acoustic losses vary significantly across different transmission media, such as air, water, and aluminium, primarily due to their vastly different acoustic impedances. Acoustic impedance increases with the density and sound velocity of the medium, resulting in higher transmission efficiency in denser materials. While coupling agents are commonly used in ultrasonic applications to minimise impedance mismatches, they also contribute to energy dissipation in ultrasonic energy transmission (UET) systems, such as heat. Additionally, surface irregularities or imperfections at the transducer-metal interface can create air gaps, further increasing acoustic losses beyond theoretical estimates.

In an idealised free-field environment without reflections or interference, the transmitted energy decreases nonlinearly with increasing distance. This attenuation is strongly influenced by the medium's acoustic properties and the operating frequency of the ultrasonic signal.

In practical applications, reflections are inevitable, even in an anechoic chamber. These reflections introduce interference, as illustrated in Figure 4-9, which shows the predicted and measured results of received power across three different media at various distances.

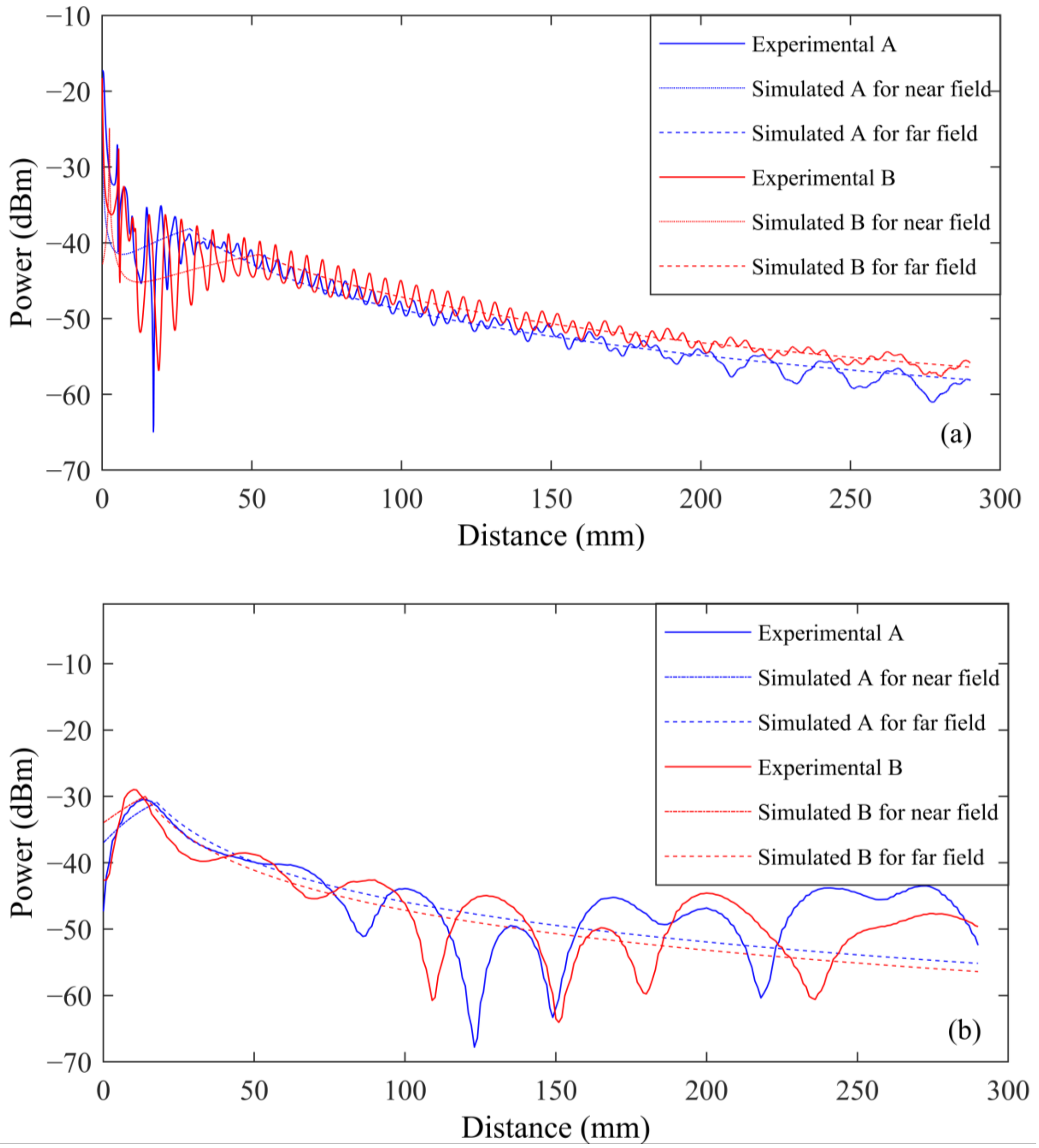

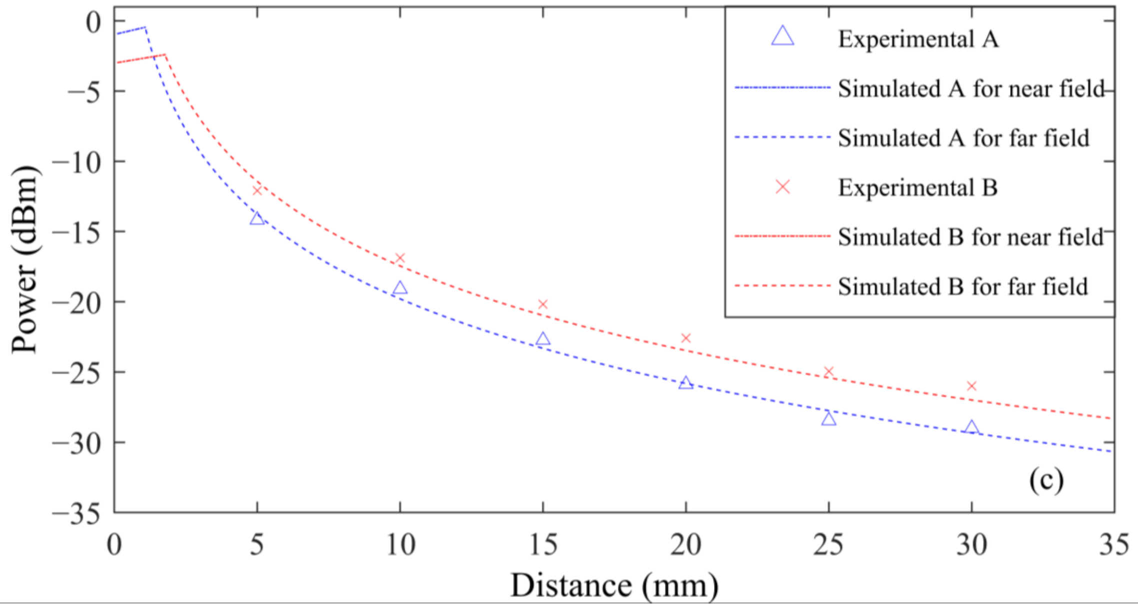

Figure 4-9. Transducer energy transmission test results for three transmission media: (a) air, (b) water, and (c) metal. In the setup, the transmitter is fixed at one end and driven by a 20 dBm source. Meanwhile, the receiver is fixed on the other end and connected to a spectrum analyser. The results were recorded by sampling at different transmission distances.

As the transmission distance increases, the energy received by the transducer decreases, aligning with the model. However, interference causes energy fluctuations with peaks and troughs.

In the air, reflections from the receiver's surface generate interference at 1/4 wavelength intervals. The predicted values from the model align well with the experimental results. However, for transducer A, when the transmission distance is less than 29 mm, the transmission operates in the near field, resulting in a larger discrepancy between the predicted and measured values. At transmission distances exceeding 200 mm, the measured values fall below the predicted values, primarily due to the reduced energy received. Similarly, for transducer B, when the transmission distance is less than 47 mm, the near-field effect causes a significant error between the test and predicted values. For distances greater than 250 mm, the measured values are lower than the predicted values, again attributed to low received energy.

In water, when the transmission distance is less than approximately 16 mm, the system operates in the near field. In water, the ultrasonic wavelength of transducer A is 61.8 mm, and that of transducer B is 82.4 mm. However, the test water tank is limited in size, measuring only 370 × 160 × 220 mm, resulting in significant energy reflections from the tank walls. These reflections lead to multiple wave interferences, causing irregular peaks and troughs. As the receiver approaches the water tank wall, the reflected energy increases, introducing significant errors in the test results, particularly when the transmission distance exceeds 200 mm. The discrepancies between the test and predicted values are primarily constrained by the limited size of the water tank, but the overall trend is in line with expectations.

In aluminium alloys, the model employs a correction factor to correct errors resulting from metal surface roughness and air gaps. Moreover, due to the short transmission distance in the metal medium and the high energy levels at the receiver, the difference between the measured and predicted values is minimal.

The model's predicted trends align with the measured trends across all three media. In order to quantitatively evaluate the models, an error analysis is performed. The error analysis technique is a mean relative average error. The average error can be calculated as:

$$e = \sqrt{\left(\frac{1}{N}\sum_{i=1}^{N}\left(\frac{X_{Ei} - X_{Si}}{X_{Si}}\right)\right)^2} \times 100, \tag{4-1}$$

in which, X_{Ei} is the experimental value, and X_{Si} is predicted simulation value. N is the number of elements. It is worth noting that the calculated average error value is decided by the effective test range for different media. For air, transducer A's calculated range is from 29 mm to 200 mm, and transducer B's calculated range is from 47 mm to 250 mm. For water, the calculated range is from 21 mm to 200 mm, and transducer B's calculated range is from 20 mm to 200 mm. For aluminium, only six points were calculated.

Error analysis was performed for all the results presented in this section. The purpose is to quantitatively validate the models by calculating the percentage error between experimental and theoretical results, providing a clear metric for evaluating the proposed method. The summarized error analysis is shown in Table 4-5

Table 4-5. Error analysis for different media.

Medium	Transducer	Average Error
Air	A	2.54%
	B	3.11%
Water	A	27.37%
	B	19.68%
Aluminium	A	1.12%
	B	1.76%

For both air and aluminium, the average error remains below 3.2%. However, in the water, the error is higher, primarily due to constraints in the testing environment. The water tank used for the experiment was insufficiently large, resulting in multiple reflections of the ultrasonic waves off the tank walls, which interfered with the results. Utilizing a larger tank would reduce wall interference, thus decreasing the model's error.

4.3.6 Optimal Energy Transfer and Loss Mitigation

Maximising energy transfer efficiency is a central objective in ultrasonic energy transmission systems. Ideally, the ultrasonic transducer should be positioned at a resonant peak where energy transfer is most efficient. However, in metal-enclosed or constrained environments, the physical positioning of the transducer is often limited. In such cases, frequency tuning becomes a practical and effective strategy, as the location of the peak is wavelength-dependent and can be adjusted by selecting appropriate operating frequencies.

An in-depth analysis of link losses across the UET system reveals several key strategies for loss mitigation and performance optimisation:

Electrical losses can be effectively reduced through the design of impedance-matching networks or the careful selection of components with matched impedances, as described by Equation 3-11. Proper matching ensures maximum power transfer between electrical subsystems and minimises reflection and dissipation[191]. The intrinsic material and structural properties of the transducer primarily influence transducer losses. High electromechanical coupling coefficients (high k^2) and wide-bandwidth transducers allow for greater tolerance to resonance shifts that may occur in varying environmental conditions. This adaptability helps maintain efficient operation even when minor detuning occurs, as Equations 3-17 and 3-18 indicate. Acoustic losses can be mitigated by improving acoustic matching between the transducer and the medium. As shown in Equation 3-19, better acoustic impedance matching reduces reflections at interfaces and enables more effective energy transfer through the medium. Medium losses are highly dependent on the physical and material characteristics of the propagation path. According to Equations 3-36 and 3-37, both the transducer's size and operating frequency influence losses. Selecting a transducer with suitable dimensions and frequency based on the specific application environment can significantly reduce these losses.

In summary, this study developed a comprehensive UET system model that tracks energy flow from the input source to the load. By systematically analysing the loss mechanisms along the transmission path, strategies were identified for minimising inefficiencies and enhancing performance. The model's predictions were validated under various application scenarios, demonstrating its utility in guiding practical UET system design and optimisation.

The proposed model was compared to related work. In this regard, applications are considered. The comparison factors are analysed, such as transfer media materials, transmission distance, frequency range, and errors. The average error was calculated based on the comparison of the model with the measured results. The comparison is described in Table 4-6 [140, 141, 142, 144, 192].

Table 4-6. Comparison with related works.

Work	Medium	Distance	Frequency	Error
[139]	Stainless steel	74.8 mm	4 MHz	-
[140]	Alumina ceramic	50 mm	97-300 kHz	1.59-3.64%,
[141]	Aluminium	100 mm, 200 mm	738 kHz 1040 kHz	10.2-10.6%, 5.0-7.6%
	Steel	100 mm, 200 mm	738 kHz	6.1-6.9%
[143]	Aluminium	1.5 mm	0.35-1.96 MHz	1.14-2.67%
[177]	Aluminium	50 mm	656-978 kHz	21%
Present work	Air Water Aluminium	0-290 mm 0-290 mm 0-35 mm	19–42 kHz	2.54-3.11% 19.68-27.37% 1.12-1.76%

This model not only compares performance across different transmission media but also analyses transmission distance continuously rather than at discrete points. Additionally, the model accounts for variations in frequency and impedance of the transducer under different application conditions. The model demonstrates an error margin of less than 3.2% for air and metal media. Although the error is higher for water, this discrepancy is attributed to the testing conditions. Using a larger water tank for testing could reduce wall interference, thereby decreasing the error.

4.4 Conversion Circuit Test

The conversion circuit is responsible for harvesting RF energy, storing it, and subsequently transferring it to the ultrasonic transducer drive circuit through energy management to enable ultrasonic energy emission. To suit different application environments, various design solutions are available for the conversion circuit. For testing purposes, the circuit was designed and evaluated based on its functional modules, including the rectifier circuit, boost circuit, switching circuit, oscillator, and power amplifier. Detailed information on the circuit schematic and the layout of the evaluation board is presented in the appendix under Evaluation PCB. This modular approach facilitates systematic testing and optimisation of individual components to ensure overall performance and reliability.

4.4.1 Rectifier Circuit

The rectifier circuit was evaluated using two configurations: a full-wave rectifier and a charge pump. The full-wave rectifier employed a dual-diode design, while the charge pump utilised a Dickson structure with a gain of 9 to achieve higher voltage output from RF energy. A key challenge in the design was selecting rectifier diodes suitable for high frequency operation, as high-frequency rectification requires diodes with short reverse recovery times. Despite the availability of diodes for high-voltage applications, options for high-frequency rectification are limited. moreover, reverse recovery time is often omitted from the data sheets of many Schottky diodes, necessitating empirical evaluation. Four diodes commonly used in RF energy harvesting (SMS7630, BAT6302, 1PS76SB17, and BAS140W) were selected for testing. The main parameters of the diode are shown in Table 4-7.

Table 4-7. Parameters of the four kinds of Schottky diodes

Parameter	SMS7630	BAT6302	1PS76SB17	BAS140W	Unit
Breakdown voltage	2	3	4	40	V
Forward current I_F	50	100	30	120	mA
Forward voltage V_F	60-120	190-300	300-600	250-1000	mV
Reverse current I_R	5	10	2	1	μA
Diode capacitance	0.38	0.65	1	3	pF

The test conditions included an RF input power of 10 dBm and a load resistance of 100 KΩ. The rectifier circuit's output performance under these conditions is presented in Figure 4-10, providing a comparative analysis of the diodes' effectiveness in high-frequency RF energy harvesting.

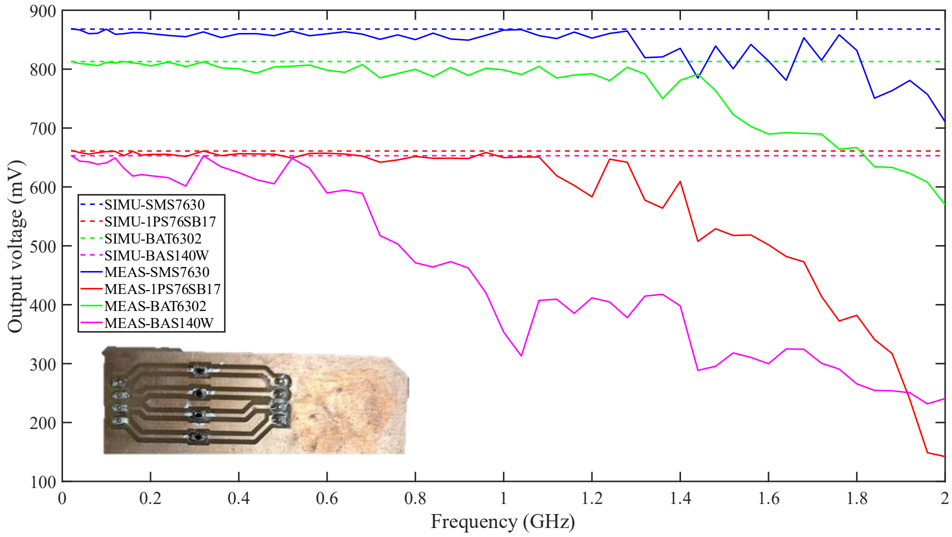

(a) full-wave rectifier result

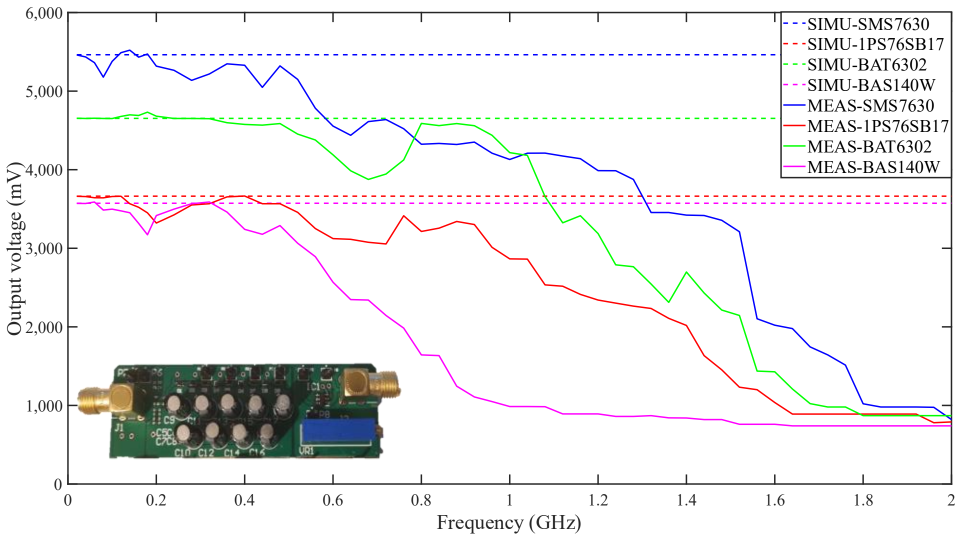

(b) Dickson charge pump result

Figure 4-10. Rectifier circuit diode test results for full-wave rectifier (a) and Dickson charge pump (b).

The performance of different diodes in rectifier circuits varies considerably under identical input conditions, primarily due to differences in their forward voltage drop and breakdown voltage. A lower forward voltage drop typically yields a higher output voltage; however, diodes exhibiting low forward voltage drops often have correspondingly low breakdown voltages. This trade-off constrains the rectifier's input voltage range. Although RF energy harvesting systems generally operate within a limited input range, diodes with low breakdown voltages limit the rectifier's capacity to handle higher input power levels, rendering them less suitable for high-power applications.

In the case of the full-wave rectifier, simulated output voltages for the tested diodes were 868 mV, 616 mV, 661 mV, and 813 mV, respectively. Experimental results showed a decline in output voltage with increasing frequency. Across a frequency range of 0.01 GHz to 2 GHz, the measured output voltages of SMS7630, BAT6302, and 1PS76SB17 aligned well with simulation results up to approximately 1.3 GHz, beyond which deviations became apparent. In contrast, the output from BAS140W began to diverge from the simulation at frequencies above 0.5 GHz. These discrepancies are primarily attributed to the reverse recovery time of the diodes, which significantly affects rectification performance at higher frequencies. When the input frequency exceeds a diode's cutoff frequency, its ability to block current effectively diminishes due to limitations associated with junction capacitance.

The simulated output voltages for the charge pump configuration were 5,463 mV, 4,653 mV, 3,663 mV, and 3,573 mV, respectively. Experimental observations indicated that SMS7630 maintained an output voltage near the simulated value up to 0.5 GHz, but it dropped below 5 V at frequencies above 0.6 GHz. BAT6302 exhibited consistency with simulation results up to 0.5 GHz, followed by a gradual reduction in output voltage beyond 1 GHz. The performance of 1PS76SB17 and BAS140W followed a similar trend to that of SMS7630. BAT6302 demonstrated the most robust performance among the tested diodes at higher frequencies.

In application scenarios, full-wave rectifiers are commonly employed in systems requiring stable and low-ripple DC output from AC or RF input, especially where the available input voltage is moderate and power levels are limited. Their relatively simple design and high efficiency at low to mid frequencies make them well-suited for compact and energy-constrained systems, such as low-power sensors or biomedical implants.

Charge pumps, on the other hand, are advantageous in applications that require voltage multiplication without the use of inductors. This makes them especially attractive for fully integrated circuit (IC) designs and high-voltage generation from low-voltage inputs. They are particularly effective when compact size, scalability, and on-chip integration are critical, though their efficiency can decrease at higher frequencies due to parasitic capacitances and switching losses.

These findings highlight that rectifier performance is frequency-dependent and strongly influenced by the reverse recovery time of the diode. For optimal rectifier performance, diodes with high cutoff frequencies should be selected. Moreover, a balance between breakdown voltage and cutoff frequency is necessary to ensure the rectifier's reliability and suitability for the intended application.

4.4.2 Boost Circuit

The boost circuit is responsible for increasing the voltage of collected RF energy to a level suitable for storage and subsequent use by downstream circuits. For this study, two mature ICs, the LTC3108 and the BQ25570, were selected for testing. The primary objectives of the tests were to evaluate the relationship between input and output voltages for each IC and to assess their efficiency under various operating conditions.

These tests aimed to determine the suitability of these ICs for RF energy harvesting applications, focusing on their ability to maintain high efficiency and stable voltage conversion over a wide input voltage range. The results provide insights into the performance characteristics of the boost circuits and their adaptability to different RF energy harvesting scenarios. The test results are shown in Figure 4-11.

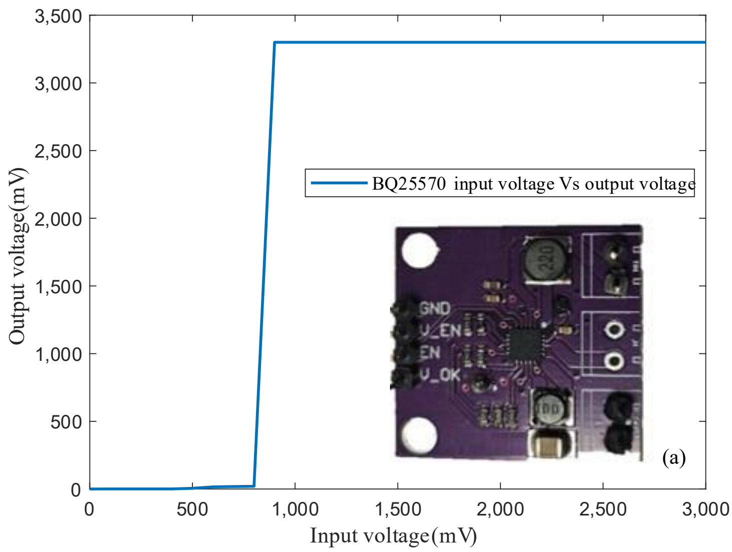

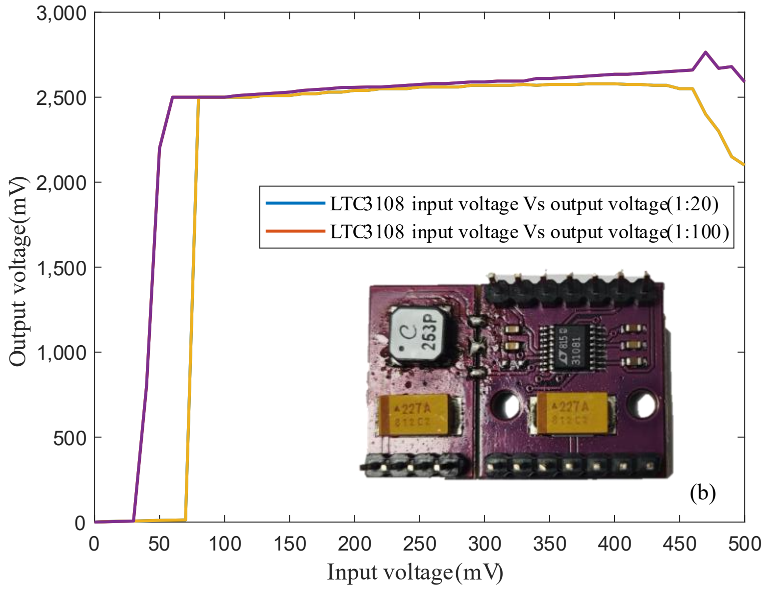

Figure 4-11. Boost circuit output test results for BQ25570 (a) and LTC3108 (b).

The test results of the boost circuit indicate that the BQ25570 has a startup voltage of 800 mV, whereas the LTC3108 exhibits a significantly lower startup voltage. When paired with a 1:100 transformer, the LTC3108 can start at 30 mV, while with a 1:20 transformer, the startup voltage increases to 70 mV. However, BQ25570 supports a wider input voltage range, reaching up to 5.5 V, whereas LTC3108 has a maximum input voltage of only 0.5 V.

These findings highlight the trade-off between startup voltage and input voltage range in boost module selection. Modules with ultra-low startup voltages typically have a restricted input voltage range, while those capable of handling higher input voltages often require a higher startup voltage. Therefore, selecting an appropriate boost module must be based on the specific RF energy input conditions in the intended application environment, ensuring compatibility with both startup constraints and operational voltage ranges.

4.4.3 Switching Circuit

The switch circuit is designed to control the activation and deactivation of the ultrasonic drive circuit. When integrated with a voltage sampling circuit, it facilitates energy management by regulating the flow of energy. For this study, the ADG821 was selected as the switching element. The circuit's performance was tested in conjunction with a resistor-based voltage sampling system to monitor its charging and discharging behaviours with a 2 F supercapacitor.

The tests aimed to evaluate the switching efficiency and stability of the circuit under different operational conditions. Key observations included the circuit's ability to transition between states and its overall energy management efficiency. The test results are shown in Figure 4-12.

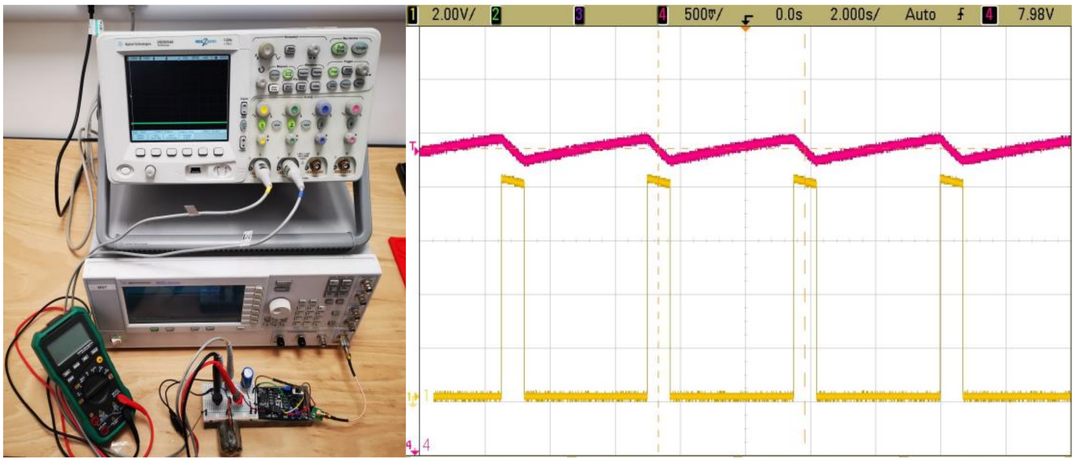

Figure 4-12. Switching circuit test results.

After the actual circuit test, the actual test result shows that the efficiency is 71.2% to a 1 kΩ resistor.

4.4.4 Oscillator

The oscillator functions as the signal source for the ultrasonic transducer, generating a stable excitation signal tuned to match the transducer's resonant frequency. In this study, several oscillator types were considered, each suited to different application scenarios. For experimental validation, the LTC6906 was selected due to its flexibility and compatibility with the operating frequency requirements of various transducers.

The oscillator’s performance was assessed by examining the characteristics of its output waveform and evaluating its operational efficiency. Key metrics included signal stability, frequency precision, and the oscillator’s ability to maintain consistent output under load. These factors are critical to ensuring effective energy transfer and reliable system operation. The corresponding test results are presented in Figure 4-13.

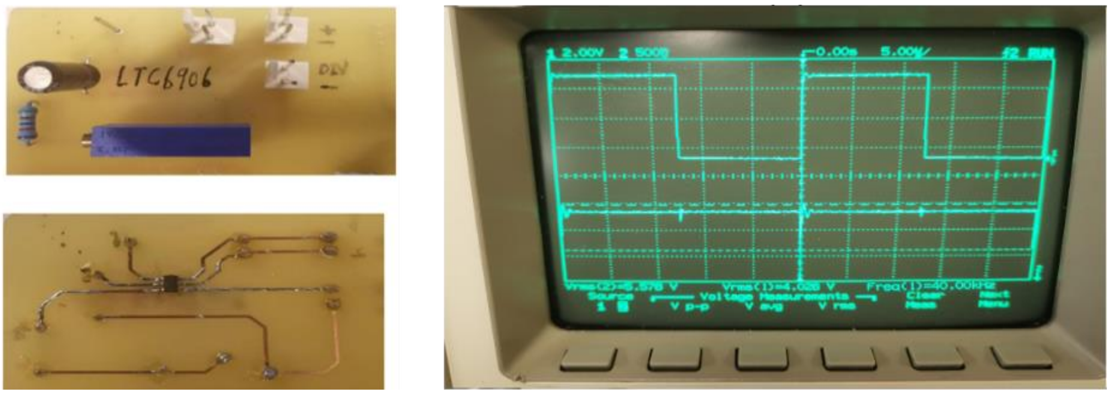

Figure 4-13. Oscillator Test Results.

The test results indicate that the oscillator produces a stable and consistent output waveform, with minimal frequency drift over time. Additionally, the output frequency is easily adjustable across a wide range, allowing for precise tuning to match the resonant frequency of different ultrasonic transducers. This tunability and stability are critical for ensuring efficient energy transfer and reliable system performance in various application scenarios.

4.4.5 Power Amplifier

The power amplifier elevates the oscillator’s output signal to a power level sufficient to drive the ultrasonic transducer effectively. Among the various available amplifier topologies, a Class E amplifier was selected for this study due to its high efficiency, low switching losses, and well-established suitability for ultrasonic energy transmission applications.

The amplifier was designed to deliver an output power of 200 mW at an operating frequency of 40 kHz, powered by a 5 V supply. The component parameters were calculated based on the standard Class E amplifier design methodology to ensure optimal performance. These calculations considered key factors such as load impedance, operating frequency, quality factor (Q), and target efficiency. The selected component values were carefully matched to the electrical characteristics of the ultrasonic transducer, thereby maximising the system's overall energy conversion efficiency.

The detailed derivation and values of the circuit components used in the Class E amplifier design are presented below.

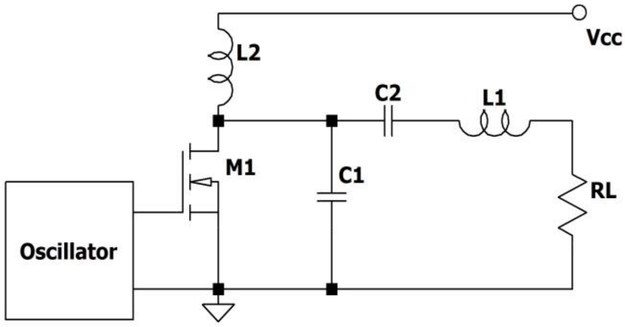

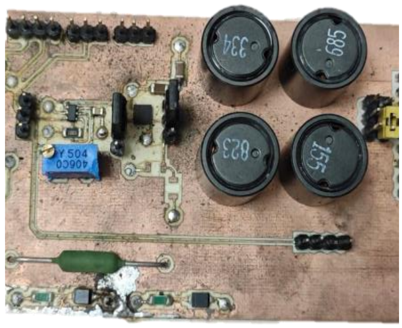

$$R_L = 0.577\left[\frac{(Vcc - Vo)^2}{P}\right] \times \left(1 - \frac{0.414}{Q_L} - \frac{0.578}{{Q_L}^2} - \frac{0.206}{{Q_L}^3}\right)$$

$$C_1 = \frac{1}{34.222 f R_L}\left(1 + \frac{0.914}{Q_L} - \frac{1.032}{{Q_L}^2}\right) + \frac{0.6}{(2\pi f)^2 L_2}$$

$$C_2 = \frac{1}{2\pi f R_L}\left(\frac{1}{Q_L - 0.105}\right)\left(1 - \frac{1.015}{Q_L - 1.788}\right) - \frac{0.2}{(2\pi f)^2 L_2}$$

$$L_1 = \frac{Q_L R_L}{2\pi f} \tag{4-2}$$

Where: R_L is the represents the impedance of the load transducer at its resonant frequency, determining how the amplifier interfaces with the transducer. Vcc is the driving voltage supplied to the circuit. Vo refers to the saturation voltage of the MOSFET (M1), P denotes the output power, set at 200 mW in this design. f is the output frequency, which matches the transducer's resonant frequency of 40 kHz. Q_L is the quality factor, typically chosen around 5 for this application to balance bandwidth and efficiency. C_1, C_2, L_1 are the resonant components that define the Class E amplifier's operation, tuned to achieve zero-voltage switching and optimal energy transfer. L_2 is the DC isolation inductor, selected to provide effective isolation while supporting the required driving current. For this design, a 10 mH inductor was chosen to meet these criteria.

Each parameter was carefully selected and calculated to ensure efficient energy transfer, minimal signal distortion, and reliable operation under the specified conditions. This design provides a robust foundation for driving the ultrasonic transducer effectively. The circuit output is as follows Figure 4-14.

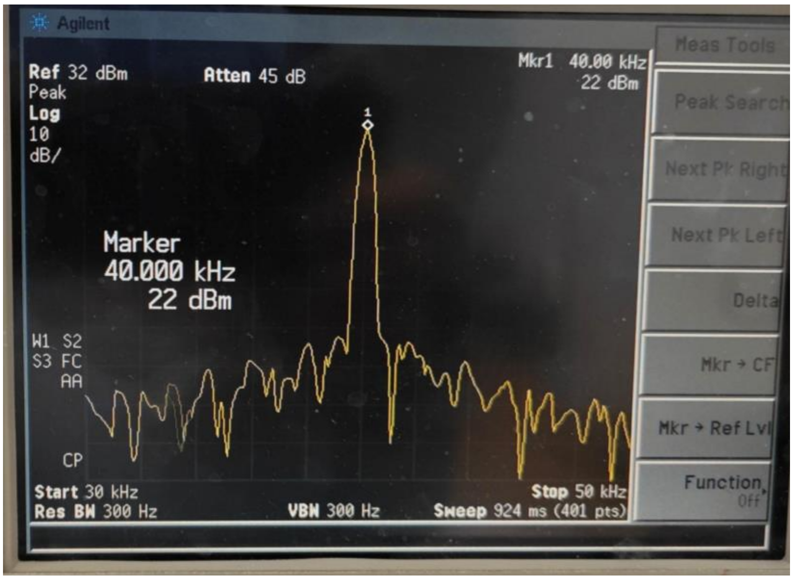

Figure 4-14. Class E power amplifier output test results

Testing involved verifying the amplifier’s output power, efficiency, and signal fidelity to ensure compatibility with the ultrasonic transducer and adherence to the design specifications.

4.5 System Case

According to the system components, a system capable of penetrating 5 mm metal plates to enable a hybrid wireless power supply for BLE devices was designed. For testing convenience, the signal generator replaced the RF input source in the RF link, and the RF input power was adjusted to simulate varying RF transmission distances. The RF rectifier circuit employs a diode full-wave rectification configuration, while the boost circuit is implemented using LTC3108. The energy storage element in the conversion circuit consists of a 1.5 F supercapacitor, and the energy management circuit utilizes an SPST ADG16112 IC switch controller with resistor sampling. The oscillator also employs LTC6906 IC, and the power amplifier circuit is configured using a Class E topology. The transducer, made of PZT-8 material, is firmly secured with a 3D-printed bracket to ensure stability during operation. For further details regarding the transducer holder, refer to the Transducer Holder appendix.

The ultrasonic receiving circuit mirrors the RF acquisition circuit and utilizes a diode full-wave rectifier and an IC booster. The supercapacitor in the receiving circuit has a capacity of 2.2 F, ensuring sufficient power supply time to complete Bluetooth connection establishment and data reading tests. The Figure 4-15 illustrates the test system diagram.

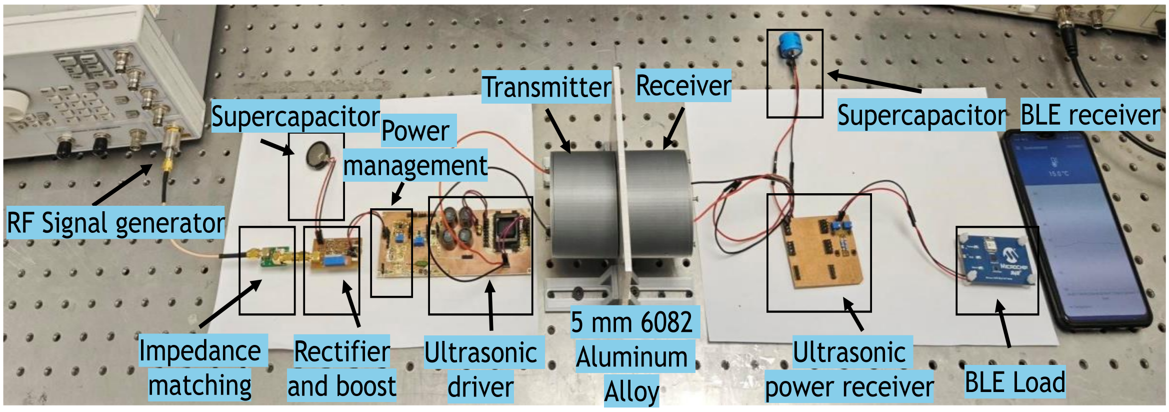

Figure 4-15. A system case test diagram that can penetrate 5 mm metal plates to facilitate a hybrid wireless power supply for BLE devices. The system provides 1 minute of operational runtime for the BLE device after an energy accumulation period of 136 minutes. Temperature data was successfully transmitted and read via the Bluetooth connection with the mobile phone receiver.

The following Table 4-8 is shown the system case test main parameters of experimental settings.

Table 4-8. Main parameters of experimental settings

Components	Model	Components	Model
RF signal generator	Agilent E8257D	Oscillator	LTC6906
Rectifier diode	SMS7630	Power amplifier	Class E
Booster	LTC3108	Transducer	PZT-8
Converter Cap	KR-5R5V155-R (1.5 F)	Ultrasonic receiver Cap	80-FT0H225ZF (2.2 F)
Power management	ADG1612	Load	AVR BLE IoT Node

The core component of the CRFU-WPT system is the conversion circuit, which is responsible for collecting electromagnetic energy and utilizing the antenna to drive the ultrasonic transducer to emit mechanical energy. Due to the limited energy that can be harvested through long-distance wireless transmission while adhering to safe RF exposure limits, the collected energy is insufficient to directly power the ultrasonic transmitter. Thus, incorporating an efficient energy management circuit is critical for managing the limited energy effectively.

This design employs a time-sharing energy management strategy, where RF energy is accumulated over an extended period and then released to the ultrasonic drive circuit in a short burst to sustain system operation. By configuring the operating voltage range, the energy management circuit automatically controls the accumulation time (charging duration) and release time (discharge duration). Figure 4-16 illustrates the operating status of the power management within the conversion circuit under a 3 dBm RF energy input.

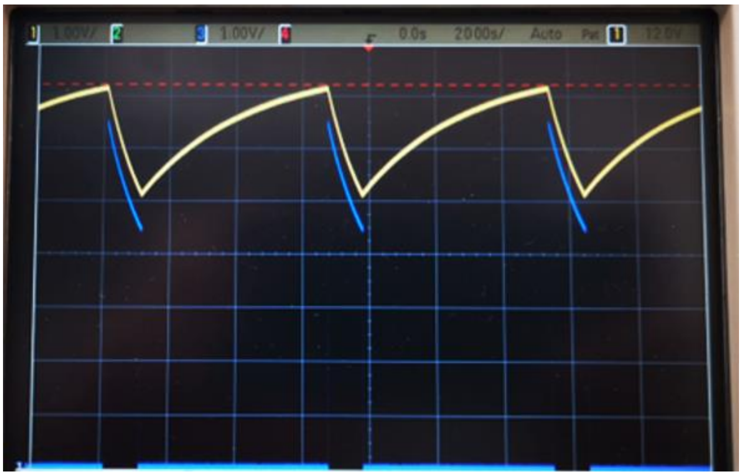

Figure 4-16. The operating status of the energy management circuit under 3dBm RF energy input. The yellow line is the supercapacitor voltage, and the blue line is the ultrasonic drive circuit voltage.

The operational results of the energy management circuit demonstrate that during the energy accumulation phase, the ultrasonic driving circuit is deactivated to minimize losses. Once sufficient energy is accumulated to meet the driving requirements, the ultrasonic driving circuit is reactivated. By cycling this process, the system effectively achieves coupling between the RF link and the ultrasonic link. The charging time varies based on the RF input power and is automatically regulated by the energy management circuit. When the ultrasonic drive circuit is switched on, the voltage is slightly smaller than the capacitor voltage, which is due to the loss of the conversion circuit.

Similarly, the ultrasonic receiving circuit encounters challenges with insufficient input power when the transmission distance of the ultrasonic link is extended. To address this, the ultrasonic receiving circuit can also implement time-sharing energy management to ensure the reliable operation of the load. Figure 4-17 illustrates the power management operation of the conversion circuit and the ultrasonic receiving circuit under a 0 dBm RF input in the system configuration.

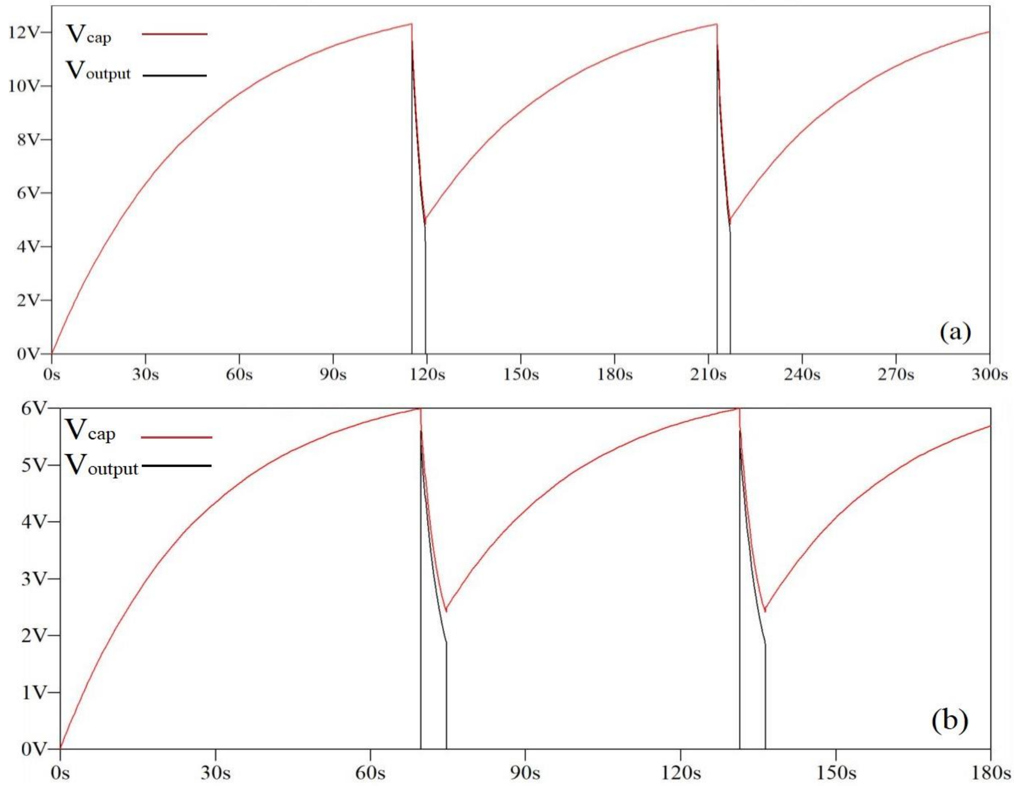

Figure 4-17. Conversion circuit (a) and ultrasonic receiving circuit (b) power management operating voltage test results.

According to the test waveforms shown in Figure 4-17Figure 4-17. Conversion circuit (a) and ultrasonic receiving circuit (b) power management operating voltage test results., the power management results demonstrate effective energy accumulation and transfer between different subsystems. The following observations can be made.

In Figure 4-17 (a), the conversion circuit processes the rectified RF energy, which is then amplified and stored in a capacitor via a two-stage boost converter. During the charging phase, the capacitor voltage V_{cap} increases steadily. Once the voltage reaches the predefined threshold of 12 V, the energy management circuit switches to drive the ultrasonic transmission stage, resulting in a rapid voltage drop during the discharge phase. The observed charge-to-discharge time ratio in this process is about 17:1.

In Figure 4-17 (b), the ultrasonic receiving circuit exhibits a shorter energy cycle. Owing to the relatively higher voltage received through ultrasonic transmission, the capacitor charges more quickly, yielding a charge-to-discharge time ratio of approximately 8:1.

These results confirm the system's capability for time-division control and energy accumulation, supporting sustained power delivery in low-power applications. Under conditions of 0 dBm input power and a BLE load of approximately 3 mW, the system achieves a charge-to-discharge time ratio of 136 to 1. The overall system efficiency under these conditions is 2.21%, with the primary losses attributed to the transducer and ultrasonic link. In the following section, the efficiency of the conversion circuit is analysed based on the established ultrasonic transmission model.

The impedance results of the transducer in the system are shown in Figure 4-18.

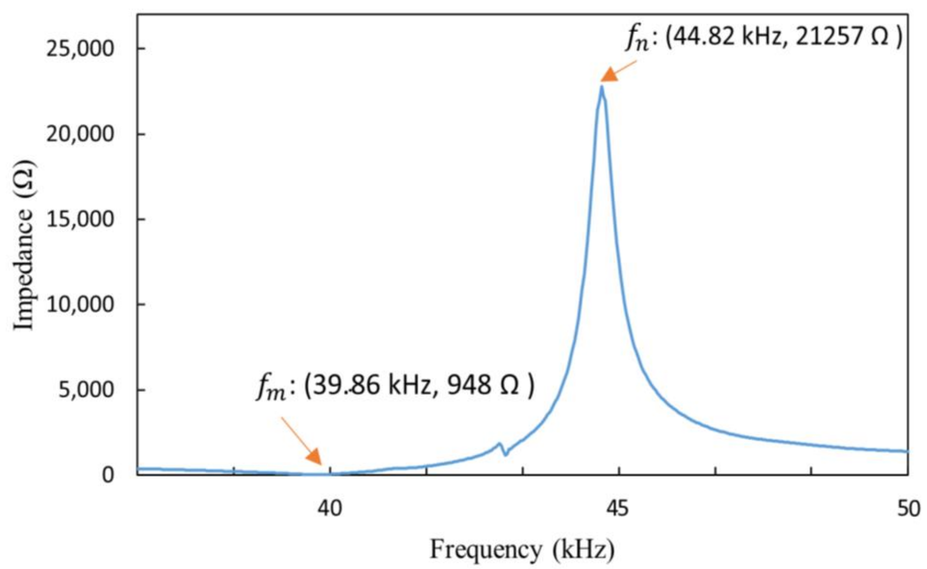

Figure 4-18. The impedance characteristics of transducers for system.

According to the ultrasonic link model (Equation 3-40), the electrical loss (Equation 3-11), transducer loss (Equation 3-18), acoustic loss (Equation 3-19), and dielectric loss (Equations 3-36 and 3-37) are calculated respectively. The evaluation board has been designed with electrical impedance matching based on the transducer's impedance, and the transducer material is consistent with the dielectric medium. Therefore, electrical and acoustic losses are calculated under ideal matching conditions. The primary source of ultrasonic link loss is the transducer loss and medium loss, which can be calculated as follows:

$$Transducer\ loss\ (dB) = -10\,log(k^2) = \frac{\pi}{2}\frac{44.82}{39.86}tan\left[\frac{\pi}{2}\left(\frac{44.82-39.86}{39.86}\right)\right] = 4.56$$

and the 5mm aluminium alloy transmission medium loss can be calculated using the following equation:

$$Medium\ loss\ (dB) = -10\log\left\{\frac{Z_{E2}}{Z_{E1}} \times \left[\frac{4r}{ka^2} sin\left(\frac{ka}{2}\right) e^{j\frac{k}{2}(\sqrt{r^2+a^2}+r-a)}\right]^2\right\} = 3.43$$

Where: Z_{E1} is the electrical impedance of the driver circuit, Z_{E2} is the electrical impedance of the transducer, for ideal matching, $Z_{E1} = Z_{E2}$, k is the wave number, calculated as $k = \frac{2\pi f}{c} = \frac{2\pi\times 39860}{6420} = 39.01$, r is transmission distance, which is 0.005 m, a is the radius of transducer, equal to 0.015 m.

Under these conditions, the calculated medium loss is approximately 3.43 dB. Based on the calculated transducer loss, medium loss, and the ultrasonic receiver circuit power management ratio of 8:1 for the 3 mW to the load, the output power of the conversion circuit is determined to be approximately 6.75 mW. Given the 17:1 ratio observed in the conversion circuit, its efficiency can be estimated as:

$$Concerter = -10\log\frac{\mathrm{P}_{In}}{\mathrm{P}_{Out}} = \log\left(\frac{6.75}{17}\right) = 4.01$$

For conversion circuit efficiency is:

$$\eta = \frac{6.75}{17} \times 100\% = 39.7\%$$

4.6 Summary

The system tests cover the RF link, ultrasonic link, and conversion circuit, following the overall system architecture. The RF link test validates the RF energy transmission model, measures link losses, and explores ways to improve transmission efficiency. The ultrasonic link test verifies the proposed transmission model, compares transducer performance across different media, and analyses loss factors affecting the link. The conversion circuit test evaluates the performance of key sub-circuits and demonstrates a practical application case. Designed to meet specific application needs, the conversion circuit ensures efficient operation. By combining the RF and ultrasonic transmission models, the system enables flexible matching across various distances. Together, these tests offer a comprehensive understanding of the performance, limitations, and optimisation potential of the hybrid wireless power transfer system.

5 Conclusion and Future Work

WPT overcomes the limitations of cables and batteries, offering an innovative power supply method. Hybrid WPT, by integrating two distinct WPT technologies, mitigates the limitations of individual approaches, enabling reliable power delivery to sensors in challenging environments such as underwater, underground, and enclosed metal structures. This study introduces a novel CRFU-WPT system that combines RF-WPT and U-WPT, achieving both long-distance wireless energy transmission and safe penetration through metal, water, and biological tissues. The system architecture is comprehensively described, including the RF link, ultrasonic link, and conversion circuit.

Based on link loss analysis, an energy transmission relationship is established, allowing for precise power budgeting tailored to specific applications. This facilitates the optimisation of RF transmission distances, ultrasonic transmission distances, and conversion circuit configurations. The study presents two RF energy transmission models, one for indoor applications and another for outdoor environments, while the ultrasonic energy transmission model accounts for multiple influencing factors. Due to the absence of a standardised model for ultrasonic WPT, this research develops a customised energy transmission model based on different transmission media and transducers, providing a unified calculation formula.

Given the energy disparity between RF and ultrasonic links, this study proposes a specialised conversion circuit that integrates RF and ultrasound, detailing its implementation, including RF energy harvesting, energy management, and ultrasonic emission. A key innovation of this project is the development of a time-sharing energy management solution. By efficiently accumulating limited RF energy and employing ultrasonic drive switching control, the system minimises energy conversion losses, seamlessly connecting the RF and ultrasonic links. This integration harnesses the advantages of both WPT methods, offering a groundbreaking solution for wireless power supply in harsh environments.

Different application environments necessitate varying circuit design strategies. This study explores multiple advanced design solutions structured according to modular architecture. Additionally, it provides a blueprint for conversion circuit design, allowing customisation of functional modules to meet diverse application requirements and optimise hybrid WPT system performance.

Finally, a practical system case is demonstrated, successfully penetrating a 5 mm metal plate and powering a low-power Bluetooth device with a 0 dBm RF input. The system achieves different wireless transmission distances at varying power levels, and the energy management system autonomously regulates ultrasonic emission, ensuring stable operation even with fluctuating RF energy inputs. This research paves the way for the further development and optimisation of hybrid WPT systems for real-world applications in challenging environments.

Future research will focus on integrating the hybrid WPT system with sensor application platforms to develop more advanced and user-friendly solutions. This integration aims to enhance the system's practicality, enabling seamless implementation in real-world scenarios across various industries such as environmental monitoring, healthcare, and industrial automation.

Additionally, further application testing will be conducted to assess the system's performance under diverse operating conditions. This includes outdoor long-distance energy transmission experiments to evaluate the feasibility of powering remote and mobile devices over extended ranges. Unstable input testing will be performed to analyse the system’s adaptability to fluctuating power sources, ensuring robust operation in environments with variable energy availability. Moreover, extreme environmental condition testing will be carried out to examine the system’s resilience in challenging settings, such as high humidity, extreme temperatures, and highly conductive or obstructive media. Furthermore, the tests to enhance system performance will explore various approaches, such as RF prisms, meta-surface antenna combinations, piezoelectric transducers made from novel materials, and integrating advanced components in the conversion circuits. These may include ultra-low forward voltage diodes, start-up voltage boost converters, and wide voltage range switching ICs.

The hybrid WPT system can be further optimised through these advancements to enhance its efficiency, reliability, and adaptability for a wide range of practical applications. Future work will also explore improvements in system miniaturisation, energy management strategies, and compliance with industry standards to facilitate widespread adoption and commercialisation.

Appendices

This appendix contains the basic formulas for U-WPT, used to fabricate and test the evaluation board and transducer holder developed during this work.

Transducer Ultrasonic Infinite Plane Piston Acoustic Model

The transducer mode is equivalent to a pair of piston models.

Before the circular piston model, we need to understand the pulsating sphere model. This is because we can see that the circular piston is composed of infinite pulsating spheres. The equation for the pulsating sphere is:

$$u_r = u_0 e^{j(\omega t - kr)}$$

The movement of the sphere is sinusoidal.

The pressure at r is:

$$p(r,t) = \frac{A}{r} e^{j(\omega t - kr)}$$

Where:

r is distance from the centre.

A is determined by an appropriate boundary condition.

K is the wave number, defined as:

$$k = \frac{2\pi}{\lambda} = \frac{\omega}{c}$$

The pulsating sphere model is similar to a spring system. In the pulsating sphere model, the impedance of the system is defined as:

$$Z_m = \frac{F}{U}$$

Where:

F is the force.

U is the particle velocity.

For a plane wave:

$$Z = \frac{p}{U} = \rho c$$

For a spherical wave:

$$Z = \frac{p}{U} = \rho c \cos e^{j\theta}$$

Where:

ρ is the density of medium.

c is the wave speed.

In the pulsating sphere:

$$\begin{cases} p(r,t) = \dfrac{A}{r} e^{j(\omega t - kr)} \\ p(r,t) = UZ = u_0 e^{j(\omega t - kr)} \rho c \cos e^{j\theta} \end{cases}$$

So, boundary conditions A is:

$$A = \rho c \, \mathrm{U} \, \mathrm{r} \cos \theta_r e^{j(kr + \theta_r)}$$

For distances greater than r, the pressure at a of the sphere is:

$$p(r,t) = \rho c \, \mathrm{U} \left(\frac{a}{r}\right) \cos \theta_a e^{j(\omega t - k(r-a) + \theta_a)}$$

When the radius of the sphere is small enough compared to the wavelength (θ $close$ to $\frac{\pi}{2}$):

$$p(r,t) = \rho c\,\mathrm{U}\left(\frac{a}{r}\right)\,\cos\frac{\pi}{2}\,e^{j\left(\omega t - k(r-a) + \frac{\pi}{2}\right)}$$

$$= j\rho c\,\mathrm{U}\frac{1}{\lambda}\,\frac{1}{r}\,e^{j(\omega t - kr)}$$

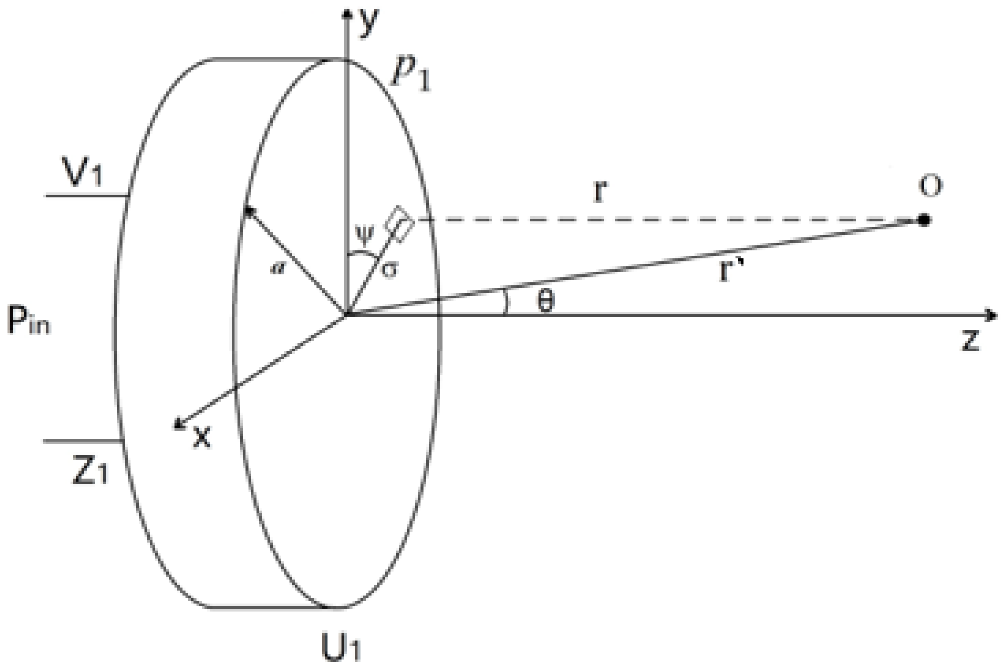

For the axial piston system, where $\sigma \in (0, a)$, the pressure of area S is:

$$p(r,\theta,t) = \int j\rho c\,\mathrm{U}\frac{1}{\lambda}\frac{1}{r}\,e^{j(\omega t - kr)}\,ds$$

Axial pressure:

$$p = \frac{j\rho c k}{2\pi r}\,U e^{j(\omega t - kr)} \int_0^a \sigma\,d\sigma \int_0^{2\pi} e^{jk\sigma \sin\theta \cos\psi}\,d\psi,$$

Evaluation PCB

- Rectifier

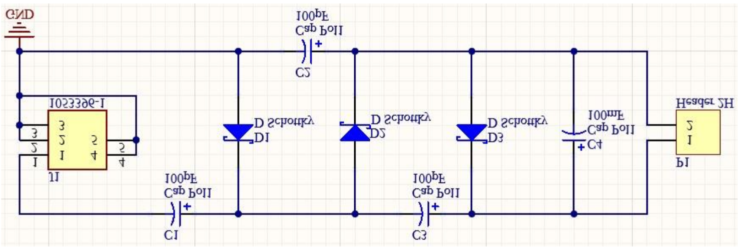

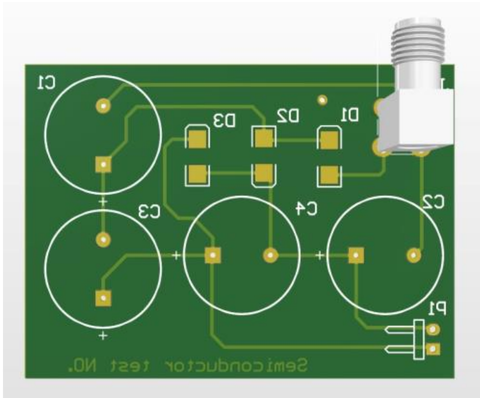

- Rectifier + Oscillator

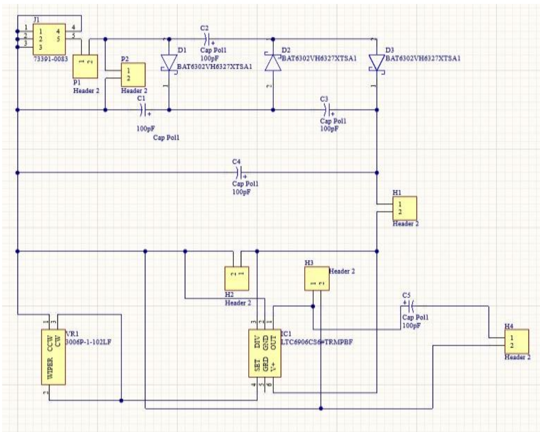

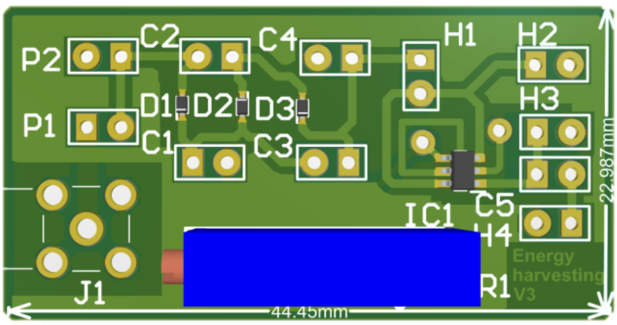

- Power management

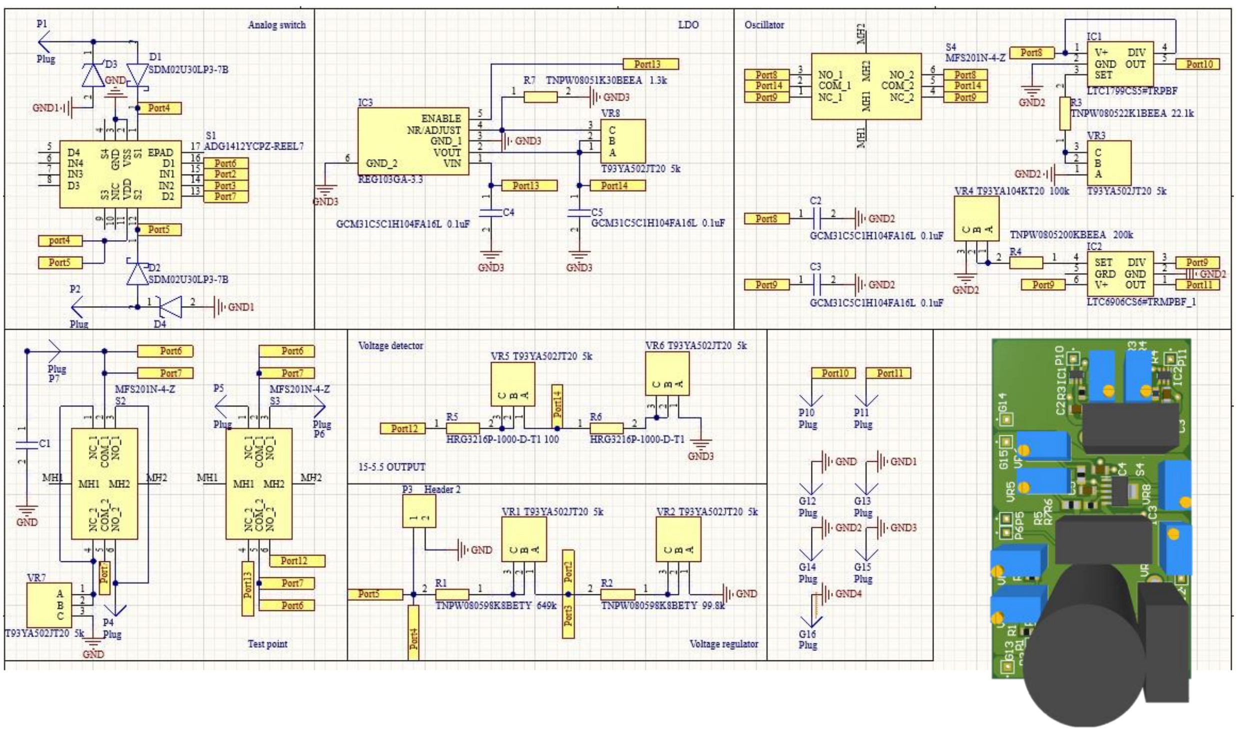

- System case

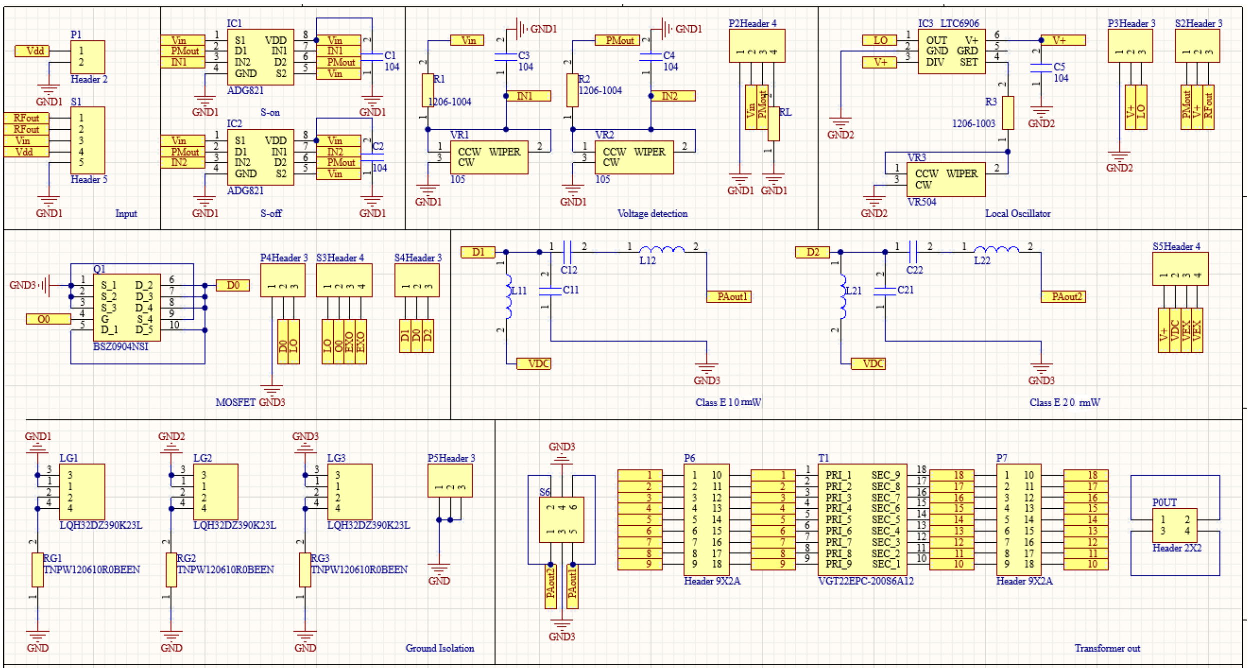

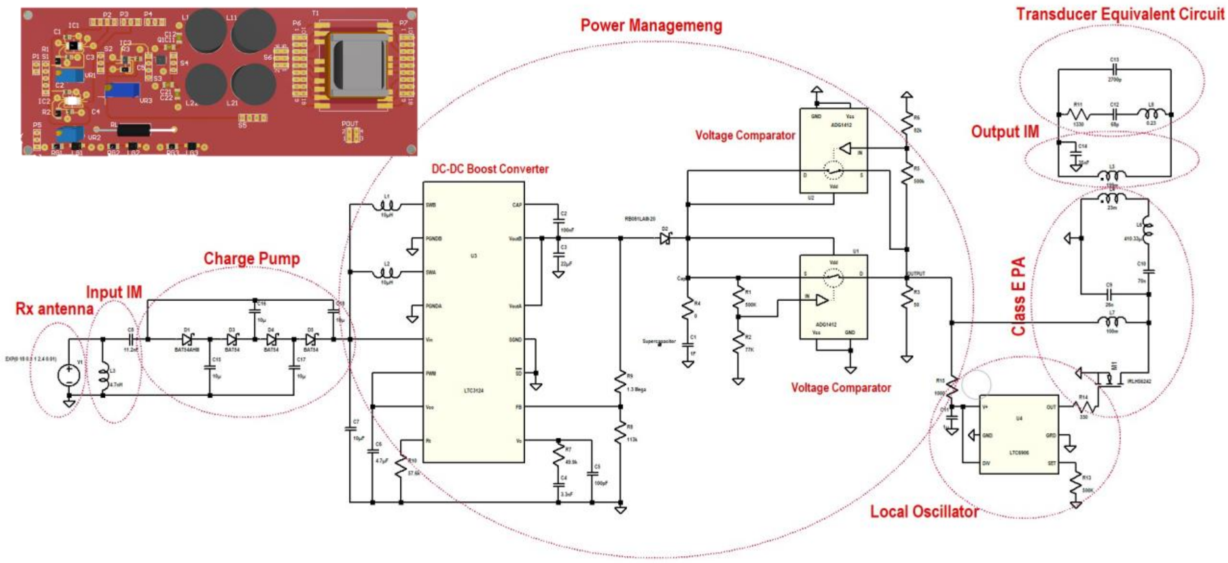

- Receiver

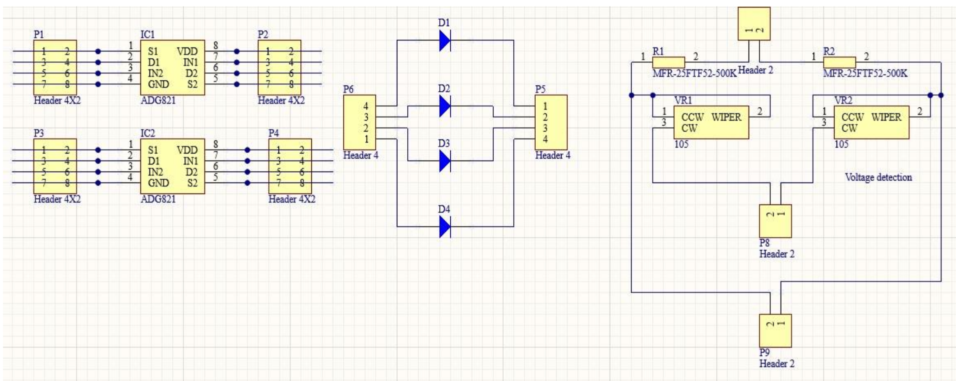

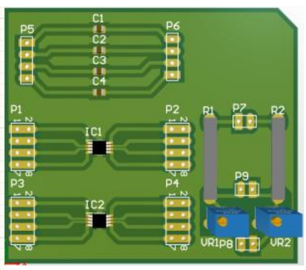

Transducer Holder

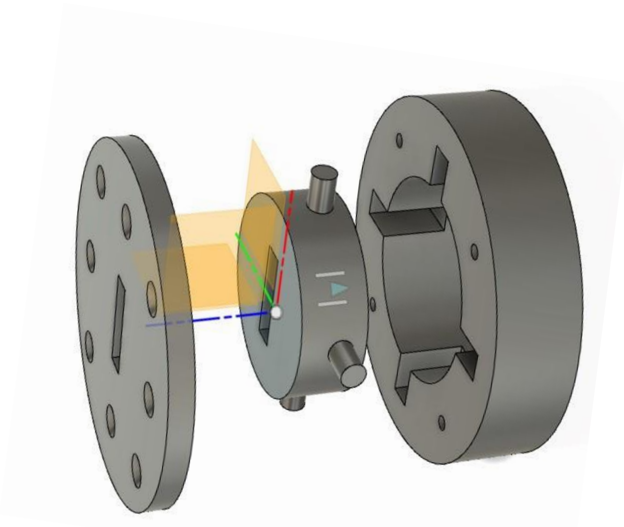

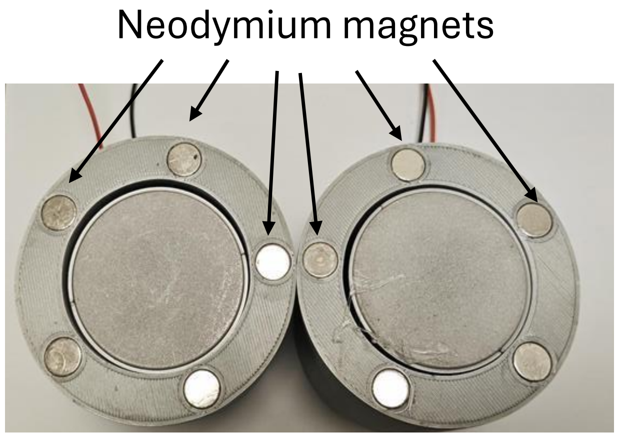

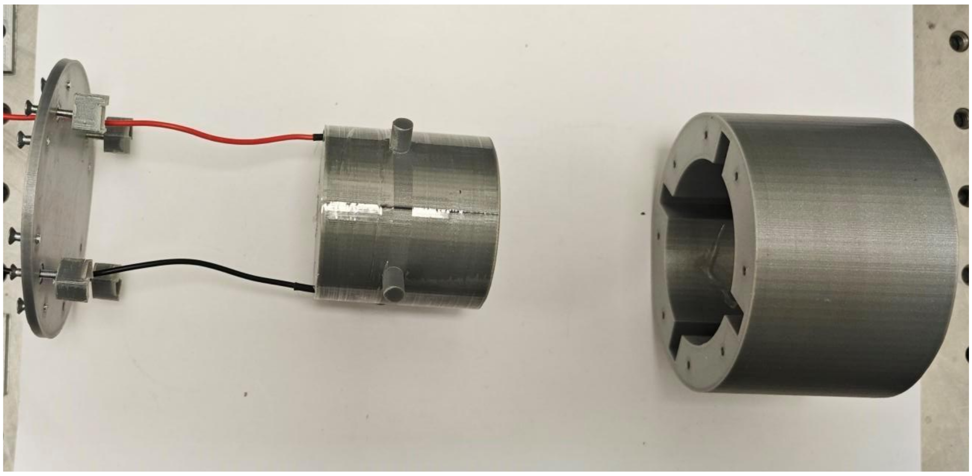

List of References

[1] H. N. S. Aldin, M. R. Ghods, F. Nayebipour, and M. N. Torshiz, "A comprehensive review of energy harvesting and routing strategies for IoT sensors sustainability and communication technology," *Sensors International,* vol. 5, p. 100258, 2024/01/01/ 2024, doi: https://doi.org/10.1016/j.sintl.2023.100258.

[2] G. K. Ijemaru, K. L. Ang, J. K. Seng, A. O. Nwajana, P. L. Yeoh, and E. U. Oleka, "On-Demand Energy Provisioning Scheme in Large-Scale WRSNs: Survey, Opportunities, and Challenges," *Energies*, vol. 18, no. 2*,* doi: 10.3390/en18020358.

[3] M.-u.-R. Ashraf Virk, M. F. Mysorewala, L. Cheded, and A. Aliyu, "Review of energy harvesting techniques in wireless sensor-based pipeline monitoring networks," *Renewable and Sustainable Energy Reviews,* vol. 157, p. 112046, 2022/04/01/ 2022, doi: https://doi.org/10.1016/j.rser.2021.112046.

[4] F. Mazunga and A. Nechibvute, "Ultra-low power techniques in energy harvesting wireless sensor networks: Recent advances and issues," *Scientific African,* vol. 11, p. e00720, 2021.

[5] N. Lakal, A. H. Shehri, K. W. Brashler, S. P. Wankhede, J. Morse, and X. Du, "Sensing technologies for condition monitoring of oil pump in harsh environment," *Sensors and Actuators A: Physical,* vol. 346, p. 113864, 2022.

[6] S. Rysgaard *et al.*, "A mobile observatory powered by sun and wind for near real time measurements of atmospheric, glacial, terrestrial, limnic and coastal oceanic conditions in remote off-grid areas," *HardwareX,* vol. 12, p. e00331, 2022.

[7] V. Y. Ushakov, A. V. Mytnikov, and I. U. Rakhmonov, *High-Voltage Equipment of Power Systems: Design, Principles of Operation, Testing, Monitoring and Diagnostics*. Springer Nature, 2023.

[8] Y. Furuhata, *Climatic media: Transpacific experiments in atmospheric control*. Duke University Press, 2022.

[9] D. R. Gawade *et al.*, "A smart archive box for museum artifact monitoring using battery-less temperature and humidity sensing," *Sensors,* vol. 21, no. 14, p. 4903, 2021.

[10] G. Janssens-Maenhout, F. De Roo, and W. Janssens, "Contributing to shipping container security: can passive sensors bring a solution," *Journal of environmental radioactivity,* vol. 101, no. 2, pp. 95-105, 2010.

[11] M. Abedin and A. B. Mehrabi, "Health monitoring of steel box girder bridges using non-contact sensors," in *Structures*, 2021, vol. 34: Elsevier, pp. 4012-4024.

[12] F. Engmann, F. A. Katsriku, J.-D. Abdulai, K. S. Adu-Manu, and F. K. Banaseka, "Prolonging the lifetime of wireless sensor networks: a review of current techniques," *Wireless Communications and Mobile Computing,* vol. 2018, no. 1, p. 8035065, 2018.

[13] Y. K. Tan and S. K. Panda, "Review of energy harvesting technologies for sustainable wireless sensor network," *Sustainable wireless sensor networks,* vol. 2010, pp. 15-43, 2010.

[14] J. V. Porkka, "Technology, recycling and sustainability of a wireless condition monitoring sensor," 2023.

[15] L. Sun, D. Ma, and H. Tang, "A review of recent trends in wireless power transfer technology and its applications in electric vehicle wireless charging," *Renewable and Sustainable Energy Reviews,* vol. 91, pp. 490-503, 2018.

[16] Z. Bi, T. Kan, C. C. Mi, Y. Zhang, Z. Zhao, and G. A. Keoleian, "A review of wireless power transfer for electric vehicles: Prospects to enhance sustainable mobility," *Applied energy,* vol. 179, pp. 413-425, 2016.

[17] J. Huang, Y. Zhou, Z. Ning, and H. Gharavi, "Wireless power transfer and energy harvesting: Current status and future prospects," *IEEE wireless communications,* vol. 26, no. 4, pp. 163-169, 2019.

[18] M. J. Makhetha, E. D. Markus, and A. M. Abu-Mahfouz, "Integration of wireless power transfer and low power wide area networks in IoT applications—A review," *Sensors International,* p. 100284, 2024.

[19] H. Xie *et al.*, "Wireless energy: Paving the way for smart cities and a greener future," *Energy and Buildings,* vol. 297, p. 113469, 2023.

[20] Z. Liu, T. Li, S. Li, and C. C. Mi, "Advancements and Challenges in Wireless Power Transfer: A Comprehensive Review," *Nexus,* 2024.

[21] V. F.-G. Tseng, S. S. Bedair, and N. Lazarus, "Acoustic power transfer and communication with a wireless sensor embedded within metal," *IEEE Sensors Journal,* vol. 18, no. 13, pp. 5550-5558, 2018.

[22] H. Basaeri, D. B. Christensen, and S. Roundy, "A review of acoustic power transfer for bio-medical implants," *Smart Materials and Structures,* vol. 25, no. 12, p. 123001, 2016/11/11 2016, doi: 10.1088/0964-1726/25/12/123001.

[23] A. Alabsi *et al.*, "Wireless power transfer technologies, applications, and future trends: a review," *IEEE Transactions on Sustainable Computing,* 2024.

[24] S. Singh, M. Kumar, and R. Kumar, "Powering the future: A survey of ambient RF‐based communication systems for next‐gen wireless networks," *IET Wireless Sensor Systems,* vol. 14, no. 6, pp. 265-292, 2024.

[25] Y. Zheng *et al.*, "Wireless laser power transmission: Recent progress and future challenges," *Space Solar Power and Wireless Transmission,* 2024.

[26] N.-T. Nguyen, *Low-power and Energy Efficient Communications*. University of Technology Sydney (Australia), 2022.

[27] Z. Liu, T. Li, S. Li, and C. C. Mi, "Advancements and challenges in wireless power transfer: A comprehensive review," *Nexus,* vol. 1, no. 2, p. 100014, 2024/06/18/ 2024, doi: https://doi.org/10.1016/j.ynexs.2024.100014.

[28] M. Haerinia and R. Shadid, "Wireless power transfer approaches for medical implants: A review," *Signals,* vol. 1, no. 2, pp. 209-229, 2020.

[29] W. Liu, K. Chau, X. Tian, H. Wang, and Z. Hua, "Smart wireless power transfer—opportunities and challenges," *Renewable and Sustainable Energy Reviews,* vol. 180, p. 113298, 2023.

[30] L. Meile, A. Ulrich, and M. Magno, "Wireless power transmission powering miniaturized low power IoT devices: A Revie," in *2019 IEEE 8th International Workshop on Advances in Sensors and Interfaces (IWASI)*, 2019: IEEE, pp. 312-317.

[31] C. Lin, *Wireless Rechargeable Sensor Networks for Internet of Things: Theories and Technical Paradigms*. Springer Nature, 2024.

[32] D. a. Wang *et al.*, "Modern advances in magnetic materials of wireless power transfer systems: A review and new perspectives," *Nanomaterials,* vol. 12, no. 20, p. 3662, 2022.

[33] Y. Hu, X. Li, W. Dong, H. Zhang, and X. Wang, "The application progress of wireless power transfer in space utilization field," in *International Conference on Wireless Power Transfer*, 2023: Springer, pp. 520-532.

[34] M. Tamura, T. Segawa, and M. Matsumoto, "Capacitive Coupler for Wireless Power Transfer to Intravascular Implant Devices," *IEEE Microwave and Wireless Components Letters,* vol. 32, no. 6, pp. 672-675, 2022, doi: 10.1109/LMWC.2022.3160688.

[35] L. Yang *et al.*, "Analysis and design of four-plate capacitive wireless power transfer system for undersea applications," *CES Transactions on Electrical Machines and Systems,* vol. 5, no. 3, pp. 202-211, 2021, doi: 10.30941/CESTEMS.2021.00024.

[36] B. Luo, T. Long, L. Guo, R. Dai, R. Mai, and Z. He, "Analysis and Design of Inductive and Capacitive Hybrid Wireless Power Transfer System for Railway Application," *IEEE Transactions on Industry Applications,* vol. 56, no. 3, pp. 3034-3042, 2020, doi: 10.1109/TIA.2020.2979110.
[37] C. Cai, X. Liu, S. Wu, X. Chen, W. Chai, and S. Yang, "A Misalignment Tolerance and Lightweight Wireless Charging System via Reconfigurable Capacitive Coupling for Unmanned Aerial Vehicle Applications," *IEEE Transactions on Power Electronics,* vol. 38, no. 1, pp. 22-26, 2023, doi: 10.1109/TPEL.2022.3198529.
[38] S. R. Hui, "Magnetic resonance for wireless power transfer," *IEEE Power Electronics Magazine,* vol. 3, no. 1, pp. 14-31, 2016.
[39] J. Rahulkumar *et al.*, "An empirical survey on wireless inductive power pad and resonant magnetic field coupling for in-motion EV charging system," *IEEE Access,* vol. 11, pp. 4660-4693, 2022.
[40] A. Rajagopalan, A. K. RamRakhyani, D. Schurig, and G. Lazzi, "Improving power transfer efficiency of a short-range telemetry system using compact metamaterials," *IEEE Transactions on Microwave Theory and Techniques,* vol. 62, no. 4, pp. 947-955, 2014.
[41] S. D. Barman, A. W. Reza, N. Kumar, M. E. Karim, and A. B. Munir, "Wireless powering by magnetic resonant coupling: Recent trends in wireless power transfer system and its applications," *Renewable and Sustainable energy reviews,* vol. 51, pp. 1525-1552, 2015.
[42] B. L. Cannon, J. F. Hoburg, D. D. Stancil, and S. C. Goldstein, "Magnetic resonant coupling as a potential means for wireless power transfer to multiple small receivers," *IEEE transactions on power electronics,* vol. 24, no. 7, pp. 1819-1825, 2009.
[43] C. Raja, M. Ramachandran, and M. Selvam, "Opportunities and Challenges for Wireless Power Transfer System," *Journal on Applied and Chemical Physics,* vol. 1, no. 1, pp. 14-21, 2022.
[44] T. Campi, S. Cruciani, F. Maradei, and M. Feliziani, "Electromagnetic interference in cardiac implantable electronic devices due to dynamic wireless power systems for electric vehicles," *Energies,* vol. 16, no. 9, p. 3822, 2023.
[45] G. Monti *et al.*, "EMC and EMI issues of WPT systems for wearable and implantable devices," *IEEE Electromagnetic Compatibility Magazine,* vol. 7, no. 1, pp. 67-77, 2018.
[46] G. Palani and U. Sengamalai, "A critical review on inductive wireless power transfer charging system in electric vehicle," *Energy Storage,* vol. 5, no. 5, p. e407, 2023.
[47] C. Bharatiraja, A. Mahesh, and B. Lehman, "Power Electronic Converters in Inductive Wireless Charging Applications for Electric Transportation," *IEEE Journal of Emerging and Selected Topics in Power Electronics,* 2025.
[48] W. Nattakarn, "CMOS-based optical power-transfer system for implantable and wearable medical devices," 2020.
[49] X. Mou, D. T. Gladwin, R. Zhao, and H. Sun, "Survey on magnetic resonant coupling wireless power transfer technology for electric vehicle charging," *IET Power Electronics,* vol. 12, no. 12, pp. 3005-3020, 2019.
[50] P. Maharjan, M. Salauddin, H. Cho, and J. Y. Park, "An indoor power line based magnetic field energy harvester for self-powered wireless sensors in smart home applications," *Applied energy,* vol. 232, pp. 398-408, 2018.
[51] V. Singh, R. Bhandari, Y. Singh, S. Sehrawat, and K. Pandey, "Wireless power transfer for automated industrial applications: A prototype," in *2020 8th International Conference on Reliability, Infocom Technologies and Optimization (Trends and Future Directions) (ICRITO)*, 2020: IEEE, pp. 63-67.

[52] Z. Zhang, "Fractional-order time-sharing-control-based wireless power supply for multiple appliances in intelligent building," *Journal of Advanced Research,* vol. 25, pp. 227-234, 2020/09/01/ 2020, doi: https://doi.org/10.1016/j.jare.2020.04.013.
[53] J. Xu, F. Dai, Y. Xu, C. Yao, and C. Li, "Wireless power supply technology for uniform magnetic field of intelligent greenhouse sensors," *Computers and Electronics in Agriculture,* vol. 156, pp. 203-208, 2019/01/01/ 2019, doi: https://doi.org/10.1016/j.compag.2018.11.014.
[54] Y. Jia, L. Zhao, Z. Wang, C. Tang, F. Chen, and H. Feng, "Integrated LCC-LCC Topology for WPT System With CC Output Regarding Air Gap and Load Variations," *IEEE Transactions on Power Electronics,* vol. 39, no. 10, pp. 11904-11915, 2024, doi: 10.1109/TPEL.2024.3413068.
[55] X. Liu, G. Chen, D. Su, X. Wu, W. Gong, and F. Ren, "A 100kW Magnetic Coupled Wireless Power Transfer System for Electrical Vehicles," in *2023 IEEE 5th International Conference on Power, Intelligent Computing and Systems (ICPICS)*, 14-16 July 2023 2023, pp. 48-52, doi: 10.1109/ICPICS58376.2023.10235382.
[56] M. R. Awal, M. Jusoh, T. Sabapathy, M. R. Kamarudin, and R. A. Rahim, "State‐of‐the‐Art Developments of Acoustic Energy Transfer," *International Journal of Antennas and Propagation,* vol. 2016, no. 1, p. 3072528, 2016.
[57] M. I. S. Faiz, M. R. Awal, M. R. Basar, N. A. A. Latiff, M. S. Yahya, and S. Saat, "A Comparative Review on Acoustic and Inductive Power Transfer," *Journal of Advanced Research in Applied Sciences and Engineering Technology,* vol. 44, no. 1, pp. 188-224, 2025.
[58] V. F.-G. Tseng, S. S. Bedair, J. J. Radice, T. E. Drummond, and N. Lazarus, "Ultrasonic Lamb waves for wireless power transfer," *IEEE transactions on ultrasonics, ferroelectrics, and frequency control,* vol. 67, no. 3, pp. 664-670, 2019.
[59] K. Fujimori, "Ultrasonic WPT," in *Theory and Technology of Wireless Power Transfer*: CRC Press, 2024, pp. 246-259.
[60] S. Saat *et al.*, "The Development of Wireless Power Transfer Technologies for Low Power Applications: An Acoustic Based Approach," *Journal of Telecommunication, Electronic and Computer Engineering (JTEC),* vol. 7, no. 2, pp. 129-135, 2015.
[61] T. J. Winnard, "Theoretical parametric study of through-wall acoustic energy transfer systems," Virginia Tech, 2021.
[62] Y. Zheng *et al.*, "Enhancing ultrasound power transfer: Efficiency, acoustics, and future directions," *Advanced Materials,* p. 2407395, 2024.
[63] H. Basaeri, Y. Yu, D. Young, and S. Roundy, "Acoustic power transfer for biomedical implants using piezoelectric receivers: effects of misalignment and misorientation," *Journal of Micromechanics and Microengineering,* vol. 29, no. 8, p. 084004, 2019.
[64] R. V. Taalla, M. S. Arefin, A. Kaynak, and A. Z. Kouzani, "A review on miniaturized ultrasonic wireless power transfer to implantable medical devices," *IEEE access,* vol. 7, pp. 2092-2106, 2018.
[65] R. Guida, E. Demirors, N. Dave, and T. Melodia, "Underwater ultrasonic wireless power transfer: A battery-less platform for the internet of underwater things," *IEEE Transactions on Mobile Computing,* vol. 21, no. 5, pp. 1861-1873, 2020.
[66] H. F. Leung, B. J. Willis, and A. P. Hu, "Wireless electric power transfer based on Acoustic Energy through conductive media," in *2014 9th IEEE Conference on Industrial Electronics and Applications*, 2014: IEEE, pp. 1555-1560.
[67] K. Jin and W. Zhou, "Wireless laser power transmission: A review of recent progress," *IEEE Transactions on Power Electronics,* vol. 34, no. 4, pp. 3842-3859, 2018.

[68] J. Kang, L. Sun, Y. Zhou, and Y. Bai, "Enhancing Alignment Accuracy in Laser Wireless Power Transmission Systems Using Integrated Target Detection and Perturbation-Observation Method," in *Photonics*, 2024, vol. 11, no. 11: MDPI, p. 1094.
[69] W. S. P. ALEXANDER, "Study of Optical Wireless Power Transmission to Moving Objects," Kanazawa University, 2020.
[70] H. Yigit and A. R. Boynuegri, "Pulsed Laser Diode Based Wireless Power Transmission Application: Determination of Voltage Amplitude, Frequency, and Duty Cycle," *IEEE Access,* vol. 11, pp. 54544-54555, 2023.
[71] X. Hou, S. Dong, L. Zhou, and D. Shi, "High Power Electric Generation and WPT Demonstration Mission," in *2024 IEEE Wireless Power Technology Conference and Expo (WPTCE)*, 2024: IEEE, pp. 552-556.
[72] T. Miyamoto, "Optical WPT," in *Theory and Technology of Wireless Power Transfer*: CRC Press, 2024, pp. 179-245.
[73] A. Saha, S. Iqbal, M. Karmaker, S. F. Zinnat, and M. T. Ali, "A wireless optical power system for medical implants using low power near-IR laser," in *2017 39th Annual International Conference of the IEEE Engineering in Medicine and Biology Society (EMBC)*, 2017: IEEE, pp. 1978-1981.
[74] R. M. Dickinson, "Safety issues in SPS wireless power transmission," *Space Policy,* vol. 16, no. 2, pp. 117-122, 2000.
[75] C. Zuo and T. Miyamoto, "Camera-Based Safety System for Optical Wireless Power Transmission Using Dynamic Safety-Distance," in *Photonics*, 2024, vol. 11, no. 6: Multidisciplinary Digital Publishing Institute, p. 500.
[76] L. Rizzo, J. F. Federici, S. Gatley, I. Gatley, J. L. Zunino, and K. J. Duncan, "Comparison of terahertz, microwave, and laser power beaming under clear and adverse weather conditions," *Journal of Infrared, Millimeter, and Terahertz Waves,* vol. 41, pp. 979-996, 2020.
[77] A. Elfarran, "Optimizing Laser-Based Wireless Power Transfer: A Comprehensive Study of a 4 Quadrant PV Module System and Its Powering and Tracking Capabilities," The University of North Dakota, 2024.
[78] L. Sun, J. Kang, F. Kong, and Y. Lyu, "Efficiency Analysis and Optimization for Laser Wireless Power Transmission: A Review of Recent Progress," in *Conference Proceedings of 2021 International Joint Conference on Energy, Electrical and Power Engineering: Component Design, Optimization and Control Algorithms in Electrical and Power Engineering Systems*, 2022: Springer, pp. 641-648.
[79] W. Zhou, K. Jin, M. Wang, and Q. Wu, "Efficiency evaluation of laser based wireless power transmission system," in *2020 IEEE Applied Power Electronics Conference and Exposition (APEC)*, 2020: IEEE, pp. 3147-3150.
[80] Y. Zheng *et al.*, "Wireless laser power transmission: Recent progress and future challenges," *Space Solar Power and Wireless Transmission,* vol. 1, no. 1, pp. 17-26, 2024/06/01/ 2024, doi: https://doi.org/10.1016/j.sspwt.2023.12.001.
[81] V. V. Apollonov, "Laser source for wireless power transmission in space," *Open Access Library Journal,* vol. 2, no. 10, p. 1, 2015.
[82] A. Sahai and D. Graham, "Optical wireless power transmission at long wavelengths," in *2011 International Conference on Space Optical Systems and Applications (ICSOS)*, 2011: IEEE, pp. 164-170.
[83] Q. Chen, D. Zhang, D. Zhu, Q. Shi, J. Gu, and Y. Ai, "Design and experiment for realization of laser wireless power transmission for small unmanned aerial vehicles," in *AOPC 2015: Advances in Laser Technology and Applications*, 2015, vol. 9671: SPIE, pp. 133-139.

[84] A. Mohammadnia, B. M. Ziapour, H. Ghaebi, and M. H. Khooban, "Feasibility assessment of next-generation drones powering by laser-based wireless power transfer," *Optics & Laser Technology,* vol. 143, p. 107283, 2021.
[85] H. Kaushal and G. Kaddoum, "Applications of lasers for tactical military operations," *IEEE Access,* vol. 5, pp. 20736-20753, 2017.
[86] M. A. Sennouni, B. Abboud, A. Tribak, H. Bennis, and M. Latrach, "Advance and Innovation in Wireless Power Transmission Technology for Autonomous Systems," in *Handbook of Research on Advanced Trends in Microwave and Communication Engineering*: IGI Global, 2017, pp. 316-361.
[87] X. Lu, P. Wang, D. Niyato, D. I. Kim, and Z. Han, "Wireless networks with RF energy harvesting: A contemporary survey," *IEEE Communications Surveys & Tutorials,* vol. 17, no. 2, pp. 757-789, 2014.
[88] P. S. Yedavalli, T. Riihonen, X. Wang, and J. M. Rabaey, "Far-field RF wireless power transfer with blind adaptive beamforming for Internet of Things devices," *IEEE Access,* vol. 5, pp. 1743-1752, 2017.
[89] R. La Rosa, P. Livreri, C. Trigona, L. Di Donato, and G. Sorbello, "Strategies and techniques for powering wireless sensor nodes through energy harvesting and wireless power transfer," *Sensors,* vol. 19, no. 12, p. 2660, 2019.
[90] S. Sasaki, K. Tanaka, and K.-i. Maki, "Microwave power transmission technologies for solar power satellites," *Proceedings of the IEEE,* vol. 101, no. 6, pp. 1438-1447, 2013.
[91] J. L.-W. Li, "Wireless power transmission: State-of-the-arts in technologies and potential applications," in *Asia-Pacific Microwave Conference 2011*, 2011: IEEE, pp. 86-89.
[92] E. D. Nwalike, K. A. Ibrahim, F. Crawley, Q. Qin, P. Luk, and Z. Luo, "Harnessing energy for wearables: a review of radio frequency energy harvesting technologies," *Energies,* vol. 16, no. 15, p. 5711, 2023.
[93] S. K. Divakaran, D. D. Krishna, and Nasimuddin, "RF energy harvesting systems: An overview and design issues," *International Journal of RF and Microwave Computer ‐ Aided Engineering,* vol. 29, no. 1, p. e21633, 2019.
[94] S. El Hassani, H. El Hassani, and N. Boutammachte, "Overview on 5G radio frequency energy harvesting," *ASTESJ,* vol. 4, pp. 328-346, 2019.
[95] A. S. Poon, S. O'Driscoll, and T. H. Meng, "Optimal frequency for wireless power transmission into dispersive tissue," *IEEE Transactions on Antennas and Propagation,* vol. 58, no. 5, pp. 1739-1750, 2010.
[96] M. Wagih, A. S. Weddell, and S. Beeby, "Rectennas for radio-frequency energy harvesting and wireless power transfer: A review of antenna design [antenna applications corner]," *IEEE Antennas and Propagation Magazine,* vol. 62, no. 5, pp. 95-107, 2020.
[97] J. I. Agbinya, *Wireless power transfer*. River Publishers, 2022.
[98] Y. Zeng, B. Clerckx, and R. Zhang, "Communications and signals design for wireless power transmission," *IEEE Transactions on Communications,* vol. 65, no. 5, pp. 2264-2290, 2017.
[99] L. M. Borges, R. Chávez ‐ Santiago, N. Barroca, F. J. Velez, and I. Balasingham, "Radio ‐ frequency energy harvesting for wearable sensors," *Healthcare technology letters,* vol. 2, no. 1, pp. 22-27, 2015.
[100] J. Moore, S. Castellanos, S. Xu, B. Wood, H. Ren, and Z. T. H. Tse, "Applications of wireless power transfer in medicine: State-of-the-art reviews," *Annals of biomedical engineering,* vol. 47, pp. 22-38, 2019.
[101] Z. Meng, Y. Liu, N. Gao, Z. Zhang, Z. Wu, and J. Gray, "Radio frequency identification and sensing: integration of wireless powering, sensing, and communication for IIoT innovations," *IEEE Communications Magazine,* vol. 59, no. 3, pp. 38-44, 2021.

[102] L. Schulthess, F. Villani, P. Mayer, and M. Magno, "RF Power Transmission for Self-sustaining Miniaturized IoT Devices," in *2022 29th IEEE International Conference on Electronics, Circuits and Systems (ICECS)*, 24-26 Oct. 2022, 2022, pp. 1-4, doi: 10.1109/ICECS202256217.2022.9970865.
[103] I. Colmiais, H. Dinis, and P. M. Mendes, "Long-Range Wireless Power Transfer for Moving Wireless IoT Devices," *Electronics,* vol. 13, no. 13, p. 2550, 2024. [Online]. Available: https://www.mdpi.com/2079-9292/13/13/2550.
[104] J. Tepper *et al.*, "Evaluation of RF Wireless Power Transfer for Low-Power Aircraft Sensors," in *2020 AIAA/IEEE 39th Digital Avionics Systems Conference (DASC)*, 11-15 Oct. 2020, 2020, pp. 1-6, doi: 10.1109/DASC50938.2020.9256404.
[105] S. A. A. Shah and H. Yoo, "Radiative Near-Field Wireless Power Transfer to Scalp-Implantable Biotelemetric Device," *IEEE Transactions on Microwave Theory and Techniques,* vol. 68, no. 7, pp. 2944-2953, 2020, doi: 10.1109/TMTT.2020.2985356.
[106] M. A. Tanha, F. F. Hanzaee, R. Bayford, and A. Demosthenous, "RF Wireless Power Transfer for EIT Neonate Lung Function Monitoring," in *2021 IEEE International Symposium on Circuits and Systems (ISCAS)*, 22-28 May 2021, 2021, pp. 1-5, doi: 10.1109/ISCAS51556.2021.9401148.
[107] K. S. Alam *et al.*, "Towards net zero: A technological review on the potential of space-based solar power and wireless power transmission," *Heliyon,* vol. 10, no. 9, 2024, doi: 10.1016/j.heliyon. 2024.e29996.
[108] P. Malaviya, V. Sarvaiya, A. Shah, D. Thakkar, and M. Shah, "A comprehensive review on space solar power satellite: an idiosyncratic approach," *Environmental Science and Pollution Research,* vol. 29, no. 28, pp. 42476-42492, 2022/06/01 2022, doi: 10.1007/s11356-022-19560-w.
[109] T. D. P. Perera, D. N. K. Jayakody, S. K. Sharma, S. Chatzinotas, and J. Li, "Simultaneous Wireless Information and Power Transfer (SWIPT): Recent Advances and Future Challenges," *IEEE Communications Surveys & Tutorials,* vol. 20, no. 1, pp. 264-302, 2018, doi: 10.1109/COMST.2017.2783901.
[110] M. Aboualalaa and H. Elsadek, "Rectenna systems for RF energy harvesting and wireless power transfer," *Recent Wireless Power Transfer Technologies,* pp. 1-24, 2020.
[111] powercast. "The PowerSpot creates an overnight charging zone of up to 80 feet free of wires or charging mats." https://www.powercastco.com/technologies/ (accessed 12/12, 2024).
[112] X. Zhu, K. Jin, Q. Hui, W. Gong, and D. Mao, "Long-range wireless microwave power transmission: A review of recent progress," *IEEE Journal of Emerging and Selected Topics in Power Electronics,* vol. 9, no. 4, pp. 4932-4946, 2020.
[113] I. A. Shah, M. Zada, S. A. A. Shah, A. Basir, and H. Yoo, "Flexible metasurface-coupled efficient wireless power transfer system for implantable devices," *IEEE Transactions on Microwave Theory and Techniques,* 2023.
[114] J. Soleimani and G. Karabulut Kurt, "High‐power radio frequency wireless energy transfer system: Comprehensive survey on design challenges," *IET Wireless Sensor Systems,* vol. 14, no. 6, pp. 248-264, 2024.
[115] Y. Luo, L. Pu, G. Wang, and Y. Zhao, "RF energy harvesting wireless communications: RF environment, device hardware and practical issues," *Sensors,* vol. 19, no. 13, p. 3010, 2019.
[116] J. C. Kwan and A. O. Fapojuwo, "Radio frequency energy harvesting and data rate optimization in wireless information and power transfer sensor networks," *IEEE Sensors Journal,* vol. 17, no. 15, pp. 4862-4874, 2017.

[117] C. R. Valenta and G. D. Durgin, "Harvesting wireless power: Survey of energy-harvester conversion efficiency in far-field, wireless power transfer systems," *IEEE microwave magazine,* vol. 15, no. 4, pp. 108-120, 2014.
[118] H. Mazar, *Radio spectrum Management: Policies, regulations and techniques*. John Wiley & Sons, 2016.
[119] C. Kalialakis and A. Georgiadis, "The regulatory framework for wireless power transfer systems," *Wireless Power Transfer,* vol. 1, no. 2, pp. 108-118, 2014.
[120] J. C. Lin, "Safety of wireless power transfer," *IEEE Access,* vol. 9, pp. 125342-125347, 2021.
[121] Q. Liu, K. S. Yildirim, P. Pawełczak, and M. Warnier, "Safe and secure wireless power transfer networks: Challenges and opportunities in RF-based systems," *IEEE Communications Magazine,* vol. 54, no. 9, pp. 74-79, 2016.
[122] M. Kesler, "Highly resonant wireless power transfer: safe, efficient, and over distance," *Witricity corporation,* pp. 1-32, 2013.
[123] A. Christ, M. Douglas, J. Nadakuduti, and N. Kuster, "Assessing human exposure to electromagnetic fields from wireless power transmission systems," *Proceedings of the IEEE,* vol. 101, no. 6, pp. 1482-1493, 2013.
[124] S. Chhawchharia, S. K. Sahoo, M. Balamurugan, S. Sukchai, and F. Yanine, "Investigation of wireless power transfer applications with a focus on renewable energy," *Renewable and Sustainable Energy Reviews,* vol. 91, pp. 888-902, 2018.
[125] K. Obaideen, L. Albasha, U. Iqbal, and H. Mir, "Wireless power transfer: Applications, challenges, barriers, and the role of AI in achieving sustainable development goals-A bibliometric analysis," *Energy Strategy Reviews,* vol. 53, p. 101376, 2024.
[126] G. K. Ijemaru, K. L.-M. Ang, and J. K. Seng, "Wireless power transfer and energy harvesting in distributed sensor networks: Survey, opportunities, and challenges," *International journal of distributed sensor networks,* vol. 18, no. 3, p. 15501477211067740, 2022.
[127] O. Okoyeigbo, A. Olajube, O. Shobayo, A. Aligbe, and A. Ibhaze, "Wireless power transfer: a review," in *IOP Conference Series: Earth and Environmental Science*, 2021, vol. 655, no. 1: IOP Publishing, p. 012032.
[128] M. Wagih *et al.*, "Microwave-enabled wearables: Underpinning technologies, integration platforms, and next-generation roadmap," *IEEE Journal of Microwaves,* vol. 3, no. 1, pp. 193-226, 2022.
[129] S. A. H. Mohsan and H. Amjad, "A comprehensive survey on hybrid wireless networks: practical considerations, challenges, applications and research directions," *Optical and Quantum Electronics,* vol. 53, no. 9, p. 523, 2021.
[130] X. Chen, S. Yu, and X. Yang, "Hybrid wireless power transfer," in *IECON 2017-43rd Annual Conference of the IEEE Industrial Electronics Society*, 2017: IEEE, pp. 5348-5352.
[131] M. F. Mahmood, S. L. Mohammed, S. K. Gharghan, A. Al-Naji, and J. Chahl, "Hybrid coils-based wireless power transfer for intelligent sensors," *Sensors,* vol. 20, no. 9, p. 2549, 2020.
[132] B. Luo, T. Long, R. Mai, R. Dai, Z. He, and W. Li, "Analysis and design of hybrid inductive and capacitive wireless power transfer for high‐power applications," *IET Power Electronics,* vol. 11, no. 14, pp. 2263-2270, 2018.
[133] Y. Ma, Y. Jiang, and C. Li, "Combined RF-Ultrasonic Wireless Powering System for Sensor Applications in Harsh Environment," in *2024 IEEE Radio and Wireless Symposium (RWS)*, 2024: IEEE, pp. 87-90.
[134] I. C. o. N.-I. R. Protection, "Guidelines for limiting exposure to electromagnetic fields (100 kHz to 300 GHz)," *Health physics,* vol. 118, no. 5, pp. 483-524, 2020.

[135] A. A. Aziz and F. Suratman, "Reconfigurable Intelligent Surface-Assisted RF Wireless Power Transfer for Internet of Things System: Modeling and Evaluation," *Buletin Pos dan Telekomunikasi,* vol. 22, no. 1, pp. 12-24, 2024.
[136] M. Tavana, "RF Energy Harvesting for Zero-Energy Devices and Reconfigurable Intelligent Surfaces," KTH Royal Institute of Technology, 2024.
[137] C. A. Balanis, *Antenna theory: analysis and design*, Fourth ed. (no. Book, Whole). Hoboken, New Jersey: John Wiley & Sons, Inc (in English), 2016.
[138] P. Series, "Propagation data and prediction methods for the planning of indoor radiocommunication systems and radio local area networks in the frequency range 300 MHz to 450 GHz," *ITU recommmendations,* vol. ITU-R P.1238-12, 2023.
[139] P. Series, "Propagation data and prediction methods for the planning of short-range outdoor radiocommunication systems and radio local area networks in the frequency range 300 MHz to 100 GHz," *ITU recommmendations,* vol. ITU-R P.1411-12, 2023.
[140] K. Wilt, T. Lawry, H. Scarton, and G. Saulnier, "One-dimensional pressure transfer models for acoustic–electric transmission channels," *Journal of Sound and Vibration,* vol. 352, pp. 158-173, 2015.
[141] Y. Du *et al.*, "Two-dimensional equivalent circuit model of ultrasonic wireless power transmission," *IEEE Transactions on Industrial Electronics,* vol. 70, no. 1, pp. 975-984, 2022.
[142] L. S. Mendonça, E. V. Minuzzi, J. P. S. Cipriani, M. Radecker, and F. E. Bisogno, "State-Space Model of an Electro-Mechanical-Acoustic Contactless Energy Transfer System Based on Multiphysics Networks," *IEEE Transactions on Ultrasonics, Ferroelectrics, and Frequency Control,* vol. 69, no. 1, pp. 241-253, 2021.
[143] J. Jiao, Z. Qiao, B. Liu, J. Yang, and X. Gao, "Establishment and Application of a Semianalytical Model of Ultrasonic Power Transfer," *IEEE/ASME Transactions on Mechatronics,* pp. 1-11, 2024, doi: 10.1109/TMECH.2024.3393450.
[144] M. Wu, X. Chen, C. Qi, and X. Mu, "Considering losses to enhance circuit model accuracy of ultrasonic wireless power transfer system," *IEEE Transactions on Industrial Electronics,* vol. 67, no. 10, pp. 8788-8798, 2019.
[145] Y. Ma, Y. Jiang, and C. Li, "A Universal Model for Ultrasonic Energy Transmission in Various Media," *Sensors,* vol. 24, no. 19, p. 6230, 2024.
[146] K. Uchino, "5 - Piezoelectric energy harvesting systems with metal oxides," in *Metal Oxides in Energy Technologies*, Y. Wu Ed.: Elsevier, 2018, pp. 91-126.
[147] A. D. Pierce and A. Acoustics, "Introduction to its physical principles and applications," *Acoustical Society of America and American Institute of Physics,* p. 122, 1981.
[148] D. A. Bies and C. H. Hansen, *Engineering noise control: theory and practice*. CRC press, 2003.
[149] L. E. Kinsler, A. R. Frey, A. B. Coppens, and J. V. Sanders, *Fundamentals of acoustics*. John wiley & sons, 2000.
[150] E. Meyer, *Physical and applied acoustics: an introduction*. Elsevier, 2012.
[151] H. Georgi, *The physics of waves*. Prentice Hall Englewood Cliffs, NJ, 1993.
[152] M. A. Hanson, *Health effects of exposure to ultrasound and infrasound: Report of the independent advisory group on non-ionising radiation*. Health Protection Agency, 2010.
[153] *IEC 60601-2-37 Medical electrical equipment - Part 2-37: Particular requirements for the basic safety and essential performance of ultrasonic medical diagnostic and monitoring equipment*, IEC, 2024. [Online]. Available: https://webstore.iec.ch/en/publication/78093?utm_source=chatgpt.com

[154] H. Canada, "Guidelines for the safe use of ultrasound: Part II—Industrial and commercial applications safety code 24," ed: Health Protection Branch, Environmental Health Directorate, National Health …, 1991.
[155] K. Karipidis *et al.*, "Validity of the 1984 Interim Guidelines on Airborne Ultrasound and Gaps in the Current Knowledge," *Health Physics,* p. 10.1097, 2023.
[156] M. Almalkawi, *RF and Microwave Module Level Design and Integration*. Institution of Engineering and Technology, 2019.
[157] "Full Wave Rectifier and Bridge Rectifier Theory." https://www.electronics-tutorials.ws/diode/diode_6.html?utm_source=chatgpt.com accessed.
[158] D. Vinko, T. Svedek, and T. Matic, "Modification of the Cockcroft-Walton charge pump by using switched capacitors technique for improved performance under capacitive loads," *WSEAS Transactions on Circuits and Systems,* vol. 8, no. 1, pp. 167-176, 2009.
[159] M.-D. Ker, S.-L. Chen, and C.-S. Tsai, "A new charge pump circuit dealing with gate-oxide reliability issue in low-voltage processes," in *2004 IEEE International Symposium on Circuits and Systems (ISCAS)*, 2004, vol. 1: IEEE, pp. I-I.
[160] L. EETech Group. "Understanding the Operation of a Boost Converter." https://www.allaboutcircuits.com/technical-articles/understanding-the-operation-of-a-boost-converter/?utm_source=chatgpt.com accessed.
[161] J. Zhang, M. Gu, and X. Chen, "Supercapacitors for renewable energy applications: A review," *Micro and Nano Engineering,* p. 100229, 2023.
[162] A. Nejati, S. Radfar, P. Amiri, and M. H. Maghami, "A bulk-driven differential CMOS schmitt trigger with adjustable hysteresis for ultra-low-voltage operation," *Microelectronics Journal,* vol. 114, p. 105129, 2021/08/01/ 2021, doi: https://doi.org/10.1016/j.mejo.2021.105129.
[163] M. M. M. Toledo and J. A. Hora, "Low Power Gate Voltage Controlled Schmitt Trigger with Adjustable Hysteresis and 0.1 V th Margin in 22nm FDSOI," in *TENCON 2023-2023 IEEE Region 10 Conference (TENCON)*, 2023: IEEE, pp. 301-305.
[164] P. Singhanath, A. Suadet, A. Kanjanop, T. Thongleam, S. Kuankid, and V. Kasemsuwan, "Low voltage adjustable CMOS Schmitt trigger," in *2011 Fourth International Conference on Modeling, Simulation and Applied Optimization*, 2011: IEEE, pp. 1-4.
[165] K. Lin, X. a. Wang, X. Zhang, B. Wang, and T. Ouyang, "A PVT-independent Schmitt trigger with fully adjustable hysteresis threshold voltages for low-power 1-bit digitization applications," *IEICE Electronics Express,* vol. 13, no. 17, pp. 20160650-20160650, 2016.
[166] E. Corpeño. "Exactly How Schmitt Trigger Oscillators Work." https://www.allaboutcircuits.com/technical-articles/exactly-how-schmitt-trigger-oscillators-work/ accessed.
[167] I. AspenCore. "Op-amp Multivibrator." https://www.electronics-tutorials.ws/opamp/op-amp-multivibrator.html accessed.
[168] Kevin. "The Colpitts oscillator experiment and DIY FM transmitter." https://teardownit.com/posts/the-colpitts-oscillator-experiment-and-diy-fm-transmitter accessed.
[169] I. AspenCore. "Quartz Crystal Oscillators." https://www.electronics-tutorials.ws/oscillator/crystal.html accessed.
[170] I. AspenCore. "Amplifiers." https://www.electronics-tutorials.ws/category/amplifier accessed.
[171] Y. Huang, *Antennas: from theory to practice*. John Wiley & Sons, 2021.
[172] C. Song, Y. Huang, J. Zhou, J. Zhang, S. Yuan, and P. Carter, "A high-efficiency broadband rectenna for ambient wireless energy harvesting," *IEEE Transactions on Antennas and Propagation,* vol. 63, no. 8, pp. 3486-3495, 2015.

[173] C. Song *et al.*, "A novel six-band dual CP rectenna using improved impedance matching technique for ambient RF energy harvesting," *IEEE Transactions on Antennas and Propagation,* vol. 64, no. 7, pp. 3160-3171, 2016.
[174] C. Song *et al.*, "Matching network elimination in broadband rectennas for high-efficiency wireless power transfer and energy harvesting," *IEEE Transactions on Industrial Electronics,* vol. 64, no. 5, pp. 3950-3961, 2016.
[175] L. Li, X. Zhang, C. Song, W. Zhang, T. Jia, and Y. Huang, "Compact dual-band, wide-angle, polarization-angle-independent rectifying metasurface for ambient energy harvesting and wireless power transfer," *IEEE transactions on microwave theory and techniques,* vol. 69, no. 3, pp. 1518-1528, 2020.
[176] W. Deng, S. Wang, B. Yang, and S. Zheng, "A multibeam ambient electromagnetic energy harvester with full azimuthal coverage," *IEEE Internet of Things Journal,* vol. 9, no. 11, pp. 8925-8934, 2021.
[177] J. Zhou, P. Zhang, J. Han, L. Li, and Y. Huang, "Metamaterials and metasurfaces for wireless power transfer and energy harvesting," *Proceedings of the IEEE,* vol. 110, no. 1, pp. 31-55, 2021.
[178] M. Zada, I. A. Shah, A. Basir, and H. Yoo, "Simultaneous wireless power transfer and data telemetry using dual-band smart contact lens," *IEEE Transactions on Antennas and Propagation,* vol. 70, no. 4, pp. 2990-3001, 2021.
[179] M. A. B. Abbasi, V. Fusco, O. Yurduseven, and T. Fromenteze, "Frequency-diverse multimode millimetre-wave constant-ϵ r lens-loaded cavity," *Scientific Reports,* vol. 10, no. 1, p. 22145, 2020.
[180] D. Kitayama, Y. Hama, K. Goto, K. Miyachi, T. Motegi, and O. Kagaya, "Transparent dynamic metasurface for a visually unaffected reconfigurable intelligent surface: controlling transmission/reflection and making a window into an RF lens," *Optics Express,* vol. 29, no. 18, pp. 29292-29307, 2021.
[181] S. Tang, Z. Ma, M. Xiao, and L. Hao, "Hybrid transceiver design for beamspace MIMO-NOMA in code-domain for mmWave communication using lens antenna array," *IEEE Journal on Selected Areas in Communications,* vol. 38, no. 9, pp. 2118-2127, 2020.
[182] M. Zhong, Y. Jiang, Y. Yi, and C. Li, "Bilayer Metasurfaces for Wideband Polarization Conversion with High Efficiency," *Authorea Preprints,* 2024.
[183] W. Zhang, R. Pei, J. Zhang, B. Hu, and J. Zhou, "Matching Network Elimination in Multiband Metasurface-Structured Rectennas for Wireless Power Transfer and Energy Harvesting," in *2024 18th European Conference on Antennas and Propagation (EuCAP)*, 2024: IEEE, pp. 1-4.
[184] A. Mohan and S. Mondal, "An impedance matching strategy for micro-scale RF energy harvesting systems," *IEEE Transactions on Circuits and Systems II: Express Briefs,* vol. 68, no. 4, pp. 1458-1462, 2020.
[185] Y.-X. Lin *et al.*, "Ultra-low turn-on voltage quasi-vertical GaN Schottky barrier diode with homogeneous barrier height," *Solid-State Electronics,* vol. 207, p. 108723, 2023.
[186] X. Yu *et al.*, "900 MHz RF Power Rectifier Based on Ultra-low Turn-on Voltage Quasi-vertical GaN Schottky Diode," in *2024 IEEE Wireless Power Technology Conference and Expo (WPTCE)*, 2024: IEEE, pp. 441-444.
[187] X. Yu *et al.*, "Sensitive Microwave Rectifier for High-Power Wireless Transfer Based on Ultra-Low Turn-On Voltage Quasi-Vertical GaN SBD," *IEEE Open Journal of Power Electronics,* 2024.
[188] Q.-X. Li *et al.*, "Design and Fabrication of Milliwatt and Microwatt Microwave Rectifiers Based on Low Turn-On GaN Schottky Barrier Diodes," *IEEE Microwave and Wireless Technology Letters,* 2025.

[189] P. Mayer, M. Magno, and L. Benini, "Smart power unit—mW-to-nW power management and control for self-sustainable IoT devices," *IEEE Transactions on Power Electronics,* vol. 36, no. 5, pp. 5700-5710, 2020.
[190] G. P. Gautam, "MANIPULATION OF PARTICLES AND FLUID USING BULK ACOUSTIC WAVES IN MICROFLUIDICS," New Mexico Institute of Mining and Technology, 2019.
[191] X. Yang *et al.*, "Digital non-Foster-inspired electronics for broadband impedance matching," *Nature Communications,* vol. 15, no. 1, p. 4346, 2024/05/21 2024, doi: 10.1038/s41467-024-48861-6.